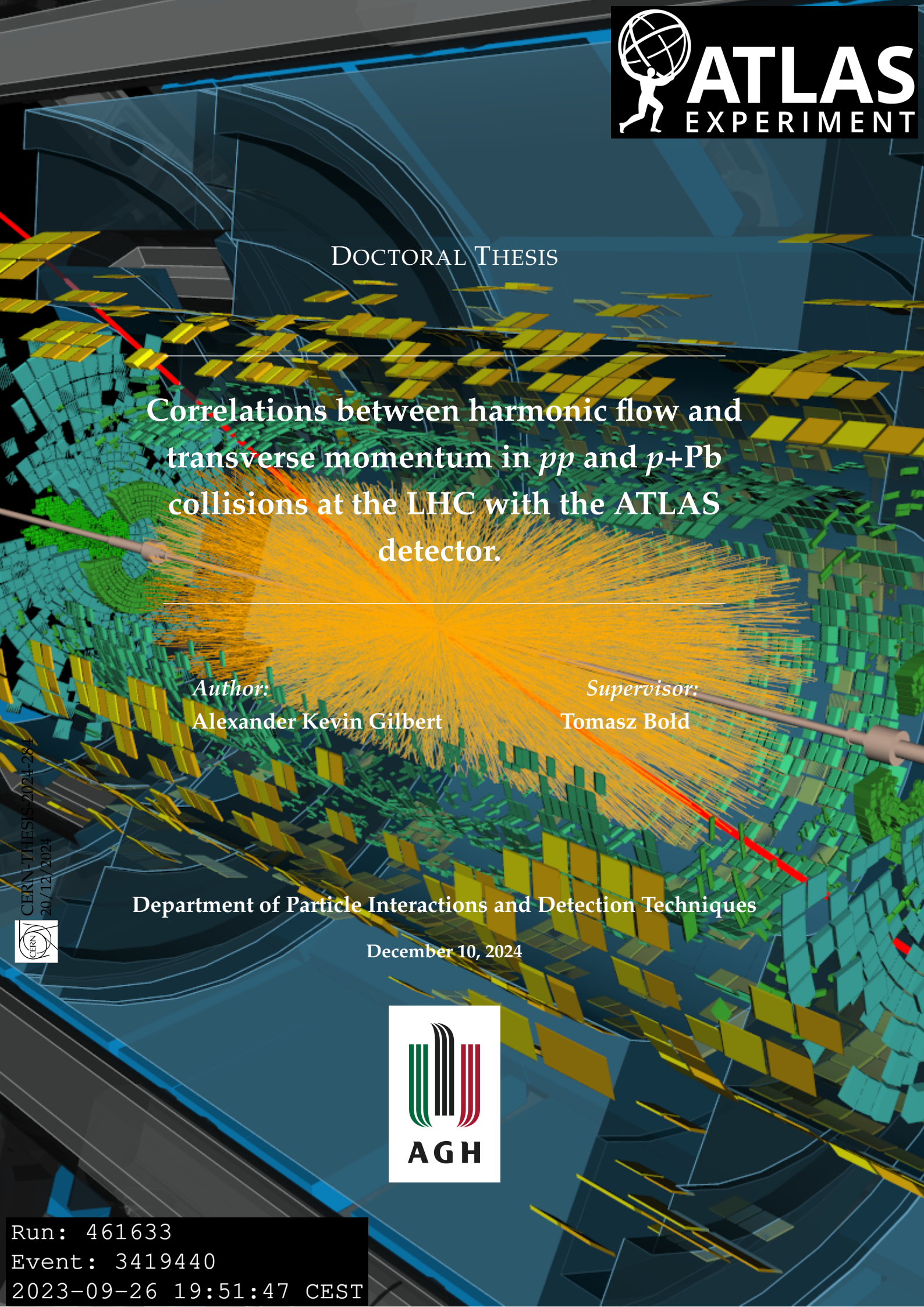

ATLAS EXPERIMENT

Doctoral Thesis

Correlations between harmonic flow and transverse momentum in pp and p+Pb collisions at the LHC with the ATLAS detector.

Author:
Alexander Kevin Gilbert

Supervisor:
Tomasz Bołd

Department of Particle Interactions and Detection Techniques

December 10, 2024

AGH

CERN-THESIS-2024-284
20/12/2024

Run: 461633
Event: 3419440
2023-09-26 19:51:47 CEST

Preface

"Quarks and leptons made us. And now we study them as if the elementary particles have a consciousness to study themselves. We are always on the journey to discover ourselves. Who we are, what our origin is, what will we be. From one quantum state to the next ones."

Doing research as a member of ATLAS Experiment is an abandoned dream came true by accident. When I was in high school, I naively dreamed all ambitious goals, and one of them is to work at CERN. Until I had a mental breakdown in the middle of my 19 during my undergraduate study. So I dropped all of those dreams. I tried to solve the problems in my country, like destruction of environment, poverty and disparity, injustice, and corruption as these problems directly affected my life as well. But they were just too much for me. The academic environment was harsh as well since I was kicked out from a class just because of wearing sandals.

So my undergraduate study stalled by a year. In that year, I stepped back to rearrange my life goal. I alone might not be able to solve those problems, but educating the next generations who will takeover the positions, for example, in government, will lead to the progressive changes. But reforming the education system requires a lot of politics, which is one of the problem sources since it is messy to begin with. Indonesia is not ready for democracy and need a benevolent dictator like Lee Kuan Yew. But what we got was a corrupt dictator who made all the messes at the first place. So instead of staying inside the loop of problems, I set out my goal to build as school using Finnish education system. And hopefully it will set as a role model, along with raising the problem solvers.

I took interest in Papua as I did a community service there, teaching children basic math since they did not meet the expectation of the curriculum due to the teachers' incompetency. Historically, Papua was not a part of Indonesia when we got our independence. The dispute with Netherland over Papua was brought to United Nation and ended in Act of Free Choice, where a sham referendum was conducted by a thousand of Papuans handpicked by Indonesian military forced to choose to join Indonesia. The human right violations still continue to this day while the world turns blind eye on them. And despite having abundant natural resources, the native people are the poorest of all the country. Therefore I decided to build the school there since they need it the most.

So I set my journey to Finland to find the connections for the teacher training. Since I am from a broken home and poor family, the only way to get there is to find the scholarship. And after two years, finally I got it in University of Jyväskylä. I initially interested in dark energy for my master thesis and spacetime quantization, for example, loop quantum gravity for doctoral research. In general relativity, gravity is not a "force" but rather a curvature in the spacetime. It is completely different paradigm compared to quantum field theory where the force is mediated by the exchange of force carrier particles. Perhaps the quantization of spacetime will work

as the quantum theory of gravity since it provides a middle ground for spacetime curvature and particle exchange interpretations.

An interesting twist of fate happened when I did not get a supervisor for those topics and Kari J. Eskola introduced me to an ALICE Experiment member who became my master thesis supervisor, Sami Räsänen. And so, my journey as experimental particle physicist began. I learned ROOT from zero without any basic in programming language with a lot of help from Oskari Saarimäki. I finished my master study and then applied PhD positions everywhere as long as it is one of LHC experiments.

Thanks to Iwona Grabowska-Bołd for offering me the opportunity to study in AGH and Tomasz Bołd who accepted me as his student. My coding skills improved a lot under his guidance. I also thank Mark Sutton for his supervision during my qualification task. Thanks also to Piotr Kotko for pointing me to the right direction in understanding small-x physics. I would like to thanks Patrycja Potępa for being a helpful friend.

During my study, I got opportunities to visit CERN. I took Run Control and Trigger shifts, digging deeper into how data taking procedure in ATLAS is done as well as witnessing how the LHC operate. The cover page on this thesis shows the hard probe event of Pb+Pb collision during the first heavy ion run in Run 3. The event display figure of this collision was created by Mateusz Dyndal on behalf of ATLAS collaboration. I was there in the control room, doing shadow shift to refresh my memory before taking the actual shifts. We got stable beam and Martin Rybar, Aaron Angerami, and Qipeng Hu pooped champagne bottles and we all drank. And a few moments later, we got a problem and the cheers turned down. So we stopped the run and started again. Such an unforgettable moment in the dynamic of data taking at the ATLAS control room. Cheers to the great people I met along the journey and help me to improve. Let this thesis lead me to the next quantum state in the life.

Kraków
January 11, 2024

List of Contribution and Acknowledgement

I declare that the research carried out in this thesis is fully my work. This includes running the analysis, modifying and extending the analysis codes, doing the studies of the obtained observables, and presenting the results to ATLAS Collaboration. Currently, the analysis is being reviewed by editorial board in ATLAS Collaboration before allowed to be published.

During my study, I contributed to the development of minimum bias trigger signature and z-finder algorithm for High Multiplicity Trigger for the Athena framework. The details are explained in section 2.2.5. I also contributed to data taking in ATLAS Experiment by doing Run Control shifts. The task consists of preparing ATLAS detector and setup before stable beam, starting the run for data taking, monitoring detectors health and responding to any issue during the run, monitoring luminosity and changing trigger configuration, and stopping the run.

I also presented the results from ATLAS Collaboration in following conferences: 8th International Conference on Physics and Astrophysics of Quark Gluon Plasma (ICPAQGP-2023) in Puri, India, 42nd International Conference on High Energy Physics (ICHEP-2024) in Prague, Czech, and results of this analysis at ATLAS Poland conferences 2023 and 2024 in Kraków.

This work was partly supported by the National Science Centre of Poland under grant number UMO-2020/37/B/ST2/01043 and by PL-GRID infrastructure. Also, this research project is partly supported by program „Excellence initiative – research university" for the AGH University of Kraków.

Abstract

Correlations between harmonic flow and transverse momentum in *pp* and *p*+Pb collisions at the LHC with the ATLAS detector.

The study of the correlation between harmonic flow v_n and mean transverse momentum $[p_T]$ in proton-proton collisions at $\sqrt{s} = 5.02$ and 13 TeV and proton-lead at $\sqrt{s} = 5.02$ TeV with the ATLAS detector has been conducted. It is performed for charged particles with pseudorapidity range $|\eta| < 2.5$ and various transverse momentum ranges. The measured observable is a modified form of Pearson's correlation coefficient ($\rho\left(v_n\{2\}^2, [p_T]\right)$) between flow $v_n\{2\}^2$ and p_T. The results are presented for harmonics n = 2 and 3, and three arrangements of sub-events.

The results for *pp* are compared with Pythia that does not contain modeling of QGP. It would allow us to study the non-flow contribution to the observed correlation. The effect of QCD color reconnection parameters in Pythia on measured correlation are shown to be significant to reproduce flow-like pattern. The Pythia reproduces qualitatively the same trend as data but fails in describing it quantitatively, indicating a missing physics in this generator. Comparison with EPOS which include hydrodynamic simulation is also studied. The results for *p*-Pb are compared to samples from HIJING in 1-subevent and IP-Glasma+MUSIC+UrQMD and 3+1D hydrodynamic with Glauber initial state.

Keywords: harmonic flow, quark-gluon plasma (QGP), initial condition, modified Pearson correlation coefficient.

Contents

1 Introduction

All particle interactions in our universe can be simplified into four fundamental interactions: electromagnetic interaction, weak interaction, strong interaction, and gravitational interaction. These fundamental interactions, except the gravity which is explained by general relativity, have their own quantum theory based on quantum field theory [**?**]: quantum electrodynamics (QED) for explaining electromagnetic interaction, quantum flavordynamics for explaining weak interaction, and quantum chromodynamics (QCD) for explaining strong interaction. The collection of these quantum theories crystallized into the standard model of particle physics which unite three out of four fundamental interactions into a single Lagrangian equation [**?**]. In this model, all materials we observe in our daily life, including ourselves, are made of the same building blocks of particles: quarks and leptons, together called fermions. As depicted in Figure 1.1 there are three generations of fermions. Quarks initially consist of up and down quarks and leptons consist of electron and electron neutrino. As physicists built more and more powerful particle accelerators, the next two generations of them which have the same quantum properties but are heavier than the first generation were discovered. The interaction between the particles in this model is illustrated as the exchange of the force carrier particles, each corresponding to the type of interaction: electromagnetic interaction is the exchange of photon, strong interaction is the exchange of gluon, and weak interaction is the exchange of $W^{\pm}$ and Z^0 bosons. All particles that have mass get their masses from the Higgs boson after the symmetry breaking in the Higgs mechanism.

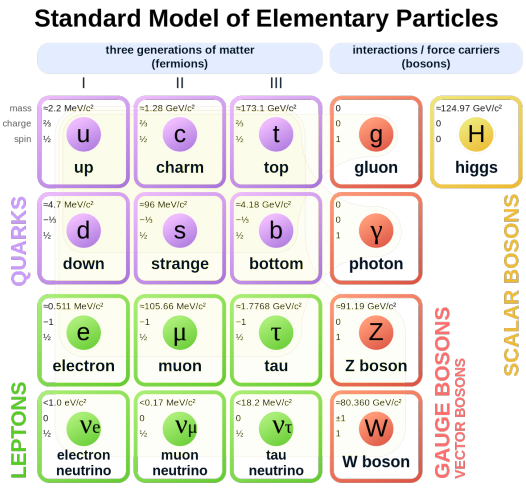

Figure 1.1: The list of the elementary particles in the standard model of particle physics. Figure from [**?**].

The standard model Lagrangian before symmetry breaking can be written as

$$\mathcal{L} = \underbrace{-\frac{1}{4}F_{\mu\nu}F^{\mu\nu}}_{\text{Gauge symmetry}} + \underbrace{i\bar{\psi}\not{D}\psi + h.c.}_{\text{Fermion sector}} + \underbrace{\psi_i y_{ij}\psi_j\phi + h.c.}_{\text{Yukawa term}} + \underbrace{|D_\mu\phi|^2 - V(\phi)}_{\text{Higgs sector}} \tag{1.1}$$

with $F_{\mu\nu}$ is the sum of the field strength tensor of the three interactions, ψ is the Fermion fields, ϕ is the Higgs field, $\not{D} = \gamma^\mu D_\mu$ is the covariant derivative D_μ with Dirac gamma matrices γ^μ, $y_{i,j}$ is the Yukawa coupling, $V(\phi)$ is the Higgs potential, and $h.c.$ is the Hermitian conjugate of its predecessor term.

The gauge symmetry term contains the kinetic energies of all gauge bosons and self-interaction of weak and strong force carriers. The fermion sector contains the kinetic energies of fermions and their interactions with another fermion mediated by the gauge boson according to its type of interaction. The interaction terms are written implicitly inside D_μ. These interactions arise because the Lagrangian needs to be invariant under local gauge transformation of the symmetry groups corresponding to their interactions: electromagnetic interaction with $U(1)$ symmetry, weak interaction with $SU(2)_L$ symmetry which only involves left-handed Fermions, and strong interaction with $SU(3)$ symmetry which only involves quarks. The fact that the right-handed neutrino has never been observed in nuclear reactions in nature implies that only left-handed fermions can undergo weak interaction in the standard model. Only quarks experience strong interaction since only they have the color charges. There are three color charges: red, blue, and green. These are quantum numbers representing strong interaction. The naming should not be confused with "color" from different wavelengths of photon spectra. Although it is an analogy, since the combination of these three color charges forms color-neutral baryons, similar to how the color spectra mix to form white light. And color-anticolor charges form "colorless" meson like two identical waves are superimposed exactly out of phase causing destructive interference.

The Yukawa term contains the interaction between any two Fermions and Higgs boson. Before symmetry breaking, all particles are massless. The Yukawa term gives the picture of how the Fermions obtain their masses from Higgs boson through the spontaneous symmetry breaking. This term evolves into Fermions' mass term which can be wrapped together with kinetic energies in the Fermion sector after the symmetry breaking. Similarly, Higgs gives $W^\pm$ and Z^0 bosons their mases in the Higgs sector which contains the kinetic energy of Higgs, its mass, and its interaction with $W^\pm$ and Z^0 bosons. Since the most dominant interaction discussed in this thesis is the strong interaction, the details about Higgs mechanism is beyond its scope. Interested readers can find more information in references [**?**] and [**?**].

1.1 QCD asymptotic freedom and phase diagram

From equation (1.1), we can separate the QCD Lagrangian once the symmetry breaking is done and the quarks gain their masses. Picking up the QCD parts from the gauge symmetry and the Fermion sector with unfolded covariant derivative for QCD, $D_\mu = \partial_\mu - ig_s A^a_\mu T^a$, the assembled Lagrangian for QCD is

$$\mathcal{L}_{\text{QCD}} = \underbrace{-\frac{1}{4} G^a_{\mu\nu} G^{\mu\nu}_a}_{\text{QCD gauge}} + \underbrace{i\bar{\psi}_q \gamma^\mu \partial_\mu \psi_q}_{\text{quarks K.E.}} - \underbrace{ig_s \bar{\psi}_q \gamma^\mu A^a_\mu T^a \psi_q}_{qq \text{ interaction}} - \underbrace{m_q \bar{\psi}_q \psi_q}_{q \text{ mass term}} \tag{1.2}$$

with $G^a_{\mu\nu}$ is the gluon field strength tensor, g_s is the strong coupling constant, A^a_μ is the gluon field with color index a, and T^a are the generators of the SU(3) color group. Local $SU(3)$ gauge transformation needs to be invariant, resulting

$$G^a_{\mu\nu} = \underbrace{\partial_\mu A^a_\nu - \partial_\nu A^a_\mu}_{\text{gluons K.E.}} + \underbrace{g_s f^{abc} A^b_\mu A^c_\nu}_{gg \text{ interaction}} \tag{1.3}$$

with f^{abc} are the structure constants of the $SU(3)$ color group. Alongside the gluon kinetic term, the non-Abelian $SU(3)$ symmetry transformation introduces an additional term for gluon-gluon interaction, which does not present in the Abelian $U(1)$ symmetry transformation. Another contrasting feature in QCD is its effective range. Unlike the electromagnetic interaction which has infinite range, strong interaction only works on a very short range. If two quarks in a hadron are separated away, it requires energy to overcome the strong interaction. At some point, this energy will be converted into a quark-antiquark pair between them. This pair will fill up the space left by the initial quarks and form two different hadron. This phenomena is due to the nature of the strong coupling constant g_s which determines the strength of interaction. This coupling constant is not really a "constant", but rather a function of momentum transfer Q from the gluon exchange. The QCD running coupling constant α_s [**?**] for the lowest order is

$$\alpha_s(Q^2) = \frac{g_s^2}{4\pi} = \frac{1}{\beta_0 \ln(Q^2/\Lambda^2_{\text{QCD}})}, \tag{1.4}$$

with β_0 is the coefficient of beta function for 1-loop diagram, and Λ_{QCD} is the energy scale limit for perturbative QCD. The value of Λ_{QCD} depends on the renormalization scheme. For the the modified minimal subtraction (MS) scheme [**?**] with 5 effective quark flavors, the value is $\Lambda_{\text{QCD}} = (210 \pm 14)$ MeV [**?**]. The behavior of α_s is shown in Figure 1.2.

At $Q = \Lambda_{\text{QCD}}$, α_s diverges, signaling the breakdown of perturbative methods. Below Λ_{QCD}, perturbative QCD is no longer effective and a non-perturbative approach such as lattice QCD becomes necessary. This behavior of α_s at low energy explains the quark confinement as we never see any free quarks directly in daily life. Since the strong interaction becomes very strong at low energy, the quarks form hadrons including proton and neutron which make up the nucleus inside every

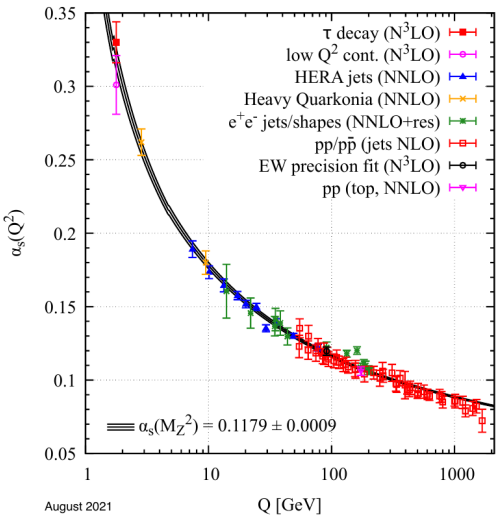

Figure 1.2: The QCD running coupling constant value as a function of momentum transfer Q. Figure from [**?**].

atom. As the energy becomes larger, α_s becomes smaller, allowing for perturbative calculations and liberating quarks from confinement. This phenomenon is known as asymptotic freedom, and is observed in high-energy particle collisions. The quarks break free from the colliding hadrons and create many quark-antiquark pairs as they move apart from each other before rehadronize into free streaming particles called jets.

Since the asymptotic freedom allows quarks to deconfine, a new state of quark matter other than hadron may be formed. Figure 1.3 illustrates the nuclear phase diagram. At low temperatures and low baryon densities, the quarks are in a bound

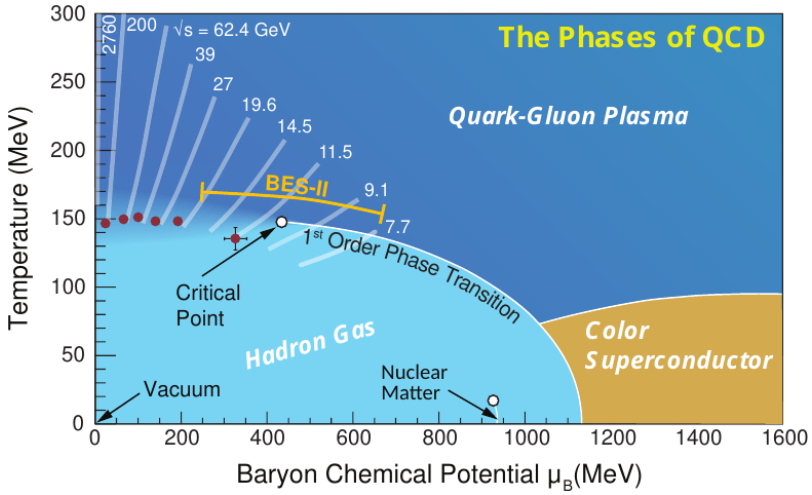

Figure 1.3: The nuclear phase diagram as a function of temperature and baryon chemical potential. Figure from [**?**].

state, forming hadrons. Also at low temperatures but very high baryon chemical potentials, hadrons are crushed until there is no boundary between them, resulting in the formation of a color superconductor state. Such extreme condition occurs in

the core of neutron stars. Meanwhile at very high temperatures, the quarks have enough energy to overcome their confinement and a primordial state of matter which existed shortly after Big Bang is recreated: the quark-gluon plasma (QGP). The lattice QCD calculation at low baryon density shows that the transition between the states of matter is crossover and occurs at temperature around 150 MeV [**?**]. The similar condition can be recreated in the laboratory by colliding heavy ion nuclei after at ultrarelativistic speed. The large number of colliding nucleon ensures enough entropy for the formation and evolution of the Quark–Gluon Plasma [**?**]. After certain baryon density, it is thought that the transition will reach critical point and it will not be a smooth crossover anymore. The high temperature evaporates hadron gas into QGP in abrupt phase transition. The search for the critical point has been conducted twice at RHIC, Brookhaven, through the Beam Energy Scan (BES) programs [**?**], by colliding heavy ions at various energy range. There is no conclusion yet about where the critical point is. Interested reader can find further information for instance in reference [**?**]. So the production of QGP has been achieved so far only via the crossover mechanism.

1.2 Geometry of heavy ion collision

In heavy ion collisions, the initial state begins when the Lorenz contracted nuclei are about to collide at ultrarelativistic speed. Upon the collisions, the events can be classified based on how many nucleons participate in the collision. The simplest picture of the initial state before collision can be modeled with Glauber model [**?**, **?**]. Figure 1.4 shows the geometry of the collision in the transverse plane. The two circles

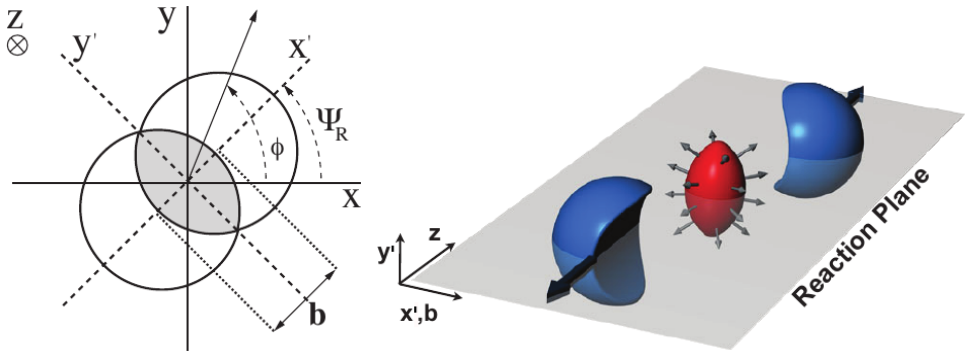

Figure 1.4: The view of mid-central heavy ions collision producing elliptic QGP fireball. **x** and **y** are the laboratory coordinate axes. The reaction plane coordinate is denoted as **x′** and **y′**. The Ψ_R is the reaction plane angle with respect to the laboratory frame and ϕ denotes emission angle of a particle. Figures from [**?**, **?**].

represent the colliding nuclei. In Glauber model, the colliding nucleons within the overlap region between the two circles are referred to as participants. Nucleons outside this region are called spectators since they are not involved in the collision. The transverse distance between the centers of both nuclei, denoted as the impact parameter b, determines how central the collision is. If $b = 0$, it is an ultracentral

collision with both nuclei completely overlap with each other. Larger b means the collision is less central with fewer participants in the collision.

However, b can not be measured directly since particle detectors only detect the final state particles created after the collision. Nevertheless, the multiplicity of charged particles N_{ch} coming out from collision and the energy deposit from the spectators along beam axis are directly related to b. These two measurable quantities can be compared with Monte-Carlo (MC) simulation of Glauber model [**?**] to determine the centrality. The details of the method for measuring the centrality can be read, for example, in reference [**?**]. And finally, instead of representing centrality in terms of b, the concept of centrality percentage is introduced. The smaller the percentage, the more central the collision is. For example 0-1% centrality means that this interval contains 1% of events that have the highest values of centrality estimator (multiplicity or energy). In more central collisions a larger QGP is created, and due to the initial geometry, the fireball is more uniform radially.

1.3 Harmonic flow

Harmonic flow analysis in heavy-ion collisions was motivated by the need to understand the collective motion of nuclear matter produced in such collisions. The sign of collectivity has been indicated since 1970s in central collision of various nuclei[**?**] and later confirmed in 1980s [**?**, **?**, **?**]. In the early 1990s, there was increasing evidence [**?**, **?**, **?**, **?**] from experiments at facilities like the Bevalac, AGS (Alternating Gradient Synchrotron), and SPS (Super Proton Synchrotron) that particles emitted in heavy-ion collisions exhibited collective flow patterns, such as the sideward deflection of nuclear matter (directed flow) and the azimuthal anisotropy in particle emission (elliptic flow). The final state particles that are produced from the colliding participants correlate with each other, and their correlation is influenced by the geometry of the overlap region upon collision [**?**].

As elliptic and directed flows were observed, a systematic analysis tool is needed to quantify these anisotropies and understand the collective behavior of the hot and dense matter created in these collisions. This led to the formalization of Fourier flow analysis, where each harmonic corresponds to different aspects of the flow and provides insight into the dynamics of heavy-ion collisions. The analysis of flow in relativistic nuclear collisions using Fourier expansion was proposed in 1994 [**?**] and became well established in 1998 [**?**]. The flow of particles in QGP evolution is studied relative to the reaction plane. This coordinate can be drawn with its x-axis, **x'** in Figure 1.4, in-line with the impact parameter but deviates by angle Ψ_R relative to x-axis of the laboratory frame. The Fourier series for the harmonic flow is [**?**]

$$E\frac{d^3N}{d^3\vec{p}} = \frac{1}{2\pi}\frac{d^3N}{p_T\,dp_T\,dy}\left(1 + 2\sum_{n=1}^{\infty} v_n \cos\left(n[\phi - \Psi_R]\right)\right), \tag{1.5}$$

with E, p_T, y, ϕ are energy, transverse momentum, rapidity, and azimuthal angle of the particle according to the laboratory coordinate, and v_n is the Fourier coefficient for the n-th harmonic. For the given p_T and y,

$$v_n(p_T, y) = \langle \cos\left(n[\phi - \Psi_R]\right) \rangle \tag{1.6}$$

with the angle bracket is the average over all particles with the corresponding p_T and y. The sine terms in the expansion cancel due to the reflection symmetry with respect to the reaction plane. The physical interpretations of this expansion is related to the order, n, of the harmonic. For the first harmonic, v_1 represents directed flow which comes from Coulomb repulsion or attraction between the colliding nucleons [**?**]. For the second harmonic, v_2 represents the pressure gradient in the expanding QGP which is well described as a nearly perfect fluid with relativistic hydrodynamics [**?**]. And for the third harmonic, v_3 represents event-by-event fluctuation in the number of participants due to variation in the nuclear density [**?**].

However, like impact parameter b, the reaction plane angle Ψ_R is not experimentally measurable. Therefore an indirect way is needed to calculate v_n. The standard way is by using two-particle azimuthal correlation method. Since equation (1.6) can be written in its Euler form, correlating one particle with azimuthal angle ϕ_1 and another particle with angle ϕ_2 will rise Ψ_R out of cancellation and absorb it to v_n:

$$\begin{aligned} \langle\langle e^{in(\phi_1-\phi_2)}\rangle\rangle &= \langle\langle e^{in(\phi_1-\Psi_R-(\phi_2-\Psi_R))}\rangle\rangle \\ &= \langle\langle e^{in(\phi_1-\Psi_R)}\rangle\langle e^{-in(\phi_2-\Psi_R)}\rangle - \delta_n\rangle \\ &= \langle {v_n}^2 + \delta_n\rangle. \end{aligned} \tag{1.7}$$

The inner angle bracket denotes an average over all particles within an event, followed by the outer angle bracket averaging over all events. The factorization give a rise to non-flow correlation δ_n independent of the reaction plane. In this method the non-flow contribution is assumed to be negligible.

Experimentally, the correlation is formed by pairing two particles from the same event within certain gaps of pseudorapidity $\Delta\eta$ and azimuthal angle $\Delta\phi$. The count of all possible combinations of pairings is the 2D correlation function $S(\Delta\phi, \Delta\eta)$ which is then need to be corrected since most detectors do not cover the entire spherical geometry. The correction function $B(\Delta\phi, \Delta\eta)$ is formed by combinatorial pairs of particles from mixed events. The corrected correlation function is

$$C(\Delta\phi, \Delta\eta) = \frac{S(\Delta\phi, \Delta\eta)}{B(\Delta\phi, \Delta\eta)}. \tag{1.8}$$

The 2D $C(\Delta\phi, \Delta\eta)$ has a wavy pattern along various $\Delta\phi$ slices as shown in Figure 1.5 (a). The distribution can be projected to $\Delta\phi$ by summing all $\Delta\eta$ slices in their respective $\Delta\phi$ slice. The result of projection is shown in Figure 1.5 (b). The v_n coefficient can be obtained after fitting a Fourier expansion to this 1D projection of

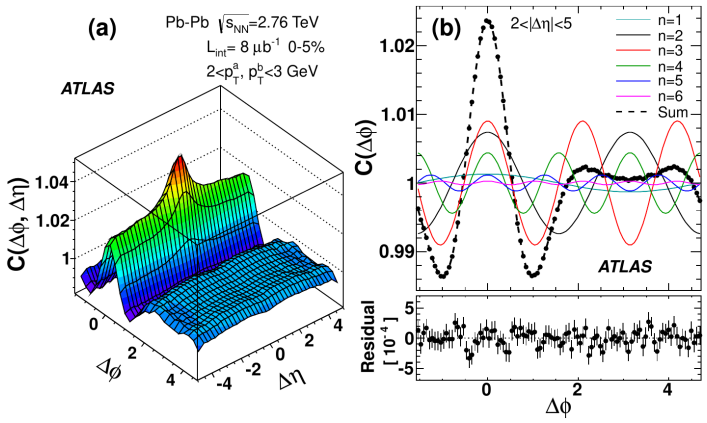

Figure 1.5: The harmonic flow in Pb-Pb collisions with centrality 0-5% fitted with Fourier decomposition. Figure from [?].

the corrected correlation function. But since the Ψ_R is avoided, the factorization in equation (1.7) implies the Fourier expansion should take the form [?]

$$\frac{dN_{\text{pairs}}}{d\Delta\phi} \propto 1 + 2\sum_{n=1}^{\infty} v_{n,n}(p_T^a, p_T^b)\cos(n\Delta\phi) \tag{1.9}$$

with a and b denote two different particles from different p_T ranges. $v_{n,n}(p_T^a, p_T^b)$ should factorize into separate $v_n(p_T^a)$ and $v_n(p_T^a)$ according to hydrodynamics picture of the expanding QGP:

$$v_{n,n}(p_T^a, p_T^b) = v_n(p_T^a)v_n(p_T^a). \tag{1.10}$$

However, the autocorrelations induced by resonance decays or fragmentation of jets break the factorization since these particles' origins are not from the main vertex of collision. There are several ways to minimize these non-flow contribution such as template fitting and large $\Delta\eta$ requirement [?, ?]. The results of v_n measurements in Pb+Pb collisions from ATLAS Experiment are shown in Figure 1.6

The same procedure is also applied in p-Pb collision [?], proton-proton (pp) collision [?], and ultraperipheral collision (UPC) of Pb+Pb [?]. Surprisingly, the value of v_2 is not zero in such systems despite several methods for removing non-flow effects have been applied. From Figure 1.7, the ridges along $\Delta\phi$ are also observed in pp and UPC. And the measured v_n values in these small systems are shown in Figure 1.8. They exhibit less dynamic compared to the head-on heavy ion collision. In Figure 1.6, the value of v_2 is rising from central to mid-central collisions since radial flow (central) produces less anisotropy than elliptic flow (mid-central) as governed by the initial asymmetry in the collision area. Compared to the small systems, this initial geometry of the overlapping region seems to be uniform, resulting in more or less monotonic value of v_2.

In UPC events, both nuclei just pass by without any hadronic interaction. One of the nuclei emits high energy gamma ray [?] and this gamma ray breaks the other

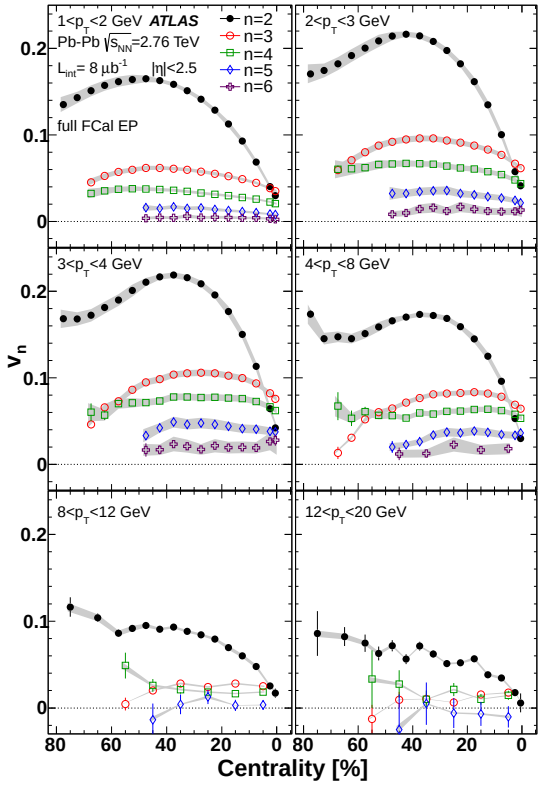

Figure 1.6: The v_n measurement results in Pb+Pb collisions as a function of centrality. Figure from [**?**].

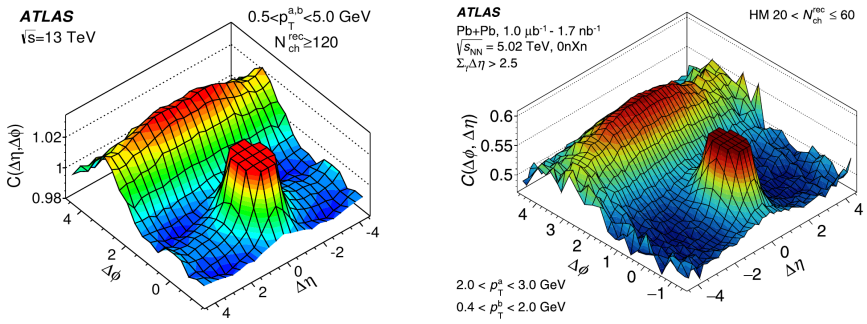

(a) **(b)**

Figure 1.7: Harmonic flow ridges observed in **(a)** *pp* 13 TeV [**?**], **(b)** ultraperipheral Pb+Pb collision [**?**].

nuclei. There is a possibility that the photon fluctuates into hadronic state upon impact and the collision is treated as meson-nucleus collision with much lower energy compared to the initial nuclei. So the chance of QGP formation exists, provided that the event has high-multiplicity which correspond to high initial entropy [**?**].

Nevertheless, there is no consensus whether or not the QGP is formed in such small systems. Even though there is a wide consensus that v_2 in heavy ion collisions originates from the hydrodynamic expansion of QGP, these observations in small systems spark a debate about the origin of the harmonic flow and the revolution [**?**] might be underway.

The interaction resulting in flow-like observations might also occur in the initial

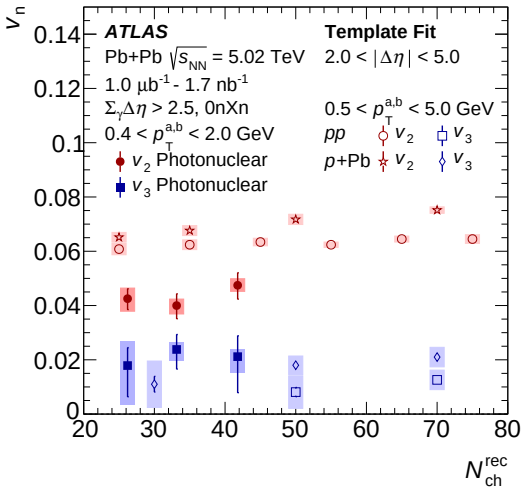

Figure 1.8: The v_n measurement results in UPC Pb+Pb, pp at 13 TeV, and p-Pb at 5.03 TeV as a function of multiplicity of the reconstructed charged particles tracks. Figure from [**?**].

state before or even without the formation of QGP. Therefore this research is carried out to find the connection between v_n and the initial-state phenomena. To explore all the possibilities, the results from the experiment will be compared to simulations with different initial state models and with or without hydrodynamic simulation.

1.3.1 Direct Flow Calculation

In general, the non-flow contribution in equation (1.7) is not negligible. There are some alternatives methods proposed to avoid the non-flow contribution, for example, by calculating flow directly from multi-particle correlations [**?**] or by generating functions with numerical interpolations [**?**]. This research uses direct cumulants method from the reference [**?**]. In this method, the cumulants are expressed in terms of moments of the magnitude of the flow vector Q_n [**?**] for n-harmonic, defined as

$$Q_n \equiv \sum_{j=1}^{M} e^{in\phi_j} \tag{1.11}$$

with M is the number of particles in the event. The single-event average two- and four-particle azimuthal correlations are defined in the following way:

$$\langle 2 \rangle = \langle e^{in(\phi_1 - \phi_2)} \rangle = \frac{1}{P_{M,2}} \sum_{j,k}' e^{in(\phi_j - \phi_k)} \tag{1.12}$$

$$\langle 4 \rangle = \langle e^{in(\phi_1 + \phi_2 - \phi_3 - \phi_4)} \rangle = \frac{1}{P_{M,4}} \sum_{j,k,l,m}' e^{in(\phi_j + \phi_k - \phi_l - \phi_m)} \tag{1.13}$$

with $P_{M,n} = M!/(M-n)!$ is the total combination of possible particle pairs, $\sum'$ denotes that all indices in the sum must be different to avoid counting the same

particle pairing with itself. Then taking the average over all events:

$$\langle\langle 2\rangle\rangle = \langle\langle e^{in(\phi_1-\phi_2)}\rangle\rangle = \frac{\sum_{\text{events}}(W_{\langle 2\rangle})_i\langle 2\rangle_i}{\sum_{\text{events}}(W_{\langle 2\rangle})_i} \tag{1.14}$$

$$\langle\langle 4\rangle\rangle = \langle\langle e^{in(\phi_1+\phi_2-\phi_3-\phi_4)}\rangle\rangle = \frac{\sum_{\text{events}}(W_{\langle 4\rangle})_i\langle 4\rangle_i}{\sum_{\text{events}}(W_{\langle 4\rangle})_i}. \tag{1.15}$$

Ideally, $(W_{\langle n\rangle})_i = P_{M,n}$. However, the event weights $(W_{\langle n\rangle})_i$ need to be corrected by taking into account the detector efficiency and the rate of fake tracks reconstructed. The harmonic flow from two- and four-particle are:

$$v_n\{2\} = \sqrt{\langle\langle 2\rangle\rangle} \tag{1.16}$$

$$v_n\{4\} = \sqrt[4]{2\langle\langle 2\rangle\rangle^2 - \langle\langle 4\rangle\rangle} \tag{1.17}$$

Looping over all possible particle pairs takes a lot of computational resource. Instead of going through all the possible combinations of particle pairs, the method uses reference flow $|Q_n|^2$ which can be separated into diagonal ($j = k$) and off-diagonal ($j \neq k$) terms. For $j = k$, the exponent becomes one, and the sum is M. Therefore

$$|Q_n|^2 = \sum_{j,k=1}^{M} e^{in(\phi_j-\phi_k)} = M + \sum_{j,k}{}' e^{in(\phi_j-\phi_k)} \tag{1.18}$$

which can be solved to obtain $\langle 2\rangle$ by substituting the exponent:

$$\langle 2\rangle = \frac{|Q_n|^2 - M}{P_{M,2}}. \tag{1.19}$$

This expression only needs a single loop over Q_n and calculate its magnitude in contrast to expression in equation 1.12 which requires two loops over j and k.

To reduce the loop for $\langle 4\rangle$, it starts from the decomposition of

$$|Q_n|^4 = Q_nQ_nQ_n^*Q_n^* = \sum_{j,k,l,m=1}^{M} e^{in(\phi_j+\phi_k-\phi_l-\phi_m)} \tag{1.20}$$

which contains terms with five different combinations. The terms where they are all different particles is equal to the exponent of four particle correlation in equation 1.13. The term where $j = k = l = m$ sums up to M. The terms where only either $j = k$ or $l = m$ are reduced to the exponent for three particle correlation which is denoted as

$$\langle 3\rangle_{2n|n,n} = \frac{1}{P_{M,3}}\sum_{j,k,l}{}' e^{in(2\phi_j+\phi_k-\phi_l)}, \quad \langle 3\rangle_{2n|n,n} = \langle 3\rangle^*_{n,n|2n}. \tag{1.21}$$

For the terms where either j or k is equal to one of the conjugates, the exponent is reduced to the one in two particle correlation $\langle 2\rangle$. The terms where $j = k$ and $l = m$ give a factor of two to the n-harmonic in the exponent of $\langle 2\rangle$. The expression of $\langle 2\rangle$

for $2n$ is denoted as

$$\langle 2 \rangle_{2n|2n} = \frac{1}{P_{M,2}} \sum_{j,l}^{\prime} e^{i2n(\phi_j - \phi_l)} = \frac{|Q_{2n}|^2 - M}{P_{M,2}} \tag{1.22}$$

Substituting the exponents with their corresponding particle correlations and counting for all possible combinations, the decomposition becomes

$$\begin{aligned} |Q_n|^4 =& \langle 4 \rangle \cdot P_{M,4} + \left[\langle 3 \rangle_{2n|n,n} + \langle 3 \rangle_{2n|n,n} \right] \cdot P_{M,3} \\ &+ \langle 2 \rangle \cdot 4P_{M,2}(M-1) + \langle 2 \rangle_{2n|2n} \cdot P_{M,2} + 2P_{M,2} + M \end{aligned} \tag{1.23}$$

In order to solve $\langle 3 \rangle_{2n|n,n} + \langle 3 \rangle_{2n|n,n}$, decomposition of $Q_{2n}Q_n^*Q_n^*$ and $Q_nQ_nQ_{2n}^*$ are needed:

$$Q_{2n}Q_n^*Q_n^* = \langle 3 \rangle_{2n|n,n} P_{M,3} + \langle 2 \rangle \cdot 2P_{M,2} + \langle 2 \rangle_{2n|2n} \cdot P_{M,2} + M. \tag{1.24}$$

After inserting the results for $\langle 2 \rangle$ and $\langle 2 \rangle_{2n|2n}$, and then add it with its conjugate $Q_nQ_nQ_{2n}^*$, the solved expression is

$$\langle 3 \rangle_{n,n|2n} + \langle 3 \rangle_{2n|n,n} = 22 \frac{\Re(Q_{2n}Q_n^*Q_n^*) - 2|Q_n|^2 - |Q_{2n}|^2 + 2M}{M(M-1)(M-2)} \tag{1.25}$$

Therefore, after solving equation 1.23 with the results from two and three particle correlations, the final expression for the four particle correlation is

$$\langle 4 \rangle = \frac{|Q_n|^4 + |Q_{2n}|^2 - 2\Re(Q_{2n}Q_n^*Q_n^*) - 4(M-2)|Q_n|^2 - 2M(M-3)}{M(M-1)(M-2)(M-3)} \tag{1.26}$$

1.4 Relativistic hydrodynamics

Hydrodynamics provides a straightforward framework for understanding the dynamics of many-body systems. It simplifies the description of the system by averaging out the complex short-distance and short-time interactions among particles. Instead of dealing with the intricacies of individual particle interactions, hydrodynamics focuses on a few conserved charges and their currents. This reduction in complexity is essential, especially when dealing with systems containing a large number of particles, as it makes the analysis more manageable [**?**].

Despite its simplicity, the hydrodynamics simulation remains a powerful and accurate tool for describing the bulk behavior of fluids. The fundamental equations of hydrodynamics are rooted in conservation laws, supplemented by an equation of state. These equations can explain a wide range of phenomena, from the aerodynamics of airplanes to QGP expansion [**?**].

In the application for QGP the hydrodynamic equations are Lorentz invariant and in the tensor form. The conservation of energy, momentum, and current are

expressed as

$$\partial_\mu T^{\mu\nu} = 0 \tag{1.27}$$

$$\partial_\mu J^\mu_{\mathrm{B}} = 0 \tag{1.28}$$

with $T^{\mu\nu}$ is the energy-momentum tensor and J^μ_{B} is the net baryon current. In ideal case where the shear viscosity and bulk viscosity are neglected, the energy-momentum tensor and the net baryon current are

$$T^{\mu\nu}_{\mathrm{ideal}} = (\varepsilon + P)u^\mu u^\nu - P g^{\mu\nu} \tag{1.29}$$

$$J^\mu_{\mathrm{B,\,ideal}} = \rho_{\mathrm{B}} u^\mu \tag{1.30}$$

where ε is the energy density, P is the pressure, $g^{\mu\nu}$ is the metric tensor, ρ_{B} is the baryon density, and u^μ is the four 4-vector flow velocity. The pressure P contains the equation of state as a function of energy density and baryon density $P(\varepsilon,\ \rho_{\mathrm{B}})$.

In the presence of shear viscosity η and bulk viscosity ζ, the energy-momentum tensor becomes

$$T^{\mu\nu}_{\mathrm{viscous}} = T^{\mu\nu}_{\mathrm{ideal}} + \Pi^{\mu\nu} \tag{1.31}$$

with $\Pi^{\mu\nu}$ is the viscous part of the stress energy tensor:

$$\Pi^{\mu\nu} = \eta\left(\nabla^\mu u^\nu + \nabla^\nu u^\mu - \frac{2}{3}\Delta^{\mu\nu}\nabla_\alpha u^\alpha\right) + \zeta\Delta^{\mu\nu}\nabla_\alpha u^\alpha \tag{1.32}$$

where $\Delta^{\mu\nu} = g^{\mu\nu} - u^\mu u^\nu$ and $\nabla^\mu = \Delta^{\mu\nu}\partial_\nu$ is the local space derivative.

There are many hydronamic simulations. Some hydrodynamic simulations focus solely on either the shear or bulk viscosity components. For instance, in the v-USPhydro simulation [**?**], only the effects of bulk viscosity are accounted for. And the longitudinal expansion is also neglected, leading to simplified 2+1D approximation which is good enough for estimating the expansion in mid-rapidity region. This approach allows for a specific emphasis on the impact of bulk viscosity on the transverse evolution of the system. Some other simulations, for example, iEBE-VISHNU [**?**, **?**], considers both bulk and shear viscosities in 2+1D framework. The iEBE-VISHNU has been applied to small system such as *pp* to determine the value of v_n from two-particle cumulant. The results are presented in Figure 1.9 and similar to the experiments to some extent. The initial states are provided by HIJING [**?**, **?**, **?**], super-MC [**?**], and TRENTo [**?**, **?**] simulations which are based on Glauber model.

On the other hand, MUSIC hydrodynamic simulation framework [**?**, **?**, **?**, **?**], a widely used tool in relativistic heavy-ion physics, provides a comprehensive approach by considering both shear and bulk viscosity effects simultaneously. The MUSIC offers a sophisticated framework for studying the complex dynamics of relativistic fluids, capturing the interplay between different dissipative mechanisms. This comprehensive treatment enables investigation of the collective behavior of the system under various conditions and to explore the influence of both shear and bulk

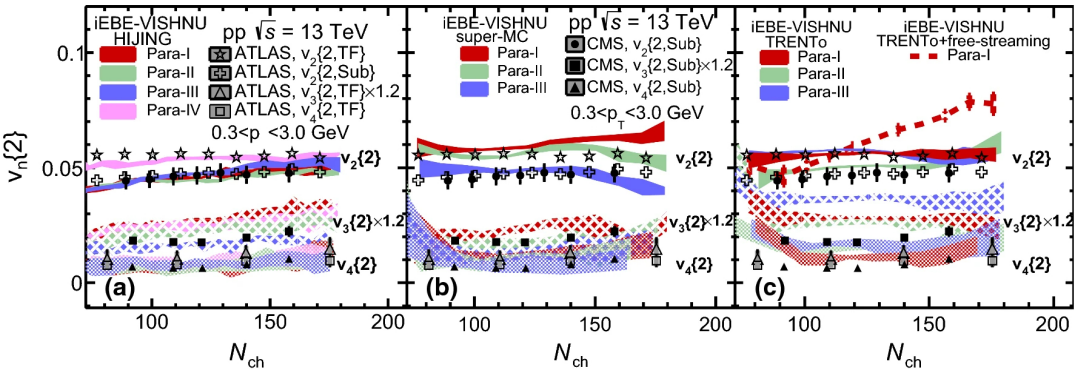

Figure 1.9: The $v_n\{2\}$ in pp from iEBE-VISHNU simulations with initial states provided by HIJING, super-MC, and TRENTo. The results are compared to ATLAS and CMS. Figure from [?].

viscosity on observables such as flow harmonics and particle spectra. The MUSIC also considers all spatial dimensions, leading to a more realistic 3+1D description of the system's evolution. With MUSIC, one can choose the initial state conditions setup. It can be a simple Glauber model or something more advance like IP-Glasma that utilizes color-glass condensate model.

1.5 Deep inelastic scattering

Deep inelastic scattering (DIS) experiments were carried out by colliding an electron and a hadron. Figure 1.10 shows the kinematic of DIS. In the inital state,

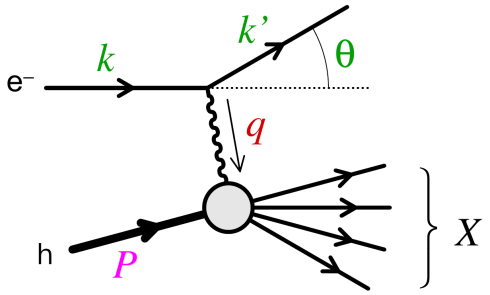

Figure 1.10: Kinematics of Deep Inelastic Scattering. Figure from [?] with some modification.

the incoming electron has the four-momentum k and the hadron's four-momentum is denoted by P. The squared center of mass energy of the system is $s = (P + k)^2$. Upon the impact, the interaction between them is electromagnetic, and the exchanged virtual photon has four-momentum q. The transfer momentum of the collision is defined as $Q^2 = -q^2$. After the impact, the electron bounces with angle θ and four-momentum k', while the hadron breaks off and the total four-momentum of all the hadron products is denoted as X. Suppose the parton (quark or gluon) struck by the electron bring some fraction of the hadron's four-momentum xP with x is the Bjorken x [?], the fraction of momentum carried by a parton in the hadron. After the

impact, the parton receives the transfer momentum and its four-momentum becomes $xP + q$. The invariant mass of the parton is

$$\begin{aligned} m_p^2 &= (xP + q)^2 = (xM_h)^2 + 2xP \cdot q + q^2 \\ -q^2 &= Q = 2xP \cdot q + (xM_h)^2 - m_p^2 \end{aligned} \tag{1.33}$$

with M_h is the mass of incoming hadron. At high energy, the mass terms can be neglected since they are much smaller than the momentum of the particles, leaving

$$x \equiv \frac{Q^2}{2P \cdot q} \tag{1.34}$$

This relation shows that Bjorken x scales the transfer momentum with the energy of collision so the value remains the same when $s \to \infty$.

1.6 Perturbative QCD and small-x physics

A baryon contains valence quarks as the primary building blocks, exchanging gluons which occasionally create virtual sea quarks in between. The probability density for finding a parton inside a hadron carrying a fraction x of the hadron's momentum at a given energy scale Q^2 is described by the Parton Distribution Function (PDF) [**?**]. The PDF can be measured in DIS experiment, and the measurement result from HERA [**?**] is presented on the left side of Figure 1.11. The curves labeled xu_v and xd_v correspond to the weighted PDF of up and down valence quarks, respectively. These distributions peak at intermediate x with the order of magnitude 10^{-1} and decrease at both small and large x. The observed peaks are a signature of the significant momentum carried by the valence quarks in the proton at intermediate x. While the weighted gluon and sea quarks distribution, denoted by $xg/20$ and $xS/20$ respectively, are increasing at small x with steeper increase on gluons compared to sea quarks. This result suggests several dynamic approaches in the perturbative regime, which depend on the magnitude of x as illustrated on the right side of Figure 1.11.

The first approach is in the Bjorken limit where x is fixed as $Q^2 \to \infty$ and $s \to \infty$. The parton evolution is governed by the Dokshitzer-Gribov-Lipatov-Altarelli-Parisi (DGLAP) evolution equation [**?**, **?**, **?**]

$$\frac{df_a(z, Q^2)}{d \ln Q^2} = \frac{\alpha_s}{2\pi} \int_z^1 \frac{dz'}{z'} P_{a \to bc}(z')\, f_b(z', Q^2). \tag{1.35}$$

The $f_a(z, Q^2)$ is the parton distribution function (PDF) of a parton a carrying momentum fraction of z from its source. The $P_{a \to bc}(z')$ is the splitting function which provides the probability of a parton a to split into b and c, with parton b carries most of the momentum fraction z' from a. There are four combinations of splitting depending on the type of parton a: a quark radiates a soft gluon (the quark carries z'),

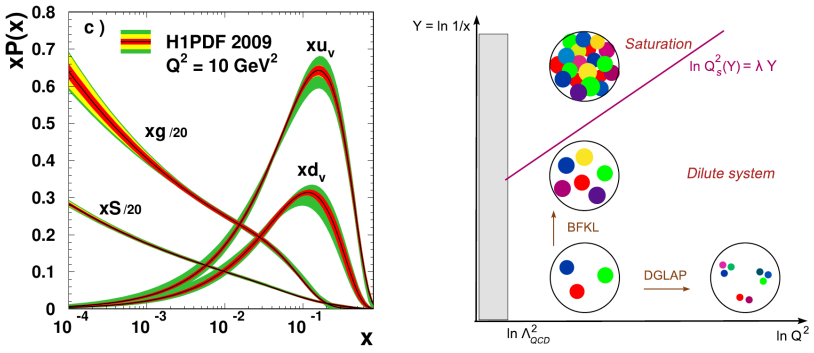

Figure 1.11: Left: the x-evolution of the gluon, sea quark, and valence quark distributions for Q^2 = 10 GeV^2 measured at HERA. Right: the "phase–diagram" for QCD evolution. Figure from [**?**, **?**].

a quark radiates hard gluon (the gluon carries z'), a gluon splits into more gluons, and a gluon creates a quark-antiquark pair. Each mode has its own splitting function. The $f_b(z', Q^2)$ is the PDF of parton b after splitting. They have probability to split again, creating more partons in the next-to-leading order or more, until a certain energy cut-off is reached where the perturbative process is no longer viable. The DGLAP evolution equation is the basis for simulating parton shower, multiplied by Sudakov form factor [**?**]

$$\Delta_s(Q^2_{\max}, Q^2) = \exp\left\{ -\int_{Q^2}^{Q^2_{\max}} \frac{dk^2}{k^2} \int_{z_{\min}}^{z_{\max}} dz \frac{\alpha_s(z,k^2)}{2\pi} P_{a\to bc}(z) \right\} \tag{1.36}$$

which give the probability that no emission occurs between a $Q^2 \leq k^2 \leq Q^2_{\max}$ interval. The probability factorizes, allowing for multiple radiations before energy cutoff, but only one emission allowed for each Q^2 interval. For example, if the emission occurs at the scale Q^2_i, there will be no emission between $Q^2_i \leq k^2 \leq Q^2_{i-1}$ and $Q^2_{i+1} \leq k^2 \leq Q^2_i$ with the i-th scale is lower than the previous one.

The second approach is in the Regge-Gribov limit where Q^2 is fixed, and x is small as $s \to \infty$. The dominant partons are gluon and the evolution is described by Balitsky-Kovchegov-Fadin-Lipatov (BFKL) equation [**?**, **?**, **?**, **?**]

$$\frac{\partial \mathcal{F}(k,Y)}{\partial Y} = \frac{\alpha_s N_c}{\pi} \int \frac{d^2q}{\pi} \frac{k^2}{q^2(k^2-q^2)} \left[\mathcal{F}(q,Y) - \frac{1}{2}\mathcal{F}(k,Y) \right] \tag{1.37}$$

where $\mathcal{F}(q,Y)$ is the unintegrated gluon distribution with transverse momentum q at rapidity $Y = \ln(1/x)$, and N_c is the number of colors. This equation describes the evolution for a gluon with transverse momentum k to emit another gluon with transverse momentum q. The first term corresponds to the real gluon emission in one-step evolution, while the second term correspond to virtual gluon self-energy corrections.

In the initial state of hadrons collision, since gluon splits into more gluons, the nucleons are packed with plenty of gluons as they are accelerated toward high energy. However, the size of nucleon does not grow significantly, and hence, the density of

gluons in the nucleon becomes extremely large. At some point, the gluon density will saturate, causing some of the gluons to recombine again. However, the BFKL equation does not take into account the probability of recombination upon gluon saturation. The non-linear saturation effect is needed to extend the BFKL equation, resulting in the Balitsky-Kovchegov (BK) equation [?, ?]

$$\frac{\partial \mathcal{N}(r,Y)}{\partial Y} = \frac{\alpha_s N_c}{2\pi} \int d^2 r_1 \, \mathcal{K}(r, r_1, r_2) \, [\mathcal{N}(r_1, Y) + \mathcal{N}(r_2, Y) - \mathcal{N}(r, Y) - \mathcal{N}(r_1, Y)\mathcal{N}(r_2, Y)] \tag{1.38}$$

where $\mathcal{N}(r, Y)$ is the dipole scattering amplitude at dipole size $r = r_1 + r_2$ and rapidity Y, and $\mathcal{K}(r, r_1, r_2)$ is the BK kernel. Here, the first three terms on the right-hand-side of the equation take care the splitting, while the non-linear one in the last term represents the recombination.

The BK equation provides a framework for the color-glass condensate model [?]. The term "color" in CGC refers to the color charge carried by gluons. The term "glass" is used metaphorically to describe the highly dense and disordered state of gluons within hadrons at very small momentum fractions and high energies. It draws an analogy with the disordered structure of a glass material in condensed matter physics. The word "condensate" refers to the fact that at very high energies and densities, gluons behave collectively and undergo a form of condensation, similar to how particles condense into a Bose-Einstein condensate at low temperatures. The effective theory of CGC is described by the Jalilian-Marian-Iancu-McLerran-Weigert-Leonidov-Kovner (JIMWLK) equation [?, ?, ?, ?, ?, ?]

$$\frac{\partial W_x[\rho]}{\partial \ln(x)} = -H_{\text{JIMWLK}} \left[\rho, \frac{\delta}{\delta \rho}\right] W_x[\rho] \tag{1.39}$$

where $W_x[\rho]$ is the weight functional which encodes the probability distribution of the color charge density ρ at small x cutoff, and H_{JIMWLK} is JIMWLK Hamiltonian as a function of ρ and the functional derivatives $\delta/\delta\rho$. The JIMWLK Hamiltonian is discussed in references [?, ?]

Shortly after the two nucleus with CGC states collide, the formation of Glasma [?, ?, ?] occurs before the system thermalizes into QGP. The Glasma state is neither CGC or QGP, but has properties of both. This state consists of strong color electric and color magnetic fields, illustrated in Figure 1.12, that evolve over time as the system expands. The Glasma is characterized by the presence of color flux tubes, which are tubes of strong gluon fields stretched between the remnants of the colliding nuclei. These flux tubes are thought to be responsible for the early-time dynamics and the development of flow patterns in the QGP. The energy density, pressure, and other properties of the Glasma serve as the initial conditions for hydrodynamic simulations that model the subsequent evolution of the QGP, where the non-equilibrium Glasma evolves into a locally thermalized QGP. The CGC framework needs to incorporate the impact parameter (IP) dependence to take into account the fluctuation of the

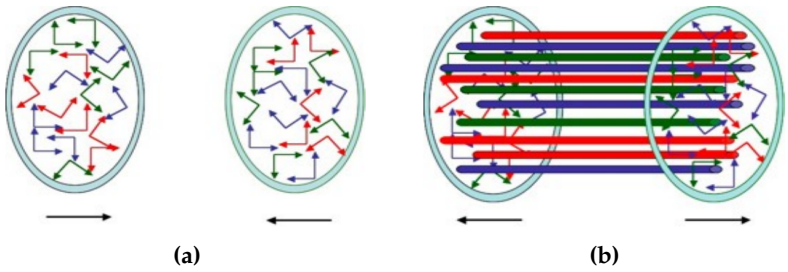

Figure 1.12: **(a)** Incoming colliding sheets of colored glass. **(b)** The Glasma as stretched flux tubes of color electric and color magnetic fields after collision. Figures from **[?, ?]**.

number of participants, and hence the full initial state model is called IP-Glasma. The model serves as a bridge between the pre-collision CGC state, the Glasma, and the subsequent hydrodynamic evolution of the QGP. By doing so, it helps connect the theoretical description of the initial conditions with the final-state observables measured in experiments.

1.7 v_n-p_T correlation

The study of correlation between v_n and p_{T} was first proposed by Piotr Bożek **[?]**. The correlation is defined as a modified Pearson correlation coefficient

$$\rho(v_n\{2\}^2, [p_{\mathrm{T}}]) = \frac{\mathrm{cov}(v_n\{2\}^2, [p_{\mathrm{T}}])}{\sqrt{\mathrm{Var}(v_n\{2\})}\sqrt{\mathrm{Var}([p_{\mathrm{T}}])}}. \tag{1.40}$$

with $v_n\{2\}$ is the v_n from two-particle correlation defined in equation (1.16), $[p_{\mathrm{T}}]$ is the mean p_{T} in every event, $\mathrm{cov}(v_n\{2\}^2, [p_{\mathrm{T}}])$ is the covariance between $v_n\{2\}$ and $[p_{\mathrm{T}}]$, $\mathrm{Var}(v_n\{2\})$ and $\mathrm{Var}([p_{\mathrm{T}}])$ are the modified variances for $v_n\{2\}$ and $[p_{\mathrm{T}}]$.

The ATLAS collaboration has done the first measurement of $\rho(v_n\{2\}^2, [p_{\mathrm{T}}])$ in reference **[?]** for Pb+Pb and p-Pb collisions. Following the results from experiment, the studies of hydrodynamic properties which give a rise to such a trend have been conducted in references **[?, ?]**. The generic form of equation (1.40) is

$$\rho_n(A, B) = \frac{\mathrm{cov}(A, B)}{\sqrt{\mathrm{Var}(A)}\sqrt{\mathrm{Var}(B)}}. \tag{1.41}$$

Observable A can be the v_n or an initial spatial eccentricity ε_n of the matter created in the nuclear overlap zone **[?]** since $v_n \propto \varepsilon_n$. Observable B serves as a predictor that influence the value of $[p_{\mathrm{T}}]$. Figure 1.13 shows that the similar trend of $\rho(v_n\{2\}^2, [p_{\mathrm{T}}])$ in heavy ions can be reproduced with predictor B chosen from initial hydrodynamic properties such as initial energy over entropy ratio E/s, initial transverse size of the fireball $1/R$, and initial entropy per elliptic area of the overlap region S/A_e. From the comparison with the experiment, it is concluded that the $[p_{\mathrm{T}}]$ is influenced mostly by the initial E/s, and not by the size of the fireball. The effect of E/s on $[p_{\mathrm{T}}]$ is a natural

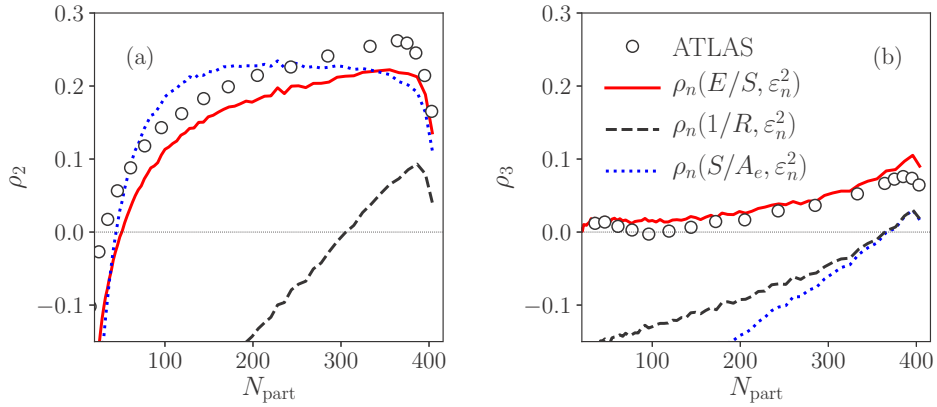

Figure 1.13: Variations of predictor in modified Pearson correlation coefficient ρ_n for (a) $n = 2$ and (b) $n = 3$. The v_n is replaced by ε_n, while $[p_T]$ is replaced by either E/s, $1/R$, and S/A_e. The simulation is compared to the first results of $\rho(v_n\{2\}^2, [p_T])$ measurement from ATLAS experiment in Pb+Pb collisions [?]. Figure from [?].

consequence of conservation laws, and might still be valid when hydrodynamics is not.

To test the sensitivity of ρ_n to the initial condition, the simulation of $\rho(v_n\{2\}^2, [p_T])$ with IP-Glasma+MUSIC+UrQMD is compared to the results from the experiment and $\hat{\rho}_{\text{est}} = \rho_n(\varepsilon_n, S/A_e)$ without hydrodynamic simulation. Figure 1.14 shows that the estimator $\hat{\rho}_{\text{est}}$ varies greatly with different initial conditions from Glauber model to IP-Glasma. However, the shape change is insignificant after IP-Glasma initial condition is followed by hydrodynamic simulation. These results indicate that ρ_n is more sensitive to the initial conditions than the details of hydrodynamic expansion.

The $\rho(v_n\{2\}^2, [p_T])$ in Pb+Pb collisions is then remeasured by ATLAS collaboration in reference [?], providing better resolution in the ultracentral region along with

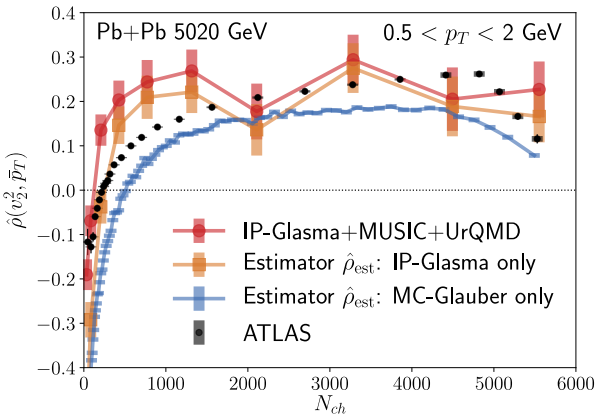

Figure 1.14: The simulation of $\rho(v_n\{2\}^2, [p_T])$ with IP-Glasma+MUSIC+UrQMD and estimator $\tilde{\rho}_{\text{est}} = \rho_n(\varepsilon_n, S/A_e)$ without hydrodynamic simulation. The initial stage for $\hat{\rho}_{\text{est}}$ is either IP-Glasma or Glauber model. The simulations are compared to the first Pb+Pb results of $\rho(v_n\{2\}^2, [p_T])$ measurement from ATLAS experiment in Pb+Pb collisions[?]. Figure from [?].

the first measurement of $\rho(v_n\{2\}^2, [p_T])$ in Xe+Xe collisions. The results are shown in Figure 1.15 and compared with several simulations. They are Trento, v-USPhydro, Trajectum [**?**], and IP-Glasma+MUSIC. The standalone Trento simulations only uses Glauber model with reduced thickness function. Both v-USPhydro and Trajectum use 2+1D hydrodynamic model with initial condition provided by Trento. While IP-Glasma+MUSIC simulates initial condition with CGC evolution and 3+1D hydrodynamic expansion later on. The IP-Glasma+MUSIC also has an option to include the contribution from initial momentum anisotropy ϵ_p provided by CGC. In general, they are in agreement with the experiment results in most central regions. However, from mid-central to peripheral centrality, the simulations deviates from data, signaling a missing physics. These results are obtained using three-subevent method where the particle correlation for v_n is taken from particles within $0.75 \leq |\eta| \leq 2.5$ and the mean p_T is calculated from the p_T of particles within $|\eta| \leq 0.5$ The more details about subevent categories are described more in Chapter 3. Later on in the same year, ALICE Collaboration also produced the similar results [**?**].

Following the studies in references [**?**, **?**, **?**, **?**, **?**], the ATLAS collaboration also demonstrates that the measurement of $\rho(v_n\{2\}^2, [p_T])$ in Pb+Pb and Xe+Xe can be used to estimate a deformed nuclear shape. In the deformed nucleus, the radius at a certain orientation is given by [**?**]

$$R(\theta, \phi) = R_0(1 + \beta\,(\cos\gamma Y_{2,0} + \sin\gamma Y_{2,2})) \tag{1.42}$$

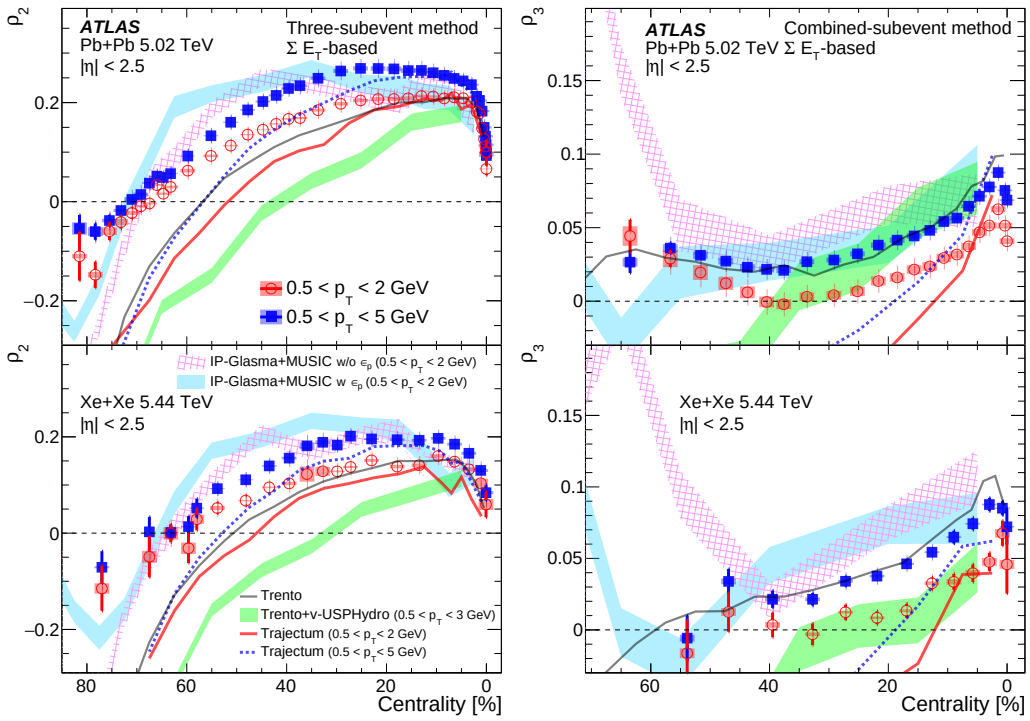

Figure 1.15: The measurement of $\rho(v_n\{2\}^2, [p_T])$ in Pb+Pb and Xe+Xe collisions for the second and third harmonic by ATLAS collaboration [**?**]. The results are compared to several model simulations.

where R_0 is the nuclear radius while it is in spherical shape, $Y_{l,m}$ are spherical harmonics, β, and γ are quadrupole deformation parameters. The parameter β is the magnitude of the deformation, with values around 0.1–0.4 [**?**], while the angle γ describes the length imbalance of the three semi-axes r_1, r_2, and r_3 of the ellipsoid, also known as triaxiality and ranges within $0 \leq \gamma \leq 60°$. As illustrated in Figure 1.16, $\gamma = 0°$, $\gamma = 60°$, and $\gamma = 30°$ correspond to the prolate ($r_1 = r_2 < r_3$), oblate ($r_1 < r_2 = r_3$), and maximum triaxiality ($2r_3 = r_1 + r_2$) cases respectively. Typically, nuclear shapes are deduced through low-energy spectroscopic analyses,

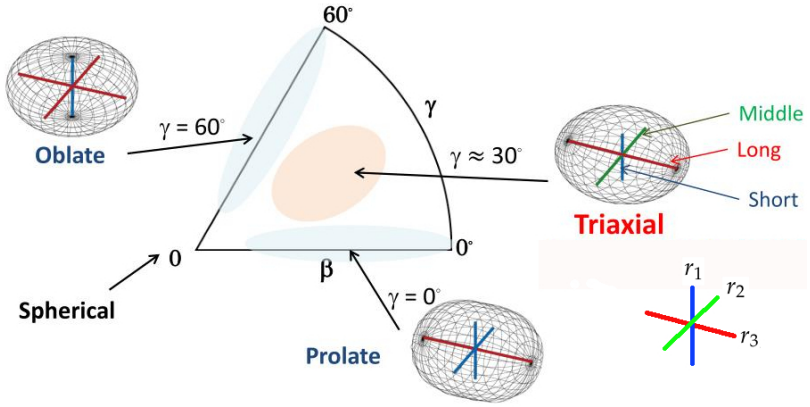

Figure 1.16: Nuclear shape deformation and its corresponding parameters. Figure from [**?**] with some modification.

which estimate the β and γ for nuclei with an even number of protons and neutrons, like ^{208}Pb [**?**]. However, determining the shape of odd-mass nuclei like ^{129}Xe relies on nuclear structure models calibrated to match data from even–even nuclei. With ρ_n measurement and precise modeling, it becomes possible to measure the triaxiality of odd-mass nuclei from experiment.

Figure 1.17a shows comparisons between ρ_2 from experimental data within the 0–20% centrality range and the calculations from the Trento model for various γ_{Xe}. The aim was to examine how triaxiality influences these results. It is shown that ρ_2 varies with different triaxiality parameter γ_{Xe} since $\beta_{\mathrm{Xe}} \sim 0.2$ is significant in the Xe nucleus. Nonetheless, the range of p_T of particles used in the analysis impacts an absolute value of ρ_n and it is not precisely described in the Trento model. To mitigate the influence of p_T-range in the experimental data, the ratios of ρ_2 between Xe+Xe and Pb+Pb for two distinct p_T ranges need to be computed and the results are shown in Figure 1.17b. The comparison between the model and data matches the best for $\gamma \sim 30°$ for Xe nuclei. These results suggest that $\rho(v_n\{2\}^2, [p_{\mathrm{T}}])$ is sensitive to the initial geometry of the colliding system.

Following the success of ρ_n measurement in heavy ion collisions to probe the initial state phenomena and the early geometry before collisions, the $\rho(v_n\{2\}^2, [p_{\mathrm{T}}])$ measurement in pp is carried out for the first time by ATLAS collaboration in this research. The $\rho(v_n\{2\}^2, [p_{\mathrm{T}}])$ measurement in p-Pb is also remeasured for the second harmonic and is done for the third harmonic and different subevent for the first time.

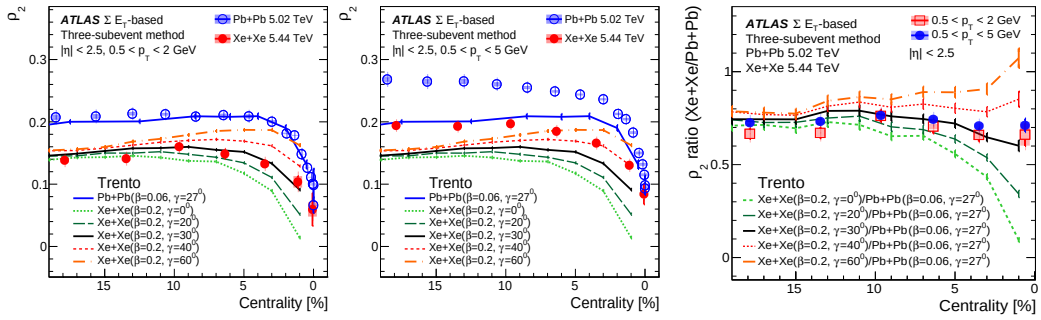

(a) **(b)**

Figure 1.17: (a) ρ_2 for Pb+Pb and Xe+Xe in two different p_{T} ranges, compared to Trento simulations. The β and γ is fixed for Pb while γ for Xe is varied as a function of at fixed β. **(b)** The ratio of ρ_2 in Xe+Xe divided by ρ_2 in Pb+Pb. The ratio is computed to remove the p_{T} dependence in experimental data. Figure from **[?]**

There are several predictions published already. Among of them are the references **[?]**, and **[?]**. In reference **[?]**, the study was conducted for d+Au, p+Au, p+Pb, O+O, Au+Au, and Pb+Pb systems. For each system, $\rho(v_n\{2\}^2, [p_{\mathrm{T}}])$ is computed from IP-Glasma+MUSIC+UrQMD simulation. Then, it is compared to estimators $\hat{\rho}_{\mathrm{est}}(\varepsilon_2^2, [s])$ and $\hat{\rho}_{\mathrm{est}}(\varepsilon_p^2, [s])$ which correlate average initial entropy density $[s]$ with the initial spatial eccentricity for the second harmonic ε_2 and the initial momentum anisotropy ε_p respectively.

Beside ρ_n, Pearson coefficients **[?, ?, ?]**

$$Q(\mathcal{E}, V_2) = \frac{\mathrm{Re}\langle \mathcal{E} V_2^* \rangle}{\sqrt{\langle |\mathcal{E}|^2 \rangle \langle |V_2|^2 \rangle}} \tag{1.43}$$

are also calculated. The $V_2 = v_2 e^{i2\psi_2}$ is a complex valued second order harmonic flow from an event plane ψ_2 **[?]**. While $\mathcal{E}$ is either the complex valued initial spatial eccentricity $\mathcal{E}_2$ or the momentum anisotropy $\mathcal{E}_p$. For $\mathcal{E}_2$, it is measured from x and y of the participants' origins

$$\mathcal{E}_2 = \varepsilon_2 e^{i2\psi_2} = \frac{\langle x^2 - y^2 \rangle + i\langle 2xy \rangle}{\langle x^2 + y^2 \rangle} \tag{1.44}$$

with $\langle ... \rangle$ an average in one event weighted by energy density. While for $\mathcal{E}_p$, the transverse components of energy-momentum tensor are needed to calculate **[?]**

$$\mathcal{E}_p = \varepsilon_p e^{i2\psi_2^p} = \frac{\langle T^{xx} - T^{yy} \rangle + i\langle 2T^{xy} \rangle}{\langle T^{xx} + T^{yy} \rangle}. \tag{1.45}$$

The results, for example, in p-Pb and d+Au are shown in Figure 1.18a. It is shown that for lower multiplicities, $\rho(v_n\{2\}^2, [p_{\mathrm{T}}])$ is positive and closer to the initial momentum anisotropy estimator $\hat{\rho}_{\mathrm{est}}(\epsilon_p, [s])$. While at higher multiplicities, $\rho(v_n\{2\}^2, [p_{\mathrm{T}}])$ becomes negative, approaching the geometric estimator $\hat{\rho}_{\mathrm{est}}(\epsilon_2, [s])$. The study concludes that the sign change in $\rho(v_n\{2\}^2, [p_{\mathrm{T}}])$ as a function of

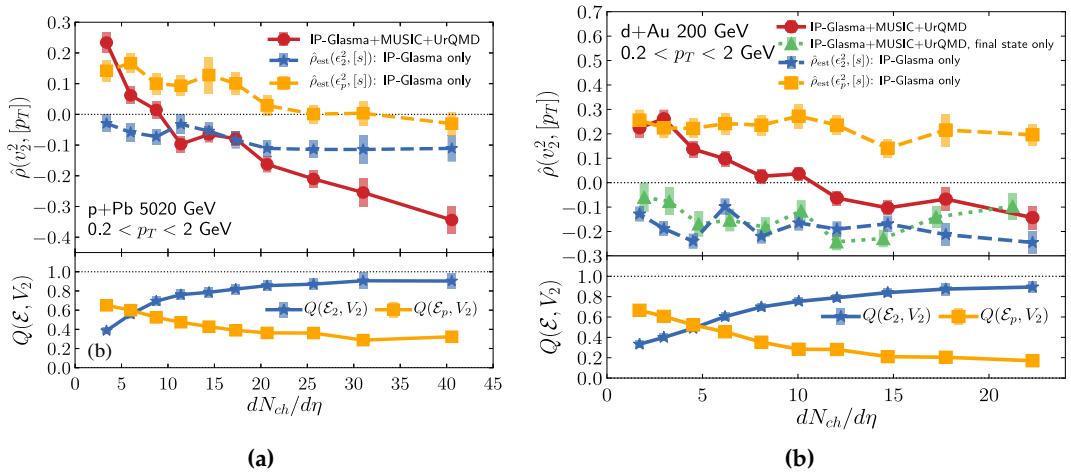

(a) **(b)**

Figure 1.18: The results from **(a)** p-Pb and **(b)** d+Au from reference [**?**]. The $\rho(v_n\{2\}^2,[p_T])$ is compared to $\hat{\rho}_{est}$ driven by either the initial spatial eccentricity ε_2 or the initial momentum anisotropy ε_p.

multiplicity indicates the origin of the elliptic flow in small systems from the initial geometry, and the presence of initial state momentum anisotropies predicted by CGC. To further support its conclusion, the study compares $\rho(v_n\{2\}^2,[p_T])$ calculation with the one that only uses the initial energy density of the IP-Glasma calculation, and starts the hydrodynamic evolution at $\tau = 0.1$ fm to compensate for the lack of initial radial flow in d+Au. The result is indicated as triangles in Figure 1.18b and there is no sign change observed. In this case, there is no initial momentum anisotropy and the results agrees with $\hat{\rho}_{est}(\epsilon_2,[s])$. Moreover, the Pearson coefficients $Q(\mathcal{E},V_2)$ in the lower panel suggest that the behavior of $\rho(v_n\{2\}^2,[p_T])$ results from geometry primarily influencing the elliptic flow in high multiplicity events since the $Q(\mathcal{E}_2,V_2)$ increases as the multiplicity grows. While the initial momentum anisotropy determines the final v_n at low multiplicity as the $Q(\mathcal{E}_p,V_2)$ decreases at the high multiplicity.

In reference [**?**], the origin of $\rho(v_n\{2\}^2,[p_T])$ is explored from another perspective with Pythia 8. This program does not include neither hydrodynamic simulation nor gluon saturation. Pythia 8 has a build-in Angantyr [**?**] to simulate heavy ion collisions. The results are shown in Figure 1.19. The $\rho(v_n\{2\}^2,[p_T])$ calculations are done with particles in the p_T range of $0.3 < p_T < 2.0$ GeV and the three-subevent method exactly like in data, and the N_{ch} in x-axis is defined as the number of charged hadrons with $|\eta| < 2.5$ and $0.5 < p_T < 5.0$ GeV. Surprisingly, the pp results can reproduce the sign change as well even without hydrodynamic flow and gluon saturation effect. While in p-Pb results, the sign change is not observed and the non-hydrodynamic flow contribution from these results are compared to $\hat{\rho}_{est}(\varepsilon_p^2,[s])$ calculation from reference [**?**].

There is also preliminary results of $\rho(v_n\{2\}^2,[p_T])$ measurement in pp at 13 TeV, p-Pb at 8.16 TeV, and Pb+Pb 5.02 TeV from the CMS experiment. The preliminary results are shown in Figure 1.20. They indicate that the sign change can be observed

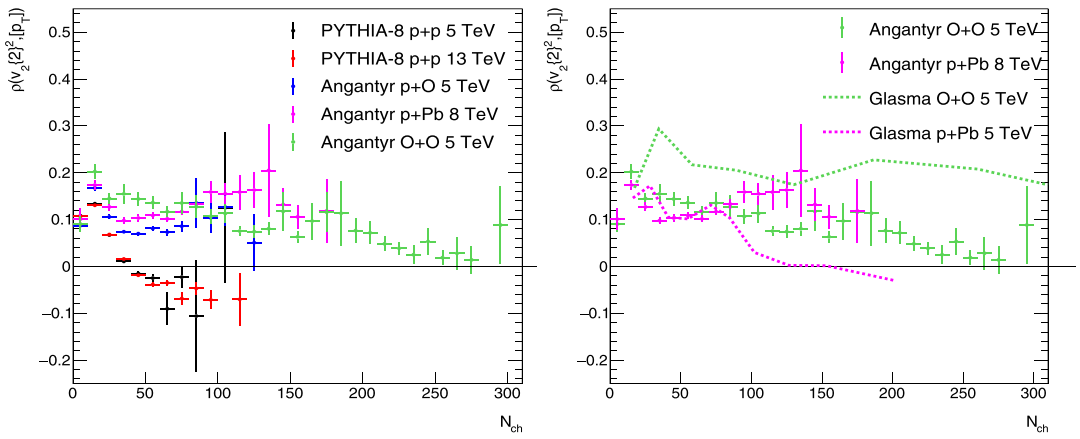

(a) **(b)**

Figure 1.19: Results of $\rho(v_n\{2\}^2, [p_T])$ calculations from the particles in the p_T range of $0.3 < p_T < 2.0$ GeV and the three-subevent region. The N_{ch} in x-axis is defined as the number of charged hadrons with $|\eta| < 2.5$ and $0.5 < p_T < 5.0$ GeV. **(a)** Pythia 8 is used to simulate the various collision systems, with a build-in Angantyr to simulate the heavy ion collisions. **(b)** The Angantyr results are compared to $\hat{\rho}_{\text{est}}(\varepsilon_p^2, [s])$ from reference [**?**]. Figure from [**?**]

in pp collision data for second harmonic and that the predictions from Pythia describe the data at least qualitatively. For the third harmonic, no sign change is observed.

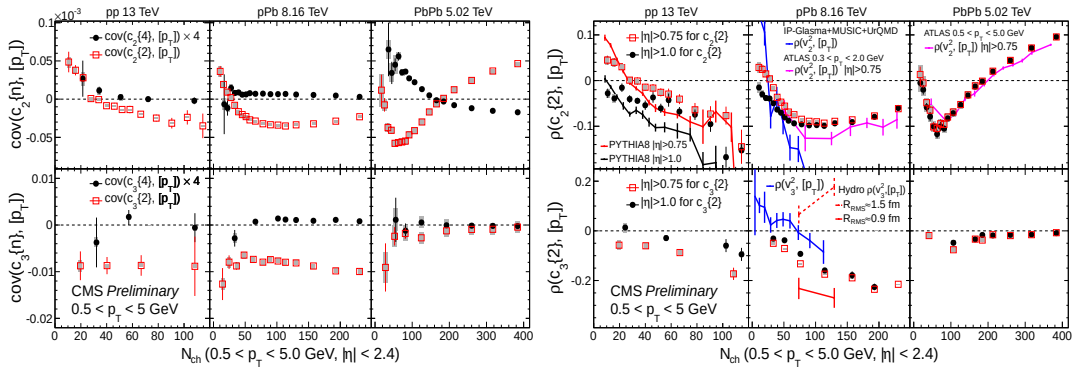

(a) **(b)**

Figure 1.20: The preliminary results from CMS experiment for **(a)** $\text{cov}(v_n\{2\}^2, [p_T])$ and **(b)** $\rho(v_n\{2\}^2, [p_T])$. The c_n is equivalent to v_n. Figure from [**?**]

1.8 Pythia

Pythia [**?**, **?**, **?**, **?**, **?**, **?**] is a Monte Carlo event generator widely used in high-energy physics. It is designed for simulating the parton (quark or gluon) interaction, evolution, and hadronization process in particle collisions as well as modeling the development of final-state particles such as resonance decay. Currently, the latest Pythia program is the generation 8 with several versions in these series. Therefore, the term Pythia 8 refers to any version within these series.

In Pythia, the simulation can be set to include or exclude certain physics by turning them on/off in the setting. The commonly used settings turned on to simulate a complete collision process are initial-state radiation (ISR), multiparton interactions (MPI) [**?**, **?**, **?**, **?**, **?**], final-state radiation (FSR), hadronization, and resonance decay. ISR, MPI, and FSR are perturbative processes while the remaining processes are non-perturbative as they occurred below Λ_{QCD} scale.

The simulation starts at the moment a $2 \to 2$ parton scattering occurs as illustrated in Figure 1.21. First, there is a hard process in the $2 \to 2$ scattering, resulting one of the

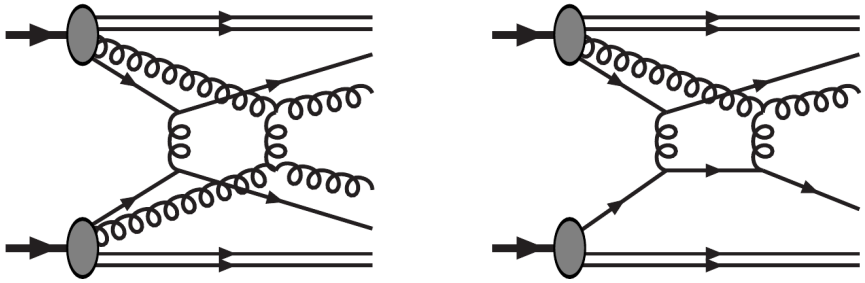

Figure 1.21: Illustration of parton scattering: **(a)** Two $2 \to 2$ processes involving $qq \to qq$ and $gg \to gg$. **(b)** A $2 \to 2$ process of $qq \to qq$ followed by scattering of outgoing quark with a gluon, resulting in multiparton scattering of $3 \to 3$ process. Figure from [**?**].

outgoing parton in the current p_{T} scale. Chronologically in the real hadrons collision, the ISR occurs first before MPI and FSR. However, ISR, MPI, and FSR are presented as competing processes instead in a simplified master equation of the interleaved evolution [**?**]

$$\frac{d\mathcal{P}}{dp_{\mathrm{T}}} = \left(\frac{d\mathcal{P}_{\mathrm{MPI}}}{dp_{\mathrm{T}}} + \sum \frac{d\mathcal{P}_{\mathrm{ISR}}}{dp_{\mathrm{T}}} + \sum \frac{d\mathcal{P}_{\mathrm{FSR}}}{dp_{\mathrm{T}}} \right) \times \exp\left(- \int_{p_{\mathrm{T}}}^{p_{\mathrm{T}_{i-1}}} \left(\frac{d\mathcal{P}_{\mathrm{MPI}}}{dp'_{\mathrm{T}}} + \sum \frac{d\mathcal{P}_{\mathrm{ISR}}}{dp'_{\mathrm{T}}} + \sum \frac{d\mathcal{P}_{\mathrm{FSR}}}{dp'_{\mathrm{T}}} \right) dp'_{\mathrm{T}} \right). \tag{1.46}$$

The exponent factor is a Sudakov-like form factor which gives the probability that nothing happens in between the previous p_{T} scale and the current one. The $d\mathcal{P}_{\mathrm{MPI}}/dp_{\mathrm{T}}$, $d\mathcal{P}_{\mathrm{ISR}}/dp_{\mathrm{T}}$, and $d\mathcal{P}_{\mathrm{FSR}}/dp_{\mathrm{T}}$ are the probabilities of a parton undergoes MPI, ISR, or FSR at the current p_{T} scale respectively. The probabilities $d\mathcal{P}_{\mathrm{ISR}}/dp_{\mathrm{T}}$ and $d\mathcal{P}_{\mathrm{FSR}}/dp_{\mathrm{T}}$ are given by DGLAP evolution equation, while probability of MPI occurs is

$$\frac{d\mathcal{P}_{\mathrm{MPI}}}{dp_{\mathrm{T}}} = \frac{1}{\sigma_{nd}} \frac{d\sigma}{dp_{\mathrm{T}}} \exp\left(- \int_{p_{\mathrm{T}}}^{p_{\mathrm{T}_{i-1}}} \frac{1}{\sigma_{nd}} \frac{d\sigma}{dp'_{\mathrm{T}}} dp'_{\mathrm{T}} \right) \tag{1.47}$$

with σ_{nd} is the non-diffractive inelastic cross section of the colliding hadrons and $d\sigma/dp_{\mathrm{T}}$ is calculated from the perturbative QCD $2 \to 2$ cross section in non-diffractive events. There can only be one of the aforementioned processes occurs at a given p_{T} scale. In the case of MPI is picked, there is a second hard interaction creating two

subsystems which can undergo ISR or FSR. While if either ISR or FSR is picked, one of the incoming or outgoing partons splits. After one of these processes occurs, the p_T scale is reduced and the competition repeats until the cutoff limit is reached. However, unless the rescattering is turned on in the setting, once MPI occurs, it will not be allowed again, leaving only ISR and FSR in the pool. Currently Pythia supports up to two parton rescattering. However, this is not well tested and the double rescattering is not integrated with parton shower algorithm, and therefore, can not be done with ISR or FSR turned on.

Due to the QCD confinement, the final partons at the end of shower must recombine into hadron. The hadronisation is carried out in Pythia using Lund string fragmentation algorithm [**?**]. For instance, suppose the last fragmentation in a parton shower produces a quark-antiquark ($q\bar{q}$) pair illustrated in Figure 1.22. The $q\bar{q}$ are

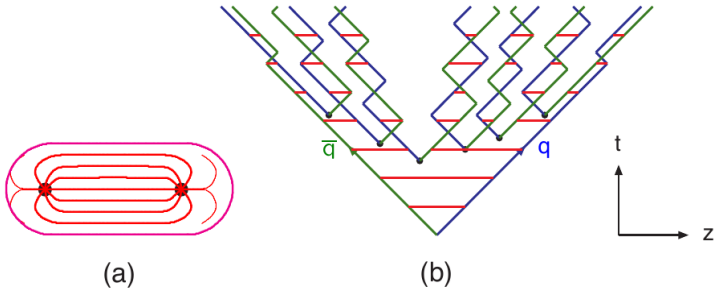

Figure 1.22: Illustration of string model for parton fragmentation. **(a)** A flux tube of quarks attracted by gluons, similar to magnetic flux between different poles. **(b)** The string breaking as quarks move apart from each other. Figure from [**?**].

connected by color strings (gluons) which will break and produce another $q\bar{q}$ pair as they move apart from each other. The string breaks due to the nature of strong interaction which only work in very short distance. As the $q\bar{q}$ move away from each other, it will become harder to overcome the potential barrier from strong interaction. As results, the $q\bar{q}$ pair lose some of their energy, and when the string break, it creates another $q\bar{q}$ pair in each loose end from the energy loss. The process continue until the quarks do not have enough energy to break the string and recombine to the nearest other quarks. The final state hadron might be unstable and has a very short lifetime even after prolonged by time dilation. Therefore, the resonance decay is simulated as well.

Just before the hadronization, in the event where MPI occurs, the color reconnection (CR) can be simulated to produce a flow-like pattern [**?**]. In this scheme, partons are classified by which MPI system they belong to. With the secondary hard interaction occurs, many colour strings will overlap in physical space which makes them hard to distinguish. The lower p_T scale of a system, the larger its spatial extent, and therefore the more likely it overlaps with other system. The color flow of two such systems can be fused, and if so, the partons of the lower-p_T system are added to the strings defined by the higher-p_T system in such a way as to give the smallest total string length and potential energy. The reconnection probability for merging the

lowest-p_{T} system with the second-lowest one is

$$P = \frac{(R \times p_{T_0}^2)}{(R \times p_{T_0}^2) + p_{\mathrm{T}}^2} \tag{1.48}$$

with R is the color reconnection range parameter which serves as a scale factor and p_{T_0} is the energy-dependent dampening parameter. If they are not merged, the lowest one is tested with the third-lowest one and so on. The probability of merging becomes $P(1-P)^{(m-1)}$ for the trial with the m-lowest system. Once the iteration for lowest-p_{T} system finishes, the same iteration is done for the second-lowest one with respect to the ones above it, then the third-lowest, and so on. With the initial probability P, it is easy to merge a low-p_{T} system to another, but difficult to merge two high-p_{T} ones. And the subsequent probability for the system to survive becomes larger if the previous merging fails. [**?**]

1.9 EPOS

The **E**nergy-conserving quantum mechanical multiple scattering approach, based on **P**arton ladders, **O**ff-shell remnants, and **S**plitting of parton ladders (EPOS) [**?**, **?**, **?**, **?**] is a successor of NEXUS simulation with initial condition based on the parton-based Gribov-Regge theory [**?**]. There are several versions developed and currently the latest one is EPOS 4. However in this analysis, the one that is used is the EPOS 2 [**?**], and further in this thesis, the EPOS simulation refers to this version.

In EPOS, the parton ladder shown in Figure 1.23 is used to represent the initial state radiations, the hard process, and the final state radiations. The evolution of these partons before the collision can be represented as a ladder of successive emissions, predominantly gluons, towards low x parton described by the DGLAP equations. Each rung of the ladder represents a splitting of a parton into two other

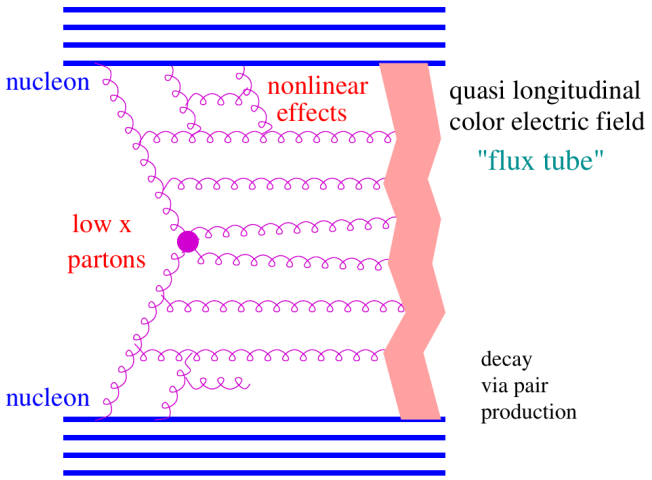

Figure 1.23: Illustration of elementary interaction in the EPOS. Figure from [**?**].

partons, typically gluons. A parton from one hadron finally interacts with a parton from another hadron in the center of Figure 1.23. The parton ladder evolves using DGLAP equations up to a point where the gluon density becomes high enough for the nonlinear gluon saturation effect in the CGC framework to become relevant. EPOS then integrates the saturation effect into its parton evolution models [**?**].

The parton ladder may be considered as a quasi-longitudinal color field of flux tube. The dynamics of the strings in the flux tube is governed by the Nambu-Goto string action [**?**, **?**, **?**, **?**]. The strings break following the Lund string fragmentation. For heavy ion collisions or very high energy proton-proton scattering, the strings will be very dense and the core-corona separation [**?**, **?**, **?**] is performed. The core represents the dense, central region of the collision where multiple parton interactions occur. This region is characterized by a high energy density, which can lead to the formation of a thermalized medium. Once the core reaches a certain energy density, it undergoes a phase transition to a QGP and the simulation of 3+1D hydrodynamic evolution with crossover equation of state is performed. The corona, which consists of more peripheral, less dense regions, does not thermalize and thus does not enter the hydrodynamic evolution.

In EPOS, the crossover temperature is set at 166 MeV. Below this temperature, hydrodynamic evolution ceases, and hadronization begins. Even after hadronization, the system continues to develop elliptic flow through hadronic scatterings [**?**, **?**, **?**, **?**, **?**]. The hadronic interactions are simulated using the hadronic cascade model UrQMD [**?**, **?**] until the system becomes so dilute that no further interactions occur. The final freeze-out position of particles is determined by their last interaction in the cascade or their current position at hadronization if no hadronic interactions take place.

1.10 Research goal

The goal of this research is to measure $\rho(v_n\{2\}^2, [p_{\mathrm{T}}])$ in pp at 5.02, and compare them with pp at 13 TeV and p-Pb at 5.02 TeV as well as the theory prediction provided by Monte-Carlo simulations. For this purpose, Pythia and EPOS simulations are chosen due to different physics content between them. The Pythia is well known to reproduce flow-like pattern with color reconnection without any hydrodynamic simulation. While the EPOS takes into account the gluon saturation effect, 3+1D hydrodynamic simulation, and hadronic cascade. The analysis method from references [**?**, **?**] is repeated for the small systems in this analysis. The measurement is done for p_{T} intervals of $0.5 \leq p_{\mathrm{T}} \leq 2$ GeV, $0.3 \leq p_{\mathrm{T}} \leq 2$ GeV, and $0.3 \leq p_{\mathrm{T}} \leq 5$ GeV. The analysis has matured and is currently being reviewed by ATLAS Collaboration to get permission for publication.

2 Experimental Setup

2.1 CERN And LHC

CERN, initially an acronym for the French name *Conseil européen pour la recherche nucléaire* (European Council for Nuclear Research), was officially founded in 1954. However, its conceptualization traces back to 1949, driven by the vision of numerous pioneering scientists. In the aftermath of World Wars, visionaries like Raoul Dautry, Pierre Auger, Lew Kowarski in France, Edoardo Amaldi in Italy, and Niels Bohr in Denmark envisioned a collaborative laboratory for scientific advancements, aiming at fostering unity and sharing the escalating costs of nuclear research facilities [**?**].

Today, CERN is dedicated to the mission of conducting science for peace, uniting people globally in the pursuit of scientific knowledge [**?**, **?**]. It strictly adheres to non-military purposes, keeping its scientific work open and accessible to everyone, thereby encouraging international collaborations. With 23 member states and numerous collaborations with non-member countries, CERN stands as a beacon of scientific cooperation.

While CERN conducts a variety of research, its primary focus is on particle physics. The epicenter of this exploration is the Large Hadron Collider (LHC), currently the world's largest particle accelerator with a circumference of 27 kilometers, as depicted in Figure 2.1. There have been three LHC Run periods so far: Run 1 in 2009–2013, Run 2 in 2015–2018, and Run 3 which is started in 2022 and planned to operate until 2025. Accelerating particles to several teraelectronvolts (TeV) requires a multi-step process, involving smaller accelerators operating in conjunction with the LHC.

For heavy ions like Pb ions, the journey begins with injection from the Electron Cyclotron Resonance (ECR) ion source into Linear Accelerator 3 (LINAC 3). The Pb ions undergo progressive acceleration through LINAC 3, Low Energy Ion Ring (LEIR), Proton Synchrotron (PS), and Super Proton Synchrotron (SPS) before being injected into the LHC.

Proton beams come from different source but follow the same path from PS onward. Before 2020, they started from LINAC 2 and Proton Synchrotron Booster (PSB) before entering PS. After 2020, LINAC 2 is replaced by LINAC 4 which became the source of proton beams during Run 3 onward [**?**].

The acceleration of particles relies on radio-frequency (RF) cavities [**?**]. These cavities operate by modulating electric potential in such a way that particles remain in tight bunches during the acceleration. Magnets guide the accelerated particles, using dipole magnets for bending trajectory in circular motion and quadrupole magnets

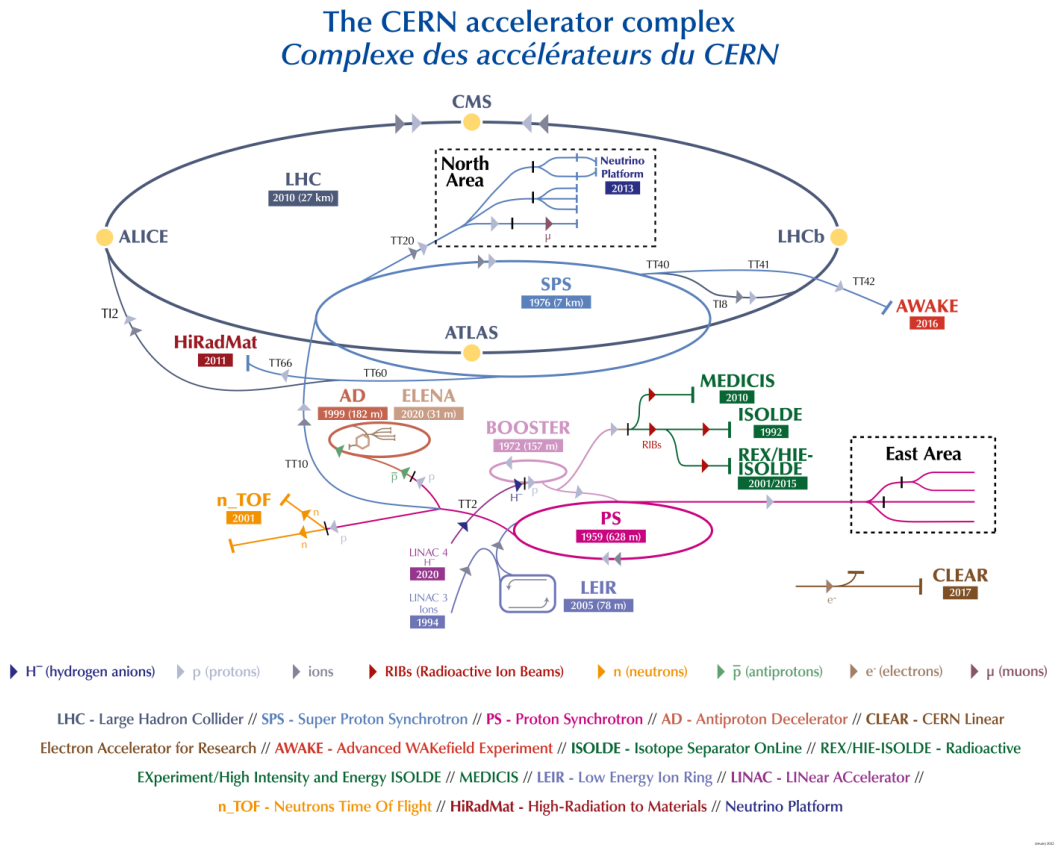

Figure 2.1: The latest CERN's accelerators complex by 2022. LINAC 2 served as the proton beam source since 1978 until 2018 and was replaced by LINAC 4 in 2020. Figure from [**?**].

for focusing. To maintain the energy efficiency of the accelerators, RF cavities and magnets are superconducting devices. They are cooled with liquid helium to the temperature of 1.9 K.

The magnets were designed to give a maximum energy of 7 TeV per beam, but it was just half of that value when the Run 1 started. To increase the strength of magnetic field, the magnets are trained by pumping electric current until they heat up and lose superconductivity (quench) [**?**]. The repeated quench training allows the magnets to accept more electric current until the desired value of magnetic field is obtained. After more quench training, the energy that magnets can deliver rose to 4 TeV later in Run 1, 6.5 TeV in Run 2, and 6.8 TeV in Run 3.

Running LHC for operational data taking starts when LHC is about to start the beam injection, and stops when the beam is dumped. The process of beam injection from SPS to LHC takes a few hours. During the injection, the beams circulate inside the LHC at 450 GeV, equivalent to the energy of the SPS. The LHC filling scheme follows a bunch pattern with some time interval between them that depends on how much the luminosity is expected to be delivered to each experiments. Once the injection finish, the magnets are ramped up with electric currents to reach the flat-top energy. The beams are then squeezed by the focusing magnets. The smaller beam

diameter maximizes the chance of the collision. Close to the physics interactions points, the special magnets adjust the beams so they point to each other and collide. And finally, stable beams are declared and the experiments start taking data. After several hours, the luminosity drops as the number of particles in bunches decreases after collision. The data taking lasts until the luminosity is too low to maintain enough collision or the beams are dumped prematurely due to a technical problem. The run cycle repeats after the beam dump.

There are eight interaction points (IP) in LHC where the beams can be collided, but currently only four of them are used for experiments. The IP1 for the ATLAS experiment [**?**]. The IP2 for the ALICE experiment [**?**]. The IP5 for the CMS experiment [**?**]. And the IP8 for the LHCb experiment [**?**]. One of the most notable achievements in the history of the LHC came in July 2012 when both ATLAS and CMS collaborations independently announced the discovery of a new particle consistent with the long-sought Higgs boson [**?**, **?**]. This discovery confirmed the existence of the last missing piece of the Standard Model of particle physics.

2.2 ATLAS Experiment

The experimental data in this research were collected using the ATLAS detector. The concept for the ATLAS experiment emerged in the mid-1990s when the LHC was in the planning stages. The collaboration formed to design and propose a general-purpose detector capable of exploring a wide range of physics phenomena. The installation of ATLAS components inside the IP1 underground cavern began in 2003, and over the next several years, the experiment underwent a thorough commissioning process to ensure that all its subsystems were working correctly and efficiently. The ATLAS detector as shown in Figure 2.2 can be grouped into three sectors: the Inner Detector (ID), Calorimeters, and Muon Spectrometer.

Over the years, ATLAS has undergone several upgrades to improve various components. The upgrades were carried out mostly during Long Shutdown (LS) periods while LHC is not operating. During the LS1 (2013 - 2015), a major addition to the ATLAS detector components was Insertable B-Layer (IBL) which was installed into pixel detector [**?**]. During LS2 (2018-2022), more detector components such as new small wheel (NSW), new muon chambers, and ATLAS Forward Proton (AFP) spectrometer were added to ATLAS detector system [**?**]. The upgrade of Trigger and Data Acquisition System (TDAQ) and hardware upgrade of the existing detector, Liquid Argon Calorimeter (LAr), were also done in this period as preparation for high-luminosity era of LHC. In the upcoming LS3 (2026-2028), the ID system is planned to be replaced by a new all-silicon inner tracker (ITk) as LHC upgrades the machine luminosity further by a factor of 5 to 7.5 [**?**]. However, since the analysis is done using the data collected during Run 2, the detector configuration discussed in this section only includes Run 2 setup.

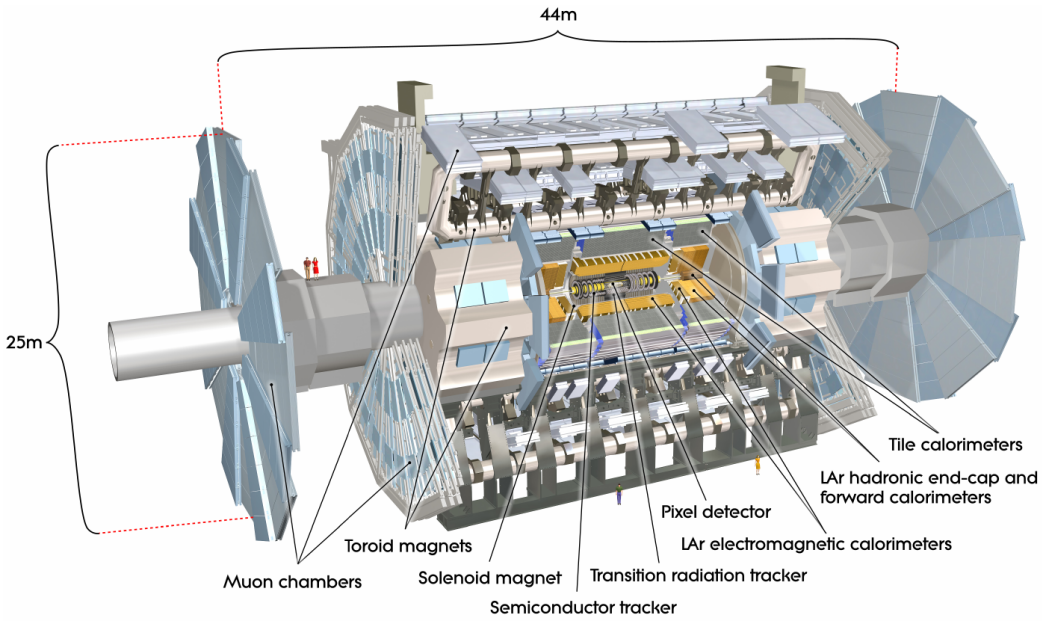

Figure 2.2: The view inside of ATLAS detector. Figure from [?].

The ATLAS experiment uses the following global coordinate systems. The z-axis is inline with the beam line and the center of the detector geometry is defined as the origin of the coordinate system. The positive x-axis is directed towards the centre of the LHC ring and while the positive y-axis extends upward. The azimuthal angle ϕ is in x-y plane starting from the x-axis with range $0 \leq \phi \leq 2\pi$. The polar angle θ ranges from $0 \leq \theta \leq \pi$ with zero starts from positive z-axis. The particle momentum vector is often expressed using its transverse momentum p_{T}, pseudorapidity η, and azimuthal angle ϕ. The η is related with the θ in by

$$\eta = -\ln\left[\tan\frac{\theta}{2}\right], \quad \theta = 2\arctan\left(e^{-\eta}\right). \tag{2.1}$$

and p_{T} is the momentum projection on the x-y plane:

$$p_{\mathrm{T}} = \sqrt{p_x^2 + p_y^2} \tag{2.2}$$

Radius R in x-y plane starts from the z-axis outward.

2.2.1 Inner Detector

The Inner Detector [?, ?] consists of the Pixel Detector, the Semiconductor Tracker (SCT), and the Transition Radiation Tracker (TRT). Each of them consists of the barrel layers enclosed with end-caps parts on both sides. Figure 2.3 shows the schematic view of the barrel layers from the innermost to the outermost. The barrels cover the entire azimuthal angle.

Closer to interaction point where the radiation dose is higher, the silicon detector type is chosen since it can resist the radiation damage for many years. The innermost

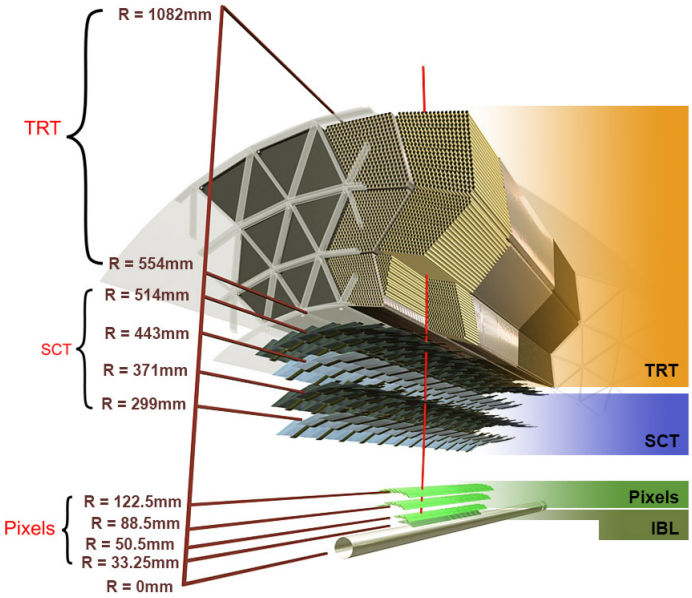

Figure 2.3: A schematic view of ATLAS Inner Detector barrel layers. Figure from [**?**].

layer is the Insertable B-Layer (IBL) [**?**] that was added to enhance primary vertex resolution and improve secondary vertex resolution needed for b-quark jets tagging. There are four layers of barrel Pixel Detector including IBL and three end-caps in both sides in total. The pixel barrel covers $|\eta| < 1.5$ and the end-caps cover $1.5 \leq |\eta| \leq 2.5$. The very high-granularity of Pixel Detector is necessary due to a high density of particles close to the interaction point. The Pixel Detector provides intrinsic resolutions of about 10 μm $\times$ 60 μm in the IBL, and 10 μm $\times$ 115 μm in the other layers [**?**].

The Pixel Detector consists of modules containing pixel sensors that are made of high-purity n-type silicon sensors [**?**]. When charged particles hit the detector and pass through it, they ionize the silicon material in the pixels. This ionization generates electron-hole pairs within the silicon. The electrons drift towards the electrodes. The read-out system registers the hit if the electric current passes the threshold.

After Pixel Detector layers, there is SCT which has four barrel layers and nine end-cap discs on each side, covering $|\eta| \leq 2.5$. The SCT is divided into many modules, each containing p-in-n silicon strip sensors [**?**]. The SCT operates with a principle similar to the Pixel Detector since both of them are based on silicon detectors. The silicon micro-strip sensors are positioned parallel to the beam pipe in the barrel region and radially on the SCT disks. These sensors are glued back-to-back in the module with stereo angle of 40 mrad as illustrated in Figure 2.4. Thanks to that, the information from the pair of modules allows for reconstruction of z coordinate of the hit. The small angle reduces the probability of unrelated hits combinations to be considered as a genuine track. The SCT provides intrinsic resolution of 17 μm $\times$ 580 μm [**?**].

And finally, the outermost layers of the inner detector is covered by TRT [**?**, **?**]. The

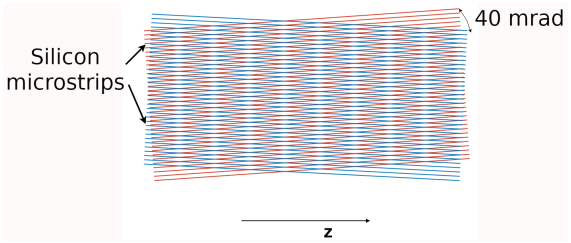

Figure 2.4: An illustration of an SCT module in barrel layers. The stereo angle is purposefully exaggerated for illustration.

TRT provides intrinsic resolution of 130 μm in R-ϕ and no z measurement. Unlike the other inner detectors, the TRT, as it is named, utilizes a different detection principle called transition radiation [**?**, **?**] to track charged particles. It consists of straw tubes array containing a gas mixture of 70% Xe, 27% CO_2, and 3% O_2, and an internal matrix of polypropylene fibers.

The straw tube were constructed from two layers of conductively-coated polyimide film. Figure 2.5 shows the cut-away view of the outermost part of a straw tube. The straw anodes are 31µm-diameter gold-plated tungsten wires at

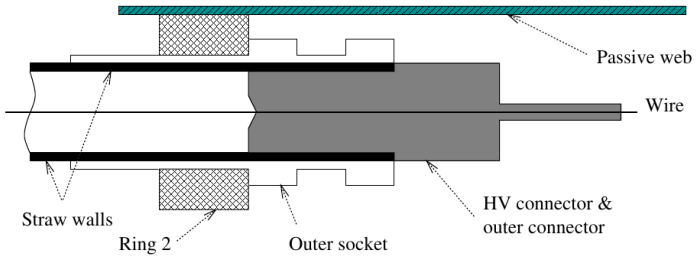

Figure 2.5: A schematic view of the outermost part of a straw tube. Figure from [**?**].

ground voltage located along the center of the tube. And the straw cathodes are operated at high voltage, surrounding the inner wall of the tube. The layout of the straw tubes was designed to optimize the probability of the detection of transition radiation as well as to maximize the number of hits along a track [**?**].

When a charged particle passes through the boundary between two materials with different dielectric properties, such as between the gas-filled straw tube and polypropylene fiber, it emits transition radiation. This radiation consists of photons with energies in the X-ray to ultraviolet range. The intensity of the radiation is proportional to the Lorentz factor $\gamma = \sqrt{1 - v^2/c^2}$ of the traversing particle (up to saturation) [**?**]. The photons ionize the gas atoms in the straw tube, producing electron-ion pairs. As the charged particle traverses the gas-filled straw tube, it ionizes the gas atoms along its path, creating additional electron-ion pairs. The electric field within the straw tube causes the free electrons to drift towards the anode wire. By measuring the arrival times of the signals at the anode wires of the straw tubes and combining this information with the known geometry of the detector, the TRT can reconstruct the hits left by the charged particle as it passes through the detector.

The TRT also provides information about the energy deposition pattern and the number of transition radiation photons emitted by the charged particle. This information can be used to distinguish between different types of particles. For example, suppose there are an electron and a heavy baryon passing the TRT with same energy. Due to the mass-energy relation $E = \gamma mc^2$, the electron has larger γ than the heavy baryon to compensate its smaller mass. And therefore, the electron emits more transition radiations that distinguish it from heavier particles with the same energy.

All ID components work together to track the charged particles by providing the hit locations in each layer. The Pixel Detector provides the 3D spatial coordinate of hits. And so does the SCT but with lower resolution of z. The TRT provides 2D radial coordinate in R-ϕ plane. These hit points can be reconstructed into the trajectory of charged particles by the tracking algorithm. The reconstructed charged particles tracks converge into a primary vertex where a collision occurs, or secondary vertices where resonance decays takes place.

2.2.2 Calorimeters

Calorimeters absorb most of the outgoing particles and therefore placed after ID layers. The calorimeter system measures the energy of the particles. It can detect both charged and neutral particles, except muon and neutrino. There are electromagnetic calorimeter and hadronic calorimeter consecutively from inside to outside as shown in Figure 2.6.

The electromagnetic calorimeter measures the energy of electrons and photons. For this purpose, liquid-argon (LAr) detector [**?**] is used. It consists of liquid-argon as the active material and lead for its absorber material. The electromagnetic calorimeters cover $|\eta| < 1.475$ and the entire ϕ for barrel and $1.475 < |\eta| < 3.2$ for end-caps (EMEC). When an electron hits the lead, it releases some of its energy by radiating bremsstrahlung photons. The high-energy photons undergo pair production inside lead nuclei, creating electron-positron pairs. And if their energy is still high enough, these pairs can produce additional bremsstrahlung photons. This process repeats, creating a cascade of particle showers, until the electrons' energy is sufficiently low and the last photons no longer have enough energy for pair production. The shower particles ionize liquid-argon which creates signal proportional to the energy loss from shower. Then the measured shower energy is summed up to determine the energy of the primary electron or photon.

The hadronic calorimeter measures hadron energy and uses both LAr detector and Tile calorimeter [**?**]. As shown in Figure 2.7, the LAr detector is used in hadronic end-cap (HEC) and forward calorimeter (FCAL), covering $1.5 < |\eta| < 3.2$ and $3.1 < |\eta| < 4.9$ respectively. While the Tile calorimeter is used in the barrel part and the extended barrel, covering $|\eta| < 1.0$ and $0.8 < |\eta| < 1.7$ respectively and the entire ϕ. For the absorber material, instead of lead, the HEC uses copper and the FCAL

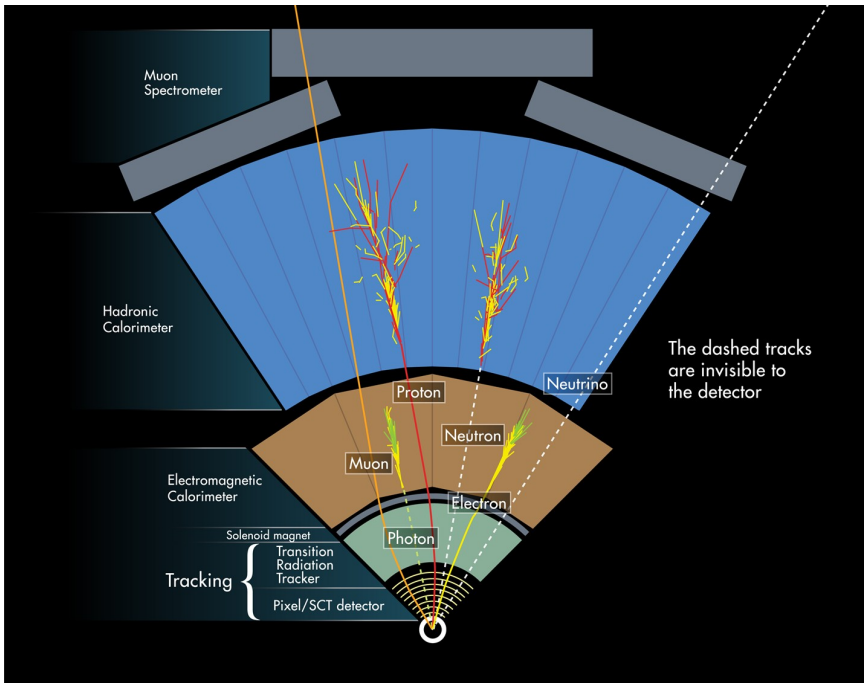

Figure 2.6: A diagram of particle paths in the detector. Electron and photon are creating a cascade of particle shower as they pass the electromagnetic calorimeter. And so do hadrons in the hadronic calorimeter. Muon is not detected in calorimeter but in Muon Spectrometer instead, while neutrino is undetected. But the presence of the neutrino is confirmed by the missing transverse energy E_T measured in a fully reconstructed event. Figure from [**?**].

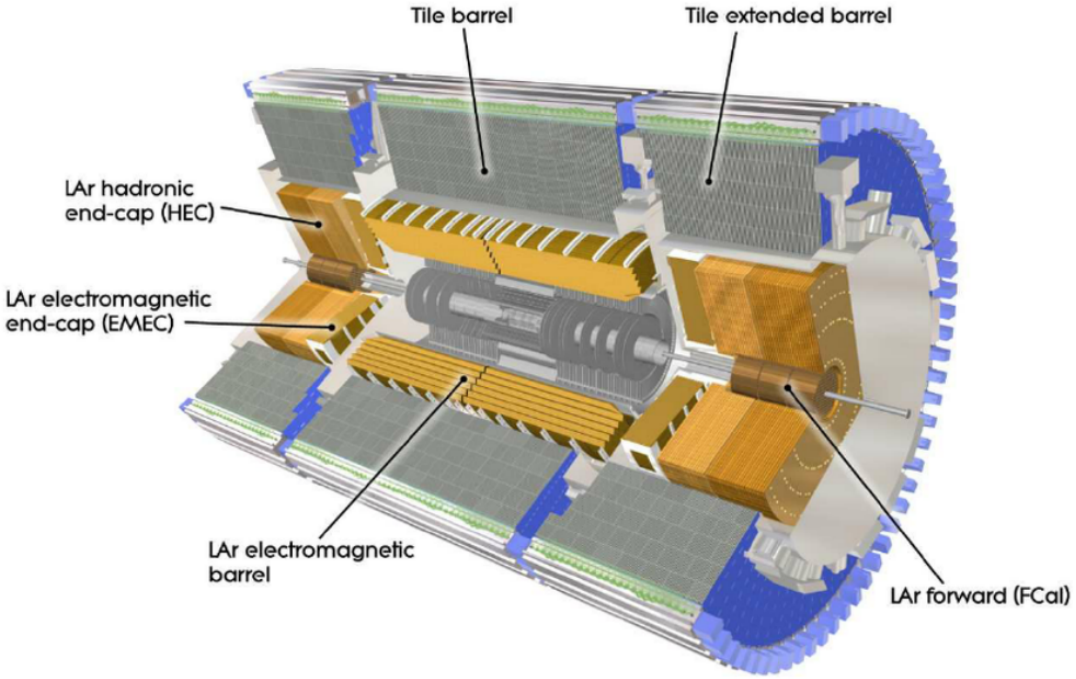

Figure 2.7: A schematic view of the calorimeter system. Figure from [**?**].

uses both copper and tungsten. The particle shower produced from the interaction between a hadron and the absorber also involves strong interaction.

The Tile calorimeter consists of steel as the absorber, scintillating tiles [?] as the active material, and photomultiplier tubes (PMT) as the read-out. When an incoming hadron from interaction point hits the steel plate, it produces a hadronic shower which then hit the active material. The scintillating tiles are plastic scintillators which emit photons when they interact with the hadronic shower. The emitted photons is detected by PMT and their quantity is amplified for read-out.

2.2.3 Muon Spectrometer

Muon is about 207 times heavier than electrons. Because of its greater mass, it is less susceptible to acceleration while traversing electron clouds and electric field. It does not interact strongly with nuclei as well. These allow muon to penetrate both ID and calorimeters without undergoing significant energy loss from bremsstrahlung or scattering. Therefore, the Muon Spectrometer (MS) [?] is placed on the outermost layers in ATLAS, providing the measurement of muons tracking. The MS is immersed in the toroidal magnetic field and thus also provides momentum measurement. As illustrated in Figure 2.8, the MS consists of Monitored Drift Tube (MDT) chambers, Cathode Strip Chambers (CSC), Resistive Plate Chambers (RPC), and Thin Gap Chambers (TGC). These components are gas ionization detectors, each with different structure and gas mixture filling.

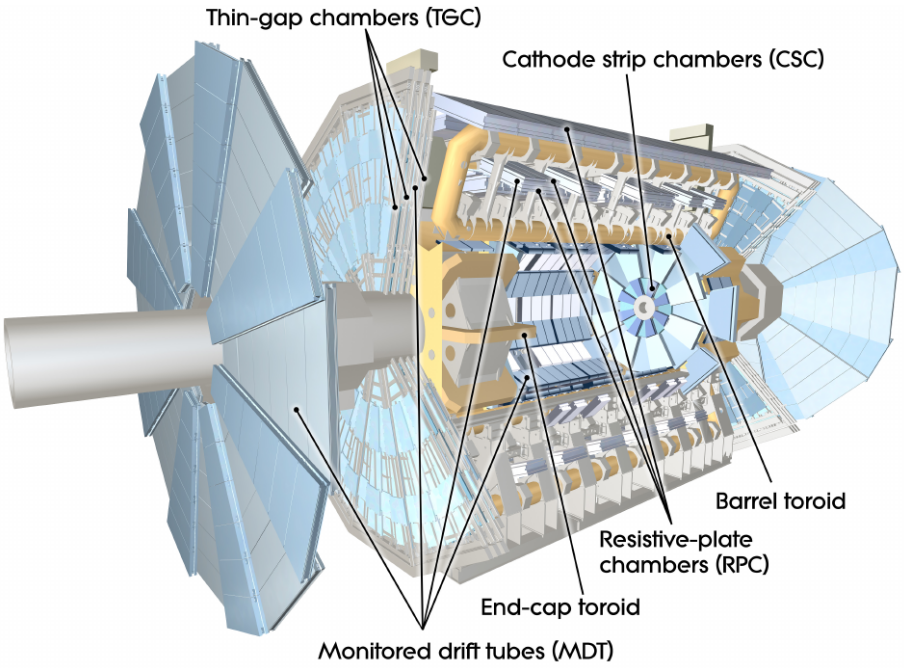

Figure 2.8: A schematic view of the muon spectrometer. Figure from [?].

The MDT chambers are based on wire chamber detector and cover a range of $|\eta| < 2.7$. They typically consist of three to eight layers of aluminum tubes filled

with 93% Ar and 7% CO_2 gas mixture. The CSC are a type of multiwire proportional chambers (MWPC), covering $2.0 < |\eta| < 2.7$. The gas mixture is chosen to be 80% Ar and 20% CO_2. The composition containing hydrogen atom is avoided in the gas mixture to reduce the sensitivity to neutron since CSC are placed in the innermost end-caps of the spectrometer.

The RPC cover the barrel region in $|\eta| < 1.05$. The gas mixture for RPC is 94.7% $C_2H_2F_4$, 5% Iso-C_4H_10, and 0.3% SF_6. While the TGC are similar to MWPC, positioned in the end-caps between $1.05 < |\eta| < 2.4$ with gas mixture of 55% CO_2 and 45% n-pentane. Both RPC and TGC also serve as the trigger for muon, selecting event to record when certain momentum threshold is passed and filtering muon from background particles.

2.2.4 Forward detectors

In the forward region away from interaction point, there are LUCID (LUminosity measurement using Cerenkov Integrating Detector), Zero-Degree Calorimeters (ZDC), and ALFA (Absolute Luminosity For ATLAS) [**?**]. LUCID was installed 17 m away from interaction point while the other two is farther away offsite ATLAS main detectors The ZDC is placed in the TAN (Target Absorber Neutral), located between the beam-pipes right after the split, 140 m away from the interaction point. While ALFA is located inside Roman pots at a distance of approximately 240 m from the interaction point.

The main purpose of LUCID is to detect inelastic *pp* scattering in the forward direction, allowing real-time monitoring of instantaneous luminosity L, as well as the overall beam conditions. This enables the measurement of integrated luminosity,

$$L_{\text{int}} = \int L \, dt \tag{2.3}$$

over period of time t. The integrated luminosity is proportional to the the number of inelastic event

$$N_{\text{event}} = L_{\text{int}} \, \sigma_{\text{inelastic}} \tag{2.4}$$

with $\sigma_{\text{inelastic}}$ cross section for inelastic scaterring. LUCID consists of a series of Cherenkov tubes filled with a gas that emits light when traversed by charged particles. These tubes are arranged in a cylindrical geometry around the beam pipe. Cherenkov radiation is emitted when a charged particle passes through a dielectric medium at a speed greater than the phase velocity of light in that medium [**?**]. The Cherenkov light produced in the tubes is detected by PMTs, converting light into an electrical signal which can then be measured and analyzed.

The ZDC are used only during heavy ion run. The purpose of ZDC is to detect forward neutrons with $|\eta| > 8.3$ in heavy-ion collisions. Therefore, ZDC can be used to determine the centrality of such collisions by measuring the number of spectator neutrons. Moreover, the ZDC also provide an additional minimum-bias trigger

for ATLAS. There are four ZDC modules installed on both sides. One of them is electromagnetic module and the other three are hadronic modules. The working principle of ZDC is similar to other calorimeters in general, with absorber and active materials.

The purpose of ALFA is to measure absolute luminosity from elastic scattering with very small angles at about 3 μrad or less. Normally, the beams of particles in the accelerator spread out more than this tiny angle. So, to make these precise measurements, a special beam conditions where the beams do not diverge as much. The beams need to have high β^* and reduced beam emittance to make it more focus and tighter. The detectors are then housed in movable Roman pots [**?**]. These pots can get as close as 1 millimeter to the beam. They can only move from above and below because of space constraints with the beam pipes. There are two sets of these pots placed each side, and each set has two stations 4 meters apart.

2.2.5 Trigger And Data Acquisition

Not all particle collisions yield events of interest. For instance, when searching for events where electrons are produced in electroweak processes, it is necessary to isolate those events from unrelated background events. In environments with high background activity created in collisions of hadrons, the trigger system is responsible for filtering out the background events and selecting the appropriate events for specific physics analyses. Also, due the limitation in data storage capacity, the trigger system becomes crucial in selecting only the important physics events to store.

The ATLAS trigger system [**?**, **?**] consists of two stage trigger system: Level-1 (L1) trigger implemented in the hardware, and High Level Trigger (HLT) as a collection of software selection algorithms. Figure 2.9 shows the flow chart of the trigger and data collection system during the LHC Run 2. The trigger starts when there are signals received in the front ends (FE) of calorimeters and muon detectors. While the data is buffering in FE, the L1 takes a simplified data sample from FE. L1 Calo registers the event when there are electrons, photons, taus, jets, or any energy deposit passes a certain threshold in calorimeters. While L1 Muon registers the event when there are signals in muon detectors. Both, calorimeter and muon trigger systems identify trigger objects (TOBs) that are combined in decision making process. The TOBs are handled further by both Central Trigger Processor (CTP) directly, and intermediate L1 Topological Processor (L1Topo) [**?**, **?**]. The L1Topo is used for computation of complex kinematic properties of the event such as angular separation, missing transverse energy, invariant mass, and hardness of interaction. The event is processed in L1Topo within 200 ns and then the output is transferred to CTP. The decision to accept or reject the event is made in the CTP. The entire selection process in L1 takes 2.5 μs. Once accepted, the data from FE are transferred to read-out driver (ROD) in read-out system (ROS) where they await the decision of the next stage of the trigger system.

The output of L1 trigger that becomes input for HLT are Regions of Interest (RoIs) which contain the geometrical positions (η, ϕ) of the reconstructed objects of interest.

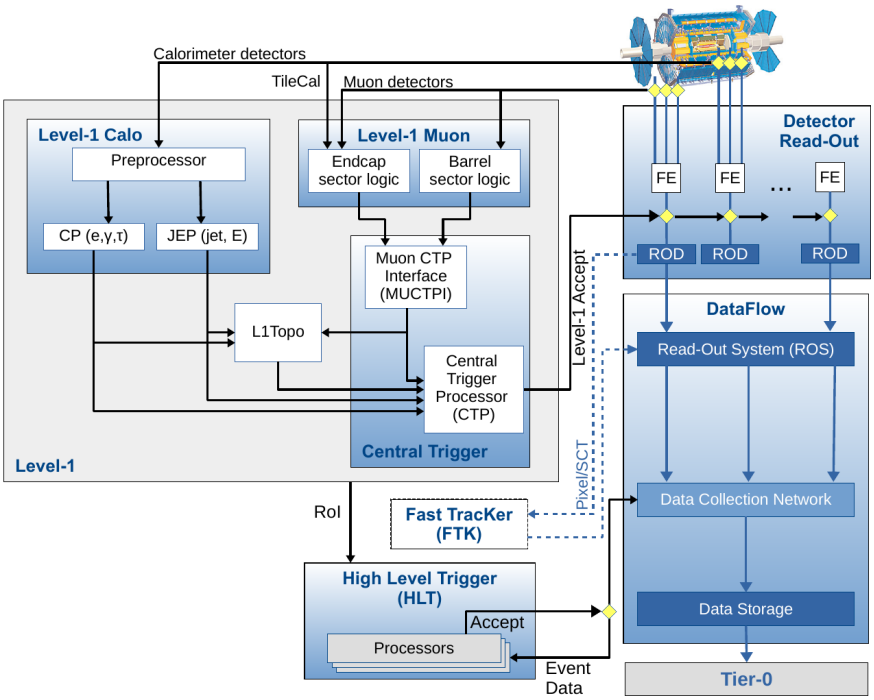

Figure 2.9: A flow chart of the ATLAS trigger system in Run 2. The Fast Tracker (FTK) was not implemented. Figure from [**?**].

In L1 Calo, the sliding window algorithm will select the region where there are local maxima of energy deposit. For example, in dijet event shown in Figure 2.10, there are two jet cones marked as red and green. The jet cones give a rise to energy

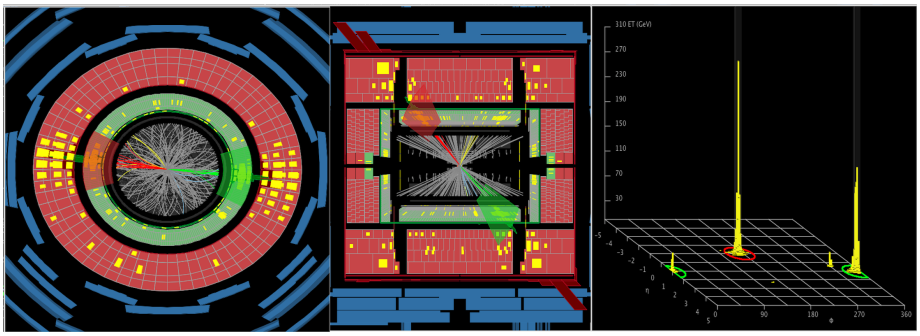

Figure 2.10: A dijet event collected by the end of April 2012. The event is viewed from R-ϕ plane (left), z (mid), and unfolded sum of energy (right). The region of interests where the jets deposit are marked by green and red shades in the calorimeter clusters and circle in unfolded towers. Figure from [**?**].

towers, signaling the hard collision has occurred which is illustrated in the unfolded histogram on the right. The L1 Calo then selects the RoI within these cones. While in L1 Muon, the RoIs constructions are done by finding coincidence of signals among detector layers, and then matching them to lookup table of the muon momentum prepared beforehand from MC simulation and calibration to obtain a crude muon momentum estimate. The RoIs are then counted and delivered to CTP. The CTP makes 512 decisions based on criteria applied on them. Only one positive decision is

needed to pass the event to HLT. For example, L1 calo works out RoI with energy 50 GeV at $\Delta\eta_1 \times \Delta\phi_1$, and another of 20 GeV at $\Delta\eta_2 \times \Delta\phi_2$. Then, if there is a requirement "pass event if there is at least one RoI of 80 GeV", and another "pass if there are two RoIs above 20 GeV", the event is passed by the second condition.

The L1 trigger output rate is about 100 kHz out of ∼40 MHz of LHC bunch crossing rate, meaning that around 1 in 400 events is selected. These events are then filtered again in the HLT with output rate slightly above 1 kHz. The processing time in HLT is around 200 ms.

In HLT, the online (real-time) reconstruction of an event need to pass selections of gradually increased strictness. First, the RoI information are unpacked to generate the initial seeding of the HLT algorithms. These algorithms cooperate to independently select from about 1000 *trigger chains* to cover broad range of physics analyses. For example, if L1 trigger detect a particle that potentially can be an electron, this information is forwarded to several electron trigger chains to examine further if it is really an electron. In a multi-step procedure, a positive decision leads to the next, more precise selection step unless the decision is to reject the hypothesis. If the HLT decision is negative for all selection chains, the event is rejected and the data buffering in ROS is cleared. Upon positive evaluation of at least one HLT trigger chain, the event is recorded. The selection process at the HLT utilizes about 2-5% of detector data. [**?**]

There are many data streams which are categorized based on the characteristic of the events. Each of them has specific trigger requirements. For example, minimum bias stream where the events are selected using triggers with minimal selection criteria to capture a broad and unbiased sample. This is achieved using triggers like the Minimum Bias Trigger Scintillators, which detect particles produced in collisions with as little bias as possible. Another one is hard probe streams which capture the hard interactions producing high energy jets. Examples of streams that are used exclusively in heavy ion run are central and UPC streams which collect central and ultra-peripheral events respectively.

The stored event is completely reconstructed again offline in order to obtain detailed physics information about the event. For this purpose, Athena framework [**?**, **?**] has been developed. The results of the offline reconstruction are saved into Analysis Object Data (AOD) file for physics analyses. During my study, I also contributed to the development of minimum bias trigger signature[1] responsible for recording inclusive and unbiased sample of elementary collisions. In particular, I have extended functionality of monitoring histograms to cover also minimum bias signatures that allowed to verify the performance of minimum bias triggers relying on charged particles tracking. I have also developed a z-finder algorithm for High Multiplicity Trigger in the Athena framework.

[1]The term "signature" is used in the ATLAS experiment for a group of chains aiming at recording similar classes of events.

Minimum Bias Trigger Scintilator

The minimum bias trigger scintillators (MBTS) [**?**] is the primary trigger for selecting events from low luminosity run with bias as small as possible. During LS1, it was replaced with a new one due the radiation damage and positioned slightly different than in Run 1. Since Run 2, they are positioned in front of the liquid-argon end-cap calorimeter cryostats at $z = \pm 3.56$ m. The MBTS are segmented into two rings in $2.08 < |\eta| < 2.76$ and $2.76 < |\eta| < 3.86$. The inner ring consists of eight azimuthal sectors, while the outer ring comprises four azimuthal sectors, and thus 12 sectors per side in total. [**?**]

MBTS provides fast signals used in the L1 trigger for the initial selection of minimum bias events. At the HLT, minimum bias algorithm uses the signals from the MBTS as part of its input. The algorithm applies criteria such as the multiplicity of hits in the MBTS, the energy deposited, and the timing information to distinguish between real collisions and background noise or pile-up events. The algorithm can also apply more complex criteria, such as requiring a certain spatial distribution of hits in the MBTS or combining MBTS information with data from other detectors like the Inner Detector or calorimeters to improve event selection both online and offline.

In preparation of offline reconstruction for Run 3, ATLAS offline software framework and HLT software underwent a major migration to adapt better to new HLT farm hardware. The change also concerned the minimum bias trigger. My contribution to this upgrade was addition and adaptation of monitoring of performance of tracking algorithms used in minimum bias trigger. For that purpose, monitoring codes operating online were adjusted to provide useful information on overall Inner Detector tracking that is watched by data quality experts during data taking. The examples of monitoring histograms for p_{T}, ϕ, and η of the tracks are shown in Figure 2.11.

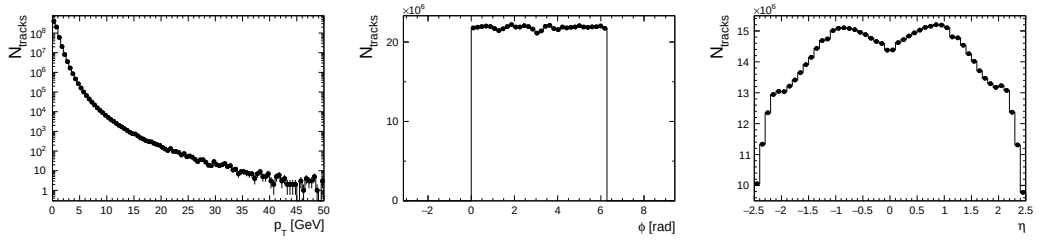

Figure 2.11: The examples of monitoring histograms showing the distribution of p_{T}, ϕ, and η of the tracks.

High-Multiplicity Tracks Trigger

The High-Multiplicity Tracks (HMT) trigger is used to select events that produce high number of particles. In Run 2, it is designed to activate when a certain threshold of number of hits in SCT, that is proportional to tracks multiplicty, are achieved However, in conditions with several collision vertices, counting SCT hits

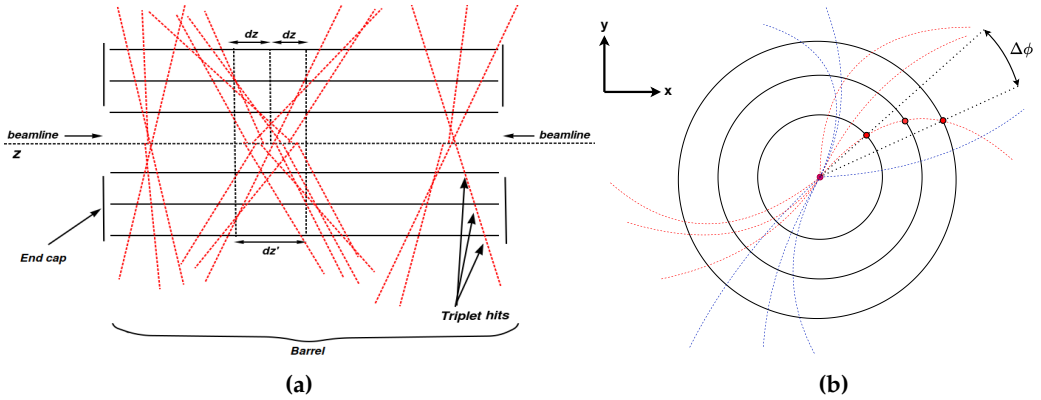

Figure 2.12: Illustration of pileup in **(a)** z, **(b)** R-ϕ plane.

can not distinguish high multiplicity event from event with several vertices of lower multiplicities. For that purpose, an algorithm that would provide a better estimate of number of tracks from a vertex is needed. The algorithm needs to be much faster than the tracking algorithm.

After further development from my contribution for Run 3, the HMT trigger can also find the z coordinate of vertices in the events with certain multiplicity threshold without utilizing full track reconstruction. Figure 2.12 illustrates the transverse and longitudinal view of an event with pileup. The charged particles form helical track due to the bending from magnetic field perpendicular to the transverse plane. The longitudinal projections of these tracks are straight trajectories which can be extrapolated to the beamline. Each projection must have at least triplet hits in the Pixel barrel layers with an angle in transverse plane $\Delta\phi$ between the first hit and the third hit. These projections converge to certain points along the z with some uncertainty dz. Some projections converge far away from the others, pointing to secondary collisions called *pileup* which increase the number of interaction per bunch crossing μ.

In the algorithm, the position of triplet hits extrapolation to z-axis are counted as shown in Figure 2.13. The z positions of vertices stands as the peaks among the

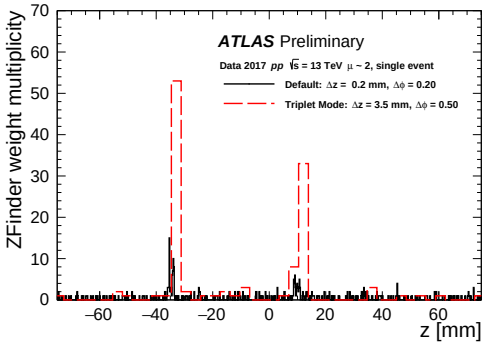

Figure 2.13: The counting of tracks between different z-finder configuration. Figure from [**?**].

background noise. The algorithm performance is controlled by two parameters:

the bin width of the projection Δz which corresponds to resolution of z, and the maximum $\Delta\phi$ of triplet. The defaults of the algorithm inherited from Run 2 were set to $\Delta z = 0.2$ mm and $\Delta\phi = 0.2$ rad which were then optimized. By increasing Δz, the resolution is reduced and might result in merging the primary interaction with pileup if it is too big. However, the peak is much lower and obscured if Δz is too small as the tracks are distributed over more bins. Increasing $\Delta\phi$ limit increases the p_{T} acceptance for low momentum tracks as the magnetic field bends them harder. However, it also increases the chance of wrong triplet hits combination, resulting in fake tracks. Therefore, the balance of Δz and $\Delta\phi$ limit are needed.

To find the optimal values, the correlations between the number of charged particles trajectories with triplet hits in pixel barrel N_{triplet} and the number fully offline-reconstructed charged particles tracks N_{tracks} for Δz and $\Delta\phi$ are studied. The study is done by plotting the number of event with N_{triplet} and N_{tracks} as the axes into a 2D histogram. Then, the profile histogram is created by taking the mean value of triplet hits trajectories in each reconstructed tracks bin, which marked by black diamond in Figure 2.14a. Several configurations of Δz and $\Delta\phi$ were explored and the best results with linear correlations are shown in Figure 2.14b.

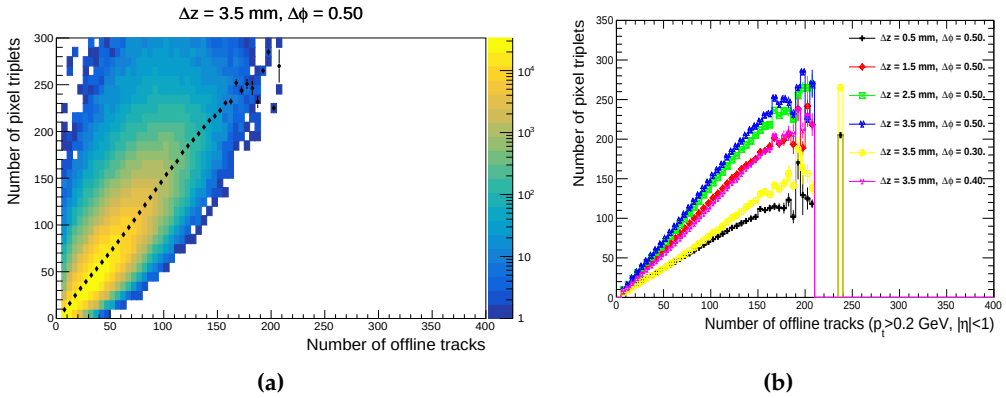

(a) **(b)**

Figure 2.14: **(a)** Correlation between the number of charged particles trajectories with triplet hits in pixel barrel and the number offline-reconstructed charged particles tracks. The profile histogram is marked by black diamond which is the mean value of triplet hits trajectories in each reconstructed tracks bin. **(b)** Several profile histograms for different Δz and $\Delta\phi$ configurations.

Figure 2.15 shows the efficiency of HMT trigger as a function of N_{tracks} for $\Delta z = 3.5$ mm and $\Delta\phi = 0.5$ rad configuration. The activation threshold increases with increasing N_{triplet} requirement which is proportional to N_{tracks}. And therefore, it works as intended to trigger high multiplicity events. However, it is insensitive to pileup as the activation thresholds remain the same for different pileup levels and my contribution stopped here. To suppress the pileup, a certain cut on N_{triplet} was added to the trigger so that lower peaks on z like in Figure 2.13 are excluded. Later on, a cut above some value of all energy sum in calorimeters is also added to the requirement. [**?**] The HMT trigger began to run online in at the start of Run 3 and its efficiency is shown in Figure 2.16.

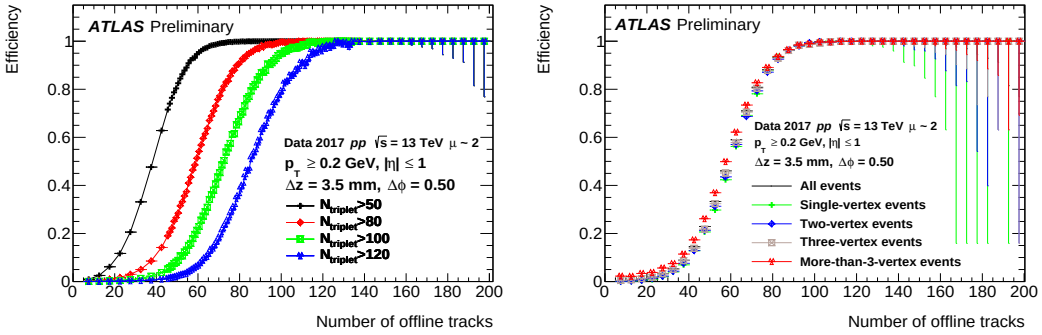

(a) **(b)**

Figure 2.15: HMT efficiency as a function of **(a)** number of trajectories with triplet hits N_{triplet}, **(b)** number of vertices. Figure from [**?**].

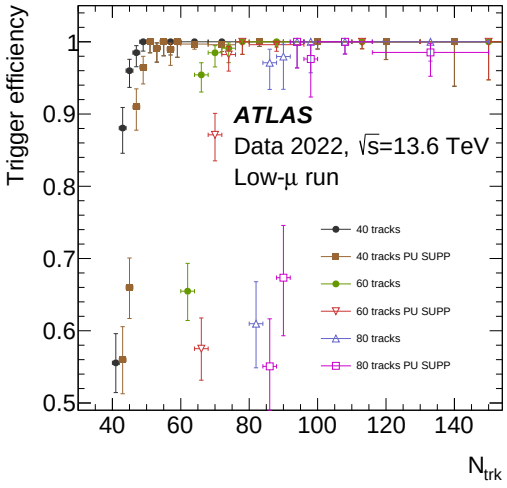

Figure 2.16: The efficiency of HMT trigger in Run 3. Figure from [**?**].

3 Analysis Method

The analysis comprises of several steps. They are described in the order in which they need to be performed.

3.1 Track weights extraction

The performance of detector, in general, is not perfect. For this purpose, a data sample from a Monte Carlo (MC) simulation is needed. The sample for *pp* is generated with Pythia 8 for both 5.02 and 13 TeV, while for *p*-Pb, the sample is generated with HIJING. These samples serve as the truth references since the actual number of particles produced in each event are known upon the event generation. Then, the MC samples undergo the detector simulation which includes the event selections by the trigger systems and the track reconstruction. These simulation and reconstruction were setup so to mimic the conditions during the data taking. The output is then compared to the truth reference to determine the efficiency and fake rate.

The efficiency and fake rate are evaluated as a function of p_{T}, η, and N_{tracks}. The efficiency ϵ is defined as

$$\epsilon(p_{\mathrm{T}}, \eta, N_{\mathrm{tracks}}) = \frac{N^{rec}_{match}(p_{\mathrm{T}}, \eta, N_{\mathrm{tracks}})}{N^{truth}(p_{\mathrm{T}}, \eta, N_{\mathrm{tracks}})}. \tag{3.1}$$

where $N^{rec}_{match}(p_{\mathrm{T}}, \eta, n_{track})$ is the number of reconstructed tracks passing the selection requirements and match to the truth tracks, and $N^{truth}(p_{\mathrm{T}}, \eta, N_{\mathrm{tracks}})$ is the total number of stable charged particles generated from MC. While the fake rate f is defined as

$$f(p_{\mathrm{T}}, \eta, N_{\mathrm{tracks}}) = \frac{N^{rec}_{not-match}(p_{\mathrm{T}}, \eta, N_{\mathrm{tracks}})}{N^{rec}_{ch}(p_{\mathrm{T}}, \eta, N_{\mathrm{tracks}})}. \tag{3.2}$$

where $N^{rec}_{not-match}(p_{\mathrm{T}}, \eta, N_{\mathrm{tracks}})$ is the number of reconstructed tracks passing the selection requirements but do not match to the truth tracks, and $N^{rec}_{ch}(p_{\mathrm{T}}, \eta, N_{\mathrm{tracks}})$ is the total number of reconstructed tracks of the particles.

In this analysis, the information is kept in 3D histograms as a function of N_{tracks}, η, and p_{T} that are accessed during the analysis loops over tracks. In practice, no evolution with N_{tracks} was observed besides from small statistical fluctuations and therefore only one bin of N_{tracks} is used. Figures 3.1 and 3.2 show the efficiency and fake rate as a function of η and p_{T} made by projecting its 3D histogram into 1D histograms.

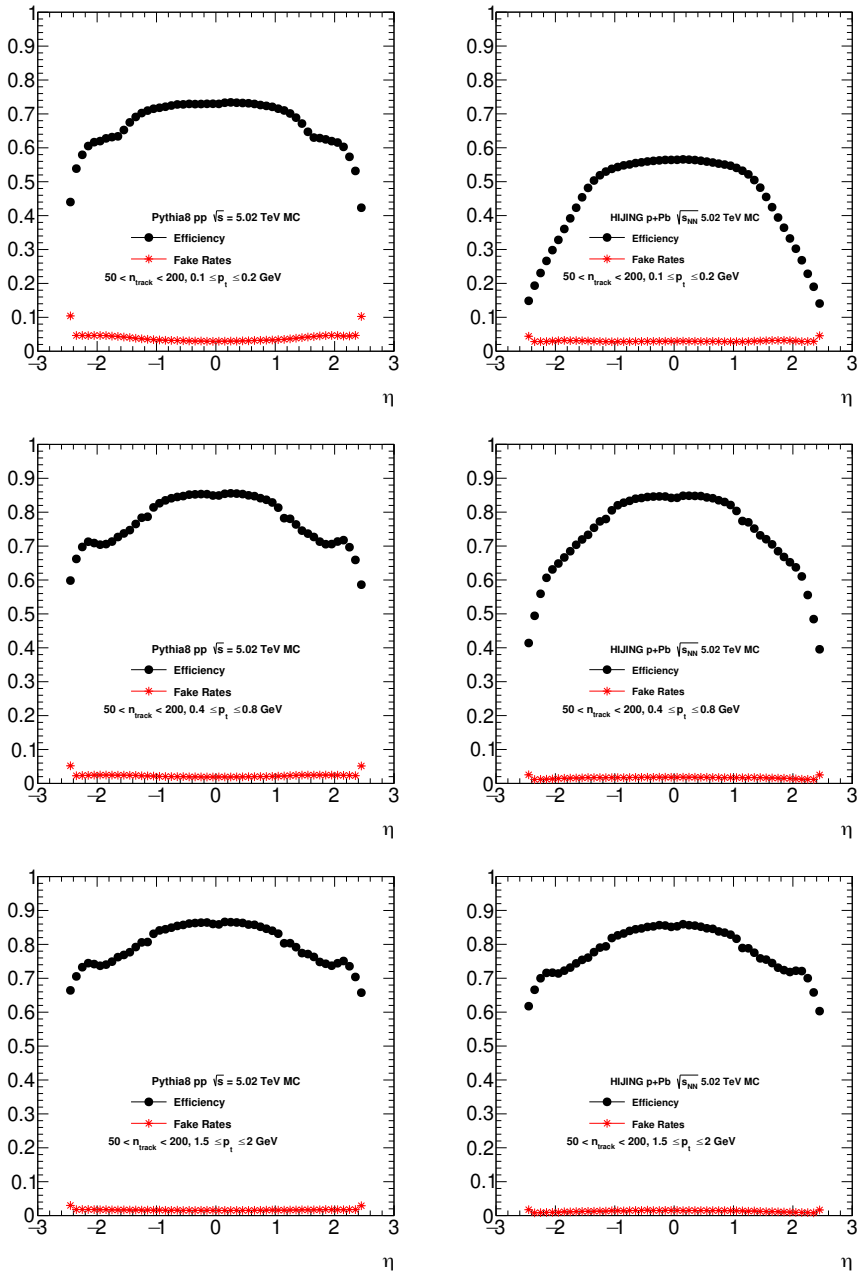

Figure 3.1: The efficiency (black dots) and fake rate (red stars) as a function of η for pp and p-Pb collisions. The MC sample for pp is generated from Pythia 8. While for p-Pb, the MC sample is from HIJING.

The efficiency drops at lower p_{T} since the soft tracks, mostly pions, are more likely to undergo hadronic absorption or significant scattering, making them unreconstructable. More fakes are also produced at low p_{T} since multiple scattering causes the low p_{T} particles to deviate from a straight path, making it difficult to accurately reconstruct their tracks. The drop of efficiency and increase of fake rate also occur at larger values of $|\eta|$ due to the transition from barrel to end-caps and larger amount of inactive detector material at large η.

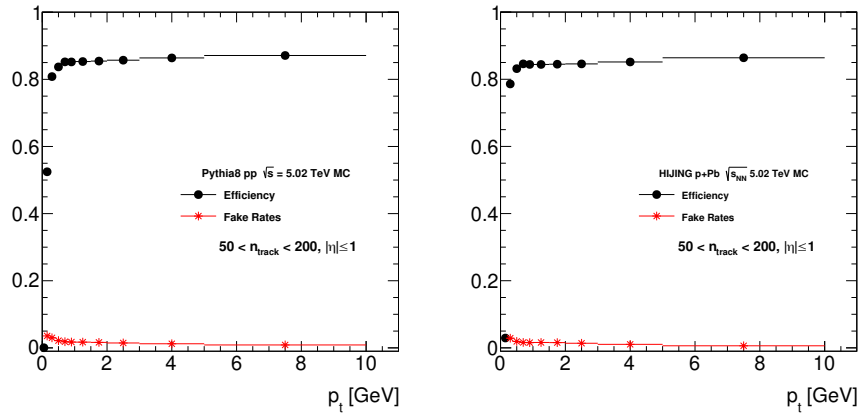

Figure 3.2: The efficiency (black dots) and fake rate (red stars) as a function of p_{T} for pp and p-Pb collisions.

From the efficiency and the fake rate, the weight for correcting the count of particle tracks can be calculated with relation

$$w(p_{\mathrm{T}}, \eta, N_{\mathrm{tracks}}) = \frac{1 - f(p_{\mathrm{T}}, \eta, N_{\mathrm{tracks}})}{\epsilon(p_{\mathrm{T}}, \eta, N_{\mathrm{tracks}})}, \tag{3.3}$$

which is then used to scale up the number of tracks in the analysis. Therefore, each track is treated as if there would be w times more of the same track. Figure 3.3 shows the closure of the p_{T} and η spectra between the reconstructed tracks before and after correction, and the truth reference. It is clear that the count of reconstructed tracks after correction by w factor is in agreement with the truth.

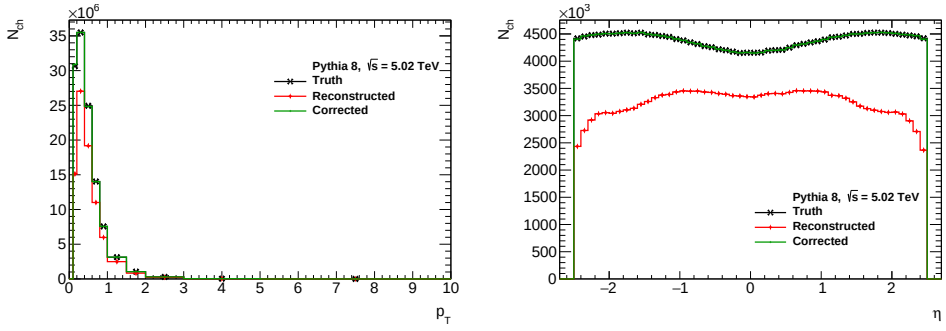

Figure 3.3: The closure of the efficiency and fakes correction as a function of p_{T} and η within $0.1 < p_{\mathrm{T}} < 10$ GeV.

3.2 q-bias correction

The ATLAS tracker covers full azimuthal angle. But in reality, not all of numerous detector modules perform equally or are functioning in any given time. Malfunctioning module would result in nonuniform detector response and thus result biased measurement of particle abundances as a function of azimuthal angle. A way to compensate for such effect is to utilize the fact that the particle distribution

as a function of ϕ, $dN/d\phi$, should be uniform when it is averaged over many events. With uniform $dN/d\phi$, the q-vectors (equation (1.11)) averaged over events should vanish. Thus, the residual values of, q-vectors are used as estimators of bias due to the detector nonuniformity. In this procedure, first, the real and imaginary parts of the q vectors for $n = 2, 3, 4, 6$ for different p_{T} and η ranges are calculated and each of them are plotted as a function of the number of reconstructed track N_{tracks}. The example of such distributions is shown in Figure 3.4. The trend over N_{tracks} is very mild. Therefore a single average value is used to describe the bias. To calculate the average, a fitting of polynomial of degree zero (horizontal straight line) is used with the range spanning in $20 \leq N_{\mathrm{tracks}} \leq 150$, giving a parameter constant that can be used as the average value. This set of average values are then saved in a separate q-bias calibration file and used to subtract q vectors in every event in the main analysis pass. The sum of the q vectors for all event will be around zero after the correction. More detailed example of for q-vectors before and after q-bias correction for various p_{T} and η ranges and different harmonics can be seen in Appendix C.

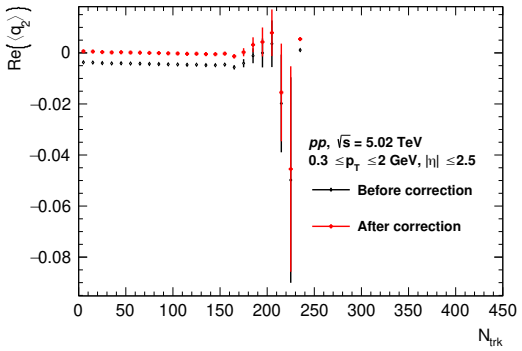

Figure 3.4: Example of q-bias correction for the real part of the second harmonic q-vector. Before correction, the values are non-zero due to detector non-uniformities. After the correction, the values are mostly canceled out.

3.3 Extraction of observables

The study is conducted using the modified Pearson's correlation coefficient $\rho(v_n\{2\}^2, [p_{\mathrm{T}}])$. The same method from reference [**?**, **?**] for calculating the correlations is repeated for pp and p-Pb in p_{T} ranges of $0.3 \leq p_{\mathrm{T}} \leq 2$ GeV, $0.5 \leq p_{\mathrm{T}} \leq 2$ GeV, and $0.3 \leq p_{\mathrm{T}} \leq 5$ GeV. The modified Pearson's correlation coefficient is defined as:

$$\rho(v_n\{2\}^2, [p_{\mathrm{T}}]) = \frac{\mathrm{cov}(v_n\{2\}^2, [p_{\mathrm{T}}])}{\sqrt{\mathrm{Var}(v_n\{2\}^2)_{\mathrm{dyn}}}\sqrt{c_k}}. \tag{3.4}$$

It is obtained from covariance between v_n and $[p_T]$, dynamical variance of $v_n\{2\}$, and the c_k. The mean p_T in each event is

$$[p_T] = \frac{\sum_i w_i p_{T,i}}{\sum_i w_i} \tag{3.5}$$

where w_i are weights correction for the detector efficiency and fake rates of charged particle track reconstruction defined in equation (3.3), and $p_{T,i}$ is the transverse momentum of the i-th particle. The $\langle [p_T] \rangle$ is defined as an average of $[p_T]$ over the total number of a given class of events. The covariance is equal to

$$\mathrm{cov}(v_n\{2\}^2, [p_T]) = \left\langle \frac{\sum_{j\neq i} \sum_{k\neq i,\neq j} e^{-in(\phi_i - \phi_j)} (p_{T,k} - \langle [p_T] \rangle)}{\sum_i \sum_{j\neq i} \sum_{k\neq i,\neq j} w_i, w_j w_k} \right\rangle \tag{3.6}$$

where $\phi_{i,j}$ are azimuthal angles of each particle, and the bracket $\langle\rangle$ is an average over the events. The summations are done is such a way so that the particle $i \neq j$, $j \neq k$, and $k \neq i$ to avoid self correlation from pairing the same particle.

The c_k is the variance of p_T averaged over all events in the given class

$$c_k = \left\langle \frac{1}{\sum_i \sum_{j\neq i} w_i w_j} \sum_i \sum_{j\neq i} w_i w_j (p_{T,i} - \langle [p_T] \rangle)(p_{T,j} - \langle [p_T] \rangle) \right\rangle \tag{3.7}$$

with $[p_T]$ is the mean p_T in each event and $\langle [p_T] \rangle$ is the average of $[p_T]$ over all events. $w_{i,j}$ is the number of particle in the event where the i,j-th particle came from. For the same reason, the summations in c_k is modified in such a way so that particle $i \neq j$.

The dynamical variance $\mathrm{Var}\left(v_n\{2\}^2\right)_{\mathrm{dyn}}$ is

$$\mathrm{Var}\left(v_n\{2\}^2\right)_{\mathrm{dyn}} = v_n\{2\}^4 - v_n\{4\}^4 \tag{3.8}$$

with $v_n\{2\}$ and $v_n\{4\}$ are two- and four-particle flow coefficients obtained from direct calculation of multiparticle cumulants mentioned earlier in Section 1.3.1. Adjusting the symbols and notation to match reference **[?]**,

$$\langle\langle 2 \rangle\rangle = \langle \mathrm{corr}_n\{2\} \rangle \;\; \& \;\; \langle\langle 4 \rangle\rangle = \langle \mathrm{corr}_n\{4\} \rangle. \tag{3.9}$$

Therefore $\mathrm{Var}\left(v_n\{2\}^2\right)_{\mathrm{dyn}}$ can be written as

$$\mathrm{Var}\left(v_n\{2\}^2\right)_{\mathrm{dyn}} = \langle\langle 4 \rangle\rangle - \langle\langle 2 \rangle\rangle^2 = \langle \mathrm{corr}_n\{4\} \rangle - \langle \mathrm{corr}_n\{2\} \rangle^2 \tag{3.10}$$

The analysis is carried out using various subevent methods. As illustrated in Figure 3.5, the three sub-events, A, B, C are established to be regions of $-2.5 < \eta < -0.75$, $|\eta| < 0.5$ and $0.75 < \eta < 2.5$ respectively. The idea is to reduce the contribution from short-range correlation induced by jets. In 1-subevent approach, the calculation for v_n and $[p_T]$ are done using all particles within the range $|\eta| < 2.5$. The 2-subevent method uses v_n from particles in sub-events A & C and the $[p_T]$ from

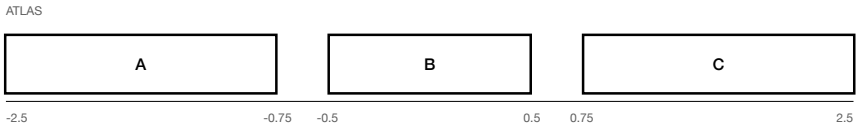

Figure 3.5: Definition of the sub-events in ATLAS.

particle in either sub-event A or C. Therefore non-hydrodynamic flow from jets in sub-event B will not contribute to the v_n correlations. The 3 sub-event measurement was already performed in **[?]** for Pb+Pb and second harmonic p+Pb. In 3-subevent, v_n is calculated from the particles in sub-events A & C and the $[p_{\mathrm{T}}]$ from the particles in sub-event B. This way, the jets in sub-events A & C will not contribute to $[p_{\mathrm{T}}]$ and the jets in sub-event B will not participate in the v_n calculation.

Following the choice of the normalization from reference**[?]**, the normalization of the covariance is done with the same c_k and $\mathrm{Var}\left(v_n\{2\}^2\right)_{\mathrm{dyn}}$ regardless of the subevent of the covariance. The c_k uses p_{T} of the particles within $|\eta| < 2.5$. And the $\mathrm{Var}\left(v_n\{2\}^2\right)_{\mathrm{dyn}}$ in equation (3.8) is modified using the combination of one- and two-subevent to reduce the non-flow effect and can be written as

$$\begin{aligned}\mathrm{Var}\left(v_n\{2\}^2\right)_{\mathrm{dyn}} &= v_n\{2\}^4_{\mathrm{2sub}} - v_n\{4\}^4_{\mathrm{1sub}} \\ &= \langle \mathrm{corr}_n\{4\}\rangle_{\mathrm{1sub}} - 2\langle \mathrm{corr}_n\{2\}\rangle^2_{\mathrm{1sub}} + \langle \mathrm{corr}_n\{2\}\rangle^2_{\mathrm{2sub}}. \end{aligned} \tag{3.11}$$

The definitions of the variables used in $\rho(v_n\{2\}^2, [p_{\mathrm{T}}])$ involve double or triple loops over the particles in the event and can take a lot of computing resources. To reduce the CPU consumption, the formulas containing more than one summation index can be simplified into one summation and thus only need single loop. An example of the derivation is demonstrated in Appendix A for the c_k. The formulas for $\mathrm{cov}(v_n\{2\}^2, [p_{\mathrm{T}}])$ are also shown there. The full derivations for each subevent can be found in Appendix B.

In the analysis procedure, first the $[p_{\mathrm{T}}]$ is obtained as a function of N_{tracks}. Figure 3.6 shows an example of the $[p_{\mathrm{T}}]$ obtained from pp data. Separation of this

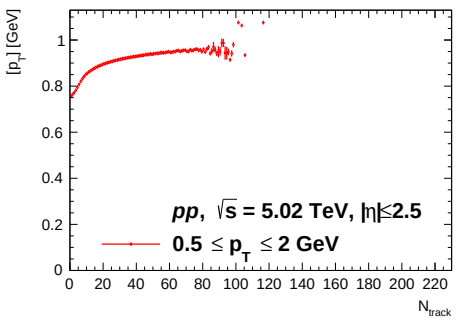

Figure 3.6: The example of $[p_{\mathrm{T}}]$ evolution with the charged tracks multiplicity in pp at centre of mass energy of 5.02 TeV.

analysis step allowed to study carefully event selection with respect to biases due to trigger as discussed in 4.2. The $[p_{\text{T}}]$ as function of N_{tracks} are then saved in a separate file. This file is then accessed when quantities that require $[p_{\text{T}}]$ such as $\text{cov}(v_n\{2\}^2, [p_{\text{T}}])$ an c_k are calculated.

3.4 N_{tracks} to N_{ch} conversion

The output of the analysis results is a function of multiplicity of the reconstructed charged particle tracks N_{tracks} with $p_{\text{T}} > 0.3$ GeV and $0.75 < |\eta| < 2.5|$ and satisfy the HILoose selection criteria which is discussed later in section 4.3. To facilitate comparisons with models at the final step, the N_{tracks} is converted to number of charged particles N_{ch} which is N_{tracks} in $|\eta| < 2.5|$ and $0.5 < p_T < 5$ GeV corrected by tracking performance discussed in section 3.1). This is done by mapping N_{tracks} and N_{ch} in a finely binned 2D histogram and taking the average of N_{ch} in a given N_{tracks} bin. The result is the averaged N_{ch} as a function of N_{tracks} shown in Figure 3.7. Since their correlation is linear, a linear function with parameters m and n

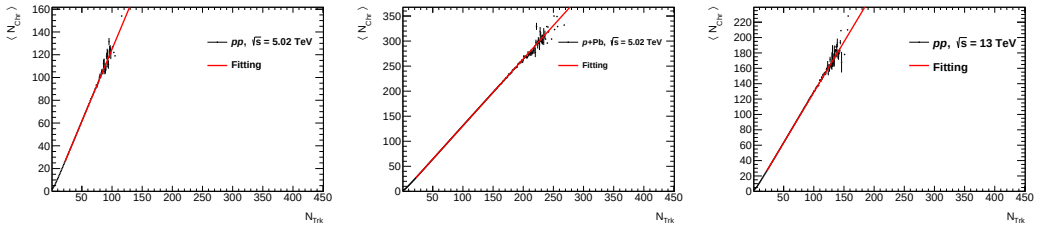

Figure 3.7: The $\langle N_{ch} \rangle$ as a function of N_{tracks} in pp and p-Pb, and their fitting to the linear functions.

$$\langle N_{ch} \rangle = mN_{\text{tracks}} + n \tag{3.12}$$

is fitted from N_{tracks} 20 to 200 for pp and 20 to 300 for p+Pb. The obtained fitting parameters are listed in table 3.1. It can be seen from parameter m that N_{ch} is around 30% higher than N_{tracks} for all collision systems. Therefore, the data points will be shifted along the x-axis after the results are converted from N_{tracks} to N_{ch}.

Data	n	m
pp 5.02 TeV	0.143±0.002	1.31217±0.00006
p+Pb 5.02 TeV	0.1532±0.0002	1.328740±0.000004
pp 13 TeV	0.1527±0.0004	1.31313±0.00001

Table 3.1: List of fitting parameter for different data sample.

All observable quantities, except $\rho(v_n\{2\}^2, [p_{\text{T}}])$ and $\text{Var}(v_n\{2\}^2)_{\text{dyn}}$, are calculated in narrow N_{tracks} bins of width 1. Then the bins are merged into wider bins. Then $\rho(v_n\{2\}^2, [p_{\text{T}}])$ and $\text{Var}(v_n\{2\}^2)_{\text{dyn}}$ are calculated from the results in wider bin. In the last stage, everything is calibrated according to the $\langle N_{ch} \rangle$ function to express the quantities as a function of N_{ch}.

3.5 Summary of analysis steps

To summarize, the analysis is carried out following these steps:

1. Calculate efficiency and fake rates of the track reconstruction.
2. Calculate the q-bias and check if the sum of the q vectors for all events are around zero after correction.
3. Calculate $\langle [p_{\mathrm{T}}] \rangle$ with weighted tracks using the output in step 1. This calculation proved that the analysis is sensitive to the trigger selection which is discussed in section 4.2.
4. Using results obtained from the earlier steps, calculate c_k, $\mathrm{cov}(v_n\{2\}^2, [p_{\mathrm{T}}])$, $\langle \mathrm{corr}_n\{2\} \rangle$, and $\langle \mathrm{corr}_n\{4\} \rangle$.
5. Using the variables obtained in the previous step, rebin them and calculate $\mathrm{Var}\left(v_n\{2\}^2\right)_{\mathrm{dyn}}$ and $\rho(v_n\{2\}^2, [p_{\mathrm{T}}])$.
6. Bootstrap procedure is used to obtain estimates of statistical uncertainties c_k, $\mathrm{cov}(v_n\{2\}^2, [p_{\mathrm{T}}])$, $\langle \mathrm{corr}_n\{2\} \rangle$, and $\langle \mathrm{corr}_n\{4\} \rangle$ which are used to calculate $\mathrm{Var}\left(v_n\{2\}^2\right)_{\mathrm{dyn}}$ and $\rho(v_n\{2\}^2, [p_{\mathrm{T}}])$. This is discussed in 5.1.
7. Convert N_{tracks} to N_{ch}.
8. To check the systematic uncertainties, the analysis is repeated without bootstrap procedure and can use the same input produced from point 1 & 2, except for different track selection and another method for correcting the detector geometry. The bootstrap procedure and systematic uncertainties are discussed in Chapter 5.2.

For the comparison with the theories, several MC simulations are also analyzed. The MC data follows the same procedure. For the truth data, step 2 is skipped because it does not simulate the detector geometry. In contrast, for the MC data undergoing detector simulation, all steps are performed. To ensure the measured observables are accurately corrected for detector geometry, efficiency, and fake rates, the MC data with detector simulation is compared with the truth data. This comparison is discussed in detail in section 5.3.

4 Data, Event, And Track Selection

4.1 Dataset

4.1.1 Experimental data

The analysis uses data from pp collisions collected in 2015 and 2017, as well as p-Pb collisions collected in 2016. For pp, there are two center of mass energies used, 5.02 TeV and 13 TeV. While for p-Pb, there is only 5.02 TeV. The data from each year consists of several runs. Each run have a run number assigned for bookkeeping. The detector configurations might change in different run. Some parts of detector module might be excluded if they have an issue, or included back after they are fixed, or calibrated differently. The analysis depends solely on the tracking and relies on the detector azimuthal uniformity upon its collections. Therefore, the q-bias might be different from one run to another as the geometry coverage might change. Some runs have similar q-bias because their detector configurations are the same, and therefore can be grouped together to use the common q-bias correction. Table 4.1 lists runs used for the analysis. In 13 TeV pp data, the separate corrections are done individually for each run. While in p-Pb, only one set of q-bias correction is used because they all are similar. In total, there are 34 millions events in pp data from all runs in 5.02 TeV, 190 millions in 13 TeV, and 231 millions in p+Pb 5.02 TeV.

Each runs has different level of pileup related to the luminosity delivered by LHC. The average number of collisions occurring in a single bunch crossing μ is given by

$$\mu = \frac{L\sigma}{f} \tag{4.1}$$

where L is the instantaneous luminosity, σ is the cross-section for inelastic collisions, and f is the LHC revolution frequency of the bunch. Higher μ means higher number of pileup event as more interactions occurred close to each other in the same bunch crossing. Run number 340973 is the 5.02 TeV pp run with very low $\mu \sim 0.1$ and other runs have higher $\mu \sim 2$. The 13 TeV data has been collected at slightly higher instantaneous luminosity with $\mu \sim 2$.

The particles involved in the correlation should come from the same source of primary vertex. While the pileup inclusion gives unnecessary fluctuation from uncorrelated particles from different vertices. Figure 4.1 shows the shape of number of event distribution as a function of N_{tracks}. The shapes of the N_{tracks} with different average pileup, in this case, for run number 340849 and 340925, are significantly different. However, the shapes of the distributions become similar after the pileup

Beams	Energy	Year	Run number	q-bias group
pp	5.02 TeV	2017	340644 340683 340849 340850 340925 340718 341027 340697	Group 1
			340814 340910 341184	Group 2
			341123 340973	Individual
	13 TeV	2015	267358 267359 267360 267385 267599 267367 329542	
		2017	330857 330875 331020 341294 341312 341419 341534 341615 341649	
p-Pb	5.02 TeV	2016	312649 312796 312837 312937 312945 312968 314199	Group 3

Table 4.1: List of data used for the analysis.

events are filtered out. Therefore, only events with one reconstructed vertex are used in the analysis.

Due the nature of harmonic flow calculation which requires pairing of particles, some events, especially at low multiplicity, may not be able to produce results since particles might not get their pairs due to some kinematic range requirements. For example, let say an event produce five particles and only one of them is within $0.3 \leq p_{\mathrm{T}} \leq 2$ GeV and $|\eta| \leq 2.5$. This particle will not have a pair and the event must be rejected. Figure 4.2 shows the ratio of rejected events from the analysis. The problem aggravates if a narrower interval of particle momenta is used or more

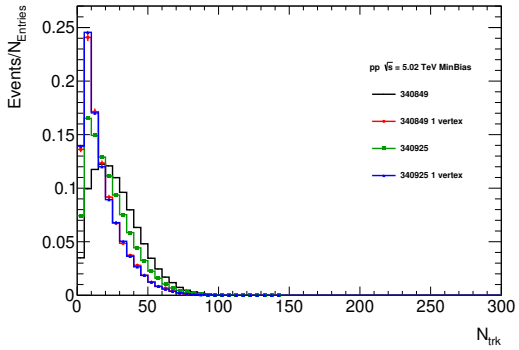

Figure 4.1: The comparison of N_{tracks} spectra shapes between inclusive pileup and one-vertex per event in two different runs of different pileup level.

sub-events are used in the calculations. For instance, in $|\eta| < 2.5$ (one-subevent), for all events with N_{tracks} >20, it is possible to perform a valid calculation. But for $0.75 < |\eta| < 2.5$ (two-subevent), around 1% of the events with $N_{\text{tracks}} = 20$ are rejected for higher p_{T} ranges. Taking into account all the methods and p_{T} intervals, the analysis does not use the events with N_{tracks} <20.

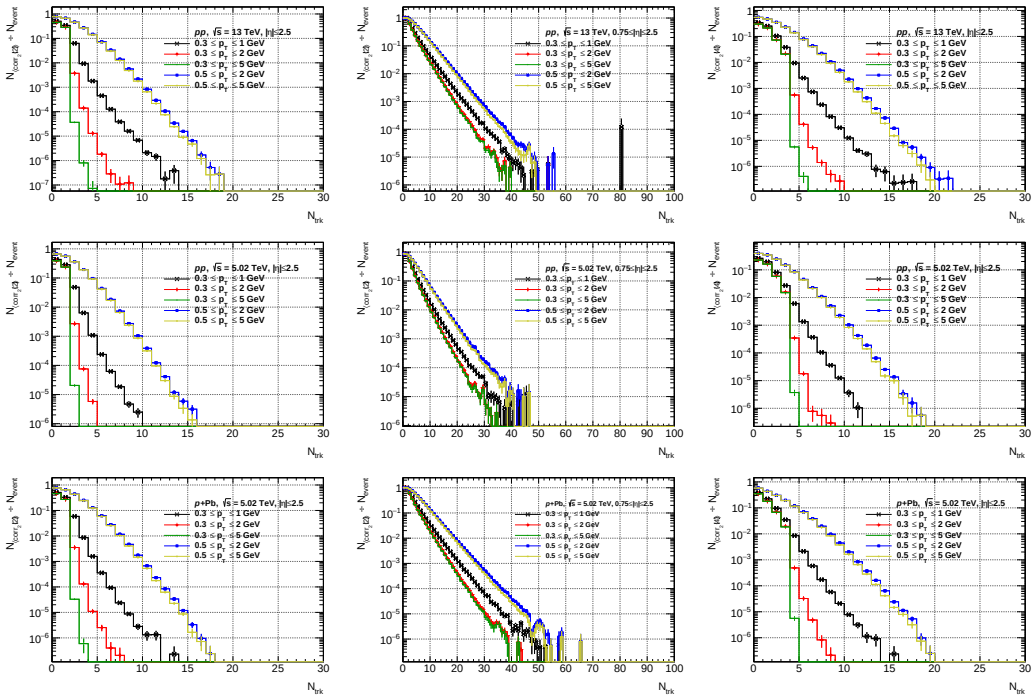

Figure 4.2: Ratio of rejected events due to flow calculation over the total events after single vertex requirement and trigger selection.

4.1.2 Simulation data

MC samples with detector simulation and track reconstruction are used to study tracking performance. The MC sample used to extract tracking performance for *pp* at 5.02 TeV and 13 TeV is Pythia 8 with Monash tuning and color reconnection setting

turned on. The number of events is 800 thousands in 5 TeV and 13 TeV sample. The sample for 13 TeV was simulated with conditions that on average describe the 2015, 2017, and 2018 experimental data, however with less precision as compared to 5 TeV data. For p+Pb, the sample was generated from HIJING and there are 4.8 millions events.

The results obtained in the analysis of experimental data are compared to predictions from MC simulation at truth level. The MC data for this purpose do not undergo detector simulation and track reconstruction. Around 50 millions events were generated for 5.02 TeV pp data, and 100 millions for 13 TeV. The results for pp are compared to Pythia 8 with the same setting as in tracking performance study, and to EPOS which include gluon saturation effect and hydrodynamic simulation. For p-Pb, the result for 1-subevent method is compared to the same HIJING sample used for the correction of tracking performance.

4.2 Trigger selection

The triggers used in this analysis are MinBias triggers. The main trigger is HLT_mb_sptrk. In addition to the main trigger, several other triggers are also used for pp 13 TeV and p-Pb 5.02 Tev data. They are listed in table 4.2.

pp 5.02 TeV	pp 13 TeV	p-Pb 5.02 TeV
HLT_mb_sptrk	HLT_mb_sptrk	HLT_mb_sptrk
	HLT_noalg_mb_L1MBTS_1	HLT_noalg_mb_L1MBTS_1
	HLT_noalg_mb_L1MBTS_1_1	HLT_noalg_mb_L1MBTS_1_1
		HLT_mb_mbts_L1MBTS_1
		HLT_noalg_mb_L1ZDC_A
		HLT_noalg_mb_L1ZDC_C
		HLT_mb_sptrk_L1MBTS_1

Table 4.2: List of triggers used for the analysis.

The names of all the triggers start with "HLT" because they need to pass the HLT, followed by "mb" which specifies the data stream for minimum bias events. Some triggers are labeled "noalg" which means that HLT does not apply any further algorithms beyond the initial selection by the Level-1. The term "sptrk" stands for space points (sp) and single reconstructed tracks (trk) requirements respectively. The space points correspond to the detector signals left by charged particles after hit. For mb_sptrk, it requires at least two reconstructed space-points in the Pixel system and three in the SCT, along with at least one reconstructed track with $p_{\mathrm{T}} > 200$ MeV. It is designed to activate for events with at least one track and reject events with random noise from the detector which typically having only a few space-points. The *seed* for initial activation of the mb_sptrk trigger is based on a random selection of bunch crossings that contain colliding bunches. The term "L1MBTS" stands for Level-1 Minimum Bias Trigger Scintilator. The MBTS triggers require a certain multiplicity threshold in their counters. L1MBTS_1 requires the events to have at least one of the

MBTS counters on any side activated. While for `L1MBTS_1_1`, the events must have at least one counter in both sides activated [**?**].

In p-Pb, the collision is asymmetric. The Pb nuclei break apart and most of the remnants scatter into forward direction along z-axis. The luminosity in p-Pb collisions is also lower so the random Level-1 trigger is inefficient. Therefore the ZDC is used for the Level-1 trigger in addition to the aforementioned triggers for pp. The term "`L1ZDC`" stands for Level-1 Zero Degree Calorimeter signal above the single neutron threshold. "`L1ZDC_A`" and "`L1ZDC_C`" mean that the event must have a signal in ZDC side A and C respectively.

The MinBias triggers begins run out of statistic for high multiplicity events with $N_{\text{tracks}} > 100$. Therefore High Multiplicity Triggers (HMT) were investigated to increase the number of these events. The HMT seed activate when an event has a certain number of space-points and multiplicity threshold. These triggers also require L1 seed of total energy (TE) in calorimeter. For example, `sp1200_trk80_hmt_L1TE20` requires at least 1200 reconstructed space-points in the SCT, 80 reconstructed tracks with $p_{\text{T}} > 400$ MeV, and a total energy of 20 GeV in calorimeter. However, the TE requirement biased HMT towards events that have higher number of high p_{T} particles. Overall, a higher value of $[p_{\text{T}}]$ is obtained for events triggered with HMT for low N_{tracks} and compared to events collected with MinBias trigger (`sptrk`) as shown in 4.3. For that reason these triggers were tried to be used only for N_{tracks} well

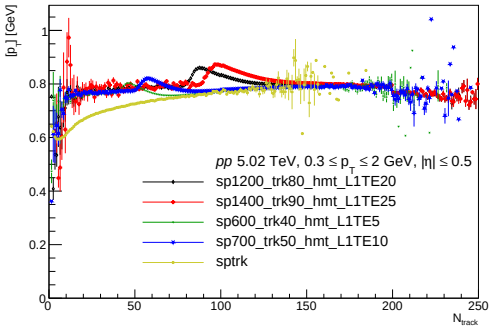

Figure 4.3: The mean p_{T} of tracks of $|\eta| \leq 0.5$ and p_{T} range p_{T} 0.3 $< p_{\text{T}} <$ 2 GeV as a function of N_{tracks} from pp events at 5.02 TeV selected by various triggers.

above their turn on threshold. For instance, the trigger designed to collect events with $N_{\text{tracks}} > 40$ was used only when $N_{\text{tracks}} > 80$. Even though the discontinuities in $[p_{\text{T}}]$ as a function of N_{tracks} were largely suppressed, the c_k still increased noticeably for HMT triggered events. This is because the requirement of large L1 calorimeter energy biases the events to have higher $[p_{\text{T}}]$ but also to prefers the events that have tail of high momentum particles. The $[p_{\text{T}}]$ distribution at fixed N_{tracks} for MinBias and HMT triggered events is shown in Figure 4.4. Given the aforementioned biases and that the focus of this analysis is at lower multiplicities, the HMT triggers were not used for the events selection.

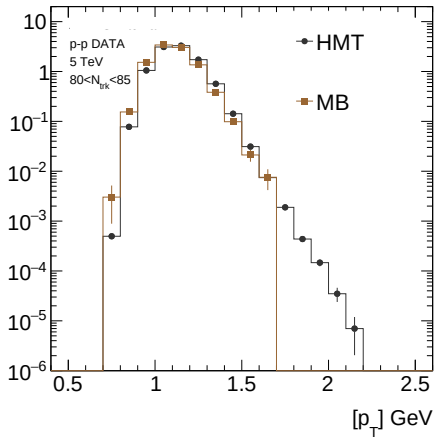

Figure 4.4: The $[p_{\mathrm{T}}]$ spectra for HMT and MinBias. The HMT has a tail towards higher $[p_{\mathrm{T}}]$

4.3 Track selection

From all the reconstructed tracks, only a fraction that satisfies stringent quality selection is used. These tracks, in comparison to all other reconstructed tracks have reduced fake rate and only slightly smaller efficiency. It is necessary for the starting points of tracks to be as close as possible to the primary vertex if they come from that source. However, the helical extrapolation upon track reconstruction can not locate exactly the starting point of each track, especially when there is no intersection between tracks. Therefore, the tracking quantities such as d_0 and z_0, which are measured relative to the primary vertex as illustrated in Figure 4.5, are taken into account. The d_0 is the transverse impact parameter. It is the shortest distance between

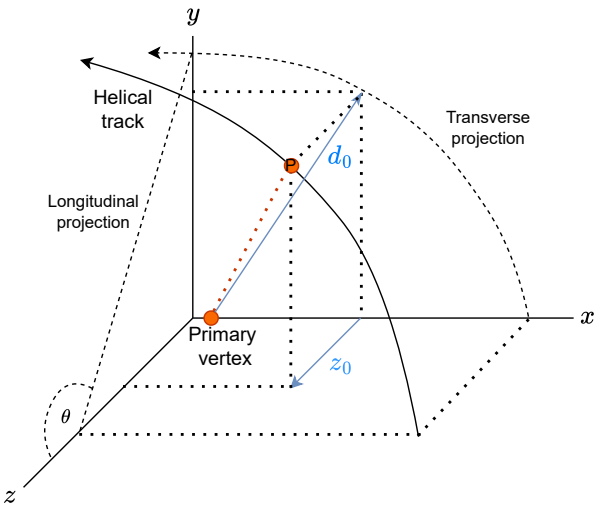

Figure 4.5: The helical track relative to detector center and primary vertex. The closest point between the track and primary vertex is marked as P.

the track of particle and the primary vertex in the plane perpendicular to the beam axis. While z_0 is the longitudinal impact parameter. It represents the distance of closest approach of the particle track to the primary vertex along the beam axis. For tracks with small θ, z_0 can be large while d_0 is small. To accommodate these tracks, the quantity $z_0 \sin(\theta)$ is chosen instead to compensate large z_0.

The main track selection in this analysis is HILOOSE. The following list is the criteria for HILOOSE track selections:

- Minimum p_{T}: 100 MeV
- Maximum $|\eta|$: 2.5
- Maximum d_0: 1.5 mm
- Maximum $z_0 \sin(\theta)$: 1.5 mm
- An innermost layer hit is required if expected, otherwise, a next-to-innermost layer hit is required if it is expected.
- Minimum pixel hits: 1
- for $0 < p_{\mathrm{T}} < 300$ MeV, SCT hits ≥ 2
- for $300 < p_{\mathrm{T}} < 400$ MeV, SCT hits ≥ 4
- for $p_{\mathrm{T}} > 400$ MeV, SCT hits ≥ 6

In addition, HITIGHT selection is also used to estimate the systematic uncertainties. The criteria for HITIGHT selection are listed below:

- Minimum p_{T}: 100 MeV
- Maximum $|\eta|$: 2.5
- Maximum d_0: 1 mm
- Maximum $z_0 \sin(\theta)$: 1 mm
- An innermost layer hit is required if expected, otherwise, a next-to-innermost layer hit is required if it is expected.
- Minimum pixel hits: 2
- Maximum chi squared per degree of freedom: 6
- for $0 < p_{\mathrm{T}} < 300$ MeV, SCT hits ≥ 4
- for $300 < p_{\mathrm{T}} < 400$ MeV, SCT hits ≥ 6
- for $p_{\mathrm{T}} > 400$ MeV, SCT hits ≥ 8

In order to assure that the performance obtained in MC data is applicable to experimental data, the per-track quantities used in the selections are compared between MC and experimental data. The distributions for HILoose selected tracks are shown in Figure 4.6, 4.7, and 4.8. The comparison was done for a fraction of one year data and concentrates on low p_{T} part of the spectra that is most relevant in this analysis. A very good agreement was observed for 5.02 TeV pp and p-Pb data. For 13 TeV data, the agreement is slightly worse. However the differences in tails of the distributions due to minor missmodeling of the efficiency are covered by the systematics related to the efficiency.

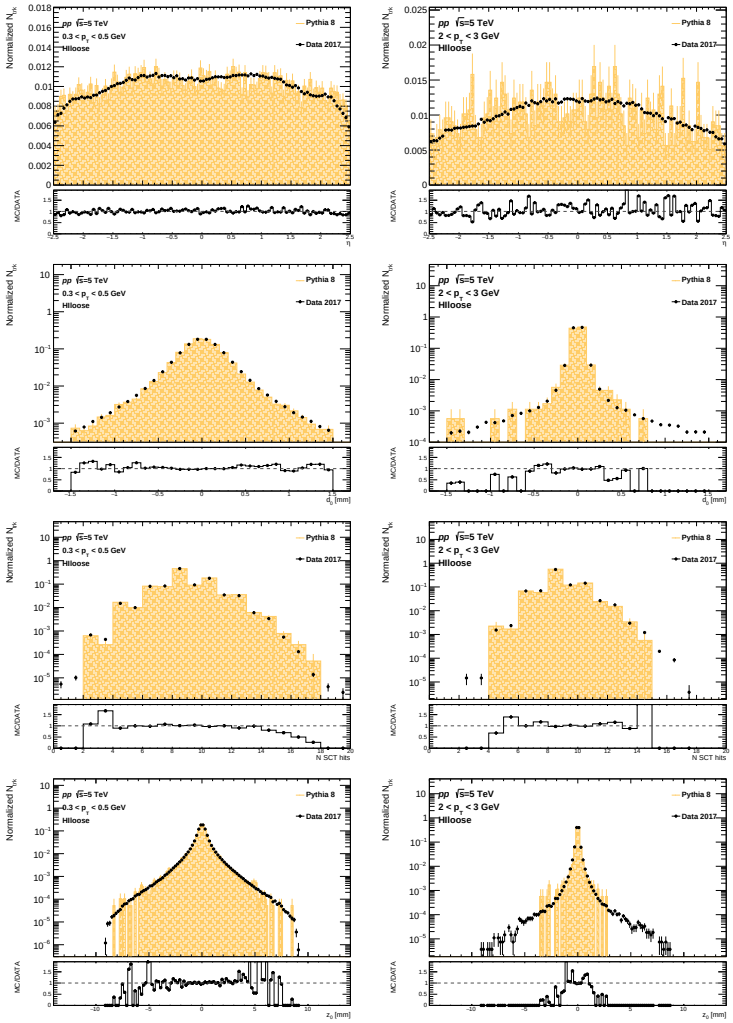

Figure 4.6: Comparison of track related quantities between the pp data at 5.02 TeV (points) and the MC (filled). It is show independently for low $0.3 < p_{\mathrm{T}} < 0.5$ GeV on the left and higher $2 < p_{\mathrm{T}} < 3$ GeV on in the left and right columns respectively. From the top the η, transverse impact parameter d_0, number of SCT hits, and z-vertices z_0 are shown. The N_{tracks} is normalized to unity.

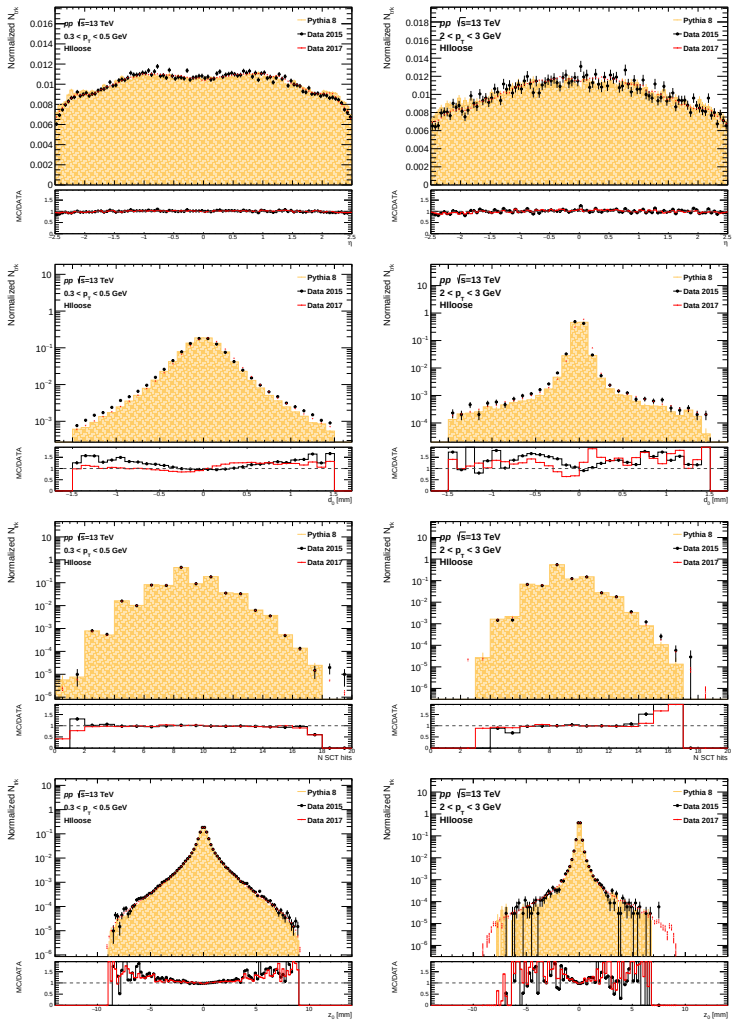

Figure 4.7: Comparison of track related quantities between the pp data at 13 TeV (points) and the MC (filled). It is show independently for low $0.3 < p_{\mathrm{T}} < 0.5$ GeV on the left and higher $2 < p_{\mathrm{T}} < 3$ GeV on in the left and right columns respectively. From the top the η, transverse impact parameter d_0, number of SCT hits, and z-vertices z_0 are shown. The N_{tracks} is normalized to unity.

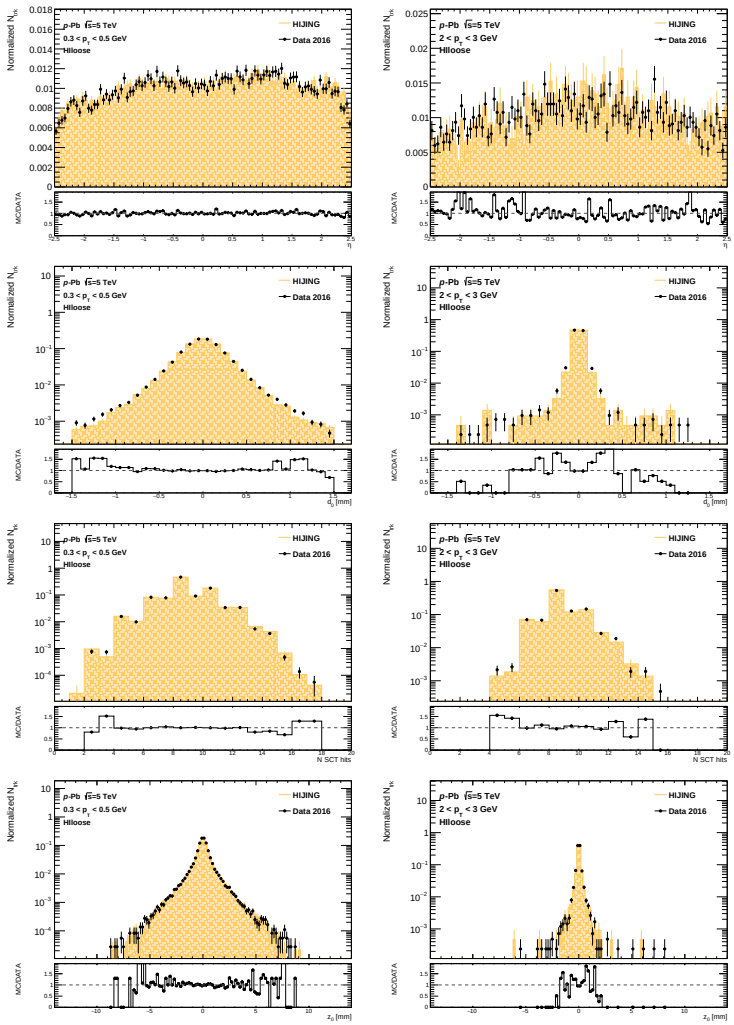

Figure 4.8: Comparison of track related quantities between the p-Pb data at 5.02 TeV (points) and the MC (filled). It is show independently for low $0.3 < p_{\mathrm{T}} < 0.5$ GeV on the left and higher $2 < p_{\mathrm{T}} < 3$ GeV on in the left and right columns respectively. From the top the η, transverse impact parameter d_0, number of SCT hits, and z-vertices z_0 are shown. The N_{tracks} is normalized to unity.

5 Measurement Uncertainties

The measurement uncertainties consist of the statistical and systematic uncertainties. The following sections explain the sampling method to determine the statistical uncertainty and the sources of the systematic uncertainties.

5.1 Statistical uncertainties

As previously done in references [**?**, **?**] for Pb+Pb and Xe+Xe, the bootstrap method [**?**, **?**] is used for estimation of statistical uncertainty. The idea of the method is to construct alternative samples of the events, obtain result using these samples, and use the variance of these results as an estimate of statistical uncertainty. One way of proceeding is to divide the original sample into sub-samples, however in such case sub-samples are less populated and are more susceptible to large statistical fluctuations. In this analysis alternative samples of the same size as the original one are obtained by selecting each event 0, 1, 2, 3, ..., k times according to the Poisson distribution

$$P(k) = \frac{\lambda^k e^{-\lambda}}{k!} \tag{5.1}$$

with a mean value λ of 1. When the weight is equal to 0 the event is discarded, if the weight is equal to 1 it is analyzed once, if 2 it is analysed twice and so on. The same weight is applied to each observable in the event. This method can be justified when the number of events in a given event class is large enough (more than 50 entries [**?**]). The sampling of the Poisson weight is repeated 50 times so that each measured point is effectively estimated 50 times. The results from samples are then used to estimate standard deviation of the measurement for statistical uncertainties of $\mathrm{cov}(v_n\{2\}^2, [p_\mathrm{T}])$, c_k, $\langle \mathrm{corr}_n\{2\} \rangle$, and $\langle \mathrm{corr}_n\{4\} \rangle$ which are used to construct $\mathrm{Var}\left(v_n\{2\}^2\right)_{\mathrm{dyn}}$ and $\rho(v_n\{2\}^2, [p_\mathrm{T}])$.

The statistical uncertainties of $\mathrm{Var}\left(v_n\{2\}^2\right)_{\mathrm{dyn}}$ and $\rho(v_n\{2\}^2, [p_\mathrm{T}])$ are calculated using the error propagation formula to the second order

$$\Delta f(x_1, x_2, ..., x_n) = \sqrt{\Sigma_{i=1}^{n} \left(\frac{\partial f}{\partial x_i}\Delta x_i\right)^2 + 2\left(\frac{\partial f}{\partial x_1}\frac{\partial f}{\partial x_2}\Delta x_1 \Delta x_2 r_{1,2} + \frac{\partial f}{\partial x_1}\frac{\partial f}{\partial x_3}\Delta x_1 \Delta x_3 r_{1,3} + ...\right)} \tag{5.2}$$

with Δx_i is the statistical uncertainties of variable x_i, and $r_{i,j}$ is the correlation factor between variable x_i and x_j. Given that variables used to construct the $\rho(v_n\{2\}^2, [p_\mathrm{T}])$ are using the same particles,the statistical uncertainties might be correlated, resulting in non-zero $r_{i,j}$.

In order to estimate that correlation, the following procedure was used: For each measurement point, a mean value μ and standard deviation σ of all bootstrap results are calculated.Then, the statistical deviations, $d = (m - \mu)/\sigma$, where m is the measurement obtained in one bootstrap iteration, are calculated. The correlation between these deviations are checked by plotting them in 2D histogram shown in Figure 5.1. The only significant correlations $r_{i,j}$ are observed between between 1- and 2-subevents $\langle \mathrm{corr}_n\{2\}\rangle$ and between 1-subevent $\langle \mathrm{corr}_n\{2\}\rangle$ and $\langle \mathrm{corr}_n\{4\}\rangle$ with the value around 0.5 for both of them. This leads to two mixed terms that are not vanishing in estimation of uncertainty for the $\mathrm{Var}\left(v_n\{2\}^2\right)_{\mathrm{dyn}}$. These correlations are taken into account in obtaining uncertainties for $\mathrm{Var}\left(v_n\{2\}^2\right)_{\mathrm{dyn}}$ but contribute only at the sub-percent level to the total uncertainty and can be neglected because they are scaled by generally small values of the uncertainties themselves. All other correlations were found to be marginally small.

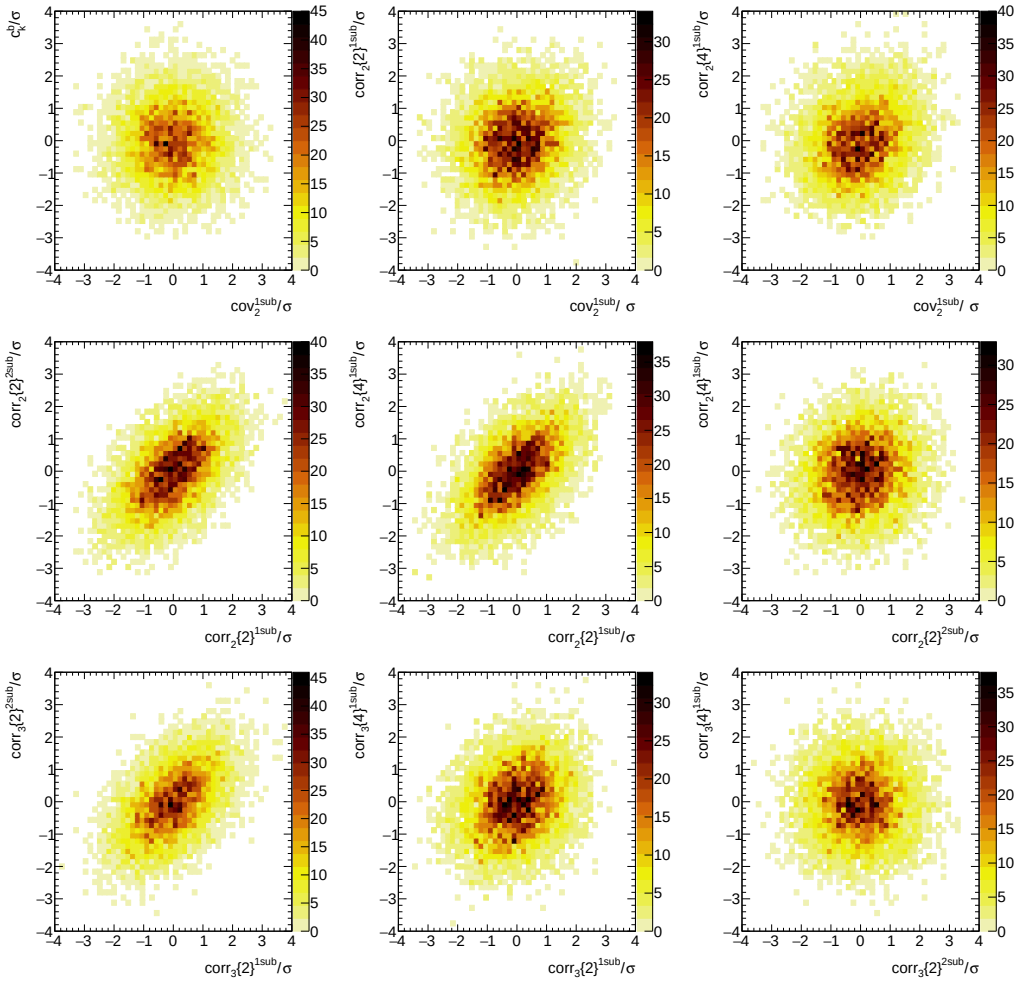

Figure 5.1: Correlations between statistical uncertainties of variables used for $\rho(v_n\{2\}^2, [p_{\mathrm{T}}])$. There are significant correlations between 1- and 2-subevents $\langle \mathrm{corr}_n\{2\}\rangle$ and between 1-subevent $\langle \mathrm{corr}_n\{2\}\rangle$ and $\langle \mathrm{corr}_n\{4\}\rangle$.

5.2 Systematic uncertainties

The estimation of systematic analysis is a challenging process in which an impact of potentially not well understood/modelled experimental quantity may affect the measurement. The sources of systematic uncertainties in this analysis are listed below.

- Track selection variation:
  As mentioned in section 4.3, the main results are calculated using tracks passing HILOOSE criteria which is optimised for efficiency. The HITIGHT track quality selections, optimised for purity, are used for systematic uncertainty related to possibly incorrect modeling of efficiency and fake track rates.

- The detector material uncertainty modeled with track momentum dependent efficiency variation:
  The tracking efficiency from subsection 3.1 is taken into account by variating the efficiency 5% up and down according to the formerly used formula [**?**, **?**].

$$\epsilon_{\pm}(p_{\mathrm{T}}) = \epsilon(p_{\mathrm{T}}) + 0.06 \cdot \frac{\epsilon(p_{\mathrm{T}}) - \epsilon(p_{\mathrm{T}}^{low})}{\epsilon(p_{\mathrm{T}}^{high}) - \epsilon(p_{\mathrm{T}}^{low})} \mp 0.03 \tag{5.3}$$

- Methods to remove residual detector azimuthal nonuniformities:
  To compare the methods for correcting the detector geometry, the analysis is repeated with *ϕ-flattening* procedure instead of q-bias correction. This method applies a phi dependent track weight by multiplication to flatten the ϕ distribution in narrow η slices of width 0.1 so that the uniformity of the detector response is recovered. The details are discussed in Appendix C.

Some systematic also can affect the q-bias correction. Examples of q-bias correction for different systematic variations in figure 5.2 show that the HITIGHT need to use its own q-bias while the tracking efficiency can use the same q-bias result from HILOOSE.

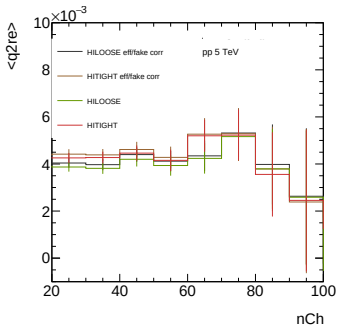

Figure 5.2: The q-bias comparison between different systematic variations.

To obtain the systematic uncertainties, the analysis is run again for each uncertainty source. After the results are rebinned, the value in each bin of the

observables obtained from each source are then subtracted from the baseline value. As mentioned in the previous chapters, the baseline of the observables are measured from HILOOSE with q-bias corrected flow vectors. The difference between these two values are set as the initial systematic uncertainties. Examples of the differences between the baseline measurement and the systematic variations are presented in Figure 5.3. The full set of systematic uncertainties plots are attached in Appendix D.

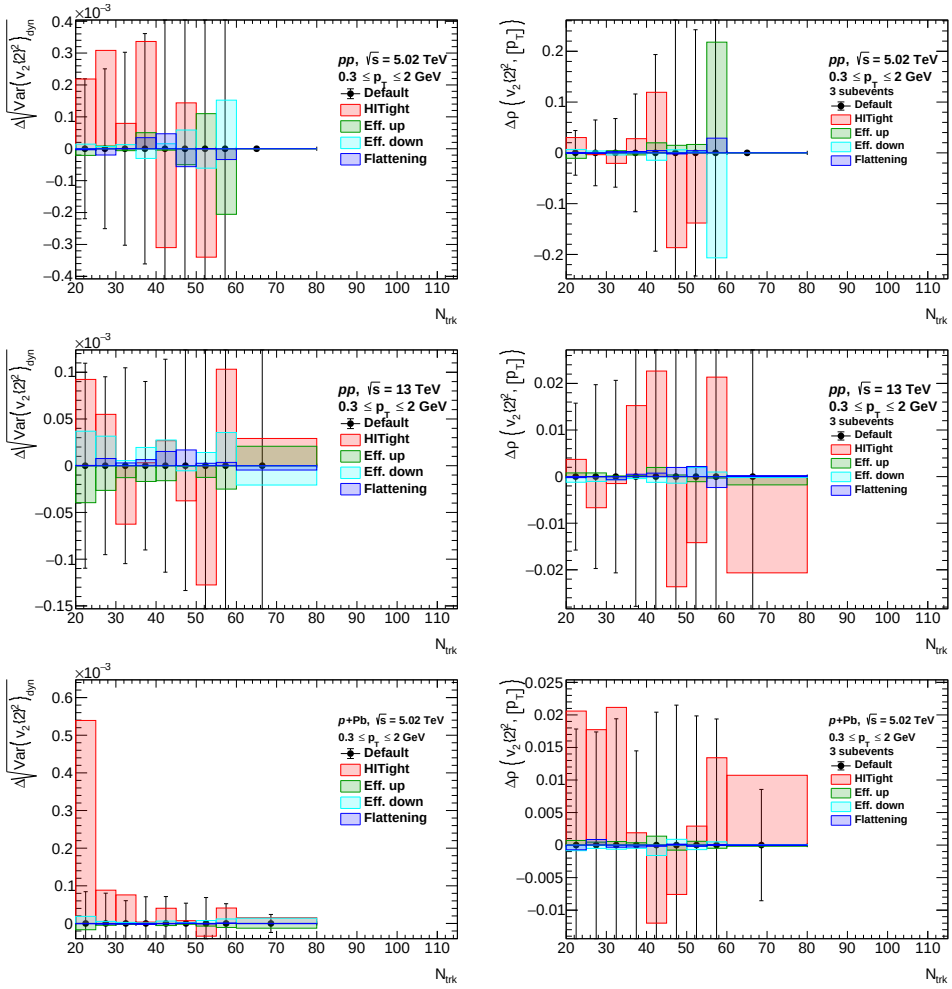

Figure 5.3: Difference between each systematic variation and baseline measurement Δ_{source} in pp at 5.02 TeV and 13 TeV, and p-Pb at 5.02 TeV for range $0.3 \leq p_{\mathrm{T}} \leq 2$ for several quantities as denoted by y-axis label. Statistical uncertainty for baseline measurement is shown as a black line.

For most of the cases systematic uncertainties are comparable or smaller to the statistical ones. However, the contribution from tight track selection and flattening uncertainties are fluctuating over significantly from bin to bin. Therefore, the average over the entire range of N_{tracks} is calculated and set for every bin.

The final value for the systematic uncertainties is

$$\Delta_{total} = \sqrt{\langle\Delta_{tight}\rangle^2 + \left(\frac{|\Delta_{eff.up}| + |\Delta_{eff.down}|}{2}\right)^2 + \langle\Delta_{flat}\rangle^2}. \tag{5.4}$$

with $\langle ... \rangle$ is the average over the number of non-zero bins within the entire multiplicity range.

5.3 Closure test

The performance and detector related corrections can potentially bias the analysis results. The tracking inefficiency is corrected using Eq.(3.3) and weights w in Eq.(3.5)-(3.7). The q-bias correction is utilized to remove detector non-uniformities. An impact of these corrections can be understood by checking the differences between results obtained with the truth reference and the reconstructed tracks from MC data undergoing detector simulation. The same Pythia sample that is used to determine efficiency and fake rate is reused for this comparison.

The example results of the comparison are shown in Figure 5.4. Within the statistical precision, the closure is observed between the truth reference and the reconstructed tracks.

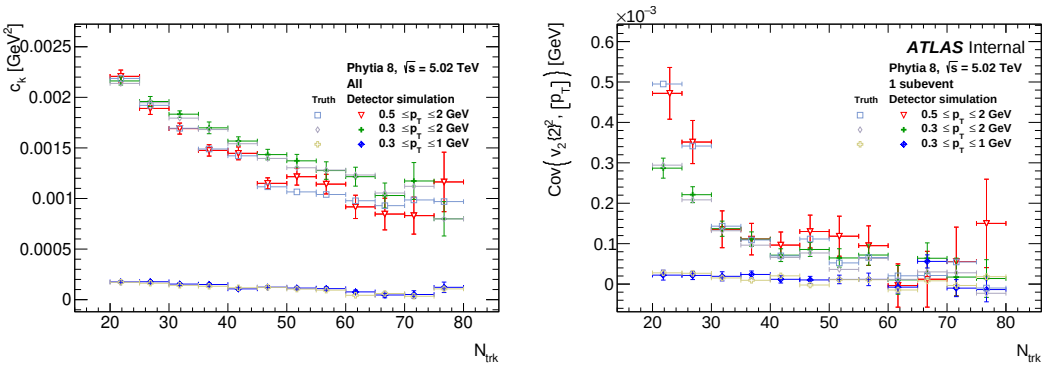

Figure 5.4: The comparison between the truth and its detector simulation. Form left to right c_k, and 1-subevent $\mathrm{cov}(v_2\{2\}^2, [p_\mathrm{T}])$. Only statistical uncertainties are shown.

5.4 Summary

For c_k, $\langle \mathrm{corr}_n\{2\} \rangle$, $\langle \mathrm{corr}_n\{4\} \rangle$, and $\mathrm{cov}(v_n\{2\}^2, [p_\mathrm{T}])$, the statistical errors are taken directly from bootstrap method. In 1-subevent, the statistical uncertainties are small, mostly less than 1%. However, in 2- and 3-subevent, the statistical uncertainties become large. Some of them, for example $\langle \mathrm{corr}_3\{2\} \rangle$ in 2-subevent, have statistical uncertainties larger than their baseline values and crossing zero. For $\mathrm{Var}(v_n\{2\}^2)_{\mathrm{dyn}}$ and $\rho(v_n\{2\}^2, [p_\mathrm{T}])$, the statistical uncertainties are derived from the error propagation relation in equation (5.2). Since both of them involve 2-subevent $\langle \mathrm{corr}_n\{2\} \rangle$, the large statistical uncertainties from this variable are propagated even in 1-subevent $\rho(v_n\{2\}^2, [p_\mathrm{T}])$.

For the systematic uncertainties, the variation of tight track selection, tracking efficiency, and flatenning of the residual detector azimuthal nonuniformities are taken

into account. The largest contribution comes from tight track selections, although the efficiency variations also might result in significant uncertainties in several bins of N_{tracks}. Similar to statistical uncertainties, the systematic uncertainties for 2- and 3-subevent are larger than the ones in 1-subevent. And difference between the baseline and its various systematic variations is more significant in the third harmonics. The final values for the systematic uncertainties are calculated using equation (5.4).

6 Results

The intermediate results are $[p_T]$, c_k, $\langle \mathrm{corr}_n\{2\} \rangle$, $\langle \mathrm{corr}_n\{4\} \rangle$, and $\mathrm{Var}(v_n\{2\}^2)_{\mathrm{dyn}}$ presented in sections 6.1 and 6.2. These results are used to normalize $\mathrm{cov}(v_n\{2\}^2, [p_T])$ presented in section 6.3 to obtain the main results: the correlation coefficient $\rho(v_n\{2\}^2, [p_T])$ which is presented in section 6.4. The comparison between collision systems and energy is presented in section 6.5. The results from experimental data are compared to MC simulations and presented in section 6.6.

6.1 Mean p_T and variance c_k

Figure 6.1 shows the $[p_T]$ trend as a function of N_{tracks} for three p_T intervals in pp at 5.02 and 13 TeV, and in p-Pb at 5.02 TeV. Above N_{tracks} of about 5 a steady rise is observed in all systems. As could be expected, the order of $[p_T]$ values directly reflect the ranges in p_T interval. The 13 TeV pp data spans slightly further in N_{tracks} compared to pp at 5.02 TeV since higher energy gives a rise to more fragmentation which increases the number of events with higher multiplicity. The higher collision energy also rises the hardness of interaction, resulting in slightly higher $[p_T]$ with the same p_T range compared to the lower energy. As the multiplicity range accessible for p-Pb is much higher the results are presented up to N_{ch} about 400 charged particles. The events with high multiplicities are more abundant compared to those in pp and therefore a significantly better precision is obtained in the same multiplicity bins. However, the other observables for p-Pb are presented with the same binning and range as in pp to accommodate the comparison between systems.

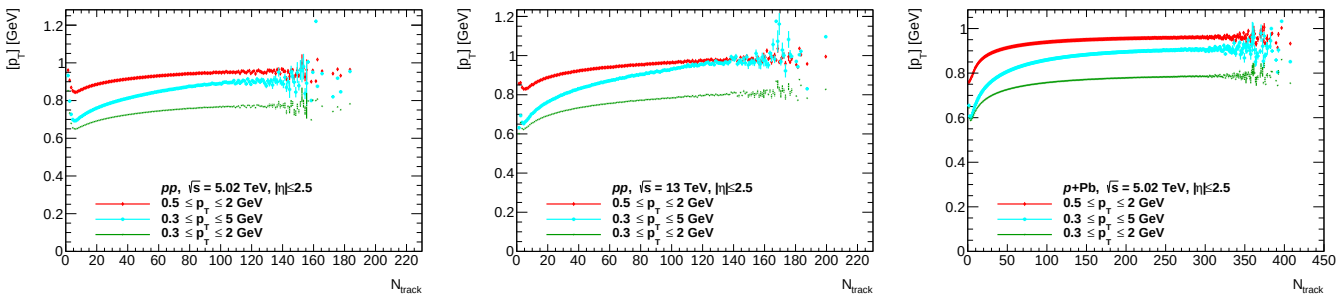

Figure 6.1: Comparison $[p_T]$ in various p_T ranges as denoted in the legend for pp at 5.02 and 13 TeV, and p-Pb at 5.02 TeV.

Figure 6.2 shows the c_k as a function of N_{ch} for pp collisions at 5.02 and 13 TeV and for p-Pb at 5.02 TeV. A fall with rising multiplicity that was observed in Pb+Pb and p-Pb **[?]** is reproduced for p-Pb and also observed in pp. The c_k, which is a measure

of fluctuations, is largest for widest range of momentum. The upper p_{T} limit mostly drives the magnitude of it. The study of p_{T} fluctuation in heavy ion collisions have been done in references [**?**, **?**] to measure the effective temperature of QGP and the speed of sound in QGP. The $[p_{\mathrm{T}}]$ presented in reference [**?**] is rising as a function of centrality, which is also observed in Figure 6.1. The observable similar to c_k in reference [**?**] is k_2, which is c_k normalized by $[p_{\mathrm{T}}]$. The same falling trend over N_{ch} is also observed in k_2 but steeper than c_k in Figure 6.2.

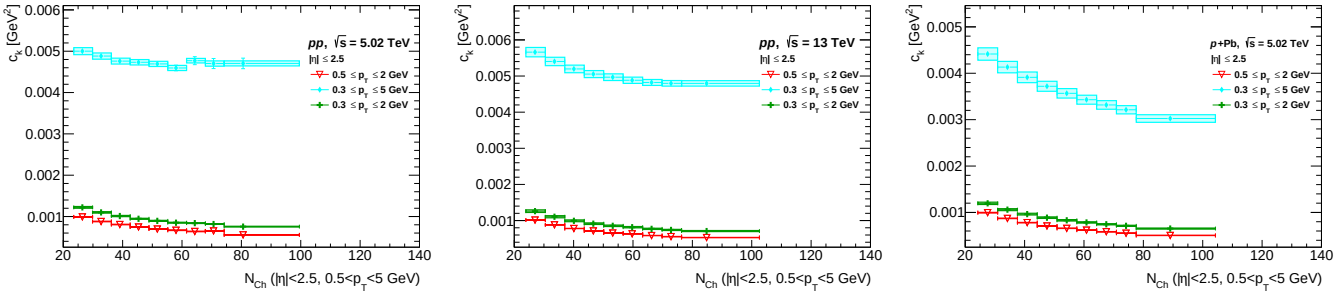

Figure 6.2: Comparison of c_k in various p_{T} ranges as denoted in the legend for *pp* at 5.02 and 13 TeV, and *p*-Pb at 5.02 TeV.

6.2 The particle correlation and dynamic variance of v_n

Figures 6.3 and 6.4 show the two- and four-particle correlations used to obtain $\mathrm{Var}\left(v_n\{2\}^2\right)_{\mathrm{dyn}}$ using equation (3.11) as a function N_{ch} for the second and the third harmonics. From left to right, the figures show the measurements for *pp* at 5.02 and 13 TeV, and in *p*-Pb at 5.02 TeV. The magnitude is sensitive to the choice of both upper and lower limits of momentum range, with more significant impact when lower limit is changed. The issue discussed in section 4.1 appears in four-particle correlation for *pp* 13 TeV and *p*-Pb 5.02 TeV at the lowest N_{ch} in the p_{T} range $0.5 \leq p_{\mathrm{T}} \leq 2$ GeV. The average value of N_{ch} in the first point of *pp* 13 TeV is shifted to the right toward $N_{\mathrm{ch}} \sim 30$, signaling very low number of pairs at low multiplicity events. While in *p*-Pb 5.02 TeV, the first point is missing, which means that not enough particles to pair after the cut in kinematic ranges.

In the second harmonic, similar values and trends are observed for 5.02 and 13 TeV *pp* data since they have similar initial spatial eccentricity. The same ordering of different p_{T} ranges is observed in the correlations, except for the third harmonic of two-particle 2-subevents correlations. The trend is falling with increasing multiplicity, except for the 2-subevents $\langle \mathrm{corr}_n\{2\} \rangle$ correlations.

In 5.02 TeV *pp*, the fluctuation appears in 2 subevent $\langle \mathrm{corr}_n\{2\} \rangle$ at high N_{ch} due to the lack of statistics. The magnitudes of correlations in the third harmonic are smaller as compared to the second harmonic. Meanwhile in *p*-Pb, the two-particle 2-subevents correlation is rising with multiplicity both for harmonic $n = 2, 3$. The 2-subevents $\langle \mathrm{corr}_3\{2\} \rangle$ in *p*-Pb shows a unique feature where the both points of p_{T}

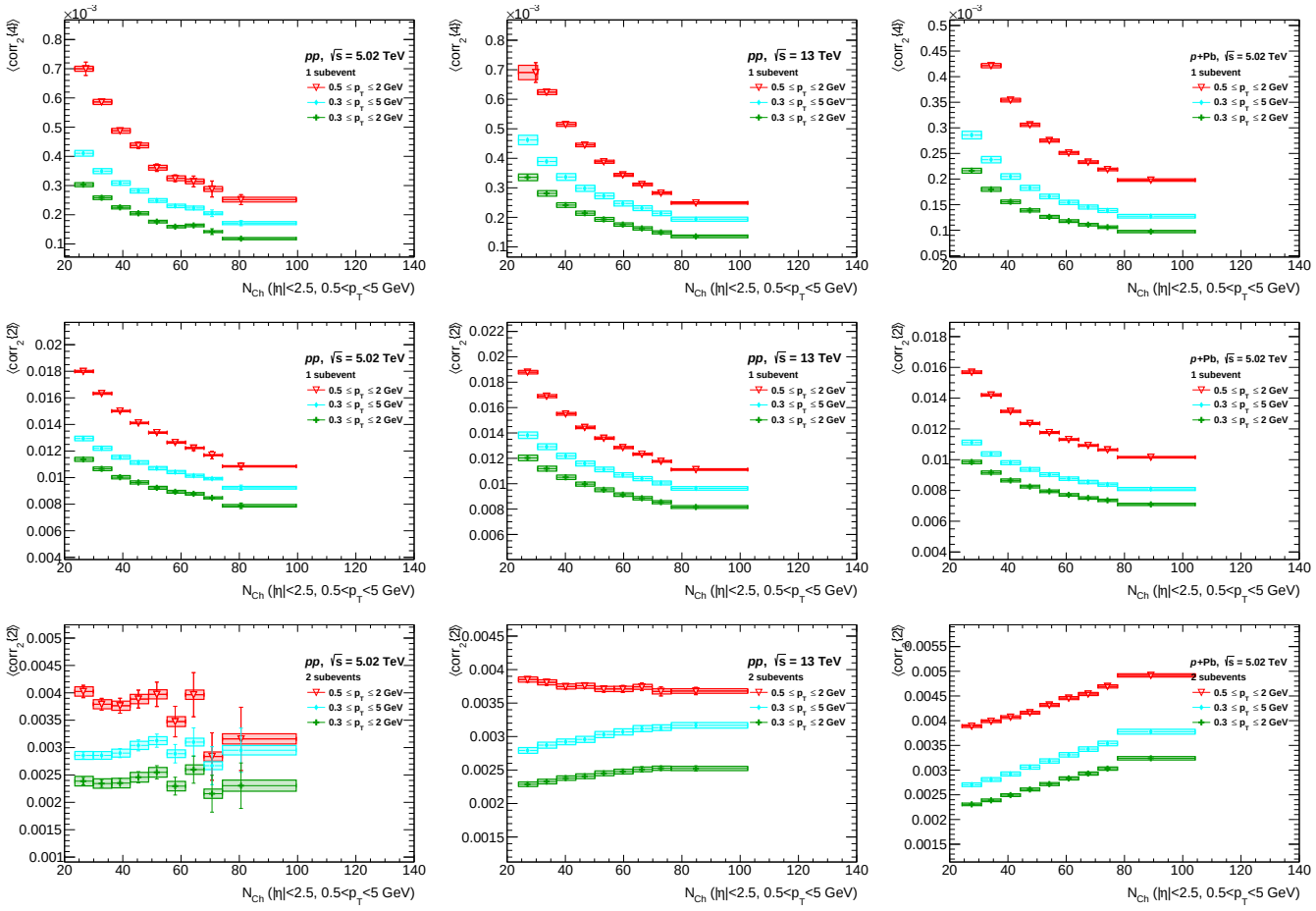

Figure 6.3: Correlations used to construct $\mathrm{Var}\left(v_2\{2\}^2\right)_{\mathrm{dyn}}$ as a function of N_{ch} for pp at 5.02 and 13 TeV, and p-Pb at 5.02 TeV, in various p_{T} ranges as indicated in the legend.

ranges with the same low p_{T} limit meet at the highest N_{ch} while points with the same upper p_{T} limit meet at lowest N_{ch}. However, this feature is not observed in pp.

The measurements of dynamical variances $\mathrm{Var}\left(v_n\{2\}^2\right)_{\mathrm{dyn}}$ are shown in Figures 6.5 and 6.6. Some significant fluctuations are the result of subtracting a very similar values and a sizeable fluctuations of 2-subevents 2-particle correlation.

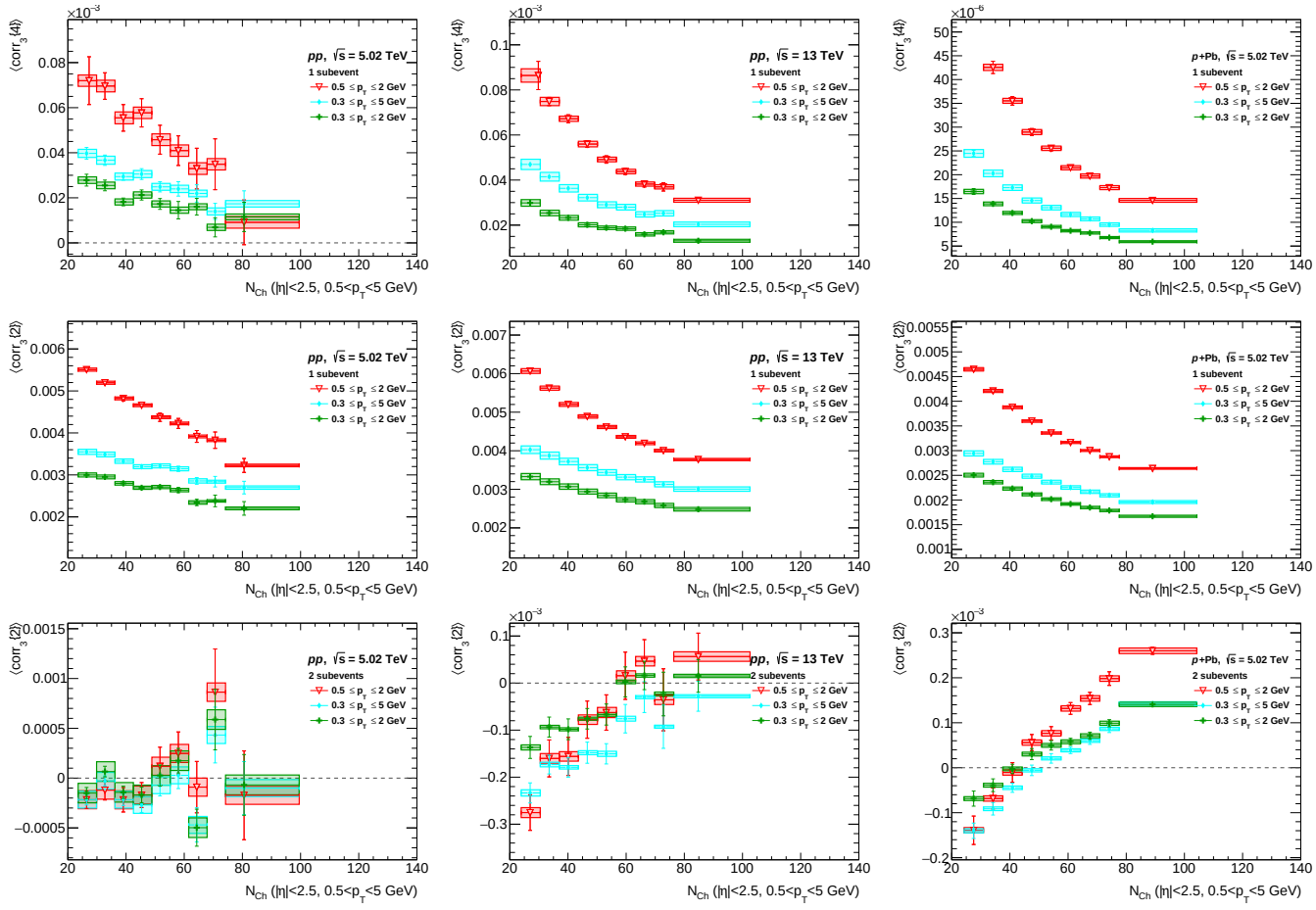

Figure 6.4: Correlations used to construct $\mathrm{Var}\left(v_2\{2\}^2\right)_{\mathrm{dyn}}$ as a function of N_{ch} for pp at 5.02 and 13 TeV, and p-Pb at 5.02 TeV, in various p_{T} ranges as indicated in the legend.

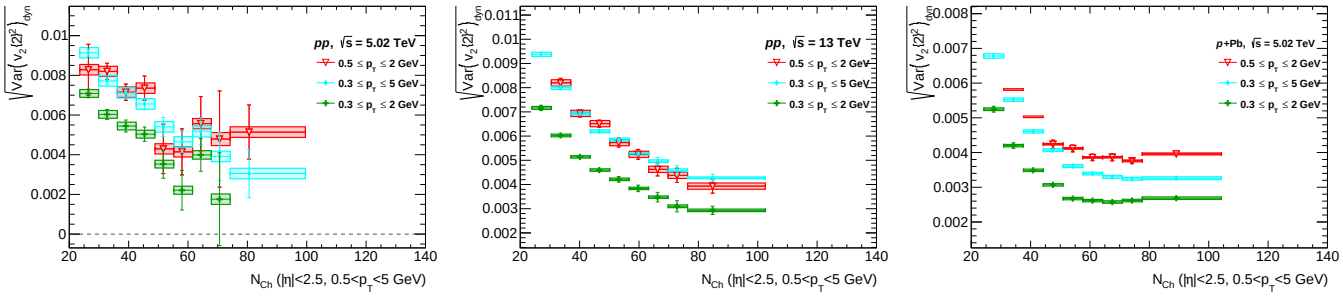

Figure 6.5: Dynamical variance $\mathrm{Var}\left(v_2\{2\}^2\right)_{\mathrm{dyn}}$ as a function of N_{ch} for pp at 5.02 and 13 TeV, and p-Pb at 5.02 TeV, in various p_{T} ranges as indicated in the legend

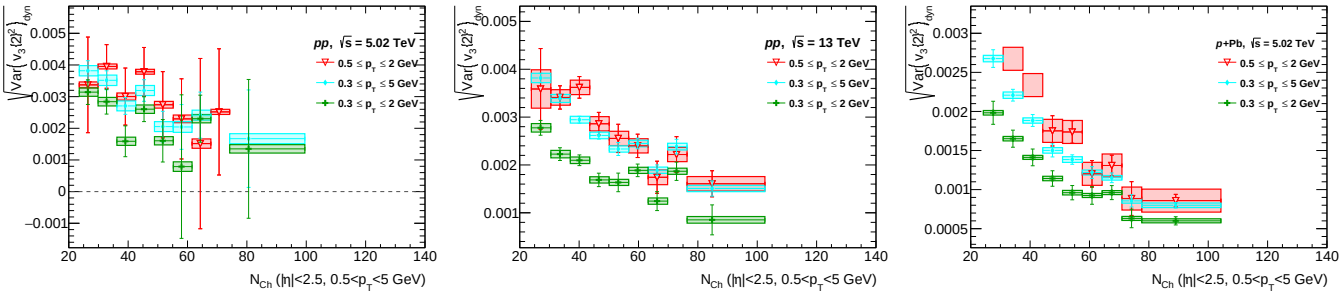

Figure 6.6: Dynamical variance $\mathrm{Var}\left(v_3\{2\}^2\right)_{\mathrm{dyn}}$ as a function of N_{ch} for pp at 5.02 and 13 TeV, and p-Pb at 5.02 TeV, in various p_{T} ranges as indicated in the legend.

6.3 Covariance of mean p_T and v_n

Figures 6.7 show $\mathrm{cov}(v_n\{2\}^2, [p_T])$ as a function of N_{ch} for the second and the third harmonics, comparing different subevent categories for p_T range $0.3 \leq p_T \leq 2$ GeV. The trends tend to converge at high multiplicity between different subevent

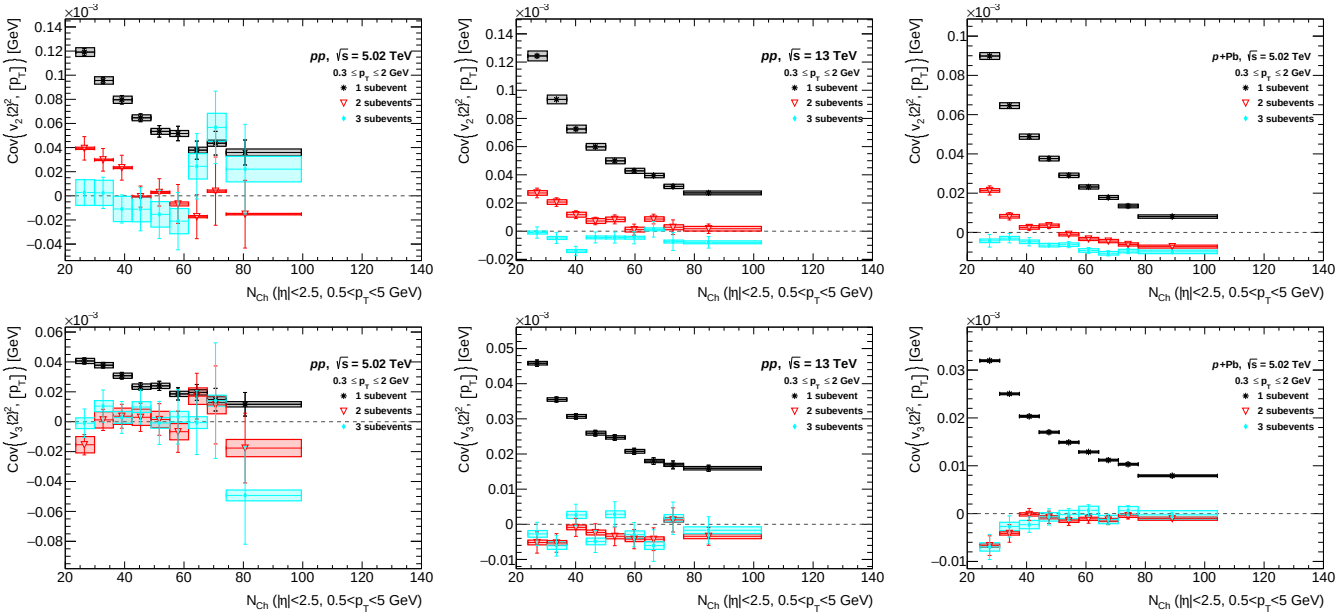

Figure 6.7: Comparison of $\mathrm{cov}(v_n\{2\}^2, [p_T])$ in various sub-events for each p_T range, from left to right columns for pp collisions at 5.02 and 13 TeV, and for p-Pb at 5.02 TeV respectively. The top rows is for $n = 2$, and the bottom row is for $n = 3$.

methods. A steeper falling trend as N_{ch} increase on 1-subevent $\mathrm{cov}(v_n\{2\}^2, [p_T])$ in comparison to 2- and 3-subevents methods is a result of a short range correlations which is reduced significantly in two and three subevents. These falling trends are from the non-flow and they are eliminated in two and three subevents and the N_{ch} dependence becomes weaker. The sign change begins to appear in 2-subevents $\mathrm{cov}(v_2\{2\}^2, [p_T])$ of pp and p-Pb at 5.02 TeV, starting from positive value at the smallest N_{ch}, crossing zero around N_{ch} ~50, and becomes negative at high N_{ch}. While the $\mathrm{cov}(v_2\{2\}^2, [p_T])$ in pp 13 TeV is simply reduced in magnitude without sign change. The 3-subevent $\mathrm{cov}(v_2\{2\}^2, [p_T])$ in pp 5.02 TeV also undergoes the sign change but fluctuates significantly in the last three bins. While in pp 13 TeV and p-Pb 5.02 TeV, the 3-subevent $\mathrm{cov}(v_2\{2\}^2, [p_T])$ is negative for this particular p_T range. For the third harmonic, the 1-subevent $\mathrm{cov}(v_3\{2\}^2, [p_T])$ has the same trend as in the second harmonic, while the 2- and 3-subevents $\mathrm{cov}(v_3\{2\}^2, [p_T])$ start at negative and rise to around zero with increasing N_{ch}.

Figures 6.8 and 6.9 show $\mathrm{cov}(v_n\{2\}^2, [p_T])$ as a function N_{ch} comparing different p_T ranges for the second and the third harmonics respectively. The trends tend to converge when moving to higher multiplicity between different p_T ranges as well. The ordering based on p_T limit is visible in 1-subevent for all systems and harmonic

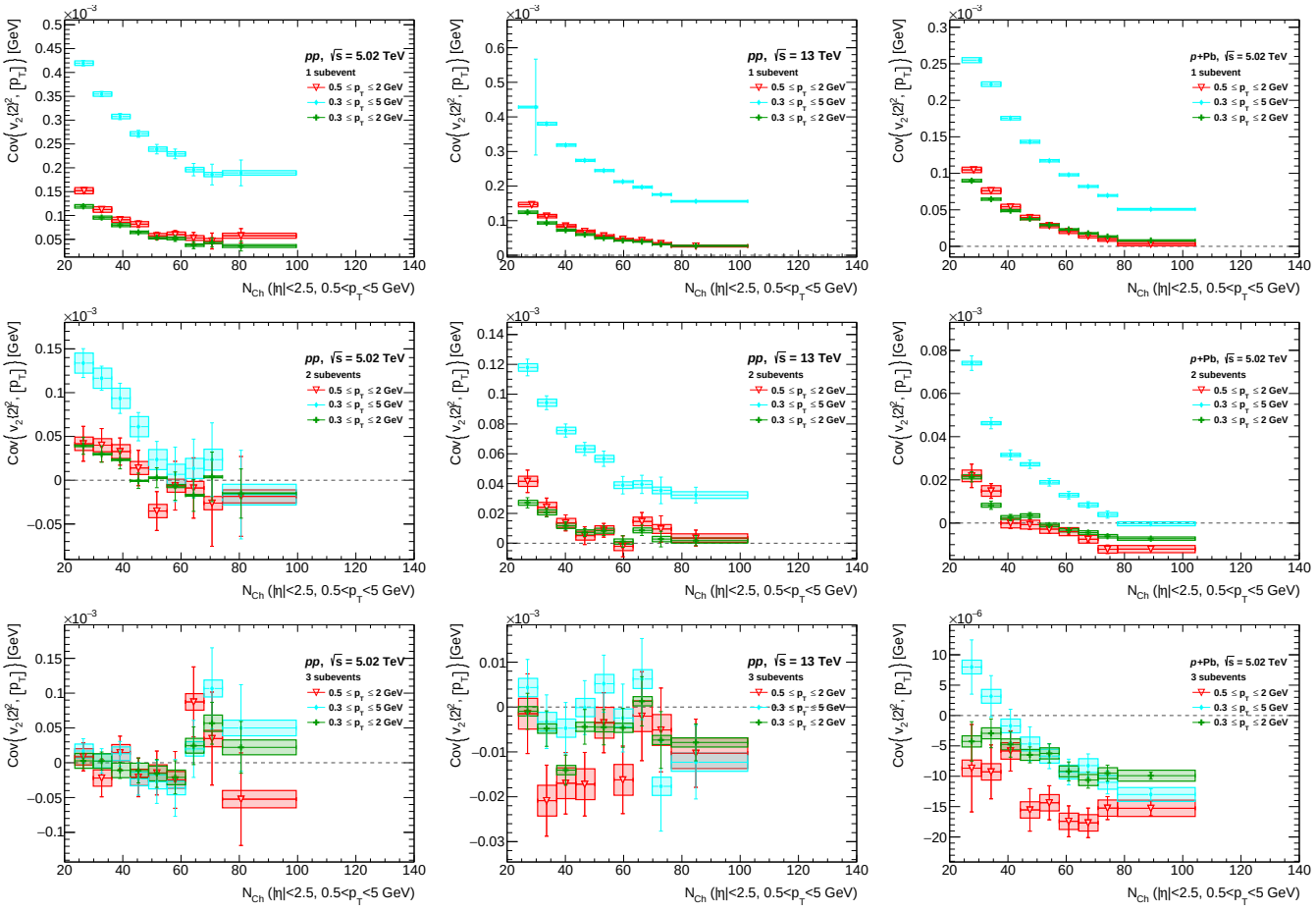

Figure 6.8: Comparison of $\mathrm{cov}(v_2\{2\}^2, [p_T])$ in various p_T ranges for 1-, 2-, and 3-subevents methods respectively from top to bottom rows, and from left to right columns for pp collisions at 5.02 and 13 TeV, and for p-Pb at 5.02 TeV respectively.

$n = 2, 3$, especially the gap between two different upper p_T limits at 2 and 5 GeV. The higher p_T limit allows the inclusion of harder particles produced in jet fragmentation, contributing to both correlation and mean p_T. However, the p_T ordering diminishes significantly in 2-subevent $\mathrm{cov}(v_2\{2\}^2, [p_T])$ and becomes obscure in three subevents as the short range correlations are reduced significantly. The two and three subevents reduce the non-flow contribution significantly but also affect severely the statistical precision. As a result, fluctuations in all measurements begin to appear for two subevent and become very significant in three subevent. In the three subevent pp at 5.02 TeV, the sign change of covariances are observed in all p_T ranges before the big fluctuations appears at N_{ch} around 60. However, the uncertainties are large enough to cross zero. While in pp 13 TeV, the three subevent covariance with the highest p_T range fluctuates around zero while the covariances with lower p_T ranges are negative. The similar negative covariances are also observed in p-Pb 5.02 TeV for the same lower p_T ranges while the highest p_T range covariance undergoes a smooth transition from positive to negative with increasing N_{ch}.

For the third harmonic, the one subevent covariances in all systems have the same

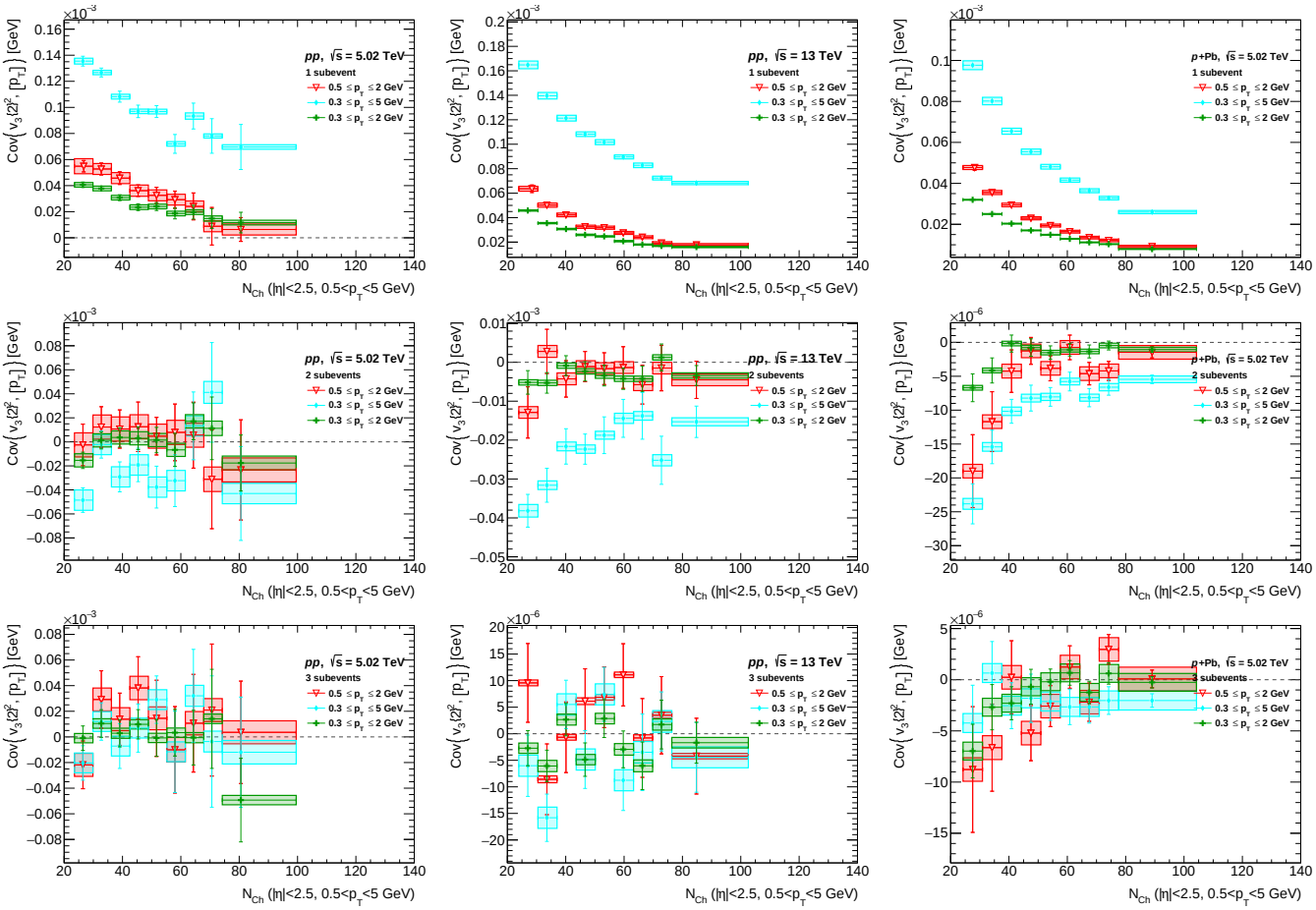

Figure 6.9: Comparison of $\mathrm{cov}(v_3\{2\}^2, [p_\mathrm{T}])$ in various p_T ranges for 1-, 2-, and 3-subevents methods respectively from top to bottom rows, and from left to right columns for pp collisions at 5.02 and 13 TeV, and for p-Pb at 5.02 TeV respectively

falling trend as in the second harmonic. However, the trends become very different in two subevent covariances. The order of p_T limit is reversed in p-Pb 5.02 TeV with covariances start at negative in the low N_ch and grow close to zero with increasing N_ch. The same trend is observed in pp 13 TeV, but the order of p_T limit is obscure for p_T ranges with upper limit 2 GeV. While in pp 5.02 TeV, the trends rise up to N_ch ∼45 and fall up to N_ch ∼60 followed by fluctuations. In three subevent, the order of p_T limit disappear and the covariances for all p_T ranges blend together. Overall, the 3-subevents method decreases the value of covariances. However, the fluctuations around zero in pp 13 TeV becomes large in 3-subevent $\mathrm{cov}(v_3\{2\}^2, [p_\mathrm{T}])$.

6.4 Correlation coefficient $\rho(v_n\{2\}^2, [p_\mathrm{T}])$

Figures 6.10 show $\rho(v_n\{2\}^2, [p_\mathrm{T}])$ as a function of N_ch for the second and the third harmonics, comparing different subevent categories for p_T range $0.3 \leq p_\mathrm{T} \leq 2$ GeV. The correlation coefficient ρ inherits most of the qualitative features from their respective covariance. The 2- and 3-subevents methods reduce significantly the short

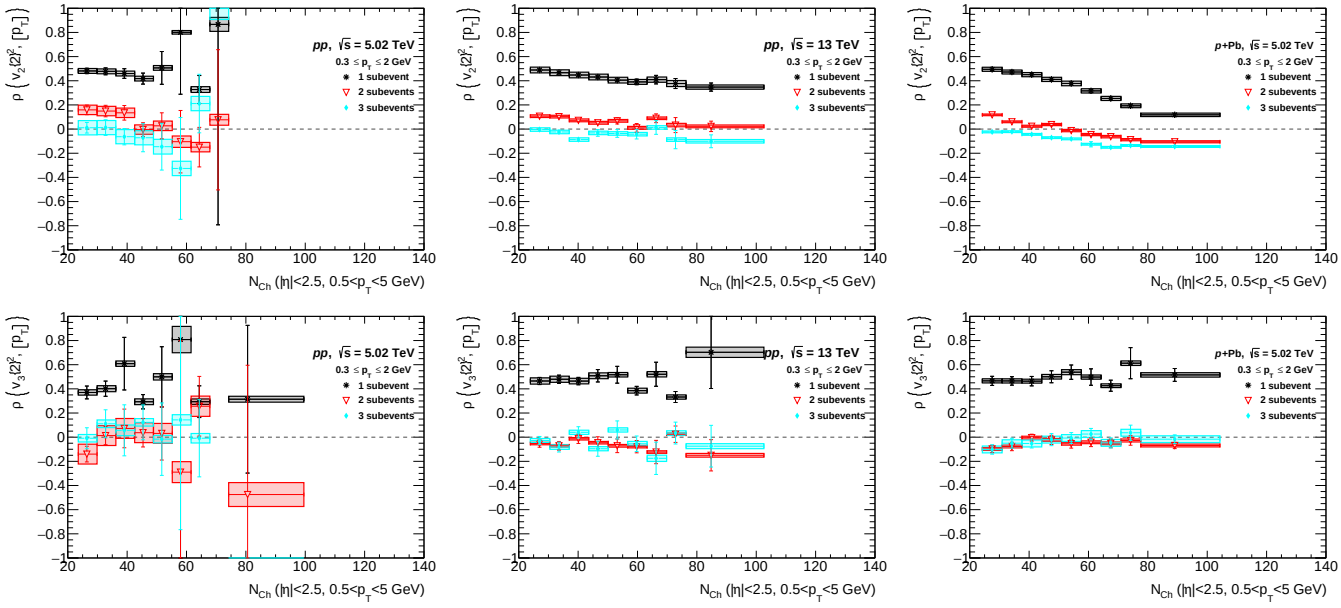

Figure 6.10: Comparison of $\rho(v_n\{2\}^2, [p_T])$ in various sub-events for each p_T range, from left to right columns for pp collisions at 5.02 and 13 TeV, and for p-Pb at 5.02 TeV respectively. The top rows is for $n = 2$, and the bottom row is for $n = 3$.

range correlations compared to 1-subevent method, resulting in lower values of $\rho(v_n\{2\}^2, [p_T])$.

Figures 6.11 and 6.12 shows $\rho(v_n\{2\}^2, [p_T])$ as a function N_{ch} comparing different p_T ranges for the second and the third harmonics respectively. Some values and uncertainties are beyond $|\rho_n| \leq 1$ which are not relevant, therefore the y-axis is set to -1 to 1 for the plots containing these values, while the others are zoomed to their magnitude ranges. All 1-subevent results are positive in all systems and $n = 2, 3$. In contrast to the 1-subevent $\text{cov}(v_2\{2\}^2, [p_T])$, the $\rho(v_2\{2\}^2, [p_T])$ for p_T ranges with upper limit 2 GeV converge in low N_{ch} while their covariances converge at high N_{ch} instead. The order is also reversed for covariance with upper limit p_T at 2 GeV. The order of p_T ranges remains the same for two and three subevents in pp 13 TeV and p-Pb 5.02 TeV. While in pp 5.02 TeV, the order becomes blurred for lower p_T ranges in two subevent and indistinguishable in three subevent.

In pp 5.02 TeV, the 2-subevents $\text{cov}(v_2\{2\}^2, [p_T])$ undergoes sign change, falling from positive at low N_{ch} to negative at high N_{ch}. The same happen in p-Pb, except for the highest p_T range. While in pp 13 TeV, the lower p_T ranges cross zero at high N_{ch} mostly by statistical uncertainties.

In three subevent $\text{cov}(v_2\{2\}^2, [p_T])$, the falling trend is observed in all systems. However, the fluctuations take over the trend at high N_{ch} in pp. In p-Pb 5.02 TeV, only the highest p_T range shows the sign change. While in pp 13 TeV, all points for the most narrow p_T range are negative with a few error bars cross zero.

For the third harmonic, the 1-subevent covariance, within large statistical uncertainties, is considered independent of N_{ch}. The trend in 2-subevents method

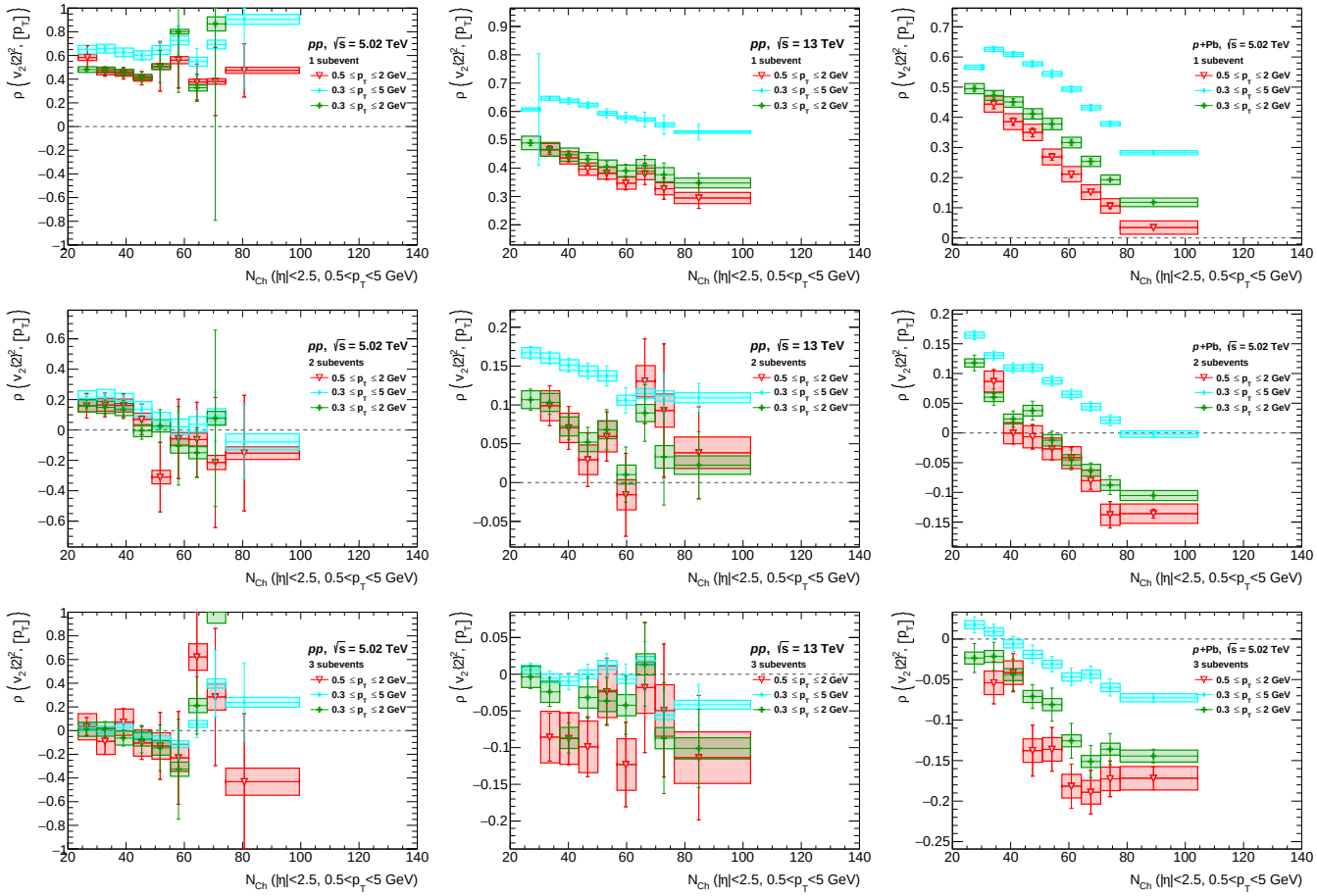

Figure 6.11: Comparison of $\rho(v_2\{2\}^2, [p_T])$ in various p_T ranges for 1-, 2-, and 3-subevents methods respectively from top to bottom rows, and from left to right columns for pp collisions at 5.02 and 13 TeV, and for p-Pb at 5.02 TeV respectively.

is rising from low N_{ch}, and falling at high N_{ch}. A clear pattern of sign change is only observed in low p_T ranges pp 5.02 TeV. Without uncertainties, the 3-subevents $\text{cov}(v_3\{2\}^2, [p_T])$ has similar trend as in 2-subevents method, exept in pp 13 TeV which is dominated by fluctuations for all p_T ranges.However, due to uncertainties, mainly statistical, the $\rho(v_3\{2\}^2, [p_T])$ trends are less pronounced. Therefore for 2- and 3-subevent methods are considered consistent with zero even though the covariances suggest that a sign change might occur with non-monotonic evolution at low multiplicities.

Figure 6.13 shows the results from Pb+Pb and Xe+Xe from previous analysis [**?**]. The trends keep rising in more central collisions for the second and third harmonic. The 1-subevent method is referred as *standard*. There is no distinction between the different subevent methods, except those in peripheral. Since the N_{ch} in central collisions is around several thousands, the relevant parts to compare with the small systems are the peripheral events. The HIJING simulation is used to estimate the non-flow contribution in the peripheral region. It shows the similar falling trend in one and two subevents, while the three subevents starts from negative value. In the

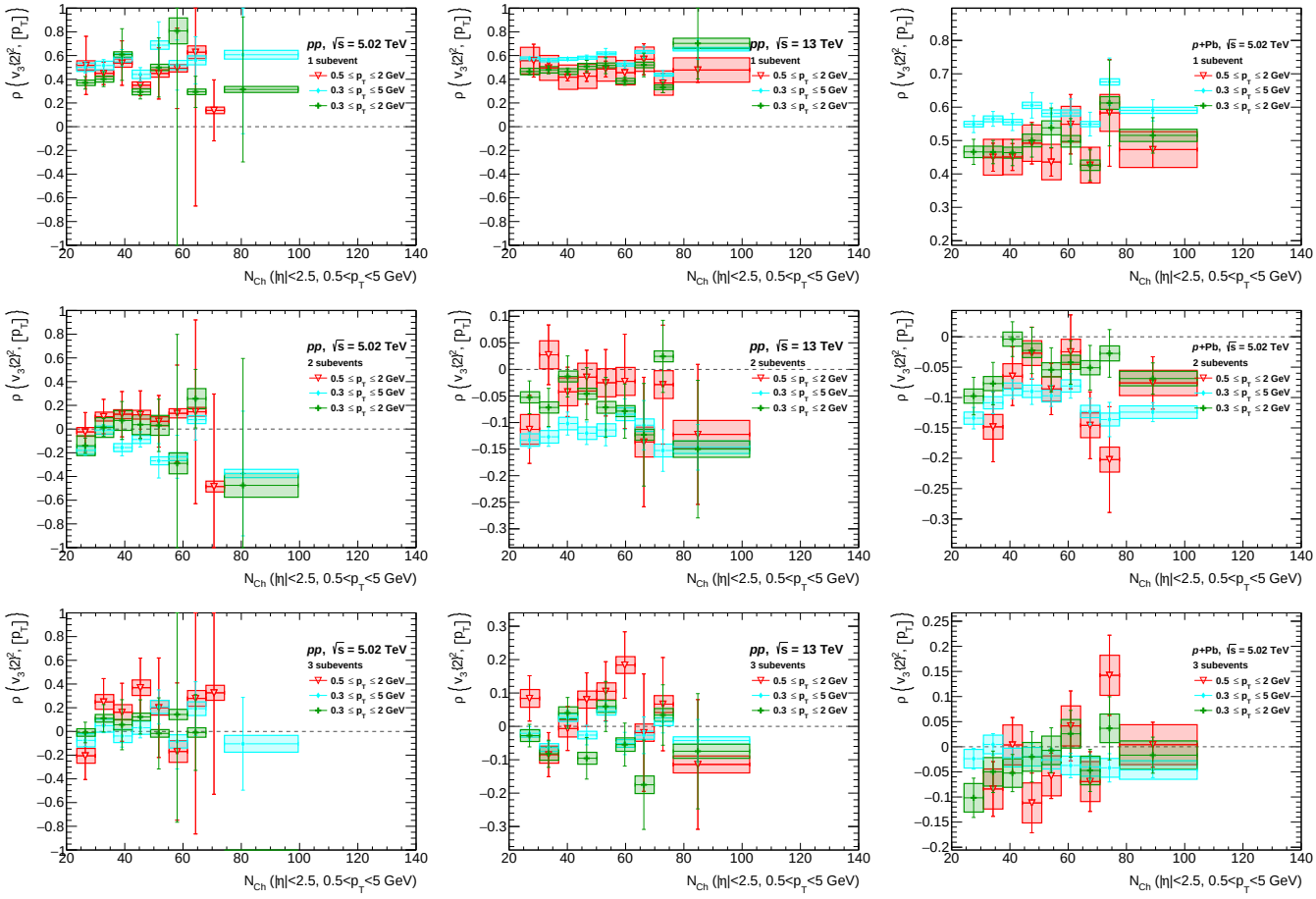

Figure 6.12: Comparison of $\rho(v_3\{2\}^2, [p_T])$ in various p_T ranges for 1-, 2-, and 3-subevents methods respectively from top to bottom rows, and from left to right columns for pp collisions at 5.02 and 13 TeV, and for p-Pb at 5.02 TeV respectively

end, they converge at semi-central collision at zero since HIJING does not simulate hydrodynamic. This trend suggests that at small systems and peripheral events, the correlation is dominated by non-hydrodynamic flow.

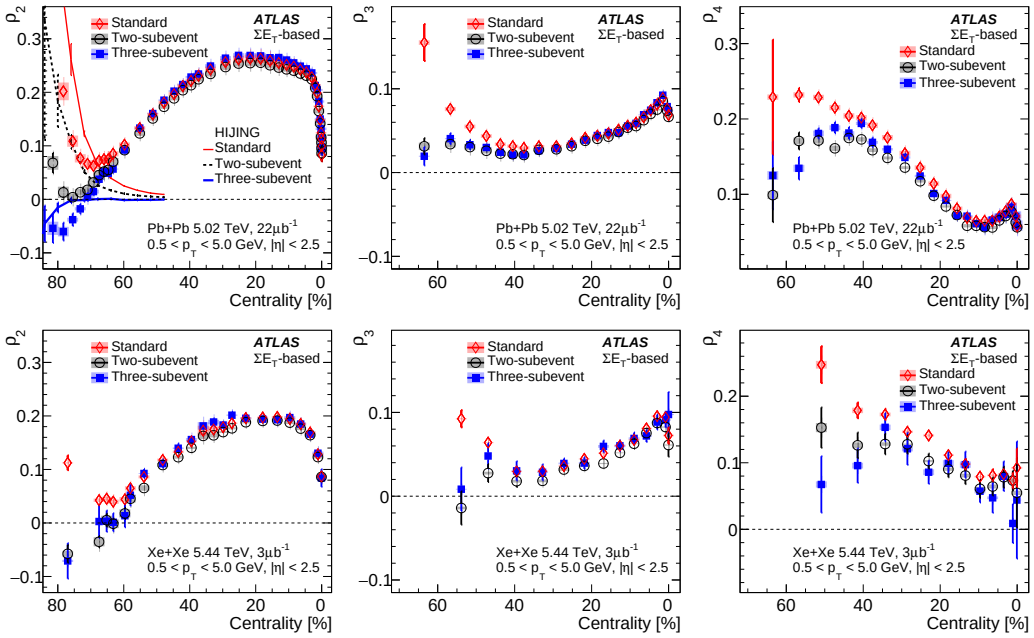

Figure 6.13: $\rho(v_n\{2\}^2, [p_{\mathrm{T}}])$ in Pb+Pb and Xe+Xe. HIJING is used to estimate the non-flow contribution in the peripheral collisions. Figure from [**?**].

6.5 Comparison between collision systems and energy

Figure 6.14, 6.15, 6.16, 6.17, and , 6.18 show the comparison of the measured variables between pp at 5.02 and 13 TeV, and p-Pb at 5.02 TeV. The results for c_k are mostly in agreement with each other within the uncertainties at p_{T} ranges below 2 GeV. However, the differences appear for higher p_{T} range. The higher collision energy gives a rise to the production of harder particles in pp 13 TeV, resulting the gap between pp data with different center of mass energy in low N_{ch}. However, they begin to converge at higher N_{ch} since the impact of jets in this p_{T} range are smeared out in high-multiplicity events as there are more soft particles. Meanwhile the c_k in p-Pb 5.02 TeV at the lowest multiplicity events is close to pp 5.02 TeV since the most peripheral events are similar to single nucleon-nucleon collisions at the same energy. The slight difference comes from the multiplicity produced from the remnants of nuclei. The gap between pp and p-Pb at 5.02 develops further at high N_{ch} as more nucleons are involved in the central collision, giving a rise to much more multiplicity of softer particles. Therefore, the agreement is gone in higher p_{T} limit.

For the dynamical variances $\mathrm{Var}\left(v_n\{2\}^2\right)_{\mathrm{dyn}}$, the agreement is observed in both pp results with different energy. However, the difference is observed between pp and p-Pb due to the difference between the initial spatial geometry of the collisions, with p-Pb yields systematically lower values.

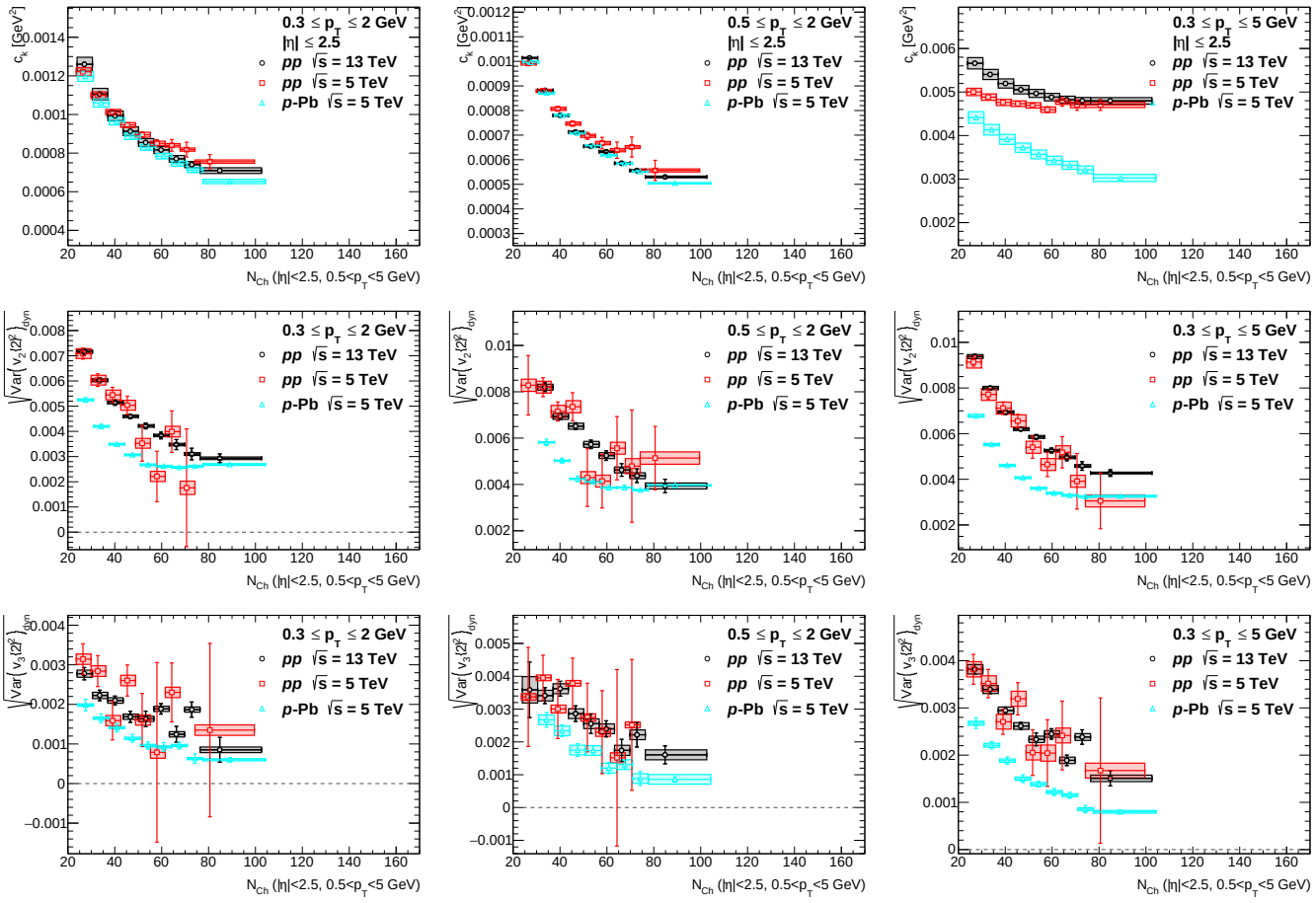

Figure 6.14: The comparison of c_k and $\mathrm{Var}(v_n\{2\}^2)_{\mathrm{dyn}}$ between different collision systems and energy.

For the $\mathrm{cov}(v_n\{2\}^2, [p_{\mathrm{T}}])$, the gaps appear between pp and p-Pb in 1-subevent and they become closer to each other in 2- and 3-subevents as the covariances move closer to zero.

For $\rho(v_2\{2\}^2, [p_{\mathrm{T}}])$, all systems start with similar values at low N_{ch}, especially in p_{T} range with lower limit 0.3 GeV, and then diverge at high N_{ch}. While in $\rho(v_3\{2\}^2, [p_{\mathrm{T}}])$, within the large uncertainties, the agreement is observed in all systems.

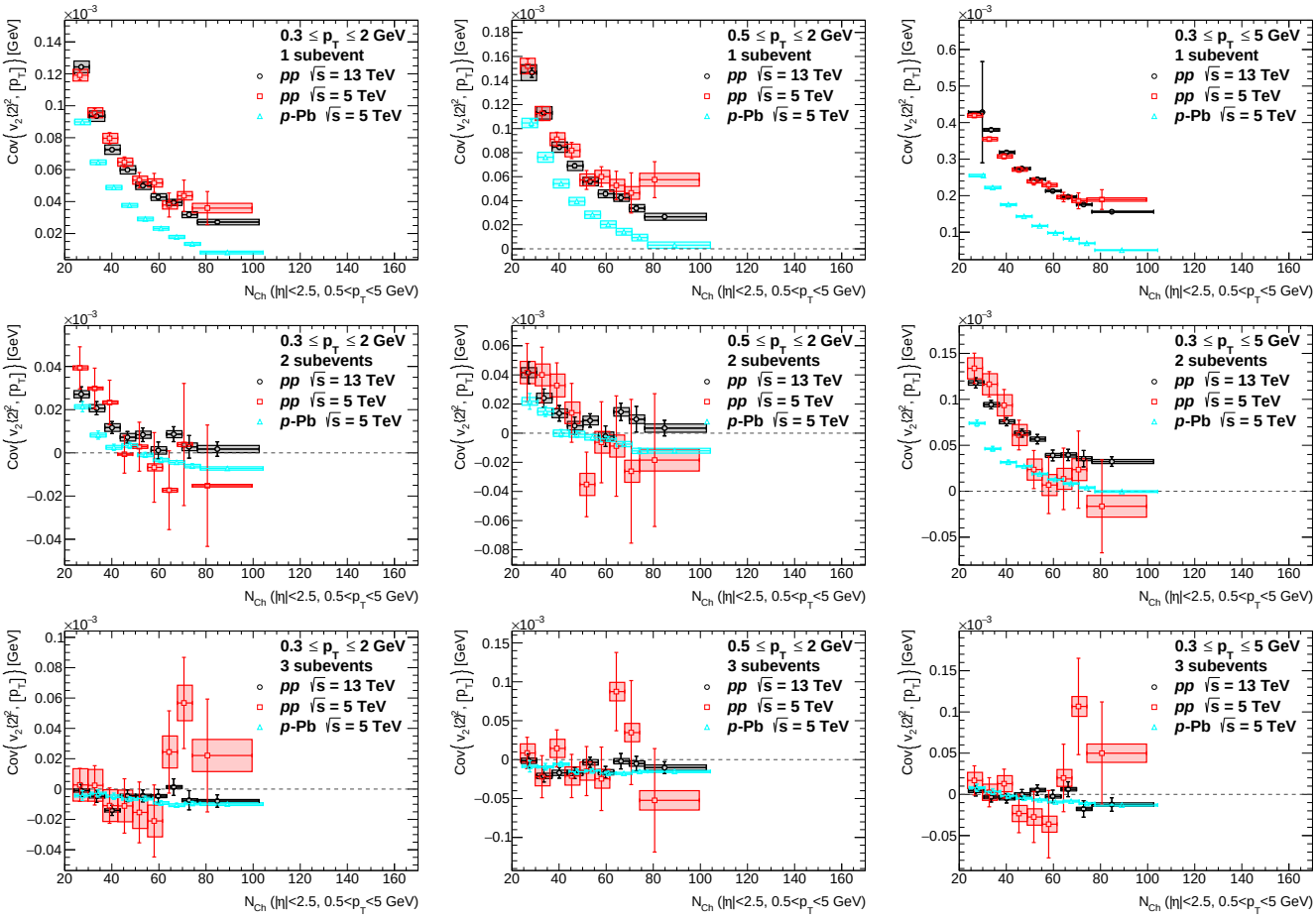

Figure 6.15: The comparison $\mathrm{cov}(v_2\{2\}^2, [p_\mathrm{T}])$ between different collision systems and energy.

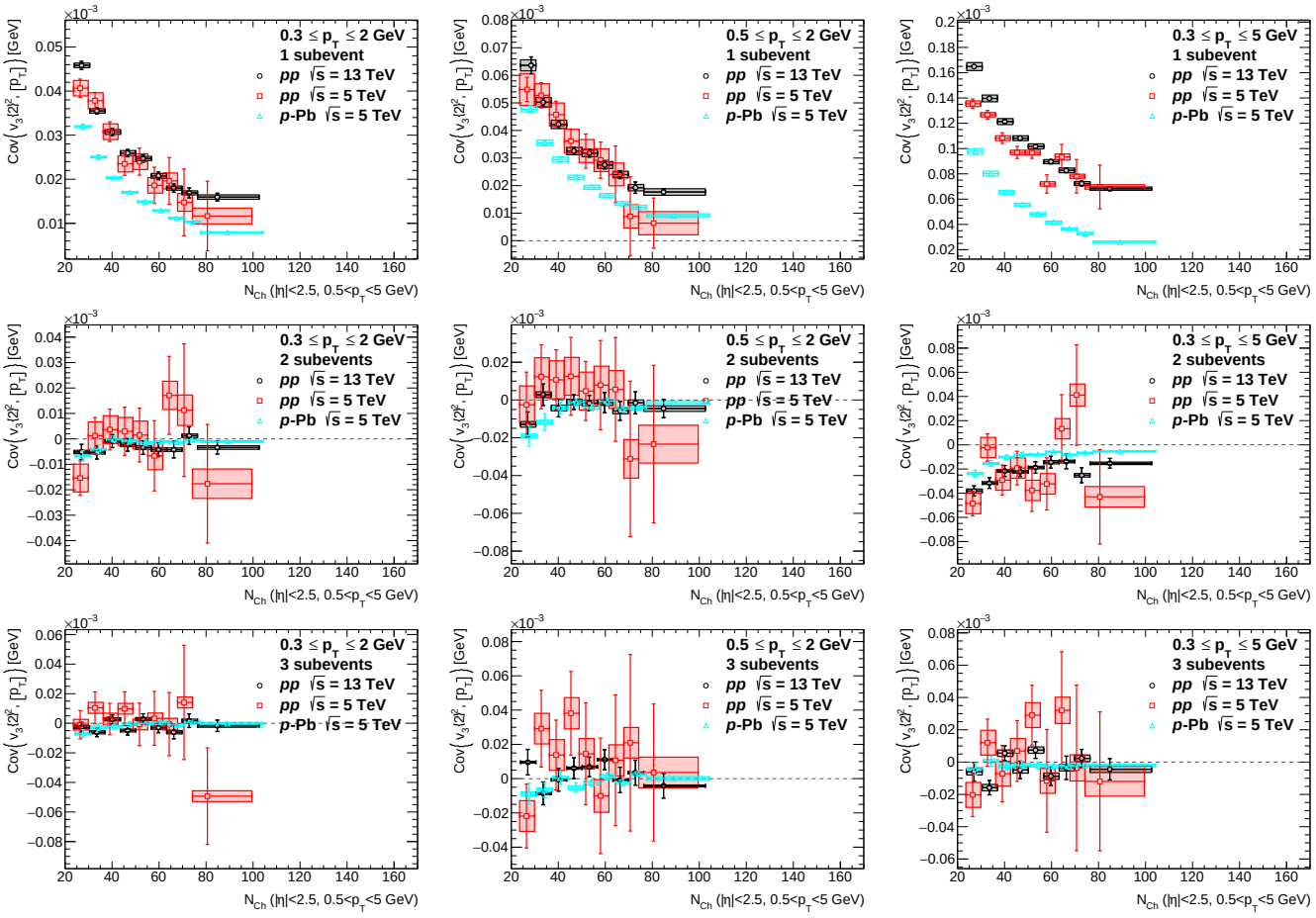

Figure 6.16: The comparison $\mathrm{cov}(v_3\{2\}^2, [p_\mathrm{T}])$ between different collision systems and energy.

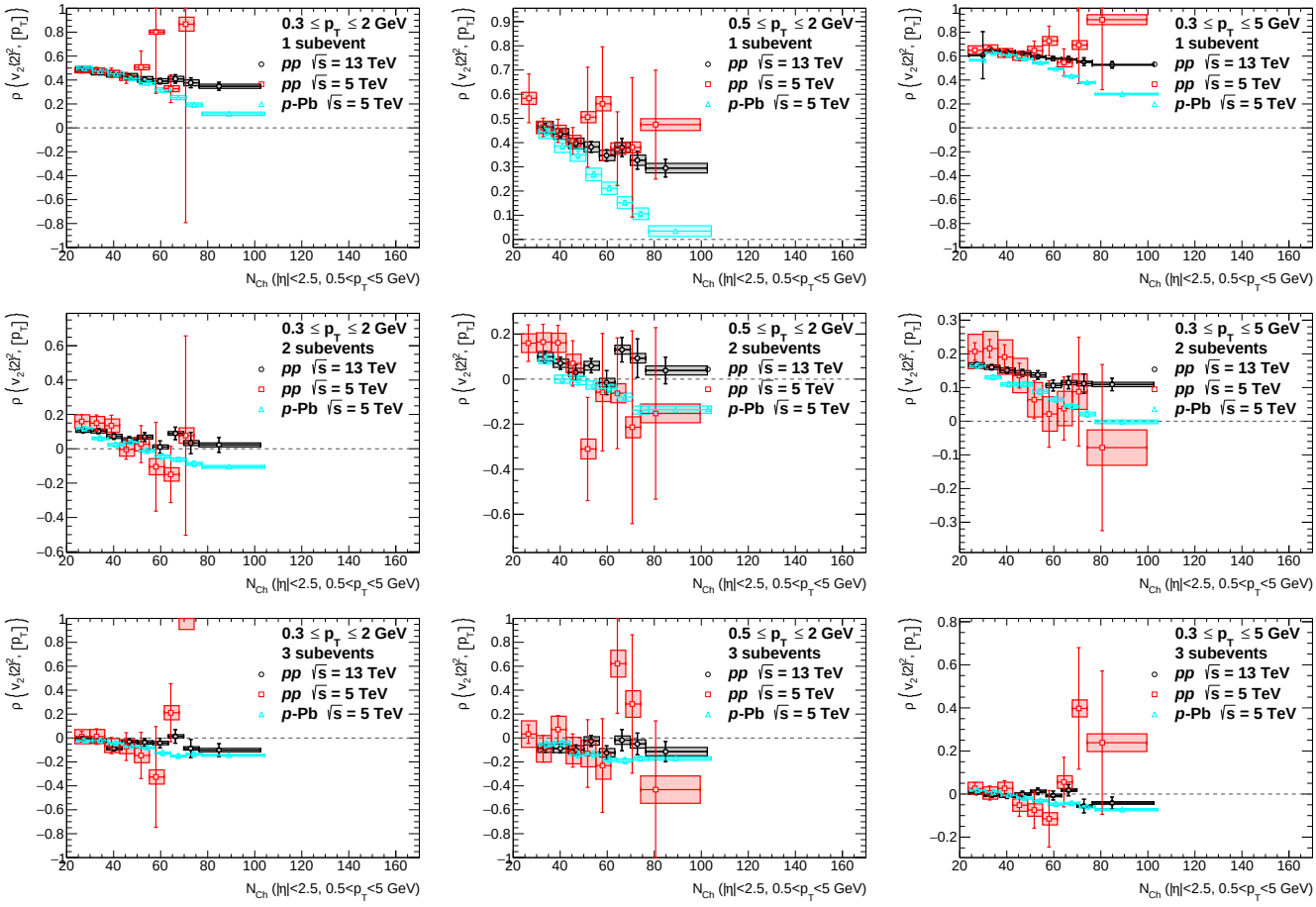

Figure 6.17: The comparison $\rho(v_2\{2\}^2, [p_{\mathrm{T}}])$ between different collision systems and energy.

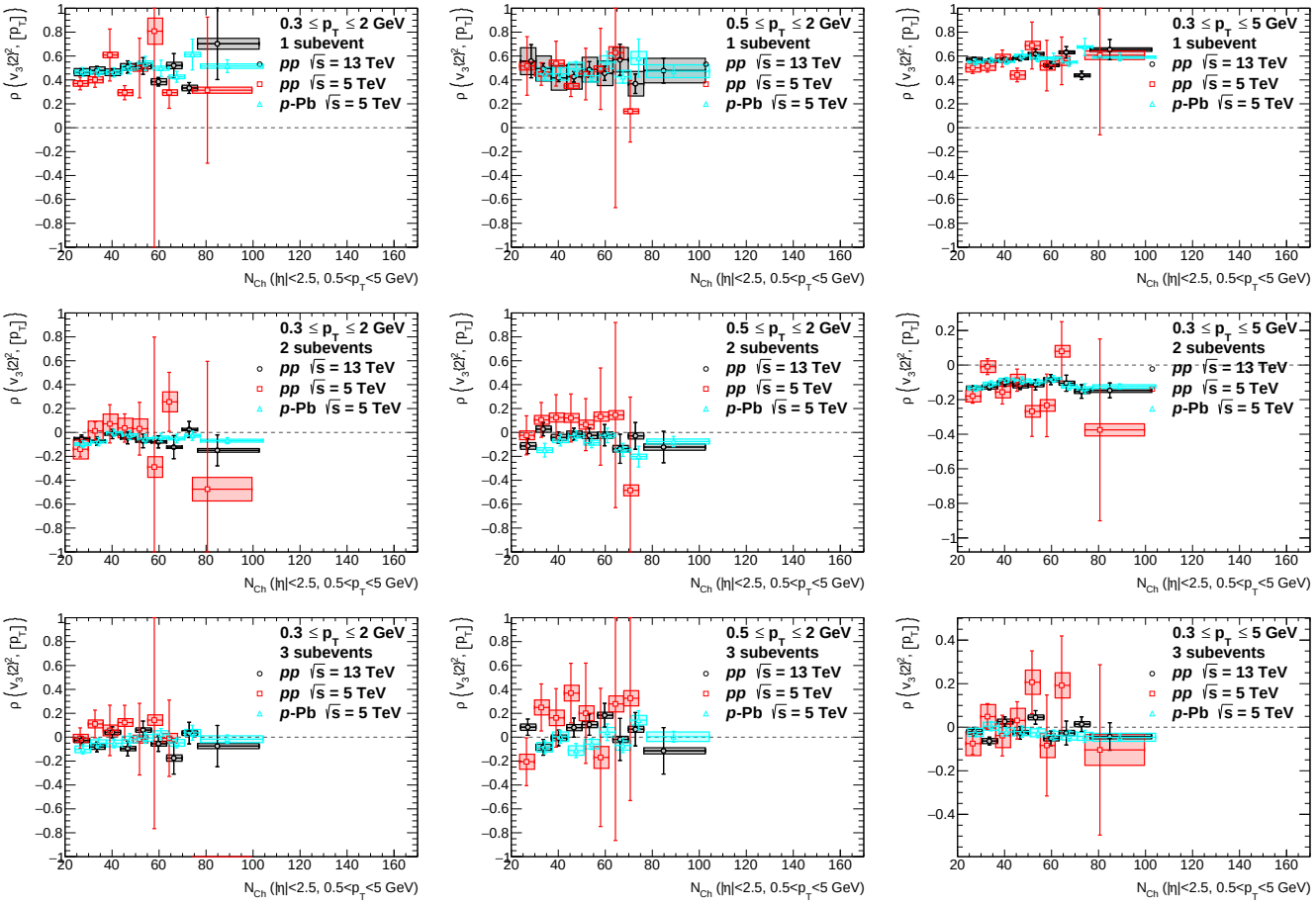

Figure 6.18: The comparison $\rho(v_3\{2\}^2, [p_T])$ between different collision systems and energy.

6.6 Comparison to models

The high multiplicity events in pp are simulated by Pythia 8 with Monash tune and EPOS. Then, the analysis are performed on them to compare their results with the results from experimental data. In Pythia the correlation would not arise from any collective dynamics and will be fully determined by the non-flow effects. Meanwhile in EPOS, the simulation includes the collective effects, gluon saturation, and hadronic cascade as well.

Figure 6.19 shows the comparison of c_k in different p_{T} ranges. Both Pythia 8 and EPOS manage to produce the same trend as in experimental data. However, Pythia 8 overestimate c_k at p_{T} ranges with upper cut of 2 GeV. While for the p_{T} range $0.3 \leq p_{\mathrm{T}} \leq 5$ GeV, the results intersect with experiment at $N_{\mathrm{ch}} \sim 30$ before falling below it at higher N_{ch}. For EPOS, the results are lower than the experiment in all p_{T} ranges.

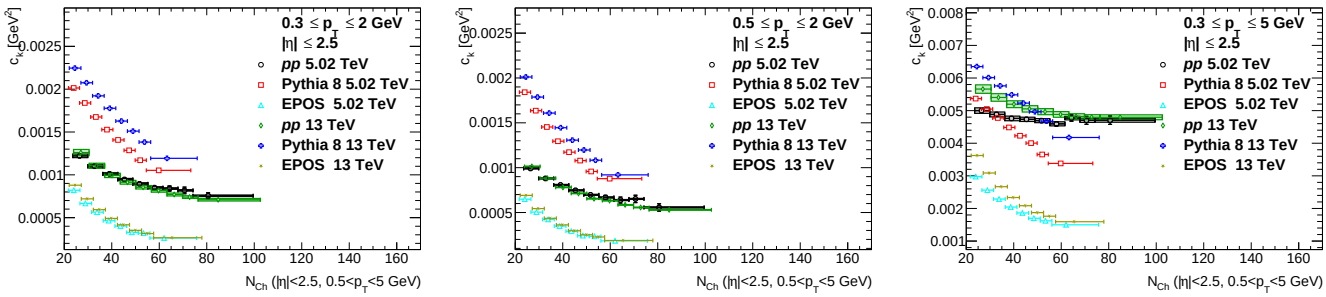

Figure 6.19: Comparison of c_k between pp and MC in various p_{T} ranges.

Figure 6.20 shows the comparison of $\mathrm{Var}\left(v_n\{2\}^2\right)_{\mathrm{dyn}}$ in different p_{T} ranges. For the second harmonic, Pythia 8 manages to produce the same trend without any hydrodynamic simulation. However, the predicted values are below those of experimental data While in EPOS, the physics that are not included in Pythia 8 certainly boost the results up, but overestimate the values. For the third harmonic, both Pythia 8 and EPOS are in agreement with each other, but the values are lower than from the experiment. These results suggest that the pp collisions have higher triangular flow which translates to more dynamic in the initial state fluctuation of the interacting partons.

Figure 6.21 shows the comparison of $\mathrm{cov}(v_n\{2\}^2, [p_{\mathrm{T}}])$ in different p_{T} ranges. In 1-subvent method, both EPOS and Pythia 8 produce lower values than the experiment, with Pythia 8 is closer to the results from experiment at the lowest N_{ch}. These results in the 1-subevent covariance suggest a missing dynamics in simulations. However, in 2- and 3-subevents methods, they are in agreement with the measurement. Since these results match with Pythia 8, it is deduced that the 2- and 3-subevent methods contain mostly the residual non-flow contribution that arises from parton evolutions.

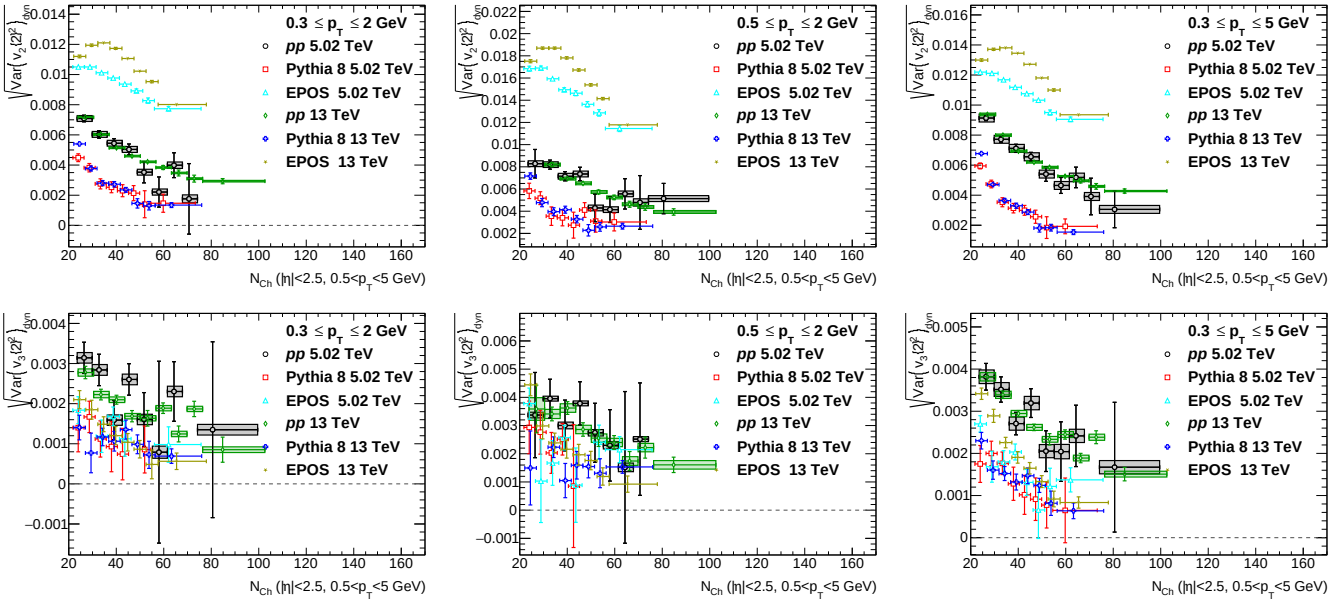

Figure 6.20: Comparison of $\mathrm{Var}\left(v_n\{2\}^2\right)_{\mathrm{dyn}}$ between pp and MC for various p_{T} ranges.

Figure 6.22 shows the comparison of $\rho(v_n\{2\}^2, [p_{\mathrm{T}}])$ in different p_{T} ranges. In the second harmonic, the EPOS overestimates $\mathrm{Var}\left(v_n\{2\}^2\right)_{\mathrm{dyn}}$ and underestimates c_k, while Pythia 8 does the opposite. Since the denominator is the square root of multiplication between $\mathrm{Var}\left(v_n\{2\}^2\right)_{\mathrm{dyn}}$ and c_k, the normalization produce the balance and the results are in agreement with experiment in 2- and 3-subevents method. The gaps in 1-subevent method are inherited from the results in $\mathrm{cov}(v_n\{2\}^2, [p_{\mathrm{T}}])$. For Pythia 8, the gaps become less significant in low N_{ch} after normalization. While for EPOS, the differences are still significant. In the third harmonic, for 1-subevent method, Pythia 8 agrees with the data while EPOS deviates at mid N_{ch}. For 2- and 3-subevents methods, the agreements are observed between the models and data as the short range correlation are reduced.

In Pythia, the impact of color reconnection and resonance decay to the correlation were tested. Figure 6.23 shows several observables contribute to $\rho(v_n\{2\}^2, [p_{\mathrm{T}}])$ are compared when the color reconnection or resonance decay is turned off. Turning off the resonance decay setting in Pythia has a miniscule impact to the correlation, while color reconnection has a significant impact when it is turned off. Furthermore, the color reconnection range parameter R is varied by 0 (turned off), 0.75, 1.8 (default), and 10. The probability of merging a parton branch with low p_{T} system increases with increasing R. The results for c_k, $\mathrm{cov}(v_n\{2\}^2, [p_{\mathrm{T}}])$, and $\rho(v_n\{2\}^2, [p_{\mathrm{T}}])$ are compared with data in Figures 6.24, 6.25, and 6.26. The ordering in c_k appears to follow the sequence of R from the lowest to the highest. At p_{T} ranges $0.3 \leq p_{\mathrm{T}} \leq 2$ and $0.5 \leq p_{\mathrm{T}} \leq 2$, the data favors $R \leq 0.75$ since the systems with low p_{T} are less likely merged in these low p_{T} ranges. However, in p_{T} range $0.3 \leq p_{\mathrm{T}} \leq 5$, the merging is favored by data.

In the covariance, for the second harmonic, the ordering flips in each p_T range for 1- and 2-subevents results. While in 3-subevents results, the ordering remains the same across different p_T ranges. For the third harmonic, the ordering is clear and remains the same in each p_T ranges for 1-subevent results. However, the boundaries of the ordering become unclear progressively from 2-subevents to 3-subevents results.

In $\rho(v_2\{2\}^2, [p_T])$, the ordering of R is the reverse of the ordering in c_k. For 1-subevent, the data favors $0.75 \leq R \leq 1.8$. While in 2- and 3-subevents, the default R matches the most with data. In $\rho(v_3\{2\}^2, [p_T])$, the impact of color reconnection is less significant since it happens right before hadronization while the source of the third harmonic is the initial state fluctuation of the participating partons.

For p-Pb, the result for 1-subevent method is compared to HIJING sample, while the 3-subevent method is compared to the results from IP-Glasma+MUSIC+UrQMD from the authors of reference [**?**] as shown in Figure 6.27. Both simulations are able to reproduce the same trend and values close to the results from experiment. Since HIJING is able to produce the similar results without hydrodynamics stage, the comparison suggests that the correlations arise mostly from non-flow parton interactions. Further additional physics in IP-Glasma+MUSIC+UrQMD, mainly the consideration of initial geometry and momentum anisotropy, improve the prediction, bringing them closer to experimental results. The result in 3-subevents method is also compared to the model from reference [**?**]. In this model, the initial state is using Glauber model simulated by GLISSANDO [**?**] and the 3+1D hydrodynamics simulation is modeled in reference [**?**]. The η range for particles entering $[p_T]$ is $|\eta| < 0.2$, while the one for $v_n\{2\}$ is $1.75 < |\eta| < 2.5$. Two scenarios for entropy deposition in the transverse plane are examined: the standard Glauber model, where entropy is placed at the locations of the participant nucleons, and the compact source model, where entropy is deposited between the two colliding nucleons. In the 0-20% centrality range, the r.m.s. radius of the fireball in the first scenario is roughly 1.5 fm, whereas in the second scenario, it is significantly smaller at about 0.9 fm. The second scenario where the source of entropy is located in the center-of-mass between of colliding nucleon is favored by experimental result.

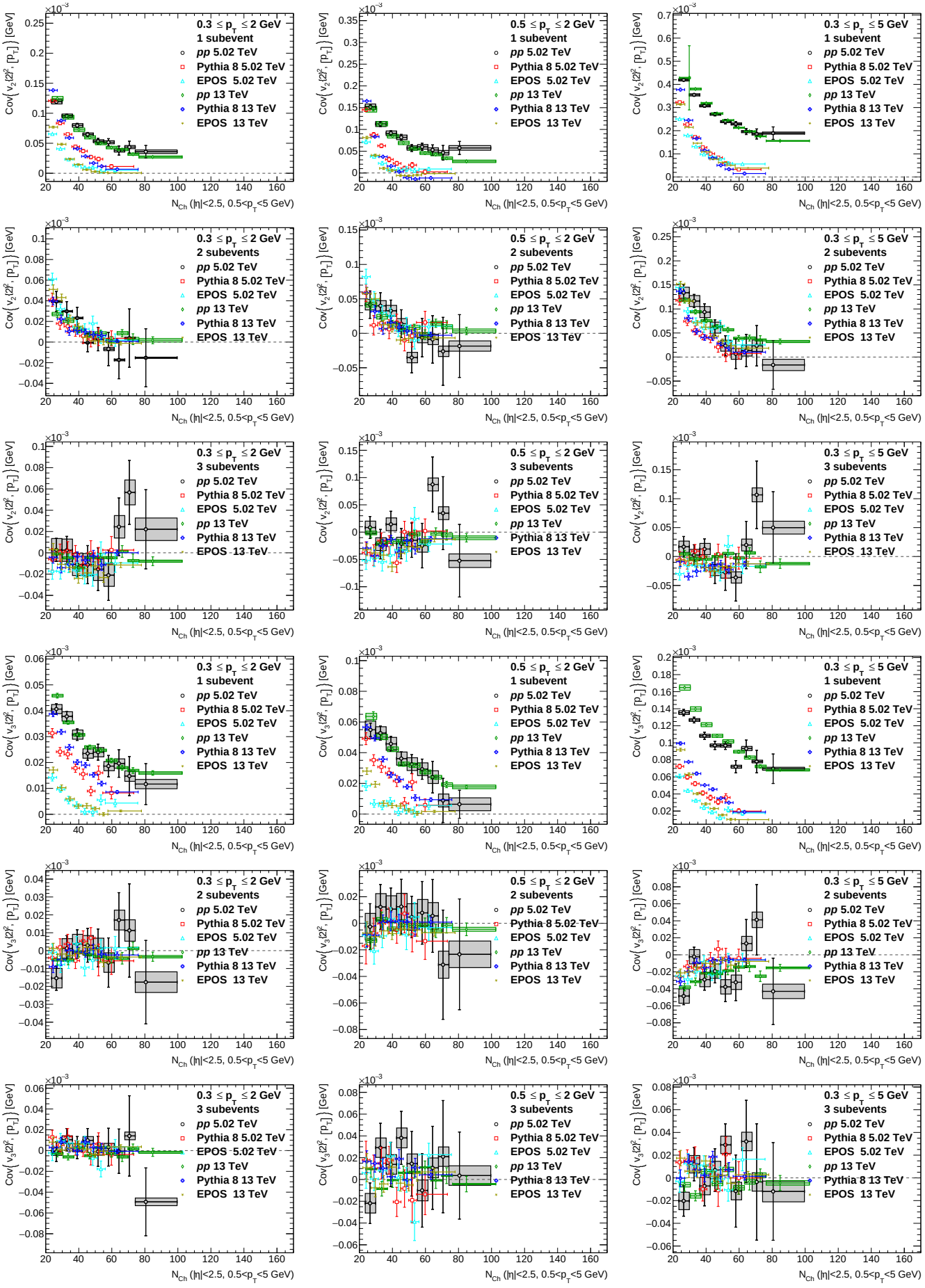

Figure 6.21: Comparison of $\mathrm{cov}(v_n\{2\}^2, [p_\mathrm{T}])$ between pp data and MC for in 1-,2-,3-subevents and different p_T ranges.

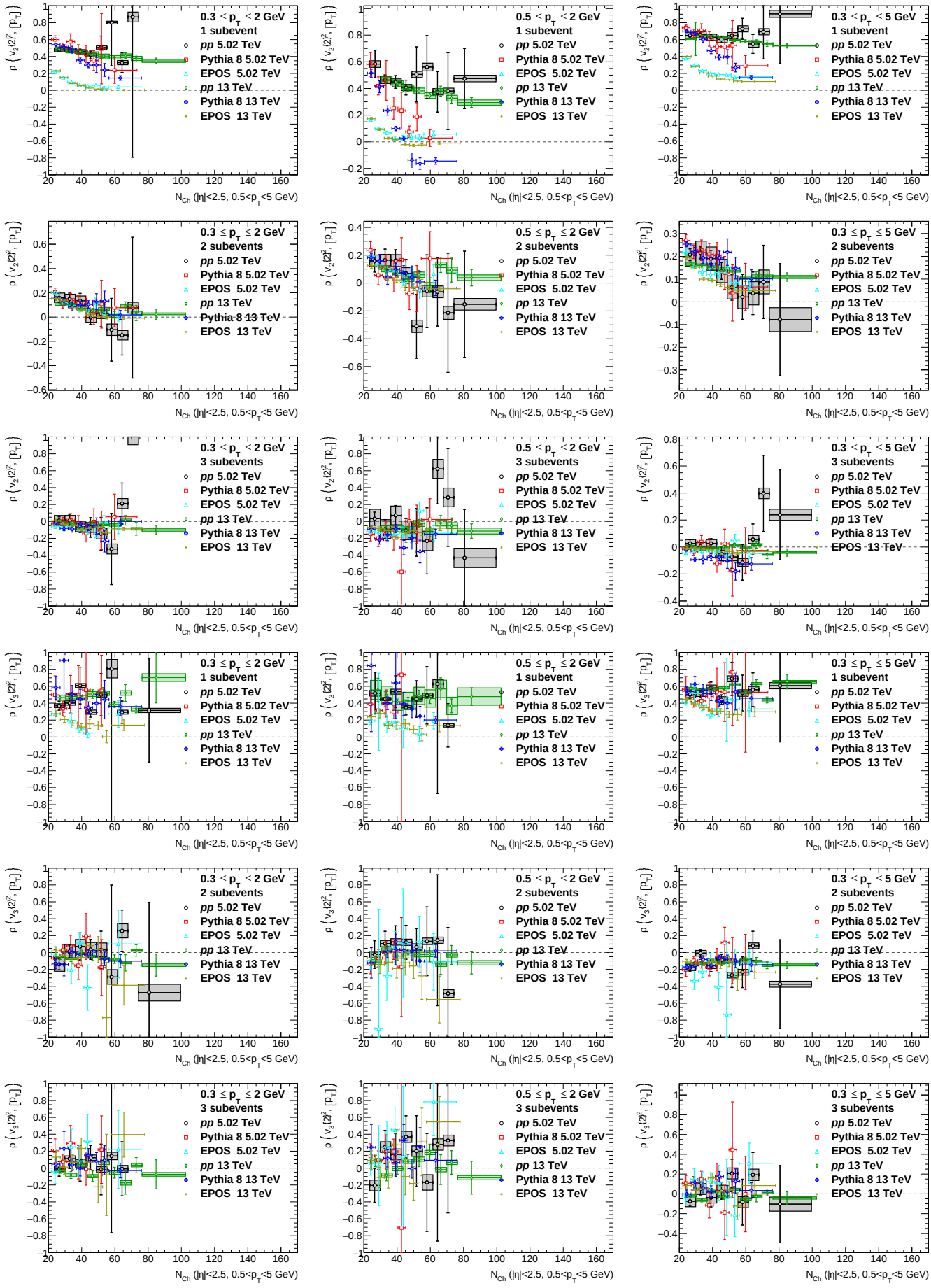

Figure 6.22: Comparison of $\rho(v_n\{2\}^2, [p_T])$ between pp data and MC for in 1-,2-,3-subevents and different p_T ranges.

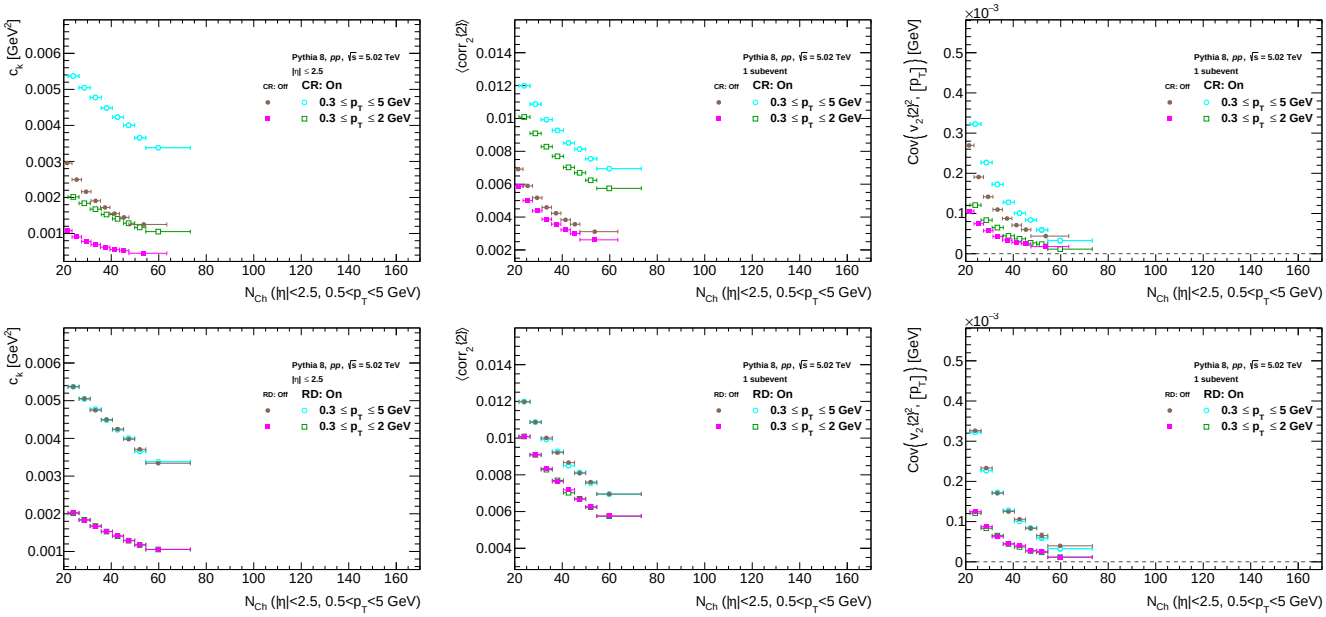

Figure 6.23: The Pythia 8 results when the color reconnection (top rows) or the resonance decay (bottom rows) settings is turned off.

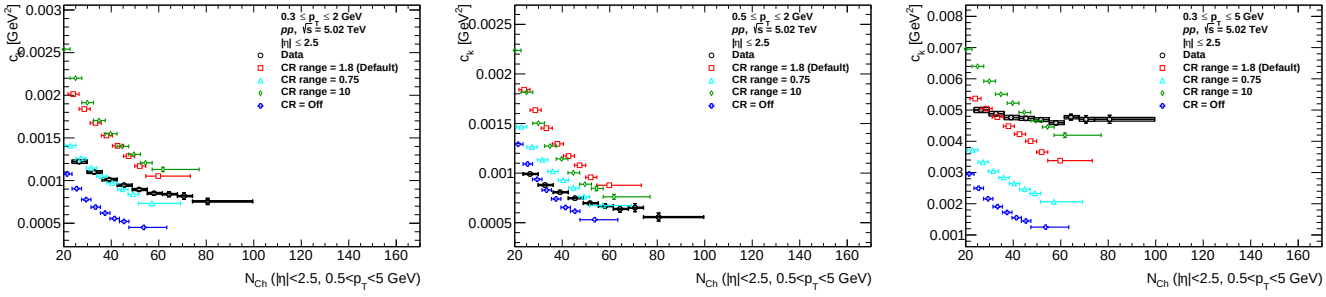

Figure 6.24: Comparison of c_k between pp and Pythia 8 with variation of color reconnection range parameters in various p_{T} ranges.

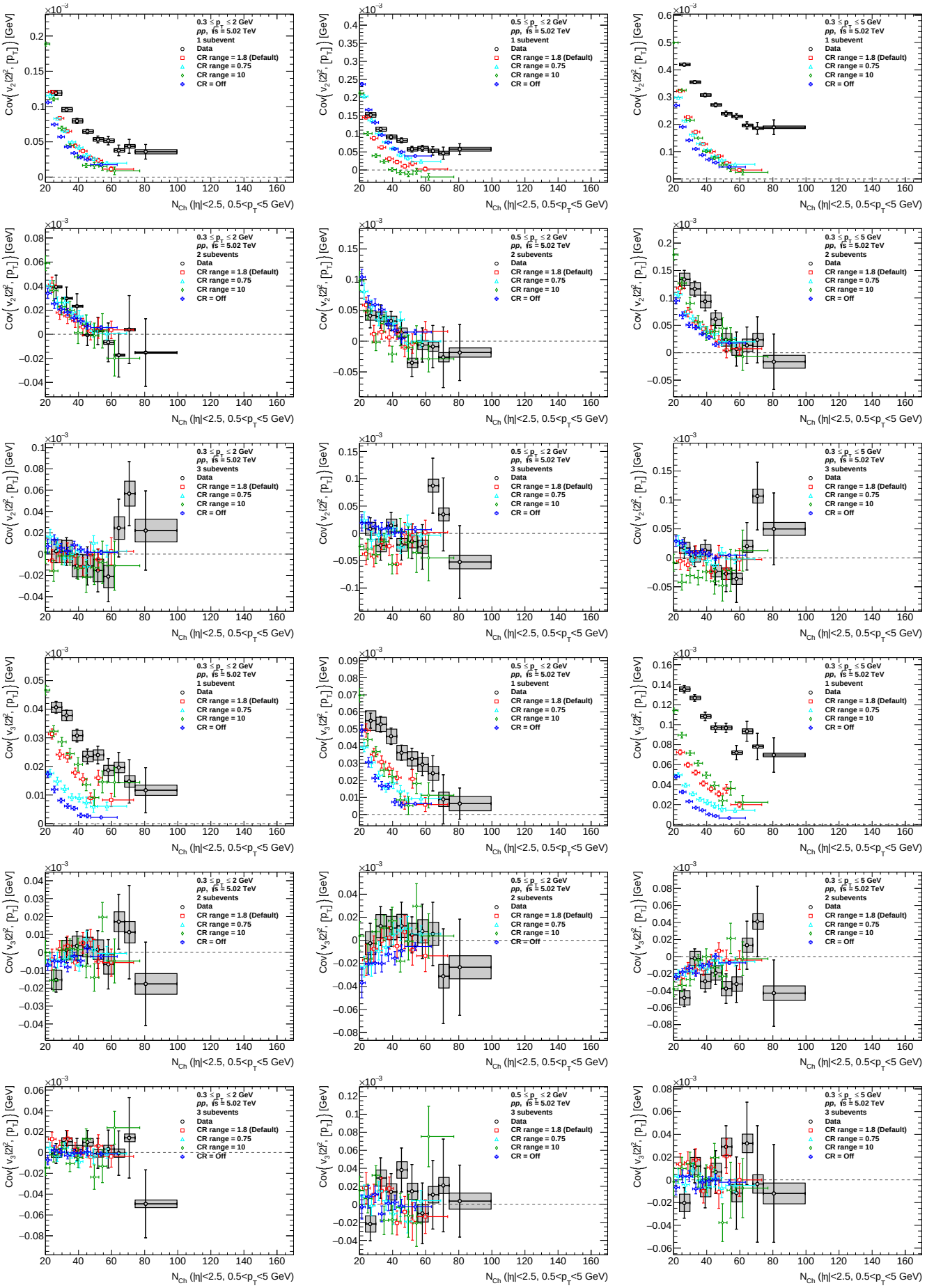

Figure 6.25: The $\mathrm{cov}(v_n\{2\}^2, [p_\mathrm{T}])$ and $\rho(v_n\{2\}^2, [p_\mathrm{T}])$ from Pythia 8 with variation of color reconnection range parameters, presented in 1-,2-,3-subevent and different same p_T ranges.

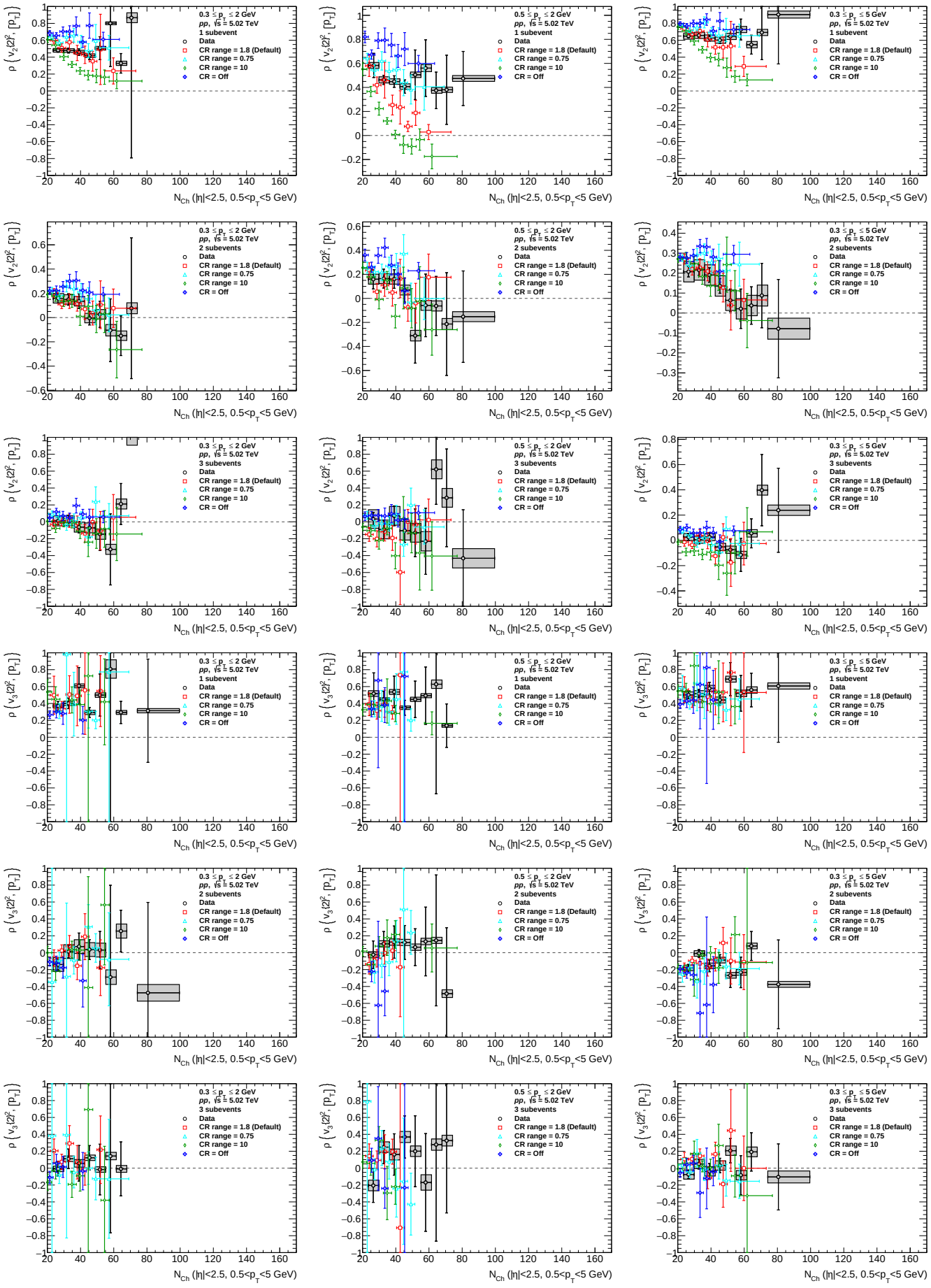

Figure 6.26: The $\mathrm{cov}(v_n\{2\}^2, [p_\mathrm{T}])$ and $\rho(v_n\{2\}^2, [p_\mathrm{T}])$ from Pythia 8 with variation of color reconnection range parameters, presented in 1-,2-,3-subevent and different same p_T ranges.

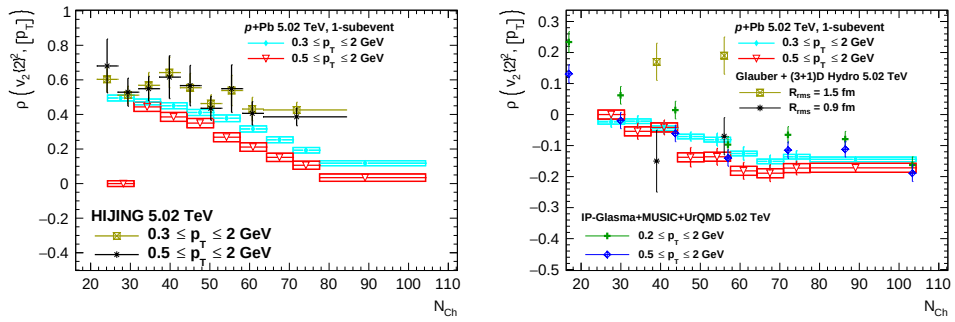

Figure 6.27: The comparison of $\rho(v_n\{2\}^2, [p_{\mathrm{T}}])$ in p-Pb 5.02 TeV. 1-subevent results are compared to HIJING while 3-subevents results are compared to IP-Glasma+MUSIC+UrQMD and Glauber+(3+1)D hydrodynamics from the authors of the models **[?]**[**?**].

7 Conclusion

The correlation coefficient $\rho(v_n\{2\}^2, [p_T])$ has been measured in pp at $\sqrt{s} = 5.02$ TeV, 13 TeV and $\sqrt{s_{NN}} = 5.02$ TeV in p-Pb. It has been obtained from various p_T intervals using 1-,2-, and 3-subevents methods that provide different degree of suppression of short range and non-flow correlations. In 1-subevent method, high positive values of coefficients for second and third harmonics were observed. The correlation obtained with 2- and 3-subevents methods are weaker.

The ρ constituents, covariance and normalising dynamical v_n variance and c_k are also presented. They exhibit the features consistent with the earlier measurement in Pb-Pb and p-Pb [**?**, **?**] for the same multiplicity range.

Within the uncertainties, results obtained for $\sqrt{s} = 13$ TeV are mostly compatible with those of pp at 5.02 TeV. The $\rho(v_n\{2\}^2, [p_T])$ obtained at pp $\sqrt{s} = 5.02$ TeV are also compared to measurement in p-Pb obtained at the same energy per nucleon. For the second harmonic, the correlation coefficients show a difference between pp and p-Pb at high N_{ch} which can be attributed to the difference in the initial geometry of collision. For the third harmonic, the correlation coefficients are found compatible with each other.

The results for pp are compared to Pythia 8 and EPOS. Pythia 8 does not contain any collective effect, while EPOS contains both collective effect, gluon saturation, and hadronic cascade which contribute to the value of v_n. The results in 1-subevent show some differences between data and MC simulations, suggesting different scheme of short-range correlation in pp data than in these MC simulations. Both Pythia 8 and EPOS results are able to reproduce overall decrease of $\rho(v_n\{2\}^2, [p_T])$ correlation coefficient calculated with 2- and 3-subevents. The comparisons suggest that the color reconnection from multi parton interactions dominate the $\rho(v_n\{2\}^2, [p_T])$ in pp. The color reconnection range parameter is constant throughout the simulation, while the experimental data favor different parameter for different kinematic ranges and multiplicity.

Comparison of p-Pb results to models was also performed with HIJING for 1-subevent method and IP-Glasma+MUSIC+UrQMD from reference [**?**] for 3-subevent methods, and a qualitative agreements were observed. HIJING manages to produce the same trend without hydrodynamics and CGC. The consideration of initial spatial geometry and momentum anisotropy in IP-Glasma+MUSIC+UrQMD improves the agreement with the data. The comparison with the result from reference [**?**] suggest that the source of entropy is located in the center-of-mass between of colliding nucleon.

These measurements will provide insights for the continued development of theoretical models and Monte Carlo simulations. Any discrepancy identified in the comparisons leads to further improvements of the accuracy and predictive power of the models. This process will enhance our understanding of the underlying physics and ensure better alignment between simulations and real-world observations.

A Single loop formula derivations

The definition of the c_k

$$c_k^{event} = \frac{1}{\Sigma_i \Sigma_{j\neq i} w_i w_j} \Sigma_i \Sigma_{j\neq i} w_i w_j (p_{\mathrm{T},i} - \langle [p_\mathrm{T}] \rangle)(p_{\mathrm{T},j} - \langle [p_\mathrm{T}] \rangle) \tag{A.1}$$

involves two double loops and thus can be computationally intensive for large N_{tracks}. It is however straightforward to find a single loop formulation as follows. For denominator:

$$\begin{aligned} \Sigma_i \Sigma_{j\neq i} w_i w_j &= \Sigma_i \Sigma_j w_i w_j - \Sigma_i \Sigma_{j=i} w_i w_j \\ &= \Sigma_i w_i \Sigma_j w_j - \Sigma_i w_i^2 \\ &= (\Sigma_i w_i)^2 - \Sigma_i w_i^2 \end{aligned} \tag{A.2}$$

The numerator

$$\begin{aligned} \Sigma_i \Sigma_{j\neq i} w_i w_j (p_{\mathrm{T},i} - \langle [p_\mathrm{T}] \rangle)(p_{\mathrm{T},j} - \langle [p_\mathrm{T}] \rangle) &= \Sigma_i \Sigma_j w_i w_j (p_{\mathrm{T},i} - \langle [p_\mathrm{T}] \rangle)(p_{\mathrm{T},j} - \langle [p_\mathrm{T}] \rangle) - \Sigma_i w_i^2 (p_{\mathrm{T},i} - \langle [p_\mathrm{T}] \rangle)^2 \\ &= \Sigma_i w_i (p_{\mathrm{T},i} - \langle [p_\mathrm{T}] \rangle) \Sigma_j w_j (p_{\mathrm{T},j} - \langle [p_\mathrm{T}] \rangle) \\ &- \langle [p_\mathrm{T}] \rangle^2 \Sigma_i w_i^2 - \Sigma_i w_i^2 p_{\mathrm{T},i}^2 + 2 \langle [p_\mathrm{T}] \rangle \Sigma_i w_i^2 p_{\mathrm{T},i} \\ &= (\Sigma_i w_i p_{\mathrm{T},i})^2 + (\langle [p_\mathrm{T}] \rangle^2 \Sigma_i w_i)^2 - 2 \langle [p_\mathrm{T}] \rangle \Sigma_i w_i p_{\mathrm{T},i} \\ &- \langle [p_\mathrm{T}] \rangle^2 \Sigma_i w_i^2 - \Sigma_i w_i^2 p_{\mathrm{T},i}^2 + 2 \langle [p_\mathrm{T}] \rangle \Sigma_i w_i^2 p_{\mathrm{T},i} \end{aligned} \tag{A.3}$$

The number of iterations for event with 50 tracks is thus reduced from 50×49 iterations to only 4×50.

A similar derivation is used in covariances and since there are three sums involved there, the performance gain is more significant.

B Derivation of direct flow calculation

The following sections are the derivation of the covariance, $\mathrm{Var}\left(v_n\{2\}^2\right)_{\mathrm{dyn}}$ and c_k terms in $\rho(v_n\{2\}^2, [p_{\mathrm{T}}])$ which have been done previously by the analysis team of reference [**?**]. First, we define the following quantities:

$$Q_{nk} = \sum_i w_i^k e^{in\phi_i} \tag{B.1}$$

$$S_{mk} = (\sum_i w_i^k)^m \tag{B.2}$$

$$O_{nk} = \sum_i w_i^k e^{in\phi_i} p_i \tag{B.3}$$

$$P_{mk} = \sum_i w_i^k p_i^m \tag{B.4}$$

$$\langle p \rangle = \frac{1}{N_{ev}} \sum_{evts} \frac{\sum_i w_i p_i}{\sum_i w_i} \tag{B.5}$$

$$\bar{p}_i = p_i - \langle p \rangle \tag{B.6}$$

$$\bar{O}_{nk} = \sum_i w_i^k e^{in\phi_i} \bar{p}_i = O_{nk} - Q_{nk}\langle p \rangle \tag{B.7}$$

$$\bar{P}_{mk} = \sum_i w_i^k \bar{p}_i^m \tag{B.8}$$

Note $P_{0k} \equiv S_{1k}$, and there is the following simple relation that are handy for our purpose later:

$$\bar{P}_{1k} = P_{1k} - S_{1k}\langle p \rangle \tag{B.9}$$

$$\bar{P}_{2k} = P_{2k} - 2P_{1k}\langle p \rangle + S_{1k}\langle p \rangle^2$$

$$\bar{P}_{3k} = P_{3k} - 3P_{2k}\langle p \rangle + 3P_{1k}\langle p \rangle^2 - S_{1k}\langle p \rangle^3 \tag{B.10}$$

B.1 Formula for Covariance

B.1.1 Standard (all-event) method

Let us derive the formula for the covariance in case of 1 subevent. Now the three particle correlation of the $\mathrm{cov}(v_n 2^2, [p_\mathrm{T}])$ is given as:

$$\mathrm{cov}(v_n 2^2, [p_\mathrm{T}]) = \frac{\sum_i \sum_j' \sum_h' w_i w_j w_h e^{in(\phi_i - \phi_j)}(p_h - \langle p \rangle)}{\sum_i \sum_j' \sum_h' w_i w_j w_h} \tag{B.11}$$

First lets expand the denominator:

$$\begin{aligned} D &= \sum_i \sum_j \sum_h w_i w_j w_h - 3 \sum_i \sum_j{}' w_i^2 w_j - \sum_i w_i^3 \\ &= S_{31} - 3[\sum_i \sum_j w_i^2 w_j - \sum_i w_i^3] - S_{13} \\ &= S_{31} - 3S_{12}S_{11} + 3S_{13} - S_{13} \\ &= S_{31} - 3S_{12}S_{11} + 2S_{13} \end{aligned}$$

Next lets expand the numerator:

$$\begin{aligned} N =& \sum_i \sum_j \sum_h w_i w_j w_h e^{in(\phi_i - \phi_j)}(p_h - \langle p \rangle) - \sum_i \sum_h{}' w_i^2 w_h (p_h - \langle p \rangle) \\ & - 2 \sum_i \sum_j{}' w_i^2 w_j e^{in(\phi_i - \phi_j)}(p_i - \langle p \rangle) - \sum_i w_i^3 (p_i - \langle p \rangle) \\ =& |Q_{n1}|^2 P_{11} - |Q_{n1}|^2 S_{11}\langle p \rangle - \{\sum_i \sum_h w_i^2 w_h (p_h - \langle p \rangle) - \sum_i w_i^3 (p_i - \langle p \rangle)\} \\ & - 2\{\sum_i \sum_j w_i^2 w_j e^{in(\phi_i - \phi_j)}(p_i - \langle p \rangle) - \sum_i w_i^3 (p_i - \langle p \rangle)\} - P_{13} + S_{13}\langle p \rangle \\ =& |Q_{n1}|^2 P_{11} - |Q_{n1}|^2 S_{11}\langle p \rangle - S_{12}P_{11} + S_{12}S_{11}\langle p \rangle + P_{13} - S_{13}\langle p \rangle \\ & - 2\Re(O_{n2}Q_{n1}^*) + 2\Re(Q_{n2}Q_{n1}^*)\langle p \rangle + 2P_{13} - 2S_{13}\langle p \rangle - P_{13} + S_{13}\langle p \rangle \\ =& |Q_{n1}|^2 P_{11} - S_{12}P_{11} - 2\Re(O_{n2}Q_{n1}^*) + 2P_{13} \\ & - \langle p \rangle \{|Q_{n1}|^2 S_{11} - S_{12}S_{11} - 2\Re(Q_{n2}Q_{n1}^*) + 2S_{13}\} \end{aligned}$$

So the covariance for the standard method becomes:

$$Cov[FSE] = \frac{|Q_{n1}|^2 P_{11} - S_{12}P_{11} - 2\Re(O_{n2}Q_{n1}^*) + 2P_{13}}{S_{31} - 3S_{12}S_{11} + 2S_{13}} \tag{B.12}$$

$$- \langle p \rangle \frac{|Q_{n1}|^2 S_{11} - S_{12}S_{11} - 2\Re(Q_{n2}Q_{n1}^*) + 2S_{13}}{S_{31} - 3S_{12}S_{11} + 2S_{13}} \tag{B.13}$$

or in terms of $\bar{p}$:

$$Cov[FSE] = \frac{|Q_{n1}|^2 \bar{P}_{11} - S_{12}\bar{P}_{11} - 2\Re(\bar{O}_{n2}Q_{n1}^*) + 2\bar{P}_{13}}{S_{31} - 3S_{12}S_{11} + 2S_{13}} \tag{B.14}$$

B.1.2 Two-subevent

The three particle correlation of the $\mathrm{cov}(v_n 2^2, [p_\mathrm{T}])$ is given as:

$$\mathrm{cov}(v_n 2^2, [p_\mathrm{T}]) = \frac{\sum_i \sum_j \sum'_h w_i w_j w_h e^{in(\phi_i - \phi_j)}(p_h - \langle p \rangle)}{\sum_i \sum_j \sum'_h w_i w_j w_h} \tag{B.15}$$

In 2-subevent case the particle i and j belong to two different subevents - A and C and are never the same.
The expansion of denominator:

$$\begin{aligned} D &= \sum_i \sum_j \sum_h w_i w_j w_h - \sum_i \sum_j w_i^2 w_j - \sum_i \sum_j w_i w_j^2 \\ &= S_{A11} S_{C11} S_{11} - S_{A12} S_{C11} - S_{A11} S_{C12} \end{aligned}$$

The expansion of numerator:

$$\begin{aligned} N =& \sum_i \sum_j \sum_h w_i w_j w_h e^{in(\phi_i - \phi_j)}(p_h - \langle p \rangle) - \sum_i \sum_j w_i^2 w_j e^{in(\phi_i - \phi_j)}(p_i - \langle p \rangle) - \sum_i \sum_j w_i w_j^2 e^{in(\phi_i - \phi_j)}(p_j - \langle p \rangle) \\ =& \Re(Q_{An1} Q^*_{Cn1}) P_{11} - \Re(Q_{An1} Q^*_{Cn1}) S_{11} \langle p \rangle - \Re(O_{An2} Q^*_{Cn1}) + \langle p \rangle \Re(Q_{An2} Q^*_{Cn1}) \\ & - \Re(Q_{An1} O^*_{Cn2}) + \langle p \rangle \Re(Q_{An1} Q^*_{Cn2}) \\ =& \Re(Q_{An1} Q^*_{Cn1}) P_{11} - \Re(O_{An2} Q^*_{Cn1}) - \Re(Q_{An1} O^*_{Cn2}) \\ & - \langle p \rangle \{ \Re(Q_{An1} Q^*_{Cn1}) S_{11} - \Re(Q_{An2} Q^*_{Cn1}) - \Re(Q_{An1} Q^*_{Cn2}) \} \end{aligned}$$

So the covariance for the 2-subevent becomes:

$$Cov[2SE] = \frac{\Re(Q_{An1} Q^*_{Cn1}) P_{11} - \Re(O_{An2} Q^*_{Cn1}) - \Re(Q_{An1} O^*_{Cn2})}{S_{A11} S_{C11} S_{11} - S_{A12} S_{C11} - S_{A11} S_{C12}} \tag{B.16}$$

$$- \langle p \rangle \frac{\Re(Q_{An1} Q^*_{Cn1}) S_{11} - \Re(Q_{An2} Q^*_{Cn1}) - \Re(Q_{An1} Q^*_{Cn2})}{S_{A11} S_{C11} S_{11} - S_{A12} S_{C11} - S_{A11} S_{C12}} \tag{B.17}$$

or in terms of $\bar{p}$:

$$Cov[2SE] = \frac{\Re(Q_{An1} Q^*_{Cn1}) \bar{P}_{11} - \Re(\bar{O}_{An2} Q^*_{Cn1}) - \Re(Q_{An1} \bar{O}^*_{Cn2})}{S_{A11} S_{C11} S_{11} - S_{A12} S_{C11} - S_{A11} S_{C12}} \tag{B.18}$$

B.1.3 Three-subevent

The three particle correlation of the $\mathrm{cov}(v_n 2^2, [p_\mathrm{T}])$ is given as:

$$\mathrm{cov}(v_n 2^2, [p_\mathrm{T}]) = \frac{\sum_i \sum_j \sum_h w_i w_j w_h e^{in(\phi_i - \phi_j)}(p_h - \langle p \rangle)}{\sum_i \sum_j \sum_h w_i w_j w_h} \tag{B.19}$$

In three-subevent case the particle i and j belong to two different subevents - A and C and particle h is from the subevent B. The i,j, and h particle are never the same.

The expansion of denominator:

$$\begin{aligned} D &= \sum_i \sum_j \sum_h w_i w_j w_h \\ &= S_{A11} S_{C11} S_{B11} \end{aligned}$$

The expansion of numerator:

$$\begin{aligned} N =& \sum_i \sum_j \sum_h w_i w_j w_h e^{in(\phi_i - \phi_j)} (p_h - \langle p \rangle) \\ =& \Re(Q_{An1} Q^*_{Cn1}) P_{B11} - \Re(Q_{An1} Q^*_{Cn1}) S_{B11} \langle p \rangle \end{aligned}$$

So the covariance for the three-subevent becomes:

$$Cov[3SE] = \frac{\Re(Q_{An1} Q^*_{Cn1}) P_{B11} - \langle p \rangle \Re(Q_{An1} Q^*_{Cn1}) S_{B11}}{S_{A11} S_{C11} S_{B11}} \tag{B.20}$$

or in terms of $\bar{p}$:

$$Cov[3SE] = \frac{\Re(Q_{An1} Q^*_{Cn1}) \bar{P}_{B11}}{S_{A11} S_{C11} S_{B11}} \tag{B.21}$$

B.2 Formula for c_k

B.2.1 Standard

Let us derive the formula for the c_k in case of 1 subevent. The two particle correlation is given as:

$$c_k = \frac{\sum_i \sum'_j w_i w_j (p_i - \langle p \rangle)(p_j - \langle p \rangle)}{\sum_i \sum'_j w_i w_j} \tag{B.22}$$

The expansion of the denominator:

$$\begin{aligned} D =& \sum_i \sum_j w_i w_j - \sum_i w_i^2 \\ =& S_{21} - S_{12} \end{aligned}$$

The expansion of numerator:

$$\begin{aligned} N =& \sum_i \sum_j w_i w_j (p_i - \langle p \rangle)(p_j - \langle p \rangle) - \sum_i w_i^2 (p_i - \langle p \rangle)^2 \\ =& \sum_i \sum_j w_i w_j \{p_i p_j - \langle p \rangle p_i - \langle p \rangle p_j + \langle p \rangle^2\} - \sum_i w_i^2 \{p_i^2 + \langle p \rangle^2 - 2 p_i \langle p \rangle\} \\ =& P_{11}^2 - 2\langle p \rangle P_{11} S_{11} + \langle p \rangle^2 S_{21} - P_{22} - \langle p \rangle^2 S_{12} + 2\langle p \rangle P_{12} \\ =& P_{11}^2 - P_{22} - 2\langle p \rangle (P_{11} S_{11} - P_{12}) + \langle p \rangle^2 (S_{21} - S_{12}) \end{aligned}$$

So the c_k is:

$$c_k = \frac{P_{11}^2 - P_{22} - 2\langle p\rangle(P_{11}S_{11} - P_{12}) + \langle p\rangle^2(S_{21} - S_{12})}{S_{21} - S_{12}} \tag{B.23}$$

or in terms of $\bar{p}$ (We should simply use this form since we can use Eq. (B.10)):

$$c_k = \frac{\bar{P}_{11}^2 - \bar{P}_{22}}{S_{21} - S_{12}} \tag{B.24}$$

B.2.2 Two-subevent

The two particle correlation is given as:

$$c_k = \frac{\sum_i \sum_j w_i w_j (p_i - \langle p\rangle_A)(p_j - \langle p\rangle_C)}{\sum_i \sum_j w_i w_j} \tag{B.25}$$

In 2-subevent case the particle i and j belong to two different subevents - A and C and are never the same.
The expansion of the denominator:

$$\begin{aligned} D =& \sum_i \sum_j w_i w_j \\ =& S_{A11} * S_{C11} \end{aligned}$$

The expansion of numerator:

$$\begin{aligned} N =& \sum_i \sum_j w_i w_j (p_i - \langle p\rangle_A)(p_j - \langle p\rangle_C) \\ =& \sum_i \sum_j w_i w_j \{p_i p_j - \langle p\rangle_C p_i - \langle p\rangle_A p_j + \langle p\rangle_A \langle p\rangle_C\} \\ =& P_{A11}P_{C11} - \langle p\rangle_C P_{A11}S_{A11} - \langle p\rangle_A P_{C11}S_{C11} + \langle p\rangle_A \langle p\rangle_C S_{A11}S_{C11} \end{aligned}$$

So the c_k is:

$$c_k = \frac{P_{A11}P_{C11} - \langle p\rangle_C P_{A11}S_{A11} - \langle p\rangle_A P_{C11}S_{C11} + \langle p\rangle_A \langle p\rangle_C S_{A11}S_{C11}}{S_{A11} * S_{C11}} \tag{B.26}$$

or in terms of $\bar{p}$:

$$c_k = \frac{\bar{P}_{A11} * \bar{P}_{C11}}{S_{A11} * S_{C11}} \tag{B.27}$$

B.3 Formula for $\mathrm{Var}\left(v_n\{2\}^2\right)_{\mathrm{dyn}}$

The variance of $v_n\{2\}^2$ is given by:

$$\mathrm{Var}(v_n 2^2) = \langle 4\rangle - \langle 2\rangle^2 \tag{B.28}$$

where $\langle 2 \rangle$ is the 2-particle correlation and $\langle 4 \rangle$ is the 4-particle correlation in an event.

B.3.1 Standard

Two-particle correlation:

$$\langle 2 \rangle = \frac{\sum_i \sum_j' w_i w_j e^{in(\phi_i - \phi_j)}}{\sum_i \sum_j' w_i w_j} \tag{B.29}$$

$$= \frac{\sum_i \sum_j w_i w_j e^{in(\phi_i - \phi_j)} - \sum_i w_i^2}{\sum_i \sum_j w_i w_j - \sum_i w_i^2} \tag{B.30}$$

$$= \frac{|Q_{11}|^2 - S_{12}}{S_{21} - S_{12}} \tag{B.31}$$

Four-particle correlation:

$$\langle 4 \rangle = \frac{\sum_i \sum_j' \sum_h' \sum_l' w_i w_j w_h w_l e^{in(\phi_i + \phi_j - \phi_h - \phi_l)}}{\sum_i \sum_j' \sum_h' \sum_l' w_i w_j w_h w_l} \tag{B.32}$$

The denominator can be expanded as:

$$\begin{aligned}
D &= \sum_i \sum_j' \sum_h' \sum_l' w_i w_j w_h w_l \\
&= \sum_i \sum_j \sum_h \sum_l w_i w_j w_h w_l - 6 \sum_i \sum_j' \sum_h' w_i^2 w_j w_h - 4 \sum_i \sum_j' w_i^3 w_j - 3 \sum_i \sum_j' w_i^2 w_j^2 - \sum_i w_i^4 \\
&= S_{41} - 6(S_{12} S_{11} S_{11} - 2 \sum_i \sum_j' w_i^3 w_j - \sum_i \sum_j' w_i^2 w_j^2 - S_{14}) - 4(S_{13} S_{11} - S_{14}) - 3(S_{22} - S_{14}) - S_{14} \\
&= S_{41} - 4 S_{13} S_{11} - 3 S_{22} - 6 S_{21} S_{12} + 12 S_{14} + 12 \sum_i \sum_j' w_i^3 w_j + 6 \sum_i \sum_j' w_i^2 w_j^2 \\
&= S_{41} - 4 S_{13} S_{11} - 3 S_{22} - 6 S_{21} S_{12} + 12 S_{14} + 12 (S_{13} S_{11} - S_{14}) + 6 (S_{22} - S_{14}) \\
&= S_{41} + 8 S_{13} S_{11} + 3 S_{22} - 6 S_{21} S_{12} - 6 S_{14}
\end{aligned}$$

The numerator can be expanded as:

$$
\begin{aligned}
N &= \sum_i \sum_j{}' \sum_h{}' \sum_l{}' w_i w_j w_h w_l e^{in(\phi_i+\phi_j-\phi_h-\phi_l)} \\
&= \sum_i \sum_j \sum_h \sum_l w_i w_j w_h w_l e^{in(\phi_i+\phi_j-\phi_h-\phi_l)} - 4\sum_i \sum_j{}' \sum_h{}' w_i^2 w_j w_h e^{in(\phi_j-\phi_h)} \\
&- 2\sum_i \sum_j{}' \sum_h{}' w_i^2 w_j w_h e^{in(2\phi_i-\phi_j-\phi_h)} - 4\sum_i \sum_j{}' w_i^3 w_j e^{in(\phi_i-\phi_j)} \\
&- \sum_i \sum_j{}' w_i^2 w_j^2 e^{i2n(\phi_i-\phi_j)} - 2\sum_i \sum_j{}' w_i^2 w_j^2 - \sum_i w_i^4 \\
&= |Q_{11}|^4 - S_{14} \\
&- 4(S_{12}|Q_{11}|^2 - 2\sum_i \sum_j{}' w_i^3 w_j e^{in(\phi_i-\phi_j)} - \sum_i \sum_j{}' w_i^2 w_j^2 - S_{14}) \\
&- 2(Q_{22}Q_{11}^* Q_{11}^* - 2\sum_i \sum_j{}' w_i^3 w_j e^{in(\phi_i-\phi_j)} - \sum_i \sum_j{}' w_i^2 w_j^2 e^{i2n(\phi_i-\phi_j)} - S_{14}) \\
&- 4(Q_{13}Q_{11}^* - S_{14}) - (|Q_{22}|^2 - S_{14}) - 2(S_{22} - S_{14}) \\
&= |Q_{11}|^4 - |Q_{22}|^2 - 2Q_{22}Q_{11}^* Q_{11}^* - 4Q_{13}Q_{11}^* - 4S_{12}|Q_{11}|^2 - 2S_{22} + 12S_{14} \\
&+ 12\sum_i \sum_j{}' w_i^3 w_j e^{in(\phi_i-\phi_j)} + 2\sum_i \sum_j{}' w_i^2 w_j^2 e^{i2n(\phi_i-\phi_j)} + 4\sum_i \sum_j{}' w_i^2 w_j^2 \\
&= |Q_{11}|^4 - |Q_{22}|^2 - 2Q_{22}Q_{11}^* Q_{11}^* - 4Q_{13}Q_{11}^* - 4S_{12}|Q_{11}|^2 - 2S_{22} + 12S_{14} \\
&+ 12(Q_{13}Q_{11}^* - S_{14}) + 2(|Q_{22}|^2 - S_{14}) + 4(S_{22} - S_{14}) \\
&= |Q_{11}|^4 + |Q_{22}|^2 - 2Q_{22}Q_{11}^* Q_{11}^* + 8Q_{13}Q_{11}^* - 4S_{12}|Q_{11}|^2 + 2S_{22} - 6S_{14}
\end{aligned}
$$

So the final form of $\langle 4 \rangle$ is:

$$
\langle 4 \rangle = \frac{|Q_{11}|^4 + |Q_{22}|^2 - 2\Re(Q_{22}Q_{11}^* Q_{11}^*) + 8\Re(Q_{13}Q_{11}^*) - 4S_{12}|Q_{11}|^2 + 2S_{22} - 6S_{14}}{S_{41} + 8S_{13}S_{11} + 3S_{22} - 6S_{21}S_{12} - 6S_{14}} \tag{B.33}
$$

B.3.2 Two-subevent

Two-particle correlation:

$$
\langle 2 \rangle_{a|c} = \frac{\sum_i \sum_j w_i w_j e^{in(\phi_i-\phi_j)}}{\sum_i \sum_j w_i w_j} \tag{B.34}
$$

$$
= \frac{\Re(Q_{A11}Q_{C11}^*)}{S_{A11}S_{C11}} \tag{B.35}
$$

Particle i is from subevent A and particle j is from subevent C. Four-particle correlation:

$$\langle 4\rangle_{aa|cc} = \frac{\sum_i \sum_j' \sum_h \sum_l' w_i w_j w_h w_l e^{in(\phi_i+\phi_j-\phi_h-\phi_l)}}{\sum_i \sum_j' \sum_h \sum_l' w_i w_j w_h w_l} \tag{B.36}$$

Particle i and j are from subevent A and particle h and l are from subevent C. The denominator can be expanded as:

$$\begin{aligned}
D &= \sum_i \sum_j' \sum_h \sum_l' w_i w_j w_h w_l \\
&= \sum_i \sum_j \sum_h \sum_l w_i w_j w_h w_l - \sum_i \sum_h \sum_l' w_i^2 w_h w_l - \sum_i \sum_j' \sum_h w_i w_j w_h^2 - \sum_i \sum_h w_i^2 w_h^2 \\
&= S_{A21}S_{C21} - (S_{A12}S_{C21} - S_{A12}S_{C12}) - (S_{A21}S_{C12} - S_{A12}S_{C12}) - S_{A12}S_{C12} \\
&= S_{A21}S_{C21} - S_{A12}S_{C21} - S_{A21}S_{C12} + S_{A12}S_{C12} \\
&= (S_{A21} - S_{A12})(S_{C21} - S_{C12})
\end{aligned}$$

The numerator can be expanded as:

$$\begin{aligned}
N &= \sum_i \sum_j' \sum_h \sum_l' w_i w_j w_h w_l e^{in(\phi_i+\phi_j-\phi_h-\phi_l)} \\
&= \sum_i \sum_j \sum_h \sum_l w_i w_j w_h w_l e^{in(\phi_i+\phi_j-\phi_h-\phi_l)} \\
&- \sum_i \sum_h \sum_l' w_i^2 w_j w_h e^{in(2\phi_i-\phi_h-\phi_l)} \\
&- \sum_i \sum_j' \sum_h w_i w_j w_h^2 e^{in(\phi_i+\phi_j-2\phi_h)} \\
&- \sum_i \sum_h w_i^2 w_h^2 e^{in2(\phi_i-\phi_h)} \\
&= |Q_{A11}Q_{C11}^*|^2 - (Q_{A22}Q_{C11}^*Q_{C11}^* - Q_{A22}Q_{C22}^*) \\
&- (Q_{A11}Q_{A11}Q_{C22}^* - Q_{A22}Q_{C22}^*) - Q_{A22}Q_{C22}^* \\
&= |Q_{A11}Q_{C11}^*|^2 - Q_{A22}Q_{C11}^*Q_{C11}^* - Q_{A11}Q_{A11}Q_{C22}^* + Q_{A22}Q_{C22}^* \\
&= (Q_{A11}^2 - Q_{A22})(Q_{C11}^2 - Q_{C22})^*
\end{aligned}$$

So the final form of $\langle 4\rangle_{aa|cc}$ is:

$$\langle 4\rangle_{aa|cc} = \frac{\Re(Q_{A11}^2 - Q_{A22})\Re(Q_{C11}^{*2} - Q_{C22}^*)}{(S_{A21} - S_{A12})(S_{C21} - S_{C12})} \tag{B.37}$$

B.4 Formulae using q-vectors

Recall the definitions:

$$Q_{nk} = \sum_i w_i^k e^{in\phi_i} \tag{B.38}$$

$$S_{mk} = (\sum_i w_i^k)^m \tag{B.39}$$

$$O_{nk} = \sum_i w_i^k e^{in\phi_i} p_i \tag{B.40}$$

$$P_{mk} = \sum_i w_i^k p_i^m \tag{B.41}$$

$$\langle p \rangle = \frac{1}{N_{ev}} \sum_{evts} \frac{\sum_i w_i p_i}{\sum_i w_i} \tag{B.42}$$

Lets define some normalized quantities:

$$\hat{q}_{nk} = Q_{nk}/S_{1k} \tag{B.43}$$

$$\hat{o}_{nk} = O_{nk}/S_{1k} \tag{B.44}$$

$$\hat{p}_{nk} = P_{mk}/S_{1k} \tag{B.45}$$

$$\tau_k = \frac{\sum_i w_i^{k+1}}{(\sum_i w_i)^{k+1}} \tag{B.46}$$

$$= \frac{S_{1,k+1}}{S_{k+1,1}} \tag{B.47}$$

1. FSE 2-particle correlation:

$$\langle 2 \rangle = \frac{|Q_{11}|^2 - S_{12}}{S_{21} - S_{12}} \tag{B.48}$$

$$= \frac{|\hat{q}_{11}|^2 - S_{12}/S_{21}}{1 - S_{12}/S_{21}} \tag{B.49}$$

$$= \frac{|\hat{q}_{11}|^2 - \tau_1}{1 - \tau_1} \tag{B.50}$$

2. 2-SE 2-particle correlation:

$$\langle 2 \rangle_{a|c} = \frac{\Re(Q_{A11} Q_{C11}^*)}{S_{A11} S_{C11}} \tag{B.51}$$

$$= \Re(\hat{q}_{A11} \hat{q}_{C11}^*) \tag{B.52}$$

3. FSE 4-particle correlation:

$$\langle 4\rangle = \frac{|Q_{11}|^4 + |Q_{22}|^2 - 2\Re(Q_{22}Q_{11}^*Q_{11}^*) + 8\Re(Q_{13}Q_{11}^*) - 4S_{12}|Q_{11}|^2 + 2S_{22} - 6S_{14}}{S_{41} + 8S_{13}S_{11} + 3S_{22} - 6S_{21}S_{12} - 6S_{14}} \tag{B.53}$$

$$= \frac{|\hat{q}_{11}|^4 + \tau_1^2|\hat{q}_{22}|^2 - 2\tau_1\hat{q}_{22}\hat{q}_{11}^*\hat{q}_{11}^* + 8\tau_2\hat{q}_{13}\hat{q}_{11}^* - 4\tau_1|\hat{q}_{11}|^2 + 2\tau_1^2 - 6\tau_3}{1 + 8\tau_2 + 3\tau_1^2 - 6\tau_1 - 6\tau_3} \tag{B.54}$$

$$= \frac{|\hat{q}_{11}|^4 + \tau_1^2(2 + |\hat{q}_{22}|^2) - 2\tau_1(\hat{q}_{22}\hat{q}_{11}^*\hat{q}_{11}^* + 2|\hat{q}_{11}|^2) + 8\tau_2\hat{q}_{13}\hat{q}_{11}^* - 6\tau_3}{1 - 6\tau_1 + 8\tau_2 + 3\tau_1^2 - 6\tau_3} \tag{B.55}$$

4. 2-SE 4-particle correlation:

$$\langle 4\rangle_{aa|cc} = \frac{\Re(Q_{A11}^2 - Q_{A22})\Re(Q_{C11}^{*2} - Q_{C22}^*)}{(S_{A21} - S_{A12})(S_{C21} - S_{C12})} \tag{B.56}$$

$$= \frac{\Re(\hat{q}_{A11}^2 - \tau_{A1}\hat{q}_{A22})\Re(\hat{q}_{C11}^{*2} - \tau_{C1}\hat{q}_{C22}^*)}{(1 - \tau_{A1})(1 - \tau_{C1})} \tag{B.57}$$

5. 3-SE Covariance:

$$Cov[3SE] = \frac{\Re(Q_{An1}Q_{Cn1}^*)P_{B11} - \langle p\rangle\Re(Q_{An1}Q_{Cn1}^*)S_{B11}}{S_{A11}S_{C11}S_{B11}} \tag{B.58}$$

$$= \Re(\hat{q}_{An1}\hat{q}_{Cn1}^*)\hat{p}_{B11} - \langle p\rangle\Re(\hat{q}_{An1}\hat{q}_{Cn1}^*) \tag{B.59}$$

$$= \Re(\hat{q}_{An1}\hat{q}_{Cn1}^*)(\hat{p}_{B11} - \langle p\rangle) \tag{B.60}$$

6. FSE Covariance:

$$Cov[FSE] = \frac{|Q_{n1}|^2P_{11} - S_{12}P_{11} - 2\Re(O_{n2}Q_{n1}^*) + 2P_{13}}{S_{31} - 3S_{12}S_{11} + 2S_{13}} \tag{B.61}$$

$$- \langle p\rangle\frac{|Q_{n1}|^2S_{11} - S_{12}S_{11} - 2\Re(Q_{n2}Q_{n1}^*) + 2S_{13}}{S_{31} - 3S_{12}S_{11} + 2S_{13}} \tag{B.62}$$

$$= \frac{|\hat{q}_{n1}|^2\hat{p}_{11} - \tau_1\hat{p}_{11} - 2\tau_1\Re(\hat{o}_{n2}\hat{q}_{n1}^*) + 2\tau_2\hat{p}_{13}}{1 - 3\tau_1 + 2\tau_2} \tag{B.63}$$

$$- \langle p\rangle\frac{|\hat{q}_{n1}|^2 - \tau_1 - 2\tau_1\Re(\hat{q}_{n2}\hat{q}_{n1}^*) + 2\tau_2}{1 - 3\tau_1 + 2\tau_2} \tag{B.64}$$

$$= \frac{|\hat{q}_{n1}|^2(\hat{p}_{11} - \langle p\rangle) - \tau_1(\hat{p}_{11} - \langle p\rangle) - 2\tau_1(\Re(\hat{o}_{n2}\hat{q}_{n1}^*) - \langle p\rangle\Re(\hat{q}_{n2}\hat{q}_{n1}^*)) + 2\tau_2(\hat{p}_{13} - \langle p\rangle)}{1 - 3\tau_1 + 2\tau_2} \tag{B.65}$$

7. 2-SE Covariance:

$$Cov[2SE] = \frac{\Re(Q_{An1}Q^*_{Cn1})P_{11} - \Re(O_{An2}Q^*_{Cn1}) - \Re(Q_{An1}O^*_{Cn2})}{S_{A11}S_{C11}S_{11} - S_{A12}S_{C11} - S_{A11}S_{C12}} \tag{B.66}$$

$$- \langle p \rangle \frac{\Re(Q_{An1}Q^*_{Cn1})S_{11} - \Re(Q_{An2}Q^*_{Cn1}) - \Re(Q_{An1}Q^*_{Cn2})}{S_{A11}S_{C11}S_{11} - S_{A12}S_{C11} - S_{A11}S_{C12}} \tag{B.67}$$

$$= \frac{\Re(\hat{q}_{An1}\hat{q}^*_{Cn1})\hat{p}_{11} - \tau_{A1}(S_{A11}/S_{11})\Re(\hat{o}_{An2}\hat{q}^*_{Cn1}) - \tau_{C1}(S_{C11}/S_{11})\Re(\hat{q}_{An1}\hat{o}^*_{Cn2})}{1 - \tau_{A1}(S_{A11}/S_{11}) - \tau_{C1}(S_{C11}/S_{11})} \tag{B.68}$$

$$- \langle p \rangle \frac{\Re(\hat{q}_{An1}\hat{q}^*_{Cn1}) - \tau_{A1}(S_{A11}/S_{11})\Re(\hat{q}_{An2}\hat{q}^*_{Cn1}) - \tau_{C1}(S_{C11}/S_{11})\Re(\hat{q}_{An1}\hat{q}^*_{Cn2})}{1 - \tau_{A1}(S_{A11}/S_{11}) - \tau_{C1}(S_{C11}/S_{11})} \tag{B.69}$$

$$= \frac{\Re(\hat{q}_{An1}\hat{q}^*_{Cn1})\hat{p}_{11} - \tau_{A1}\alpha_A\Re(\hat{o}_{An2}\hat{q}^*_{Cn1}) - \tau_{C1}\alpha_C\Re(\hat{q}_{An1}\hat{o}^*_{Cn2})}{1 - \tau_{A1}\alpha_A - \tau_{C1}\alpha_C} \tag{B.70}$$

$$- \langle p \rangle \frac{\Re(\hat{q}_{An1}\hat{q}^*_{Cn1}) - \tau_{A1}\alpha_A\Re(\hat{q}_{An2}\hat{q}^*_{Cn1}) - \tau_{C1}\alpha_C\Re(\hat{q}_{An1}\hat{q}^*_{Cn2})}{1 - \tau_{A1}\alpha_A - \tau_{C1}\alpha_C} \tag{B.71}$$

$$= \Re(\hat{q}_{An1}\hat{q}^*_{Cn1})(\hat{p}_{11} - \langle p \rangle) - \tau_{A1}\alpha_A(\Re(\hat{o}_{An2}\hat{q}^*_{Cn1}) - \langle p \rangle\Re(\hat{q}_{An2}\hat{q}^*_{Cn1})) \tag{B.72}$$

$$\{-\tau_{C1}\alpha_C(\Re(\hat{q}_{An1}\hat{o}^*_{Cn2}) - \langle p \rangle\Re(\hat{q}_{An1}\hat{q}^*_{Cn2}))\}/\{1 - \tau_{A1}\alpha_A - \tau_{C1}\alpha_C\} \tag{B.73}$$

where $\alpha_A = S_{A11}/S_{11}$ and $\alpha_C = S_{C11}/S_{11}$.

C Correction for detector azimuthal non-uniformities

Two data-driven method are used in order to correct for detector azimuthal non-uniformities. In one approach the average complex $\langle q_n \rangle$ vectors are obtained for each of the sub-event and kinematic region. These values are then used to correct the q_n in every formula involving it. For example $q_n = \sum w_k \exp(-in\phi_k)$ is replaced by $\sum w_k[\exp(-in\phi_k) - \langle q_n \rangle]$. The $\langle q_n \rangle$ biases were obtained as a function of N_{tracks} but since no obvious trends were observed an average over whole range of the N_{tracks}, obtained via fitting a constant, was used. An example of biases for a p_{T} interval and 3 sub-events used in the analysis is show in Fig. C.1. As a closure test the $\langle q_n \rangle$ is obtained after correcting each q_n vector. The $\langle q_n \rangle (N_{\text{tracks}})$ is shown in Fig. C.2 for the same p_{T} interval and the same 3 sub-events. Figures C.3 and C.4 show the sets of

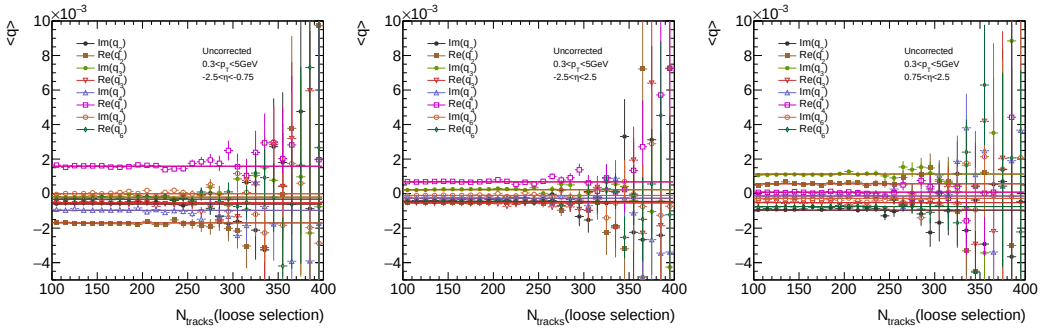

Figure C.1: Comparison of $\langle q_n \rangle (N_{\text{tracks}})$ for three sub-events, A - left, all - center, and C on the right. Fitted constant function are the mean values of q-biases used in the analysis.

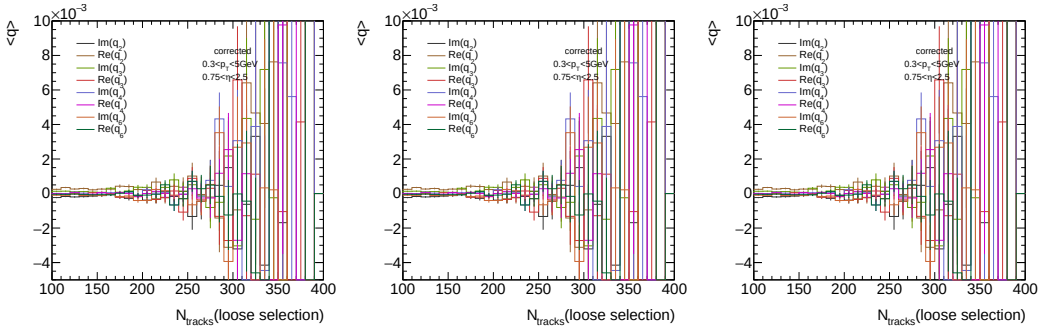

Figure C.2: Comparison of $\langle q_n \rangle (N_{\text{tracks}})$ for three sub-events, A - left, all - center, and C on the right after the mean $\langle q_n \rangle$ correction.

real and imaginary parts of the q-vectors samples for different p_{T} and η ranges before and after the corrections are applied.

Another method to correct azimuthal bias is to apply the weight to each track so that the weighted distribution in ϕ is exactly uniform. In this approach weights are obtained for ranges of track kinematics: $\Delta p_{\mathrm{T}} \times \Delta\eta \times \Delta\phi = [(0.2, 0.5), (0.5, 0.8), (0.8, 1.0), (1.0, 1.5), (1.5, 3.0), (3.0, 5.0)]\mathrm{GeV} \times 0.1 \times 2\pi/64$. They are chosen so that overall normalization in $\Delta\eta$ slices remains unchanged and therefore is equal to $w(p_{\mathrm{T}}, \eta, \phi) = N_{\mathrm{tracks}}(p_{\mathrm{T}}, \eta)/[N_{\mathrm{tracks}}(p_{\mathrm{T}}, \eta, \phi) * 64]$. For low momentum tracks the weight can be different for positively and negatively charged tracks and thus the procedure depends on the charge as well. Example map of flattening weights and $N_{\mathrm{tracks}}(\eta, \phi)$ before and after correction are show in Fig. C.5.

As a result of flattening the $\langle q_n \rangle$ biases should disappear. That is indeed the case as illustrated in Fig. C.6. (To be compared to the biases shown in Fig.C.1.)

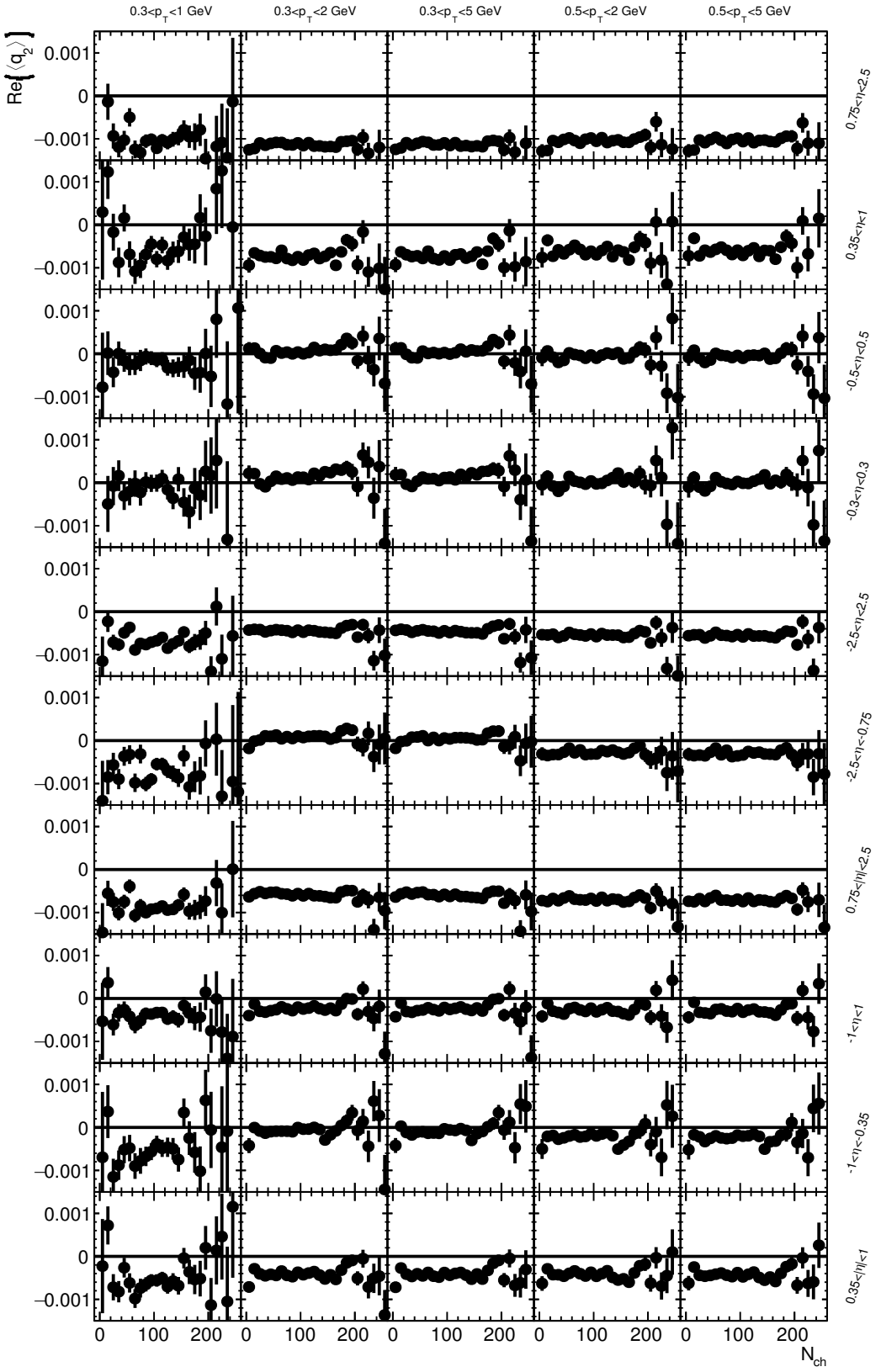

Figure C.3: Real part of q_2 for p+Pb 5.02 TeV before correction.

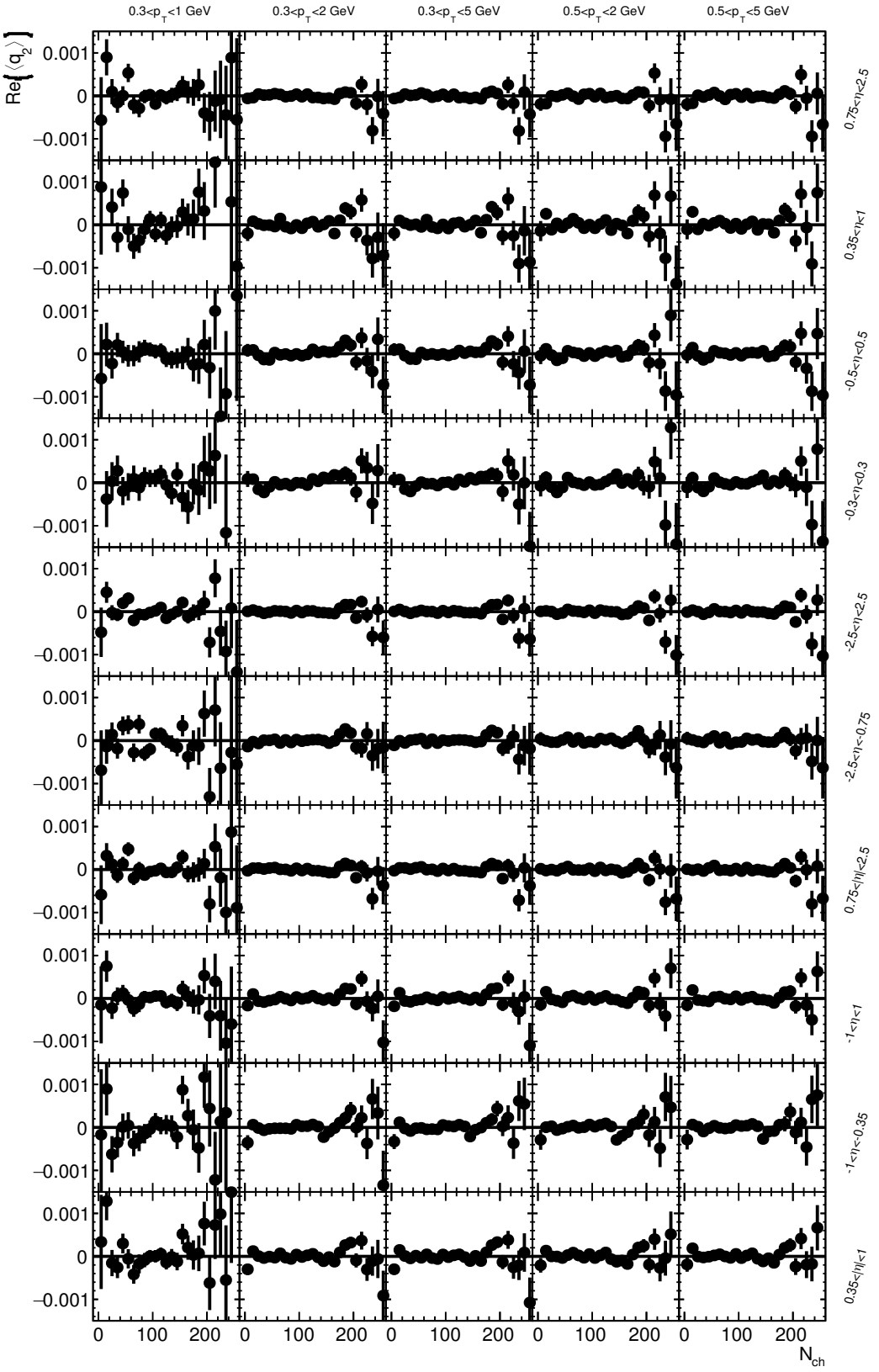

Figure C.4: Real part of q_2 for p+Pb 5.02 TeV after correction.

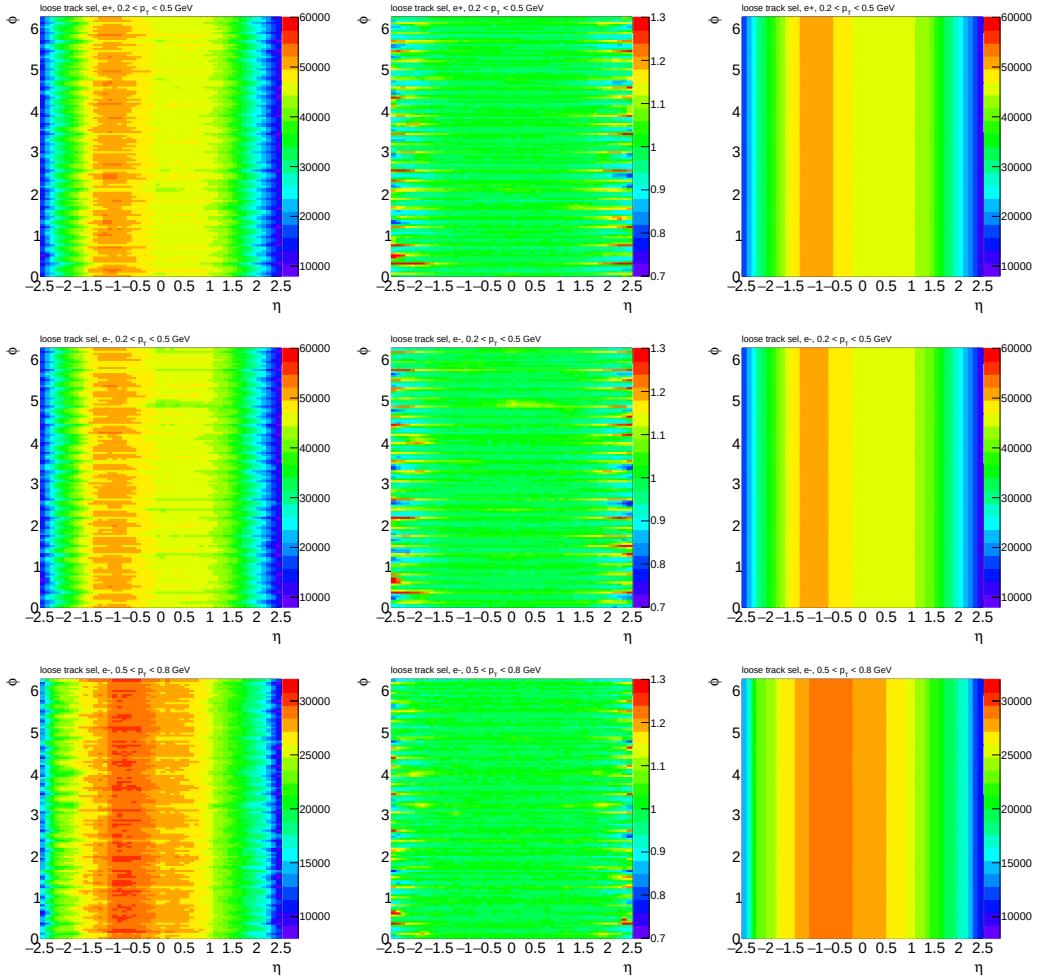

Figure C.5: $N_{\text{tracks}}(\eta, \phi)$ before (left) and after (right) the flattening procedure. In the middle the weight $w(\eta, \phi)$ are shown. The top row distributions for positively, the middle for negatively charged particles of $0.2 < p_{\text{T}} < 0.5$ GeV and the bottom row for negatively charged tracks of slightly higher p_{T} range 0.5-0.8 GeV.

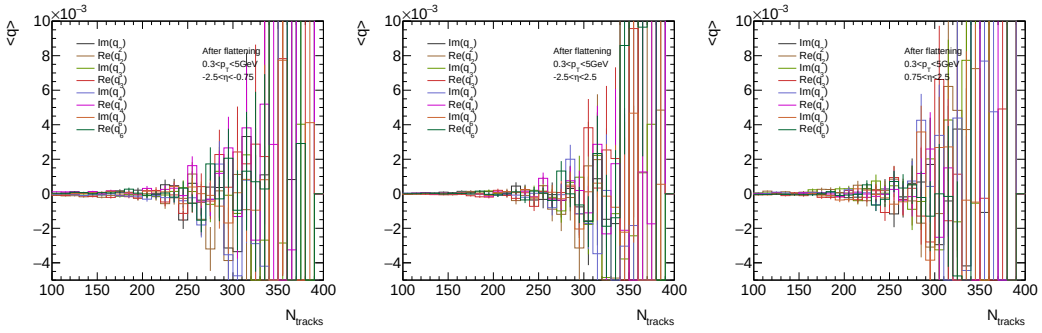

Figure C.6: The $\langle q_n \rangle (N_{\text{tracks}})$ obtained after applying flattening procedure for three sub-events, A - left, all - center, and C on the right.

D Systematic uncertainties figures

The differences between the baseline measurement and the systematic variations, and the value of statistical uncertainties (black lines) are presented in the following sections from Figure D.1-D.43.

D.1 $[p_{\mathrm{T}}]$ from systematic variations

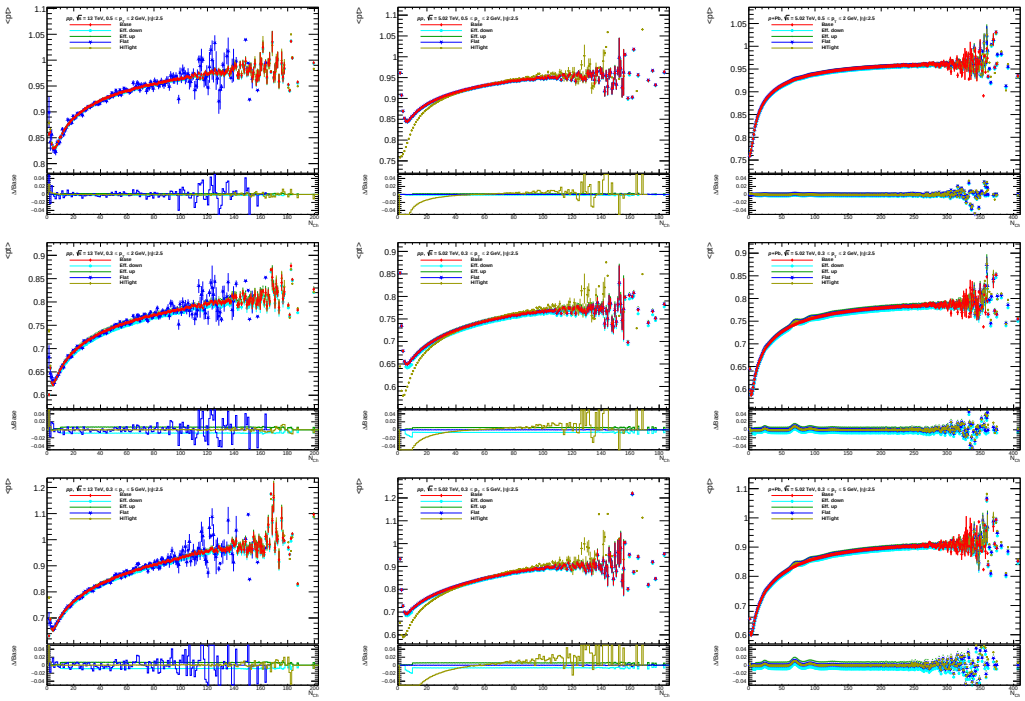

Figure D.1: The $[p_{\mathrm{T}}]$ of different systematic uncertainties sources and baseline measurement Δ_{source} in various p_{T} ranges.

D.2 Uncertainties on c_k

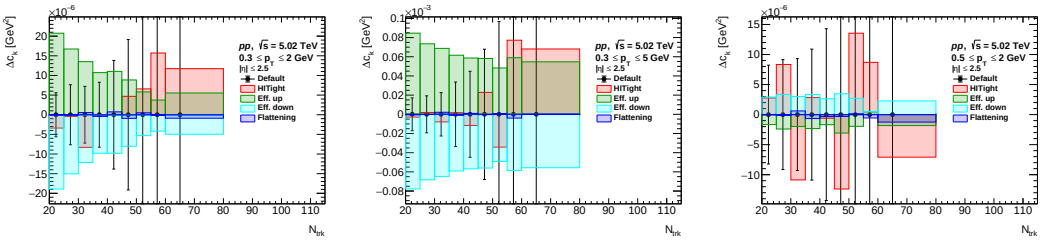

Figure D.2: Difference of c_k in pp 5.02 TeV between different systematic uncertainties sources and baseline measurement Δ_{source} in various p_{T} ranges, statistical uncertainty for baseline measurement is shown as a black line.

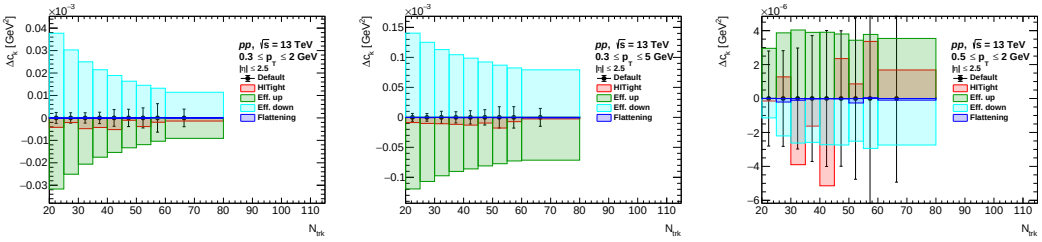

Figure D.3: Difference of c_k in pp 13 TeV between different systematic uncertainties sources and baseline measurement Δ_{source} in various p_{T} ranges, statistical uncertainty for baseline measurement is shown as a black line.

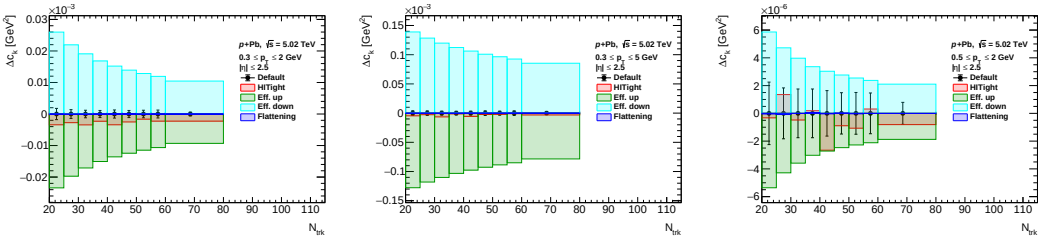

Figure D.4: Difference of c_k in p+Pb 5.02 TeV between different systematic uncertainties sources and baseline measurement Δ_{source} in various p_{T} ranges, statistical uncertainty for baseline measurement is shown as a black line.

D.3 Uncertainties on $\mathrm{Var}\left(v_2\{2\}^2\right)_{\mathrm{dyn}}$

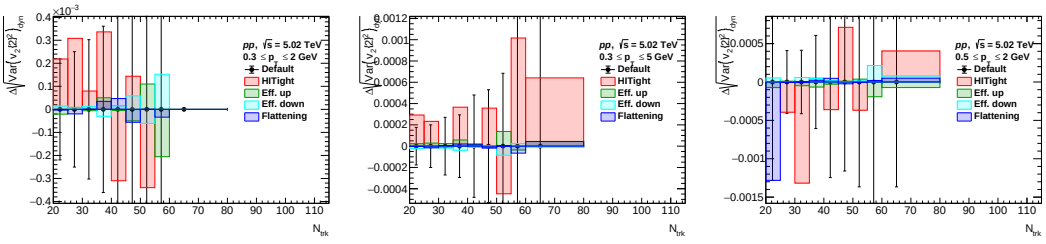

Figure D.5: Difference of 1-sub-event $\mathrm{Var}\left(v_2\{2\}^2\right)_{\mathrm{dyn}}$ in pp 5.02 TeV between different systematic uncertainties sources and baseline measurement Δ_{source} in various p_{T} ranges, statistical uncertainty for baseline measurement is shown as a black line.

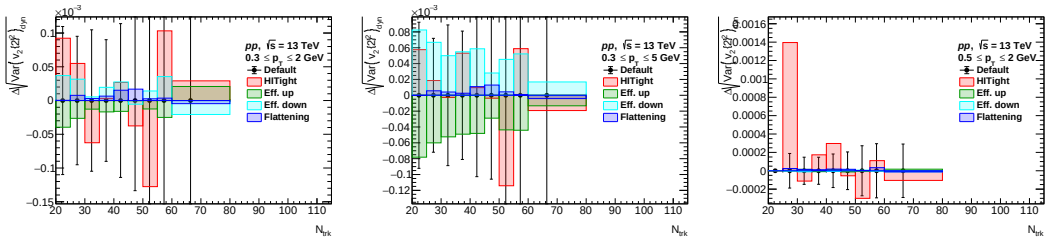

Figure D.6: Difference of $\mathrm{Var}(v_2\{2\}^2)_\mathrm{dyn}$ in pp 13 TeV between different systematic uncertainties sources and baseline measurement Δ_{source} in various p_T ranges, statistical uncertainty for baseline measurement is shown as a black line.

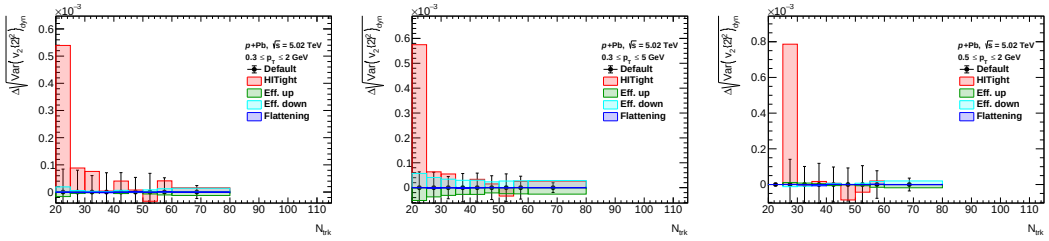

Figure D.7: Difference of $\mathrm{Var}(v_2\{2\}^2)_\mathrm{dyn}$ in p+Pb 5.02 TeV between different systematic uncertainties sources and baseline measurement Δ_{source} in various p_T ranges, statistical uncertainty for baseline measurement is shown as a black line.

D.4 Uncertainties on $\mathrm{cov}(v_2\{2\}^2, [p_\mathrm{T}])$

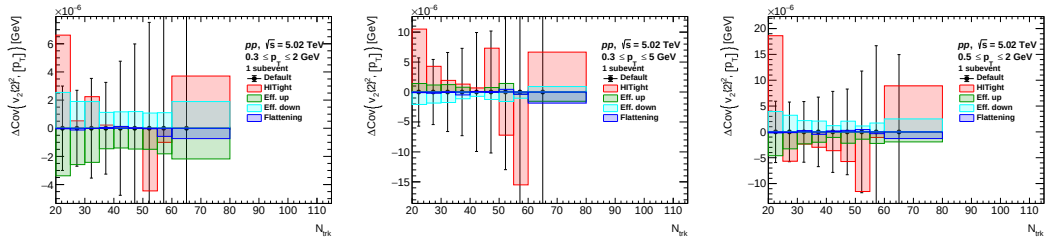

Figure D.8: Difference of 1-sub-event $\mathrm{cov}(v_2\{2\}^2, [p_\mathrm{T}])$ in pp 5.02 TeV between different systematic uncertainties sources and baseline measurement Δ_{source} in various p_T ranges, statistical uncertainty for baseline measurement is shown as a black line.

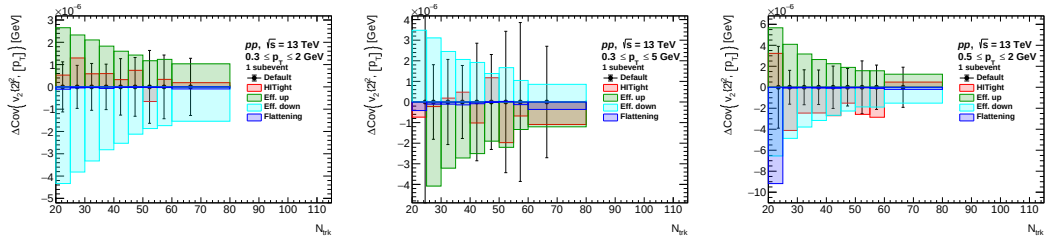

Figure D.9: Difference of 1-sub-event $\mathrm{cov}(v_2\{2\}^2, [p_\mathrm{T}])$ in pp 13 TeV between different systematic uncertainties sources and baseline measurement Δ_{source} in various p_T ranges, statistical uncertainty for baseline measurement is shown as a black line.

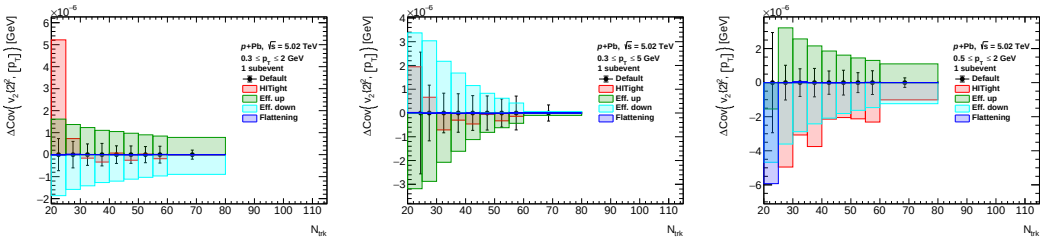

Figure D.10: Difference of 1-sub-event $\mathrm{cov}(v_2\{2\}^2, [p_\mathrm{T}])$ in p+Pb 5.02 TeV between different systematic uncertainties sources and baseline measurement Δ_{source} in various p_T ranges, statistical uncertainty for baseline measurement is shown as a black line.

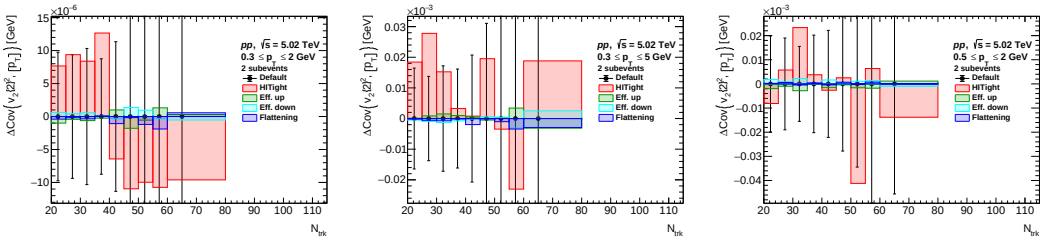

Figure D.11: Difference of 2-sub-event $\mathrm{cov}(v_2\{2\}^2, [p_\mathrm{T}])$ in pp 5.02 TeV between different systematic uncertainties sources and baseline measurement Δ_{source} in various p_T ranges, statistical uncertainty for baseline measurement is shown as a black line.

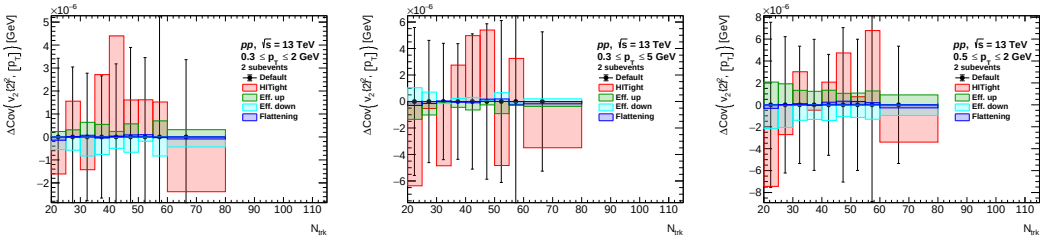

Figure D.12: Difference of 2-sub-event $\mathrm{cov}(v_2\{2\}^2, [p_\mathrm{T}])$ in pp 13 TeV between different systematic uncertainties sources and baseline measurement Δ_{source} in various p_T ranges, statistical uncertainty for baseline measurement is shown as a black line.

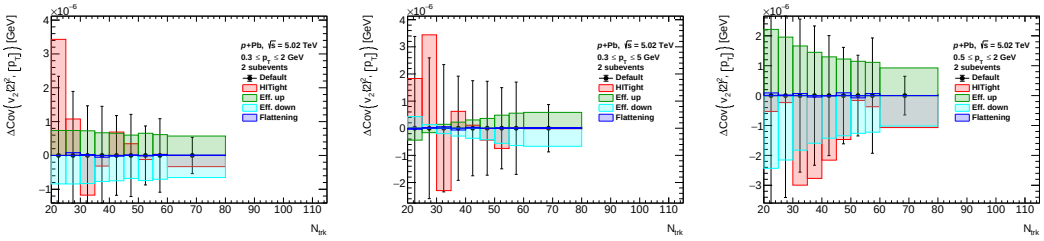

Figure D.13: Difference of 2-sub-event $\mathrm{cov}(v_2\{2\}^2, [p_\mathrm{T}])$ in p+Pb 5.02 TeV between different systematic uncertainties sources and baseline measurement Δ_{source} in various p_T ranges, statistical uncertainty for baseline measurement is shown as a black line.

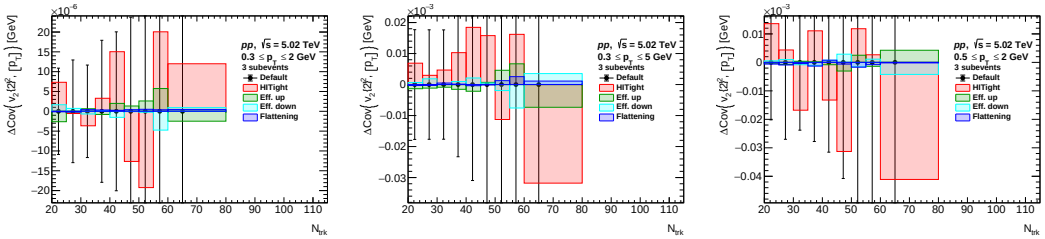

Figure D.14: Difference of 3-sub-event $\text{cov}(v_2\{2\}^2, [p_T])$ in pp 5.02 TeV between different systematic uncertainties sources and baseline measurement Δ_{source} in various p_T ranges, statistical uncertainty for baseline measurement is shown as a black line.

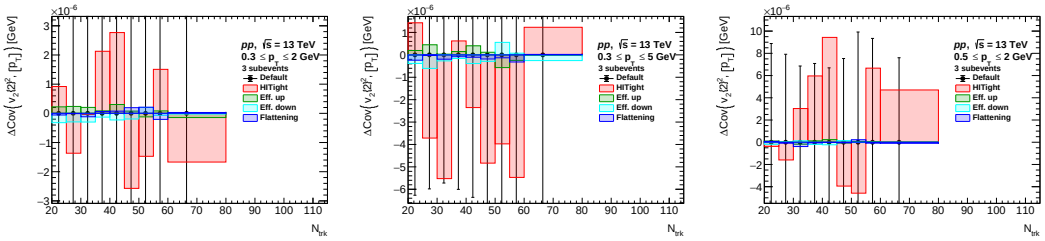

Figure D.15: Difference of 3-sub-event $\text{cov}(v_2\{2\}^2, [p_T])$ in pp 13 TeV between different systematic uncertainties sources and baseline measurement Δ_{source} in various p_T ranges, statistical uncertainty for baseline measurement is shown as a black line.

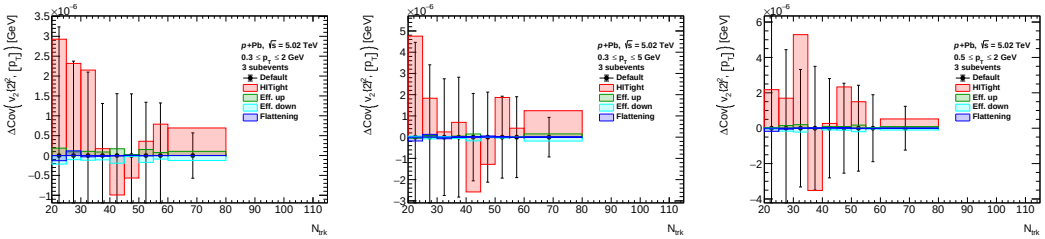

Figure D.16: Difference of 3-sub-event $\text{cov}(v_2\{2\}^2, [p_T])$ in p+Pb 5.02 TeV between different systematic uncertainties sources and baseline measurement Δ_{source} in various p_T ranges, statistical uncertainty for baseline measurement is shown as a black line.

D.5 Uncertainties on $\rho(v_2\{2\}^2, [p_T])$

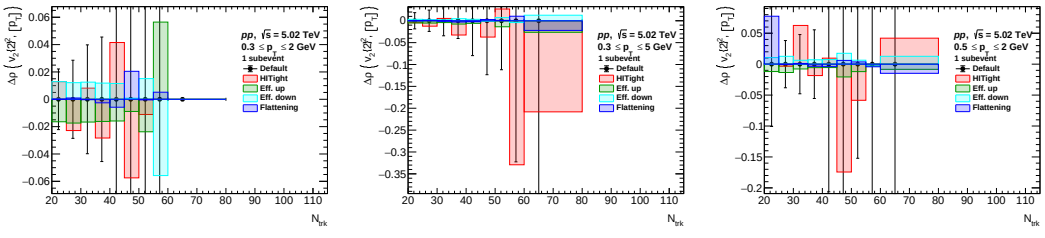

Figure D.17: Difference of 1-sub-event $\rho(v_2\{2\}^2, [p_T])$ in pp 5.02 TeV between different systematic uncertainties sources and baseline measurement Δ_{source} in various p_T ranges, statistical uncertainty for baseline measurement is shown as a black line.

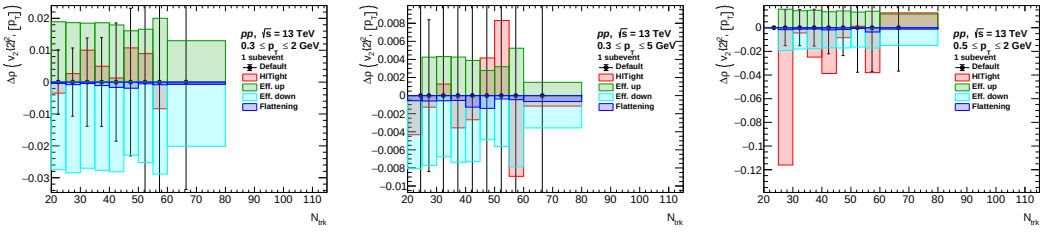

Figure D.18: Difference of 1-sub-event $\rho(v_2\{2\}^2, [p_T])$ in pp 13 TeV between different systematic uncertainties sources and baseline measurement Δ_{source} in various p_T ranges, statistical uncertainty for baseline measurement is shown as a black line.

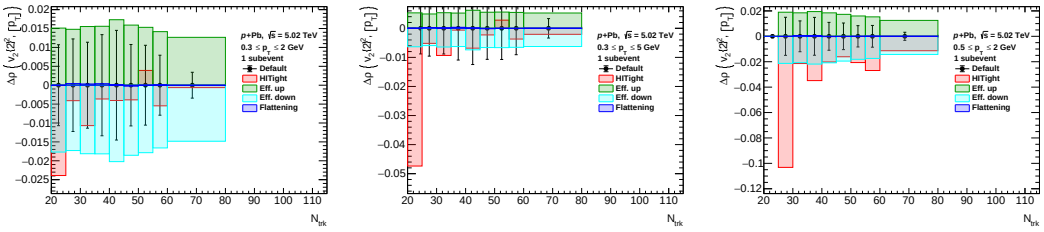

Figure D.19: Difference of 1-sub-event $\rho(v_2\{2\}^2, [p_T])$ in p+Pb 5.02 TeV between different systematic uncertainties sources and baseline measurement Δ_{source} in various p_T ranges, statistical uncertainty for baseline measurement is shown as a black line.

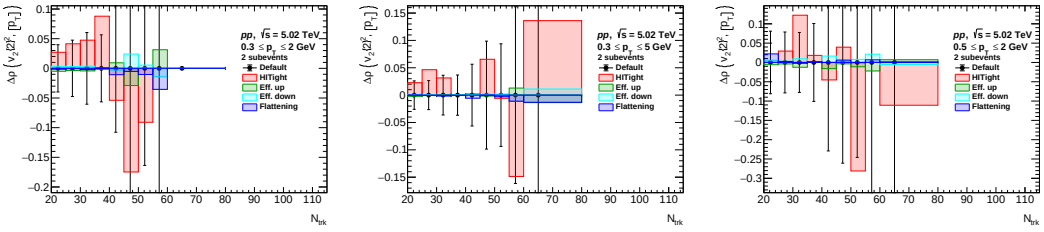

Figure D.20: Difference of 2-sub-event $\rho(v_2\{2\}^2, [p_T])$ in pp 5.02 TeV between different systematic uncertainties sources and baseline measurement Δ_{source} in various p_T ranges, statistical uncertainty for baseline measurement is shown as a black line.

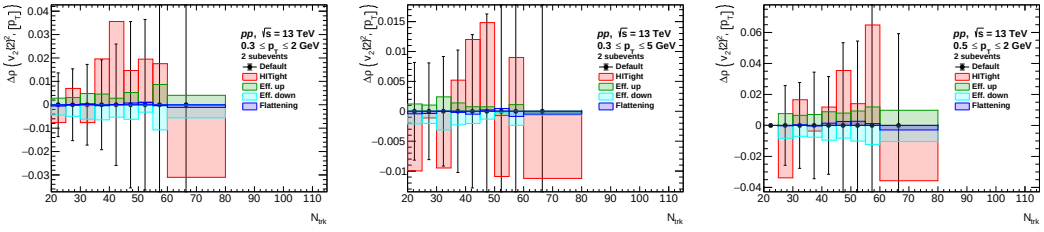

Figure D.21: Difference of 2-sub-event $\rho(v_2\{2\}^2, [p_T])$ in pp 13 TeV between different systematic uncertainties sources and baseline measurement Δ_{source} in various p_T ranges, statistical uncertainty for baseline measurement is shown as a black line.

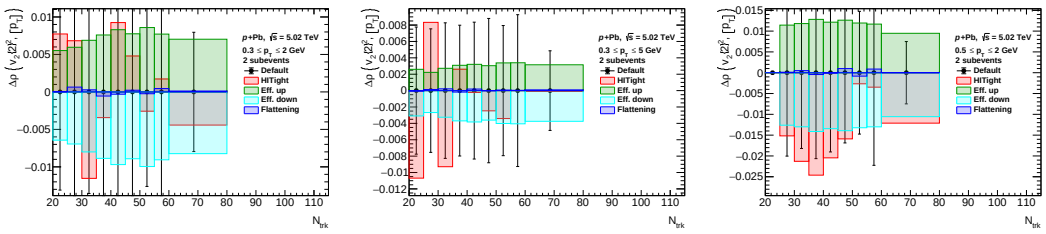

Figure D.22: Difference of 2-sub-event $\rho(v_2\{2\}^2, [p_T])$ in p+Pb 5.02 TeV between different systematic uncertainties sources and baseline measurement Δ_{source} in various p_T ranges, statistical uncertainty for baseline measurement is shown as a black line.

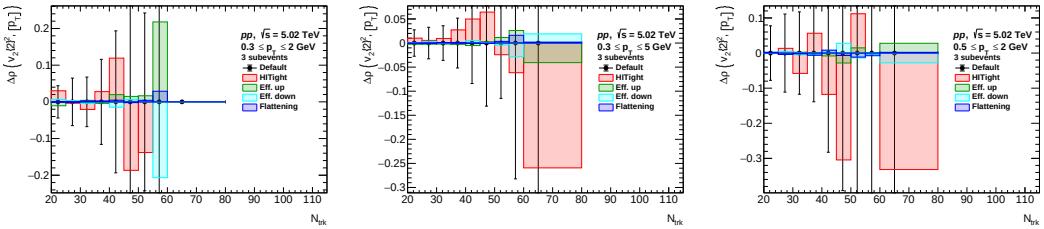

Figure D.23: Difference of 3-sub-event $\rho(v_2\{2\}^2, [p_T])$ in pp 5.02 TeV between different systematic uncertainties sources and baseline measurement Δ_{source} in various p_T ranges, statistical uncertainty for baseline measurement is shown as a black line.

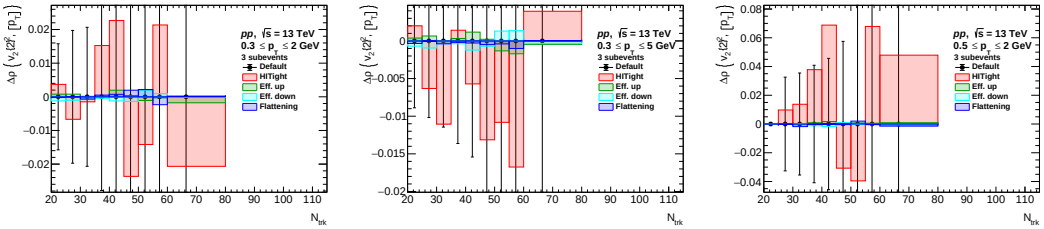

Figure D.24: Difference of 3-sub-event $\rho(v_2\{2\}^2, [p_T])$ in pp 13 TeV between different systematic uncertainties sources and baseline measurement Δ_{source} in various p_T ranges, statistical uncertainty for baseline measurement is shown as a black line.

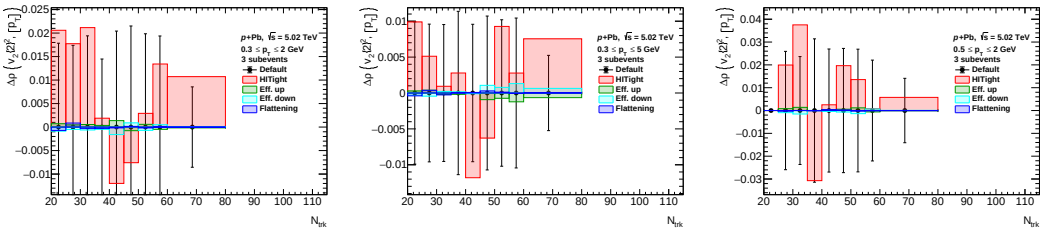

Figure D.25: Difference of 3-sub-event $\rho(v_2\{2\}^2, [p_T])$ in p+Pb 5.02 TeV between different systematic uncertainties sources and baseline measurement Δ_{source} in various p_T ranges, statistical uncertainty for baseline measurement is shown as a black line.

D.6 Uncertainties on $\mathrm{Var}\left(v_3\{2\}^2\right)_{\mathrm{dyn}}$

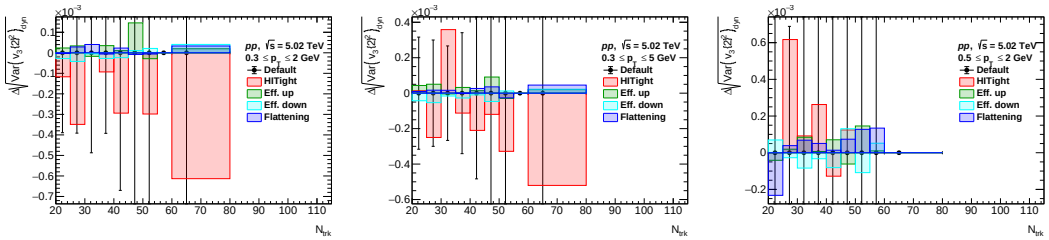

Figure D.26: Difference of $\mathrm{Var}(v_3\{2\}^2)_{\mathrm{dyn}}$ in pp 5.02 TeV between different systematic uncertainties sources and baseline measurement Δ_{source} in various p_T ranges, statistical uncertainty for baseline measurement is shown as a black line.

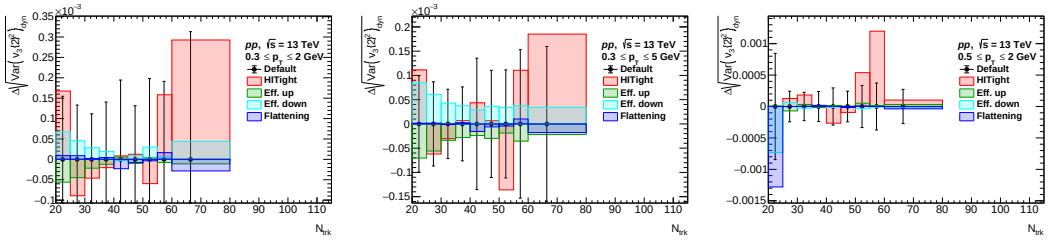

Figure D.27: Difference of $\mathrm{Var}(v_3\{2\}^2)_{\mathrm{dyn}}$ in pp 13 TeV between different systematic uncertainties sources and baseline measurement Δ_{source} in various p_T ranges, statistical uncertainty for baseline measurement is shown as a black line.

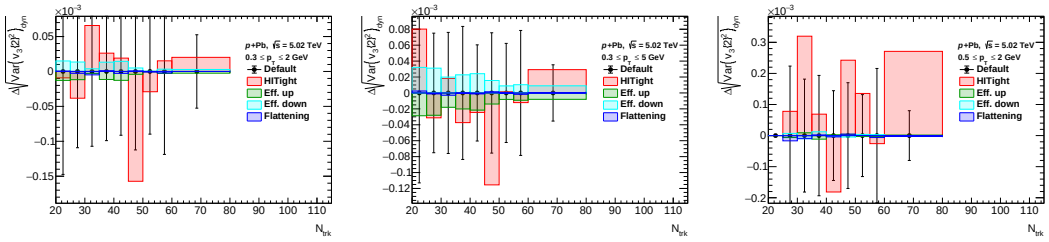

Figure D.28: Difference of $\mathrm{Var}(v_3\{2\}^2)_{\mathrm{dyn}}$ in p+Pb 5.02 TeV between different systematic uncertainties sources and baseline measurement Δ_{source} in various p_T ranges, statistical uncertainty for baseline measurement is shown as a black line.

D.7 Uncertainties on $\mathrm{cov}(v_3\{2\}^2, [p_\mathrm{T}])$

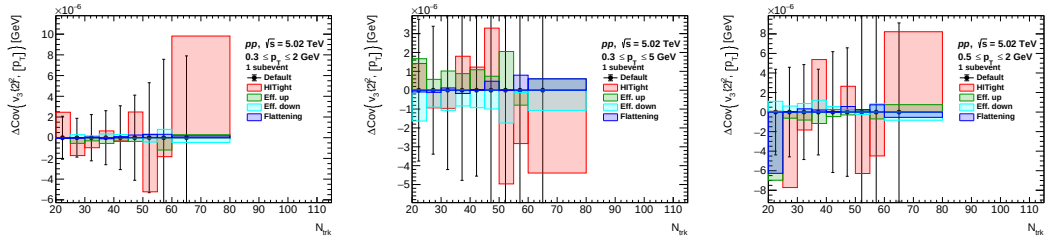

Figure D.29: Difference of 1-sub-event $\mathrm{cov}(v_3\{2\}^2, [p_\mathrm{T}])$ in pp 5.02 TeV between different systematic uncertainties sources and baseline measurement Δ_{source} in various p_T ranges, statistical uncertainty for baseline measurement is shown as a black line.

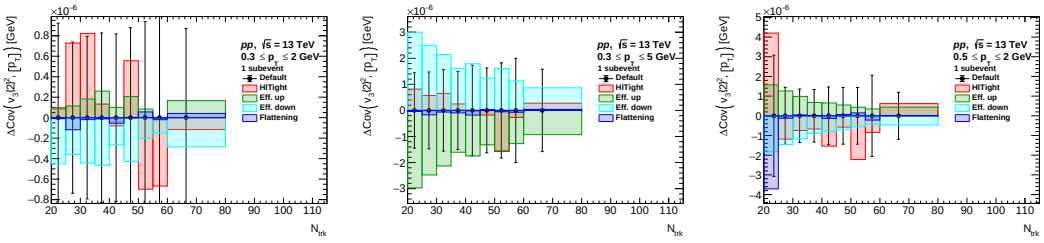

Figure D.30: Difference of 1-sub-event $\mathrm{cov}(v_3\{2\}^2, [p_\mathrm{T}])$ in pp 13 TeV between different systematic uncertainties sources and baseline measurement Δ_{source} in various p_T ranges, statistical uncertainty for baseline measurement is shown as a black line.

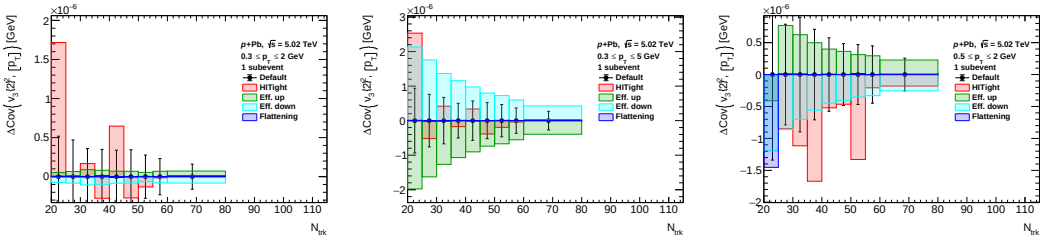

Figure D.31: Difference of 1-sub-event $\mathrm{cov}(v_3\{2\}^2, [p_\mathrm{T}])$ in p+Pb 5.02 TeV between different systematic uncertainties sources and baseline measurement Δ_{source} in various p_T ranges, statistical uncertainty for baseline measurement is shown as a black line.

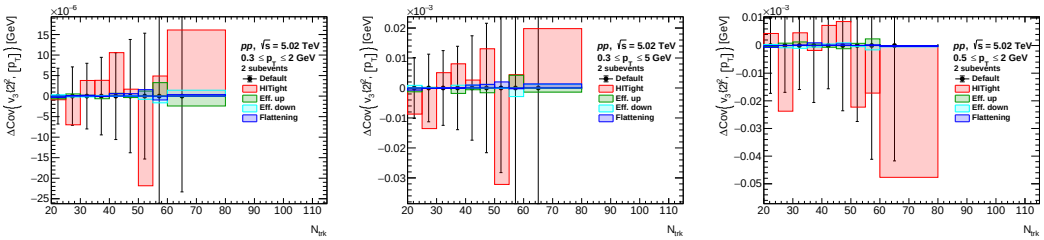

Figure D.32: Difference of 2-sub-event $\mathrm{cov}(v_3\{2\}^2, [p_\mathrm{T}])$ in pp 5.02 TeV between different systematic uncertainties sources and baseline measurement Δ_{source} in various p_T ranges, statistical uncertainty for baseline measurement is shown as a black line.

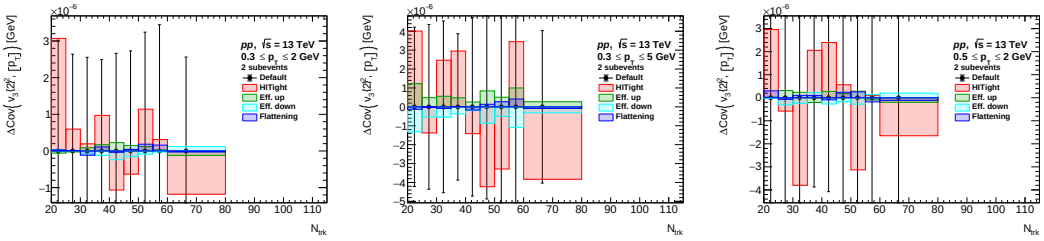

Figure D.33: Difference of 2-sub-event $\mathrm{cov}(v_3\{2\}^2, [p_\mathrm{T}])$ in pp 13 TeV between different systematic uncertainties sources and baseline measurement Δ_{source} in various p_T ranges, statistical uncertainty for baseline measurement is shown as a black line.

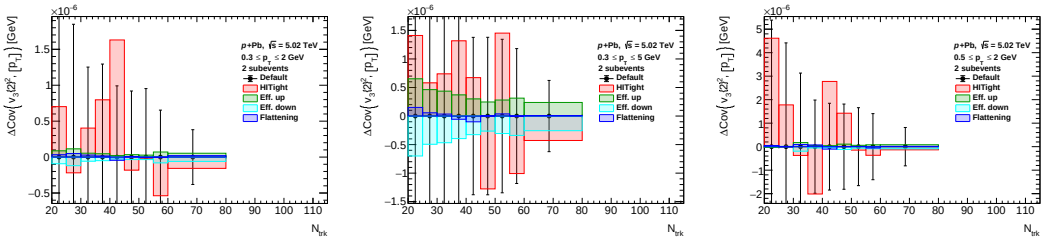

Figure D.34: Difference of 2-sub-event $\mathrm{cov}(v_3\{2\}^2, [p_\mathrm{T}])$ in p+Pb 5.02 TeV between different systematic uncertainties sources and baseline measurement Δ_{source} in various p_T ranges, statistical uncertainty for baseline measurement is shown as a black line.

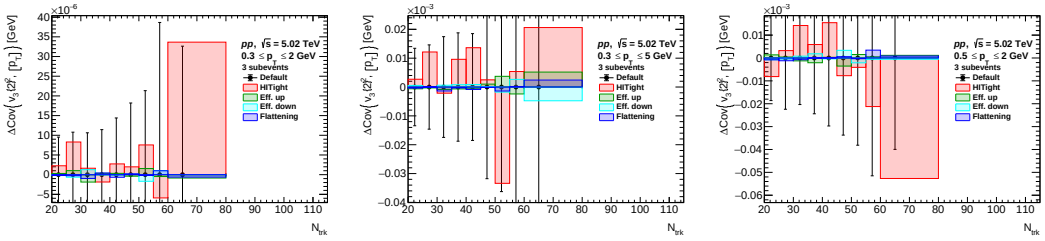

Figure D.35: Difference of 3-sub-event $\mathrm{cov}(v_3\{2\}^2, [p_\mathrm{T}])$ in pp 5.02 TeV between different systematic uncertainties sources and baseline measurement Δ_{source} in various p_T ranges, statistical uncertainty for baseline measurement is shown as a black line.

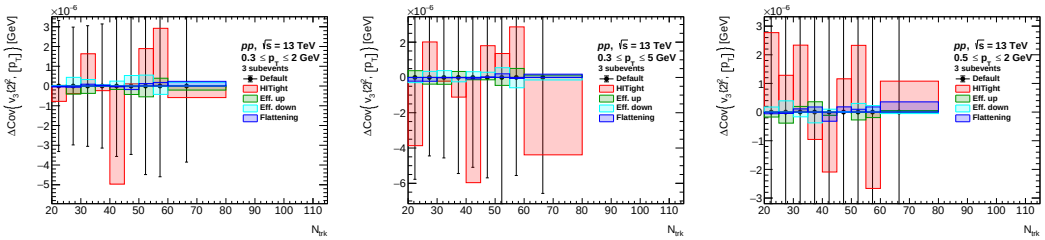

Figure D.36: Difference of 3-sub-event $\mathrm{cov}(v_3\{2\}^2, [p_\mathrm{T}])$ in pp 13 TeV between different systematic uncertainties sources and baseline measurement Δ_{source} in various p_T ranges, statistical uncertainty for baseline measurement is shown as a black line.

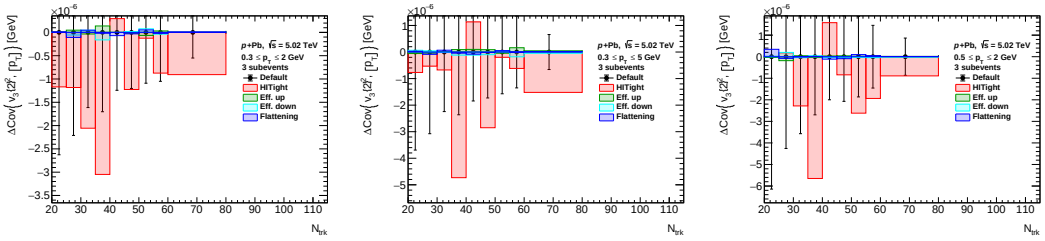

Figure D.37: Difference of 3-sub-event $\mathrm{cov}(v_3\{2\}^2, [p_\mathrm{T}])$ in p+Pb 5.02 TeV between different systematic uncertainties sources and baseline measurement Δ_{source} in various p_T ranges, statistical uncertainty for baseline measurement is shown as a black line.

D.8 Uncertainties on $\rho(v_3\{2\}^2, [p_T])$

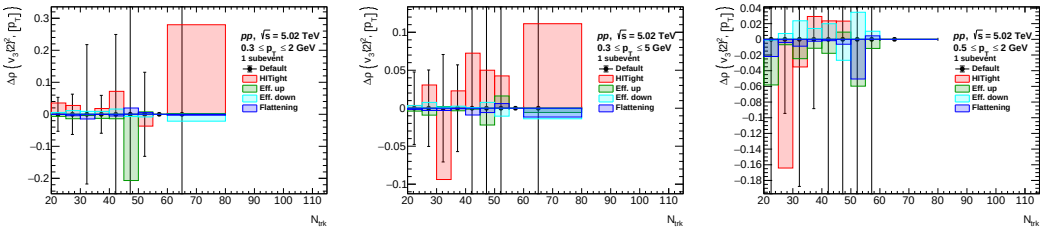

Figure D.38: Difference of 1-sub-event $\rho(v_3\{2\}^2, [p_T])$ in pp 5.02 TeV between different systematic uncertainties sources and baseline measurement Δ_{source} in various p_T ranges, statistical uncertainty for baseline measurement is shown as a black line.

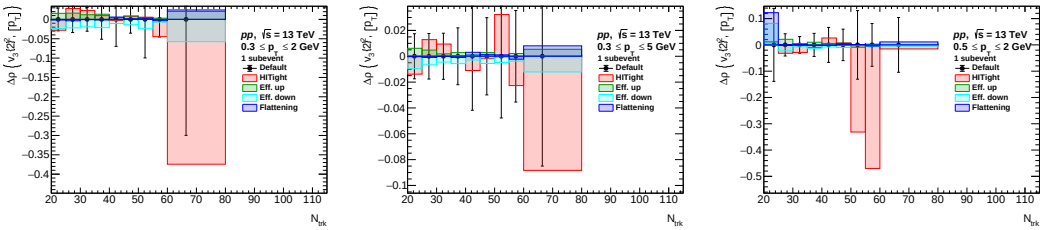

Figure D.39: Difference of 1-sub-event $\rho(v_3\{2\}^2, [p_T])$ in pp 13 TeV between different systematic uncertainties sources and baseline measurement Δ_{source} in various p_T ranges, statistical uncertainty for baseline measurement is shown as a black line.

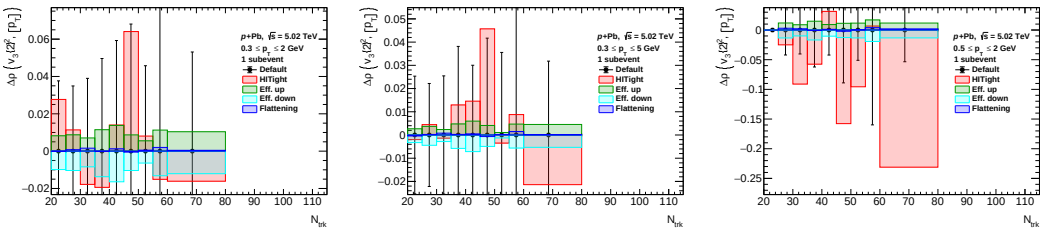

Figure D.40: Difference of 1-sub-event $\rho(v_3\{2\}^2, [p_T])$ in p+Pb 5.02 TeV between different systematic uncertainties sources and baseline measurement Δ_{source} in various p_T ranges, statistical uncertainty for baseline measurement is shown as a black line.

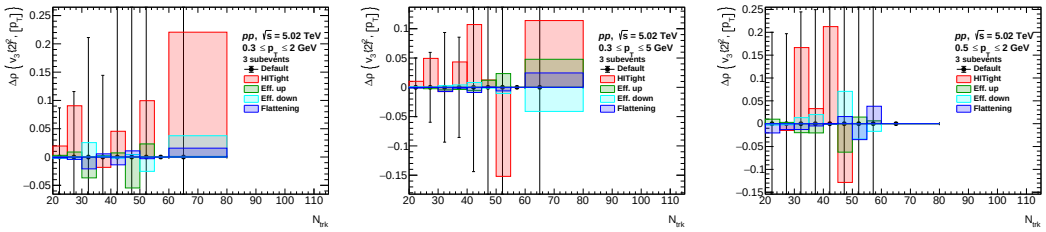

Figure D.41: Difference of 3-sub-event $\rho(v_3\{2\}^2, [p_T])$ in pp 5.02 TeV between different systematic uncertainties sources and baseline measurement Δ_{source} in various p_T ranges, statistical uncertainty for baseline measurement is shown as a black line.

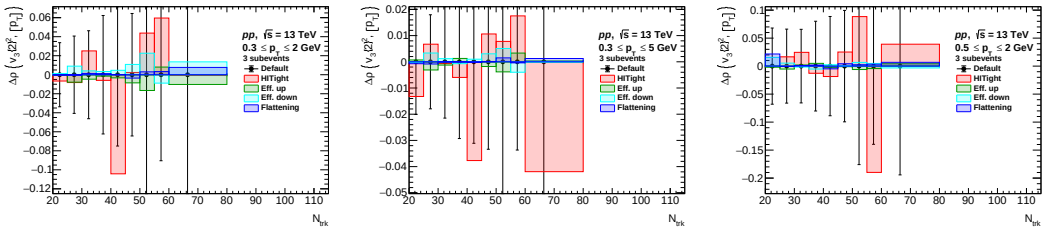

Figure D.42: Difference of 3-sub-event $\rho(v_3\{2\}^2, [p_T])$ in pp 13 TeV between different systematic uncertainties sources and baseline measurement Δ_{source} in various p_T ranges, statistical uncertainty for baseline measurement is shown as a black line.

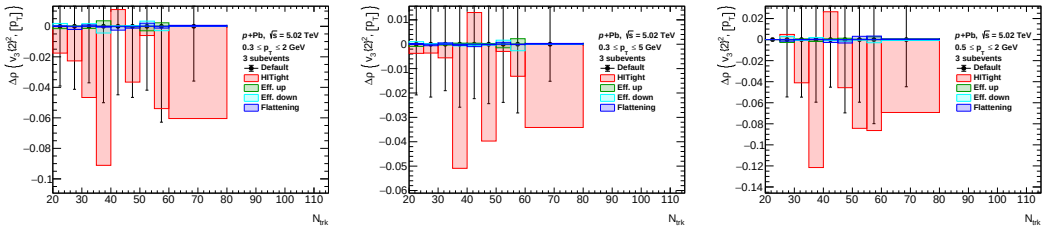

Figure D.43: Difference of 3-sub-event $\rho(v_3\{2\}^2, [p_T])$ in p+Pb 5.02 TeV between different systematic uncertainties sources and baseline measurement Δ_{source} in various p_T ranges, statistical uncertainty for baseline measurement is shown as a black line.